Molecular Gas in the Early Universe

5 - 7 NOVEMBER 2007
EUROPEAN SOUTHERN OBSERVATORY
SANTIAGO, CHILE

Paul Vanden Bout
National Radio Astronomy Observatory

Rough Outline

- Monday: Interstellar molecular gas and dust; CO in the Milky Way, nearby spirals, and starburst/IR-luminous galaxies.
- Tuesday: High-redshift molecular gas: examples of CO-emitting high-z galaxies, models and properties of these galaxies.
- Wednesday: Tuesday continued; scientific prospects and current status of ALMA.

Some Basic References

- *Tools of Radio Astronomy*, K. Rohlfs & T. L. Wilson, Springer, New York/Berlin, 2000.
- *Le milieu interstellaire*, J. Lequeux, CNRS Éditions, Paris, 2002; English edition, A&A Library, Springer, 2003.
- *Interferometry and Synthesis in Radio Astronomy*, A. R. Thompson, J. M. Moran, and G. W. Swenson, Wiley, New York, 2001.
- *The Physics of Interstellar Dust*, E. Krügel, IOP Series in Ast. & Astrophys., Bristol & Philadelphia, 2003.
- *Essential Radio Astronomy* by Condon and Ransom, [http://www.cv.nrao.edu/course/astr534/ERA.shtml].

I will approach this subject slowly. For the experts in the audience I will follow this advice:

"Never hesitate to give your audience the pleasure of hearing something they already know."

attributed to Victor Weisskopf

A motivation for many: to learn about galaxy formation in the early Universe by studying star formation in galaxies at high redshift.

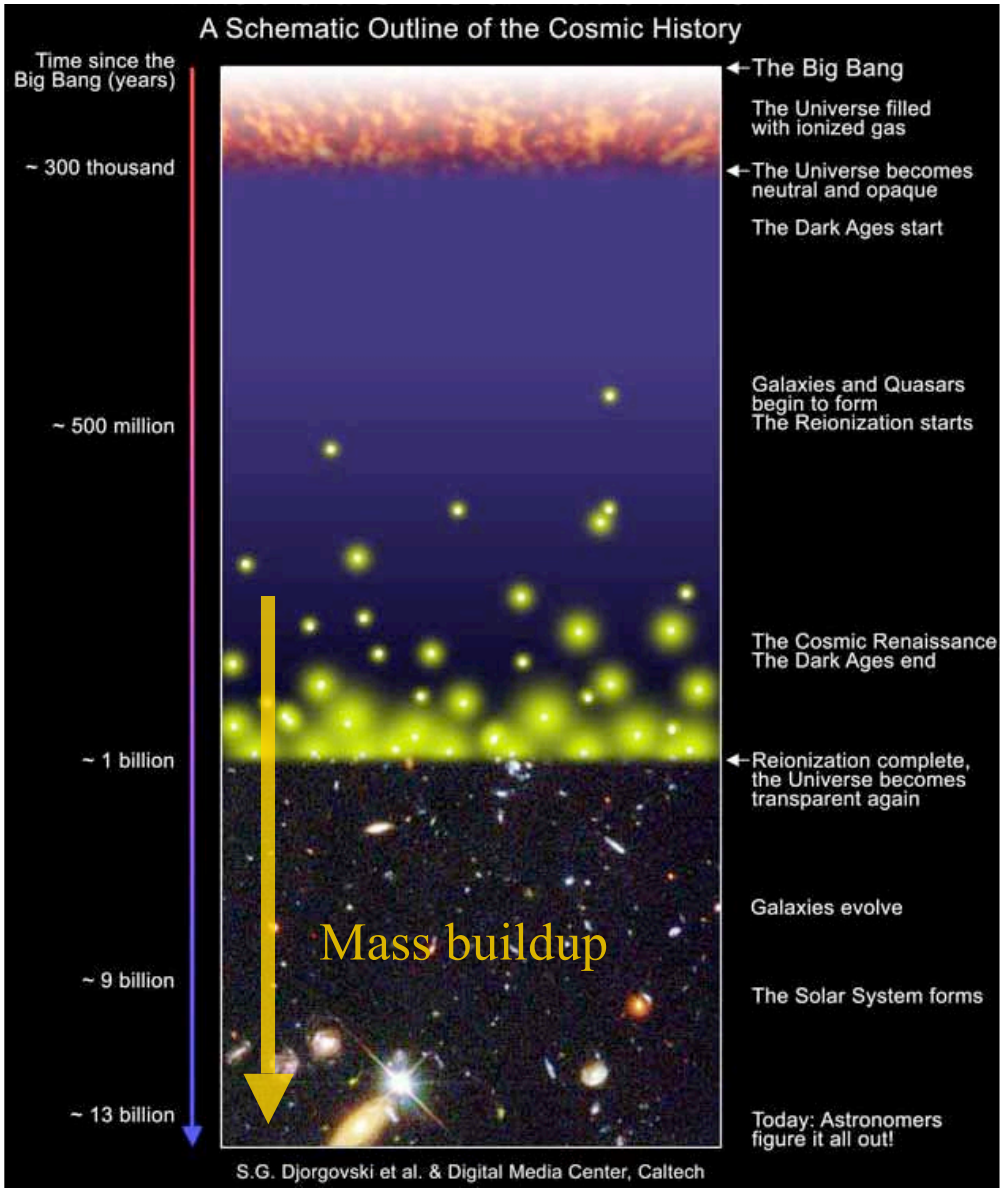

Recombination (z~1100)

First galaxies and quasars (z~10)

Re-ionization complete (z~6)

Solar System forms (z~0.5)

Galaxies today

[S. G. Gjorgovski et al. & Digital Media Center Caltech]

What Can We Learn About Star Formation in High-Redshift (z > 1) Galaxies With *Present Radio* Telescopes?

Only *global* parameters:

- Luminosity in molecular lines, leading to the mass of gas available to make stars.
- Luminosity in FIR, a measure of the rate of star formation.
- Star formation efficiency and star burst duration.
- Limited imaging (size) information.
- Some abundance information - atomic and molecular.
- Restricted to a heterogeneous sample; no blind surveys.

CO in the Milky Way: Thaddeus, Dame, et al.
(Southern Sky mapped from Cerro Tololo by Bronfman et al.)
[http://cfa-www.harvard.edu/mmw/MilkyWayinMolClouds.html]

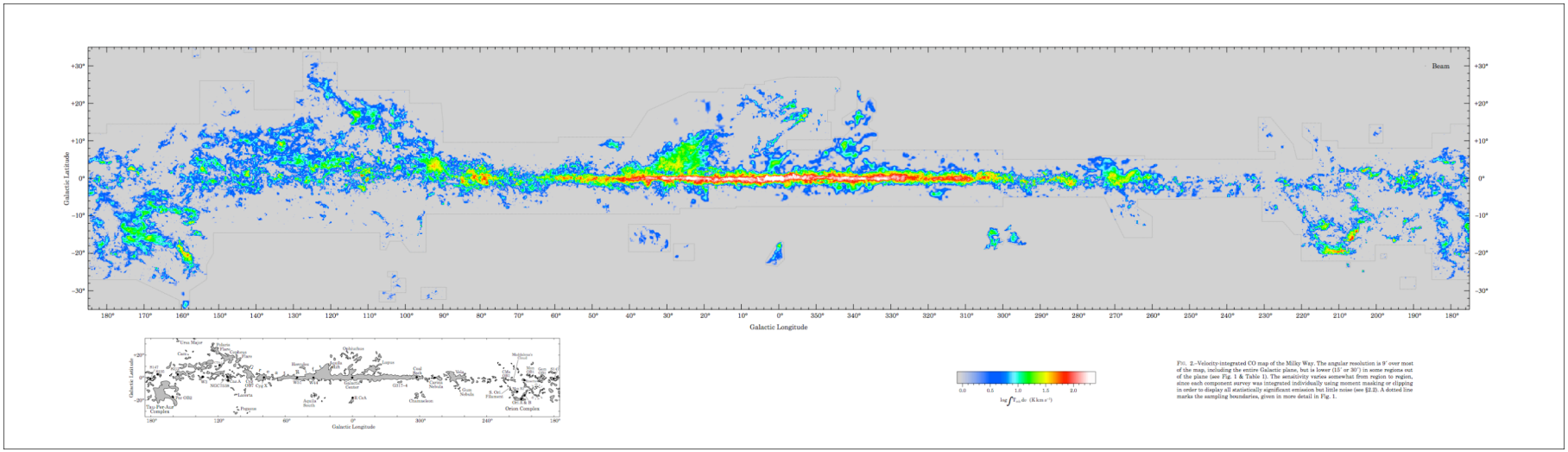

$L'(CO\ J=1\text{-}0) \sim 3 \times 10^8$ K km s^{-1} pc^2

$M(\text{molecular gas}) \sim 1.4 \times 10^9\ M_\odot \sim 1\%\ M(\text{visible disk})$

Most of the molecular gas is in ~ 6000 giant molecular clouds located in the inner 5 kpc (the so-called “Molecular Ring”).

Milky Way in the Far-Infrared

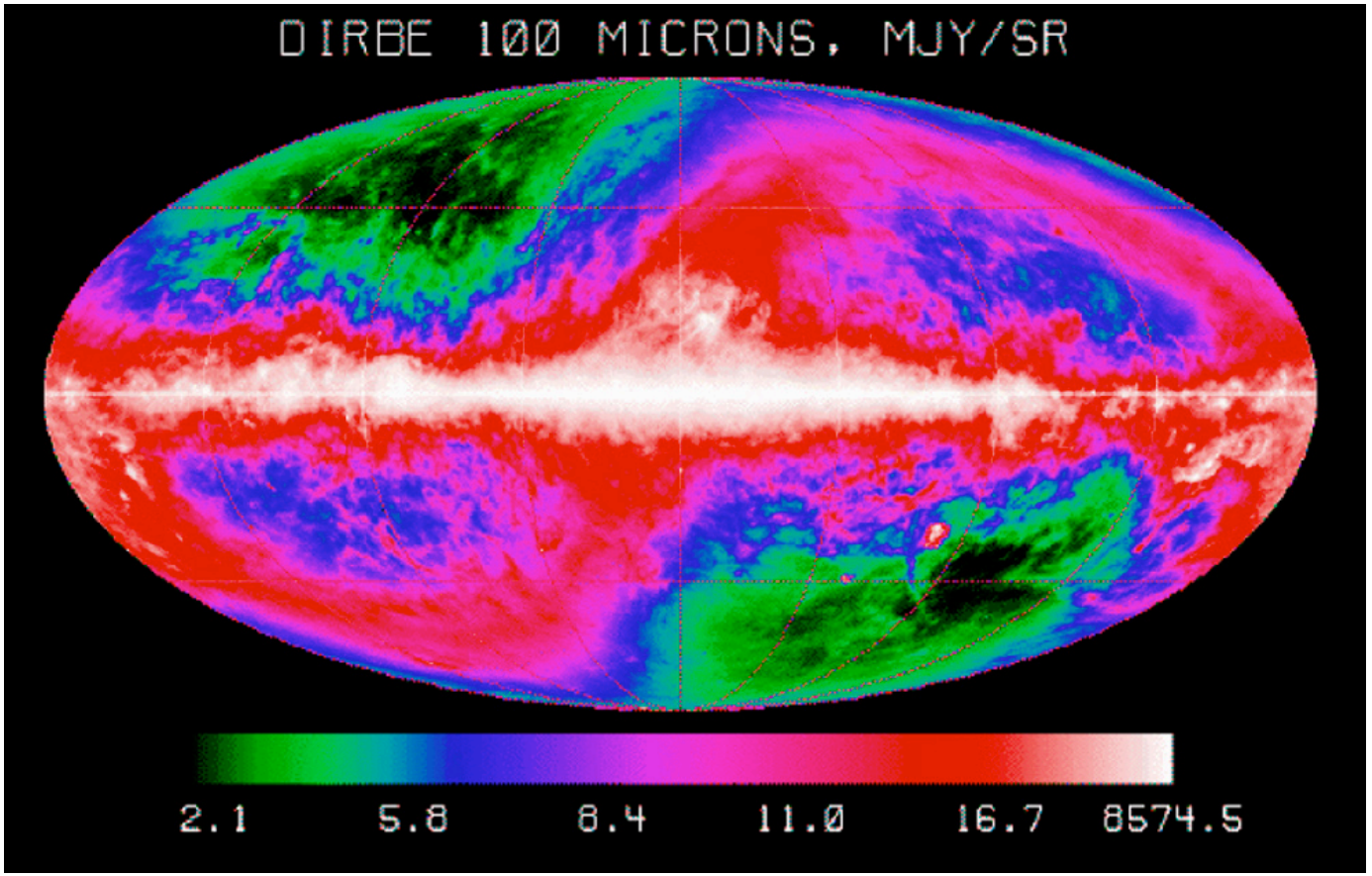

L(FIR) = 1.8 x 10^{10} $L_{\odot}$ [Wright et al. ApJ 381, 200 (1991)]

SFR ~ 3 $M_{\odot}$ per year

A Little (Familiar?) History

- In 1935/36, Adams & Dunham detected sharp optical interstellar lines later identified as CH (Swings and Rosenfeld), CN (McKellar), and CH^+ (Herzberg & Douglas).
- In 1965, OH was detected by Barrett, and NH_3 and H_2O by Townes (& their co-workers).
- A flood of ISM molecular detections followed, *of which the most important by far was CO in 1970 by Wilson, Jefferts, and Penzias.*

Interstellar Molecules

144 as of August 2007

Red Lettering => IR or UV Detections | Colored Background ==> Isomers | * no isomer possible | ** GBT molecule

Molecules with 2 atoms			
H_2	hydrogen molecule	CO	carbon monoxide
CSi	carbon monosilicide	CP	carbon monophosphide
CS	carbon monosulfide	NO	nitric oxide
NS	nitrogen monosulfide	SO	sulfur monoxide
HCl	hydrogen chloride	NaCl	sodium chloride
KCl	potassium chloride	AlCl	aluminum monochloride
AlF	aluminum monofluoride	PN	phosphorus mononitride
SiN	silicon mononitride	SiO	silicon monoxide
SiS	silicon monosulfide	NH	imidyl radical
OH	hydroxyl radical	C_2	diatomic carbon
CN	cyanide radical	HF	hydrogen fluoride
CO^+	carbon monoxide ion	SO^+	sulfur monoxide ion
CH	methylidyne	CH^+	methyliumylidene
SH	mercapto radical	LiH	lithium hydride
FeO	iron oxide	N_2	diatomic nitrogen
CF^+	flouromethylidynium ion		

Molecules with 3 atoms			
H_2O	water *	H_2S	hydrogen sulfide *
HCN	hydrogen cyanide	HNC	hydrogen isocyanide
CO_2	carbon dioxide *	SO_2	sulfur dioxide
MgCN	magnesium cyanide	MgNC	magnesium isocyanide
NaCN	sodium cyanide	N_2O	nitrous oxide
NH_2	amidyl radical *	OCS	carbonyl sulfide *
HCO	formyl radical	C_3	triatomic carbon *
C_2H	ethynyl radical *	HCO^+	formyl ion
HOC^+	hydroxymethylidyne	N_2H^+	hydrodinitrogen ion *
HNO	nitrosyl hydride	HCS^+	thiooxomethylium
H_3^+	hydrogen ion *	C_2O	ketenylidene *
C_2S	thioxothenylidene	SiC_2	silicon dicarbide
AlNC	aluminum isocyanide	CH_2	methylene *
SiCN	silicon monocyanide	SiNC	silicon isocyanide
HCP	phosphaethyne		

Compliments of J.M. Hollis and A.J. Remijan

Molecules with 4 atoms

NH_3	ammonia *	H_2CO	formaldehyde
H_2CS	thioformaldehyde	C_2H_2	acetylene
HNCO	isocyanic acid	HNCS	thioisocyanic acid
H_3O^+	hydronium ion *	$HOCO^+$	protonated carbon dioxide
C_3S	1,2-propadienylidene, 3 thioxo	H_2CN	methylene amidogen
c-C_3H	cyclopropenylidyne	l-C_3H	2-propynylidyne
HCCN	cyanomethylene	C_3O	tricarbon monoxide
C_2CN	cyanoethynyl	SiC_3	Rhomboidal SiC_3
$HCNH^+$	iminomethylium	CH_3	methyl radical *

Molecules with 5 atoms

CH_4	methane *	SiH_4	silane *
CH_2NH	methyleneimine	NH_2CN	cyanamide
CH_2CO	ketene	HCOOH	formic acid
HC_3N	cyanoacetylene	HC_2NC	isocyanoacetylene
c-C_3H_2	cyclopropenylidene	l-C_3H_2	propenylidene
CH_2CN	cyanomethyl radical	H_2COH^+	protonated formaldehyde
C_4Si	silicon tetracarbide	C_5	pentacarbon molecule
HNC_3	1,2-propadienylidene, -3-imino	C_4H	1,3-butadiynyl radical
		C_4H^-	butadiynylide ion

Molecules with 6 atoms

CH_3OH	methanol *	CH_3SH	methanethiol *
H_2CCH_2	ethylene	HCCCCH	diacetylene
CH_3CN	methyl cyanide	CH_3NC	methylisocyanide
$HCONH_2$	formamide	HC_2CHO	propynal
C_5H	2,4-pentadiynylidyne	HC_3NH^+	protonated 2-propynenitrile
C_5N	1,3-butadiynylium, 4-cyano	H_2CCCC	butatrienylidene
HC_4N	3-cyano 2-propynylidene	c-H_2C_3O **	cyclopropenone
CH_2CNH **	ketenimine		

Molecules with 7 atoms

CH_3CCH	methyl acetylene	CH_3CHO	acetaldehyde
CH_3NH_2	methylamine *	CH_2CHCN	vinyl cyanide
HC_5N	cyanobutadiyne	C_6H	1,3,5-hexatriynl
c-C_2H_4O	ethylene oxide	CH_2CHOH	vinyl alcohol
C_6H^- **	hexatrinylide ion		

Molecules with 8 atoms

CH_3COOH	acetic acid	CH_3OCHO	methyl formate
CH_3C_3N	methylcyanoacetylene	$CH_2(OH)CHO$	glycolaldehyde
H_2C_6	hexapentaenylidene	HC_6H	triacetylene
CH_2CHCHO **	propenal	C_7H	2,4,6-heptatriynylidyne
CH_2CCHCN **	cyanoallene		

Molecules with 9 atoms

$(CH_3)_2O$	dimethyl ether	CH_3CH_2OH	ethanol
CH_3CH_2CN	ethyl cyanide	CH_3C_4H	methylbutadiyne
HC_7N	cyanohexatriyne	C_8H	1,3,5,7-octateraynyl
CH_2CHCH_3	propylene	C_8H^- **	octatetraynylide
CH_3CONH_2 **	acetamide		

Molecules with 10 atoms

$(CH_3)_2CO$	acetone	$HOCH_2CH_2OH$	ethylene glycol
CH_3CH_2CHO **	propanal	CH_3C_5N **	methylcyano diacetylene

Molecules with 11 atoms

HC_9N	cyanooctatetrayne	CH_3C_8H **	methyltriacetylene

Molecules with 12 atoms

C_6H_6	benzene		

Molecules with 13 atoms

$HC_{11}N$	cyanodecapentayne		

There are 12,333 detected unique molecular line transitions in the ISM of the Milky Way

- F. Lovas maintains a list of these lines, and a second list, "Spectral Line Atlas of IS Molecules" (SLAIM), that has *calculated* frequencies for IS molecules;
- These lists & others can be found at www.splatalog.net, an (NRAO) ALMA tool developed by A. Remijan;
- Check for the latest version with handy search tools to be released to public in December 2007.

Example: the CN(3-2) hfs lines seen in the Cloverleaf (z = 2.56)

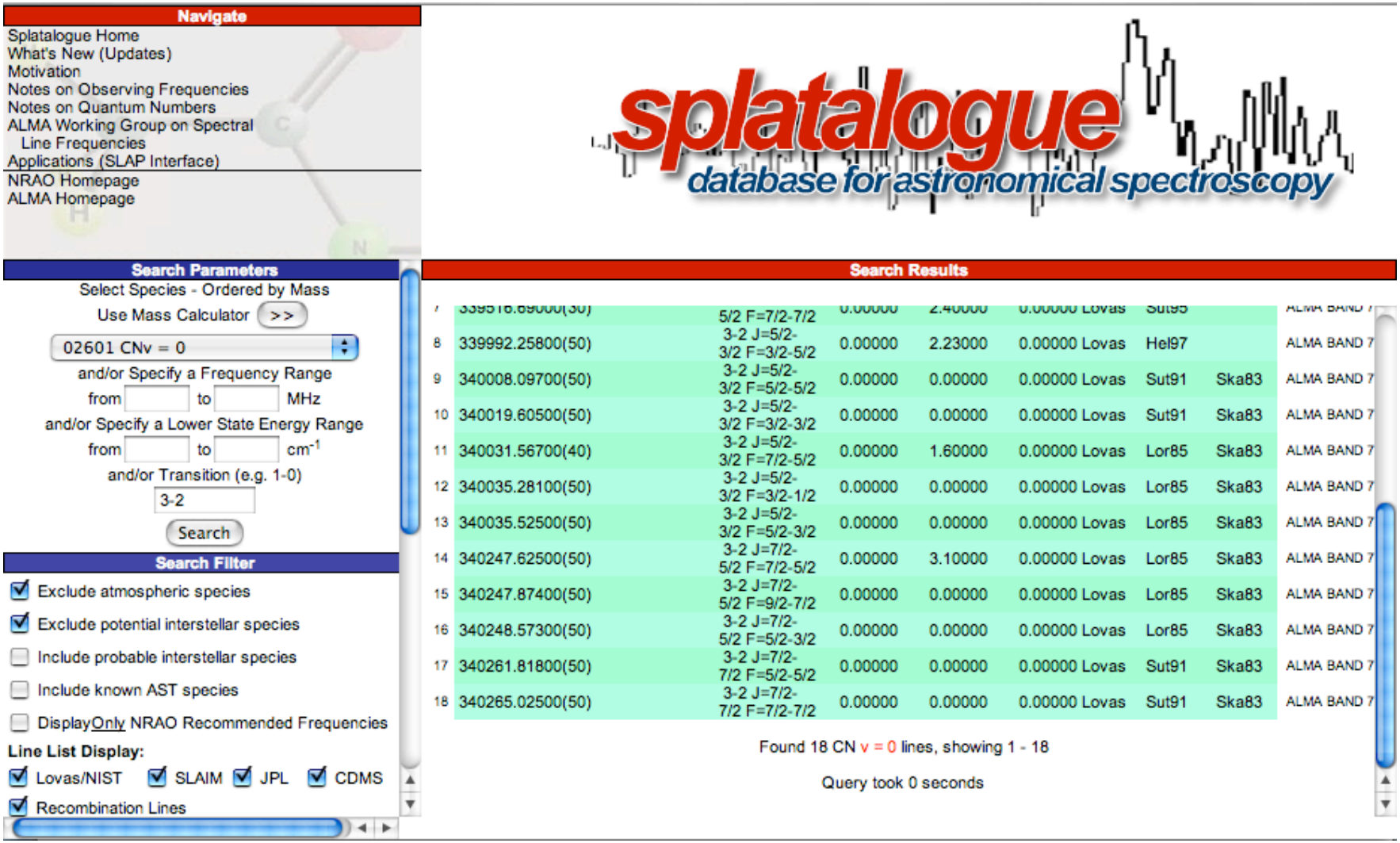

Molecular Gas "Clouds"

The IS molecular gas is said to exist in "clouds". The term makes sense in that molecular clouds are self-shielding with reasonably well-defined edges. H_2 is radiatively dissociated by UV absorption in *lines*, not by broad-band continuum absorption, due to its symmetry and electronic structure. Once the density and opacity to UV has reached a certain point, the gas makes an abrupt transition from atomic to molecular as you go into the cloud from the outside.

Crude Cloud Model

If, as you enter the cloud, $\tau_V \leq 1, 2, 3$ at the boundaries shown, then:

Hydrogen is atomic for $\tau_V \leq 1$, and molecular for $\tau_V \geq 1$;

Carbon is C^+ for $\tau_V \leq 2$, and C for $\tau_V \geq 2$;

and virtually all (gaseous) C is in CO for $\tau_V \geq 3$.

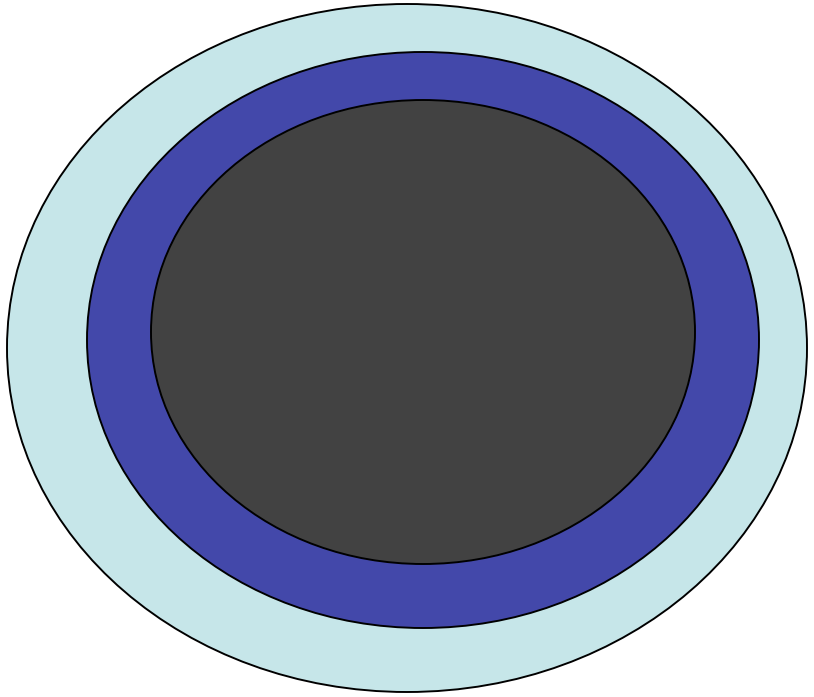

H_2 Formation

- Because of symmetry considerations, you cannot form H_2 by colliding two H atoms, as there is no allowed radiative process to carry off the excess energy of formation. A third H atom can do this, but three-body collisions are rare.
- H_2 forms on grain surfaces.
- In the early Universe, the presence of H^+ allows H_2 to form before the nucleosynthesis of heavy elements and grain formation. Once grains are present, surface reactions are dominate.

CO Is the Preeminent Signpost of Interstellar Molecular Gas

- H_2 is observable in high temperature (> 500K) - photo-dissociated or shocked - regions, but not in the typical molecular cloud where T ~ 5 - 50 K.

Spitzer Observations of H_2

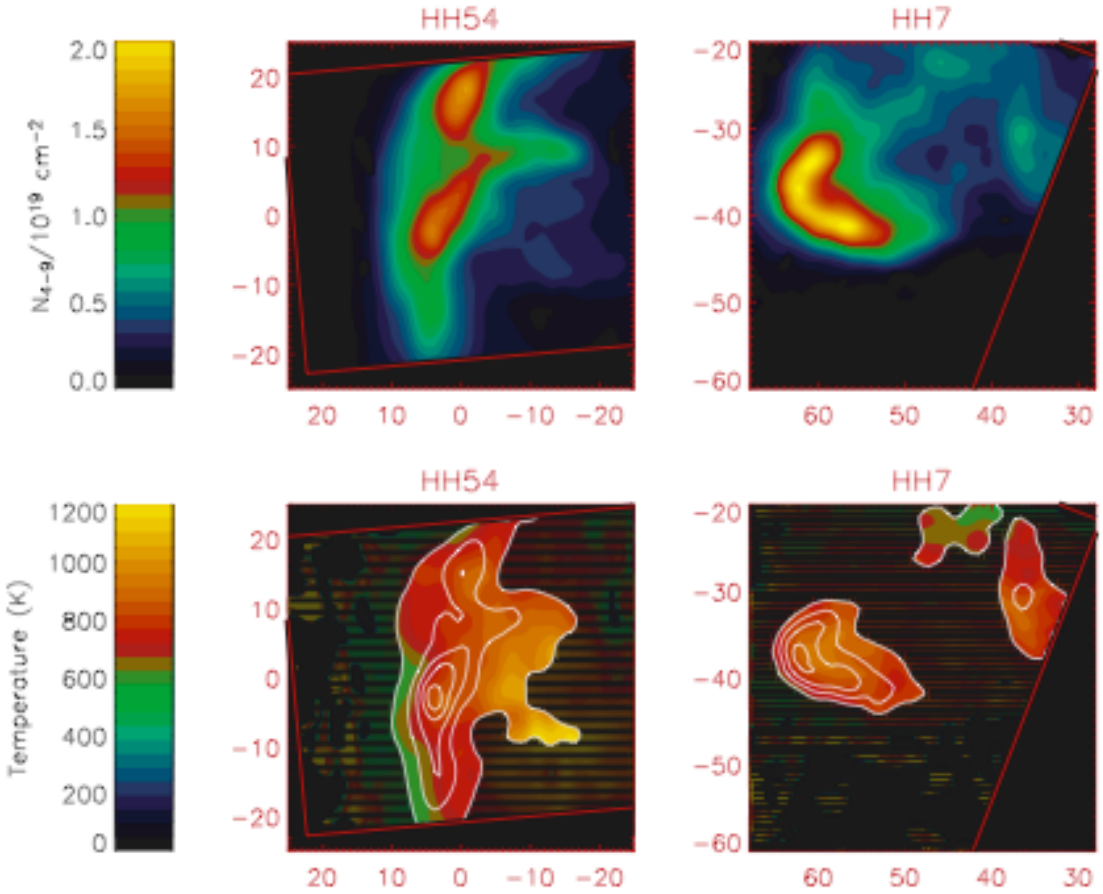

Neufeld, et al. ApJ 649, 816 (2006)

CO Is the Preeminent Signpost of Interstellar Molecular Gas

- H_2 is observable in high temperature (> 500K) - photo-dissociated or shocked - regions, but not in the typical molecular cloud where T ~ 5 - 50 K.
- CO has a high dissociation energy of 11.09 eV and is the most abundant IS molecule after H_2; relative abundance $CO/H_2 \sim 8 \times 10^{-5}$, in the Galaxy.
- CO has a small electric dipole moment, only 0.112 debye, which makes for easy collisional excitation of the rotational transitions; the critical density for J=1-0 is only ~ 100 cm^{-3}.

Molecular Rotational Spectra

- Very roughly, molecules exhibit three types of spectra: electronic (optical), vibrational (infrared), and rotational (mm, submm, radio).
- Molecules will emit in rotational transitions provided there is at least one axis of asymmetry, allowing for a permanent electric dipole moment. (CO_2, H_2, O_2, N_2, CH_4, etc. have no rotational spectra.)
- The strength of the emission depends on the square of the electric dipole moment, μ(esu-cm = debye).

Rotational Spectra of Linear Molecules (CO, HCN, etc.)

- The energy levels are given by

  $E_J = (\text{const.}/I)J(J+1)$, where I is the moment of inertia and J is the rotational quantum number, J = 0, 1, 2, …
- Allowed transitions have $\Delta J = 1$ yielding transition frequencies $f_J \approx J\, f_{J=1}$, where J denotes the upper energy level involved.
- For CO, $f_{J=1} = 115.271201$ GHz.

- Observed *frequencies* can be measured to high precision - spectrometer resolution can be > 10^6; line widths and sensitivity are the limiting factors.
- Isotopologues (for example, $^{12}C^{16}O$, $^{13}C^{16}O$, $^{12}C^{18}O$, $^{13}C^{18}O$) have well separated transitions, with frequency separations of ~ few %.
- Observations can reveal a wealth of kinematic information about the emitting gas.
- Observed *intensities* are difficult to calibrate; "good calibration" typically means 10%; the requirement for ALMA is 5% absolute and 3% relative for the lower (not the submm) frequency bands, with a goal of doing even better.

Complicating Details

- For higher J, the frequencies are not exact multiples because of centrifugal distortion.
- Some molecules exhibit fine structure & hyper-fine structure. HCN J=1-0 is split into three lines, for example, by the nuclear quadrupole moment of N.
- Formaldehyde, H_2CO, comes in two forms, depending on the alignment of the H nuclear spins, ortho (parallel) and para (anti-parallel).

- Para-H_2CO has a CO-like spectrum with mm wavelength transition;
- Ortho-H_2CO has its energy levels split into pairs, with both mm and cm wavelength transitions in its spectrum.
- Asymmetric tops have more complex rotational spectra.
- The molecules detected (so far) at high-z (CO, HCN, HCO^+, HNC) all have simple spectra, except for CN.

Excitation

- Excitation of interstellar molecules to levels above the ground state is generally due to collisions with H_2 and He, as the clouds are dark.
- Note: molecules in circumstellar shells and the near vicinity of AGN can be radiatively excited.
- The excitation balance is set by the density n and the spontaneous emission coefficient A. The critical density n_c is defined as the density at which excitation balances de-excitation:

  $n_c = A_{ul}/C_{lu}$, for CO, $C_{01} \sim 3\ C_{10} \sim 3x10^{-11}$ cm^3 s^{-1} for a kinetic T = 10-50K, and $n_c = A_{10}/C_{01} \sim 100$ cm^{-3}. At this density, ~ 10% of the CO molecules are in J=1.

  For HCN(J=1-0), $n_c \sim 3x10^4$ cm^{-3}.
- For large τ, trapping of radiation lowers n_c.

Rarer Isotopologues of CO Trace Regions of Denser Gas

Boston Univ. Survey of ^{13}CO(J=1-0) in the Milky Way

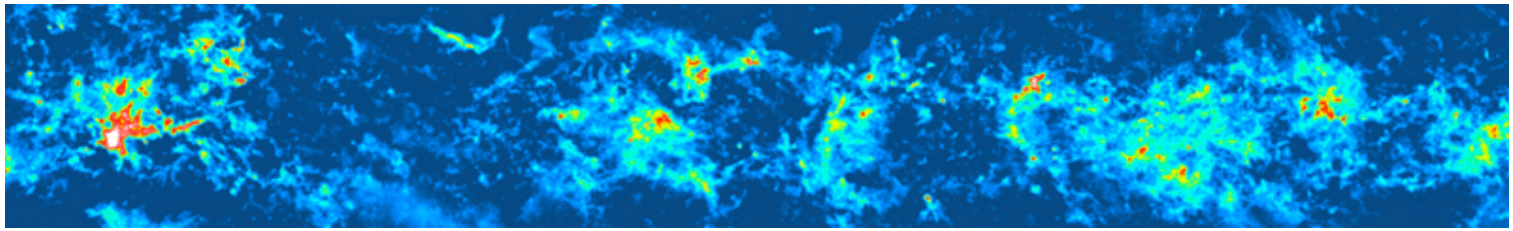

Integrated ^{13}CO J=1-0 intensity from the first 16 square degrees covered by the Boston Univ. Galactic Ring Survey.

www.bu.edu/galacticring

Molecular Probes of Physical Conditions

- As CO is so easily excited by collisions, this leads to thermalized rotational lines characterized by a rotational temperature T_r. It is a probe of the gas kinetic temperature, $T_k = T_r - T_{bk}$, where T_r is obtained from observations of an optically thick line and $T_{bk} = 2.7K$.
- Gas temperatures in Galactic IS clouds vary from 10-50K, somewhat cooler in quiescent clouds and somewhat hotter in the most active star-forming dense cloud cores.

- Ammonia, NH_3, is another good temperature probe. Recently, para-H_2CO has been used as a temperature probe in M82 by Mühle et al. [astro-ph/0708.1710].
- Studies of Galactic molecular cloud cores have used HCN and CS as density probes, as well as other molecules with large n_c. In external galaxies, particularly at high-z, HCN is the probe of choice, with high-J CO transitions also indicating dense gas.

Other Line Information

- *Line widths* can be thermal in cold, tenuous clouds and much larger than thermal in warm, dense clouds, implying a turbulent structure for the latter.
- *Line velocity* indicates the gas motion along the line of sight, providing information on the motion of the source as a whole as well as on internal motion.

Analyzing Molecular Spectra

- Radiative transfer models (turbulent, large velocity gradient, . . .) can be fitted to observed data to derive T, n, and abundance.
- The "original" LVG paper is still instructive - Goldreich & Kwan, ApJ 189, 441 (1974).
- For an on-line "LVG" model, see RADEX page at: http://www.strw.leidenuniv.nl/~moldata/radex.html (RADEX does not make the assumptions of a strictly Large Velocity Gradient model, hence, "LVG".)

  See van der Tak, et al. [A&A 432, 369 (2005); astro-ph/0411110].

Example: para-H_2CO in M82

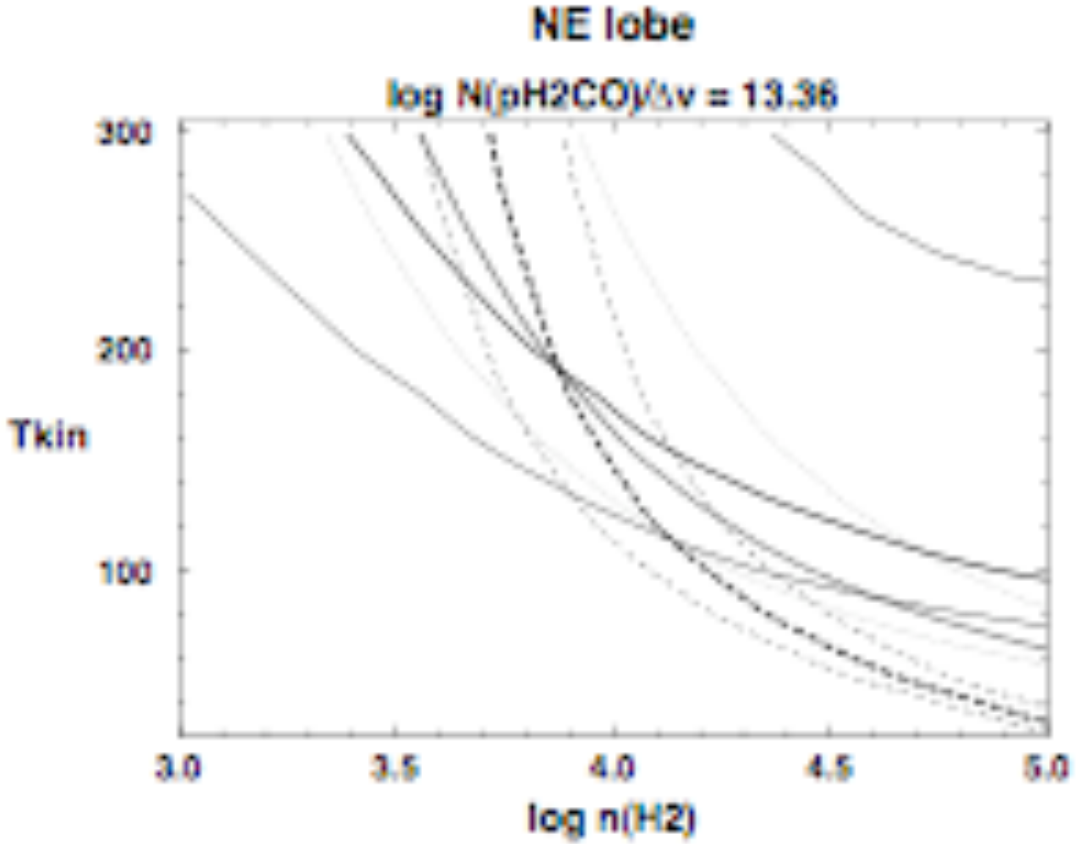

Mühle, S., et al. [arXiv:0708.1710]

Mangum et al. [arXiv:0710:2115] have reported a study of 19 IR-bright galaxies (including classic starbursts) in the K-doublet transitions of H_2CO;

The line strength ratio $(1_{10} - 1_{11})/(2_{11} - 2_{12})$ is a good density probe.

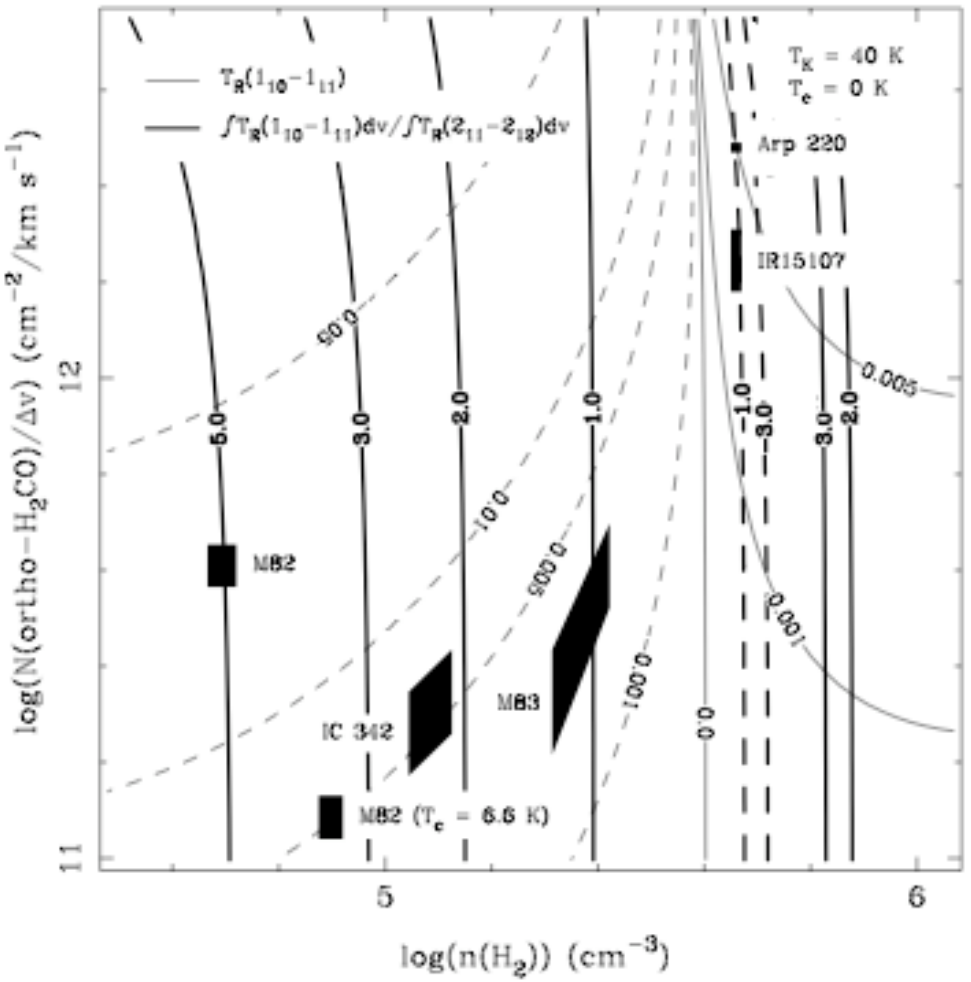

From CO to Gas (H_2 + He) Mass

- Gas mass is one of the most important physical properties CO can provide. (The conversion factor has a long, contentious history.)
- A molecular cloud's mass (in solar masses) is given by $M(H+He) = \alpha\, L'(CO\ J=1\text{-}0)$, where L' is the CO luminosity in (K km s^{-1} $pc^{2)}$ and $\alpha = 2.6n^{1/2}/T_b \sim 4.6$ (n is the gas density and T_b is the CO brightness temperature ~ kinetic temperature) *for Galactic giant molecular clouds*.
- There are three independent methods for determining α in the Galaxy, all yielding values that are consistent to within a factor of 2-3.

Calibrating α

- Correlation of optical extinction with N(^{13}CO) [Dickman, ApJS 37, 407 (1978)].
- Correlation of the flux of γ-rays, produced by cosmic rays interacting with HI, with the CO line flux from the Galactic molecular ring (Bloemen et al. A&A 154, 25 (1986); and Strong et al. A&A 207, 1 (1988)].
- Observed relationship between virial mass and CO line luminosity for Galactic giant molecular clouds [Solomon et al. ApJ 319, 730 (1987)].

Statistical Study of GMCs

- Solomon et al. [ApJ 319, 730 (1987)] studied 273 Galactic giant molecular clouds (GMCs), for line width, size, virial mass, and CO luminosity.
- They found a strong correlation between virial cloud mass and CO luminosity.
- Solomon & Barrett [*Dyn. Of Galaxies ... Proc. IAU Sym. 146, p. 235* (1991)] derive the following expression: $\alpha = 2.6n^{1/2}/T_b \sim 4.6$, using a distance to the Galactic center of 8.5 kpc.

Note: α vs. X

- α converts CO luminosity to gas mass;
- X converts the velocity integrated CO (usually ^{13}CO) antenna temperature to the column density of H_2;
- The two are equivalent but different - be mindful of the exact use by different authors.

Why L′ (K km s^{-1} pc^2) ?

- L′ is the brightness temperature of the line, integrated over the velocity distribution and surface area of the source [$L' = T_b(\Delta v)(\pi R^2)$].
- Ratios of L′ for different lines are ratios of intrinsic brightness temperatures, constraining source properties.
- Thermalized lines, such as the low-J transitions of CO, will have the same L′.
- For $z << 1$, $L' = 3.25 \times 10^{-5} \nu_{obs}^{-2} D^2 S\Delta v$, where ν(GHz), D(pc), and $S\Delta v$(Jy km s^{-1}).

More (Familiar?) History

- *"Hier ist ein Loch im Himmel!"*, F. W. Herschel, in 1784, on looking at ρ Oph.
- E. Barnard and M. Wolf's sky photography showed the existence of dark clouds (1920).
- J. S. Hall established extinction curve (1937).
- Hall & W. A. Hiltner find IS polarization (1949).
- Studies of IS dust come into their own with the advent of IR astronomy in the 1960s. (See the article by F. Low et al. in the latest ARAA.)

Dust in Molecular Clouds

- Molecular clouds are dusty by definition, as it is the dust that allows the H to become H_2, shielding the H_2 from dissociating UV and providing a *surface* for the production of H_2.
- Far-UV observations of slightly reddened stars give $N_H = 5.8 \times 10^{21} E_{B-V} = 1.9 \times 10^{21} A_V$ cm^{-2}, where H stands for all hydrogen nuclei, atomic & molecular.
- $A_V = 1.086\,\tau = 1.086\, N_H K_V$, giving a *mass extinction coefficient* $K_V = 4.9 \times 10^{-22}$ cm^2 per H nucleus, or ~ 200 cm^2 g^{-1} of interstellar matter.

- Most dust models imply $M_{dust}/M_{gas} \sim 0.5$ - 1%, the former more appropriate for diffuse gas and the latter for icy mantle grains in molecular clouds.
- A gas to dust mass ratio of 150:1 implies a mass of dust in the Milky Way of $M_d \sim 3 \times 10^7 M_\odot$.
- (Molecular clouds are extraordinarily dusty: an interstellar gas to dust ratio applied to the earth's atmosphere yields $\tau_V = d\rho K_V \sim 1$ in only d=5 cm!)
- *The ability to see into regions with large A_V (10s - 1000s!) where stars are forming from dense molecular gas is the overwhelming advantage of radio/mm/submm molecular line astronomy.*

Stars form in dense molecular clouds…

ISO Image: Infrared

VLT Image: Optical

The mm lines of trace molecules can probe these regions directly.

CSO Image: Radio CO 3-2 Line

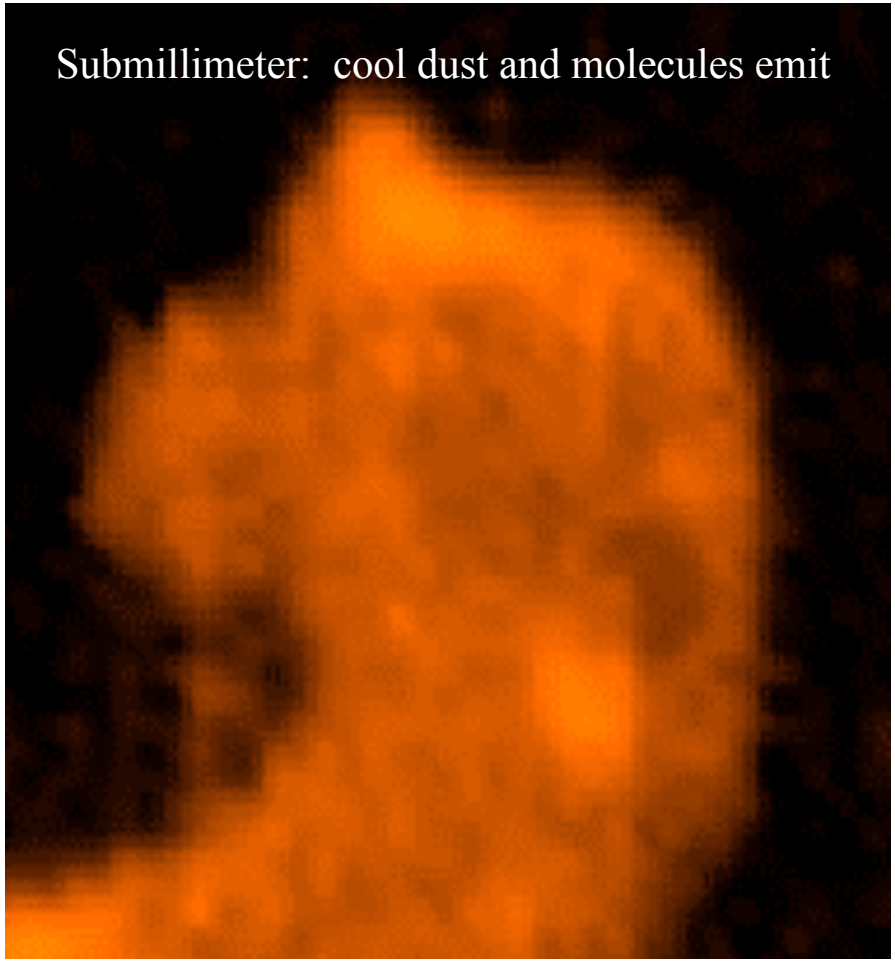

Young Stars in Serpens - Image from Spitzer c2d Legacy Project

Note strong clustering of YSOs!

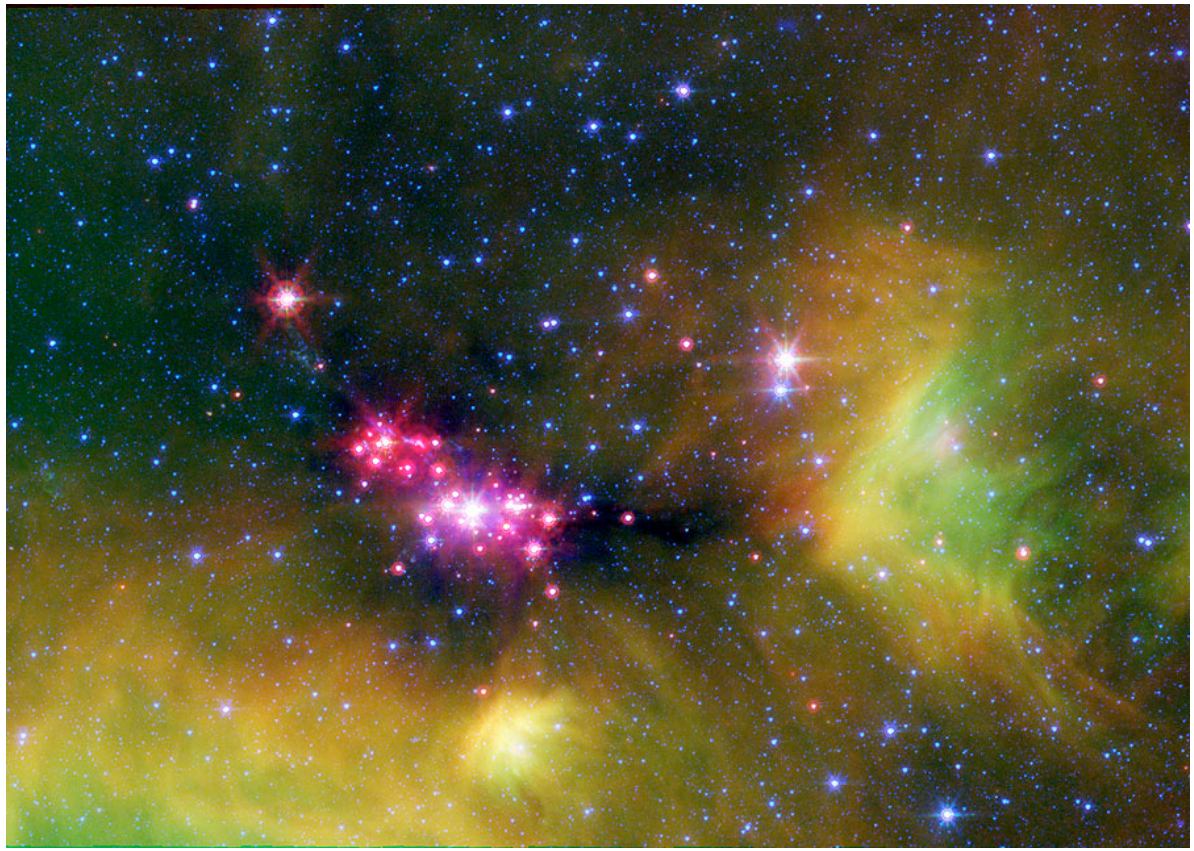

Blue = 4.5μm (stars),

Green = 8.0μm (PAHs),

Red = 24μm (dust in disks)

Star Formation in the Galaxy

- See Evans [astro-ph/0706.4116] for a review of c2d results.
- Numerous detailed studies of low-mass star formation have been made, all in clouds that lie within 500 pc. Much has been learned.
- But, the results do not necessarily speak directly to *global* star formation in a galaxy, as the local region of the Galaxy may not be typical.

Cores to Disks - c2d

- c2d is a Spitzer Legacy study of five nearby clouds, for three of which (Perseus, Serpens, & Ophiuchus) there is Bolocam (1mm) data plus extensive molecular line data.
- Star formation is in cores and highly clustered.
- Mass in cores is 1% - 4% of cloud mass within the A_V=2 contour; similarly for the mass of YSOs.
- SFR(cloud) ~ 6 - 70 $M_\odot$/Myr, $\Rightarrow$ depletion times ~ 50-90 Myr >> cloud lifetimes of 5-10 Myr.
- In contrast to the inefficiency of SF in entire clouds, the *cores* have depletion times of 3.5 Myr; *dense gas is very efficient at producing stars*.

More Elaborate Modeling of Galactic GMCs

- For recent work on modeling Galactic giant molecular clouds, see the work of Evans and his group, esp., papers by Knez, Shirley, and Wu.
- For example, Shirley et al. [ApJS 149, 375 (2003)] surveyed ~ 60 GMCs in CS(5-4) and constructed models; Wu et al. [ApJ 635, L173 (2005)] surveyed the same GMCs in HCN(1-0) to compare results.
- These high-density molecular probes and the results for the Galaxy are an important starting point for analyzing observations of high-redshift molecular gas.

Low-Mass Star Formation

Studies of molecular clouds have led to a standard model for *low-mass* star formation.

[Shu, Adams, & Lizano ARA&A 25, 23 (1987)]

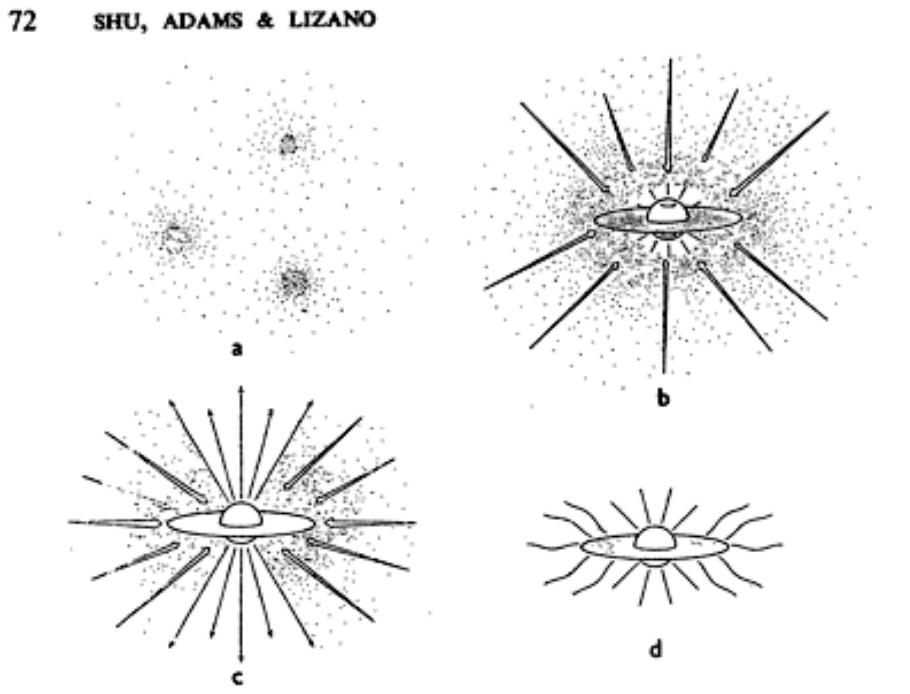

Figure 7 The four stages of star formation. (*a*) Cores form within molecular clouds as magnetic and turbulent support is lost through ambipolar diffusion. (*b*) A protostar with a surrounding nebular disk forms at the center of a cloud core collapsing from inside-out. (*c*) A stellar wind breaks out along the rotational axis of the system, creating a bipolar flow. (*d*) The infall terminates, revealing a newly formed star with a circumstellar disk.

Far less is known about *high-mass* star formation.

- With few exceptions (Orion at 440 pc), high-mass star formation in the Galaxy is distant (> 1 kpc);
- Regions of high-mass star formation are messy, complex, turbulent environments that are much more difficult to model.
- Our view of nearby external spiral galaxies is dominated by high-mass stars, and even more so for starburst galaxies at higher redshifts.
- Global measures are used for assessing star formation in distant external galaxies.

CO emission is correlated with FIR emission in Galaxy - consistent with dense gas forming stars which then heat dust

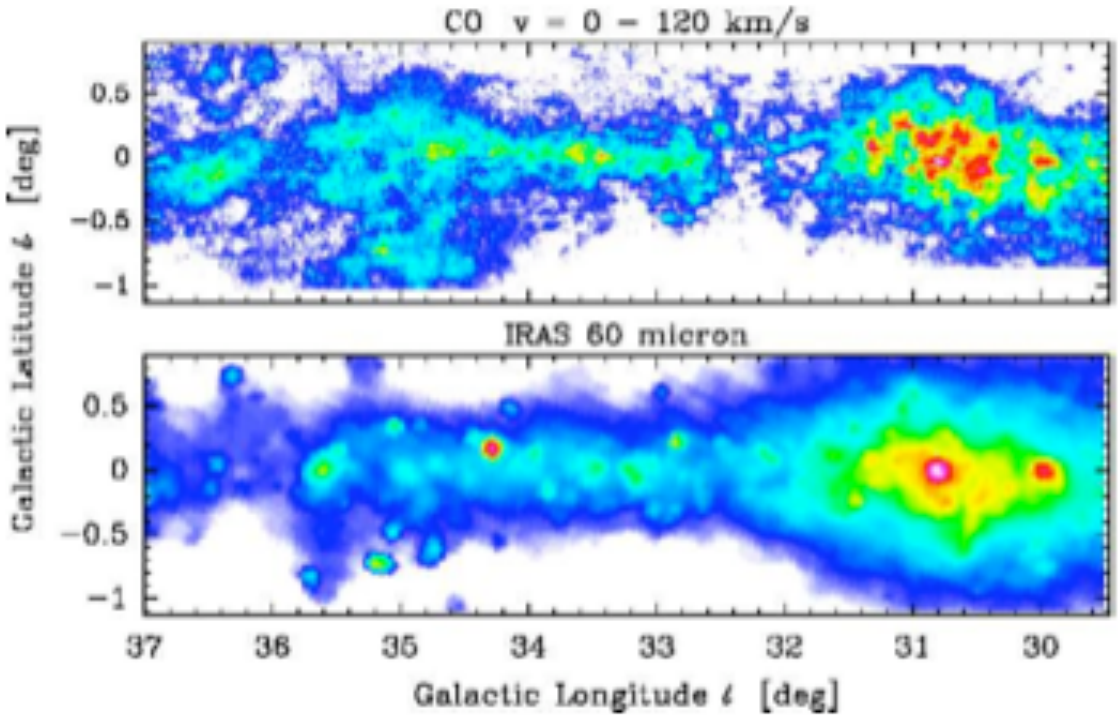

Fig. 1. Molecular clouds and FIR emission from a section of the inner Milky Way. The CO (1–0) emission in this view includes all velocities along the line of site blending many clouds. All of the strong FIR emission is associated with individual clouds and embedded H II regions. The CO is from data obtained at FCRAO (T. Mooney) with 50 arc second resolution

P. M. Solomon, in "Starburst Galaxies: Near and Far", Proceedings of a Workshop held at Ringberg Castle, Germany, 10-15 September, 2000. Edited by L. Tacconi and D. Lutz. Heidelberg: Springer-Verlag, 2001., p.173

Molecular Gas in (Nearby) Normal (Spiral) Galaxies

This is a vast subject, even with the limitations of present telescopes. Since the first detection of CO in M82 and NGC253 in 1975 by Rickard et al. [ApJ 213, 673 (1976)] a large literature of results has accumulated. Only a few examples are presented here to illustrate the advance that will come with ALMA.

A Level 1 Science Requirement for ALMA is to detect CO in normal (undisturbed) galaxies like the Milky Way to z = 3.

CO(1-0) Images of External Spiral Galaxies from the BIMASONG Survey

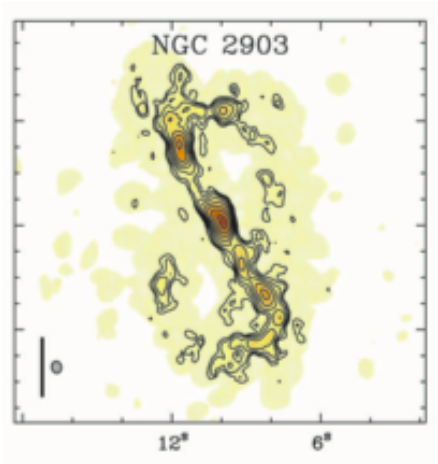

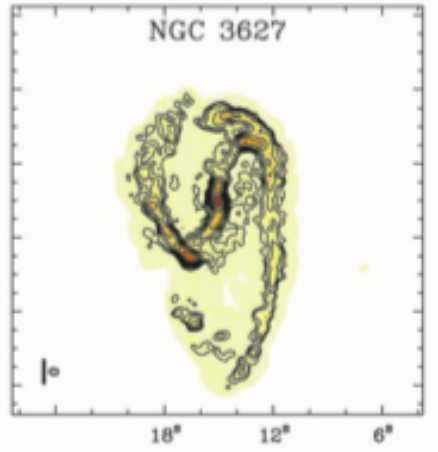

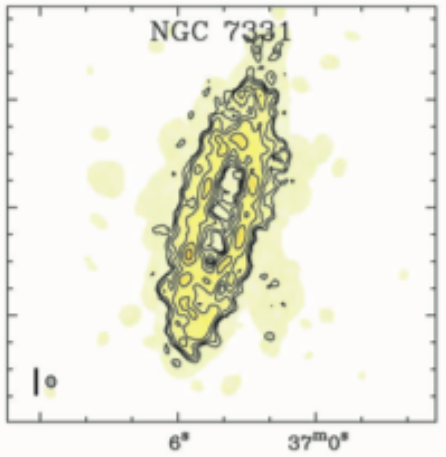

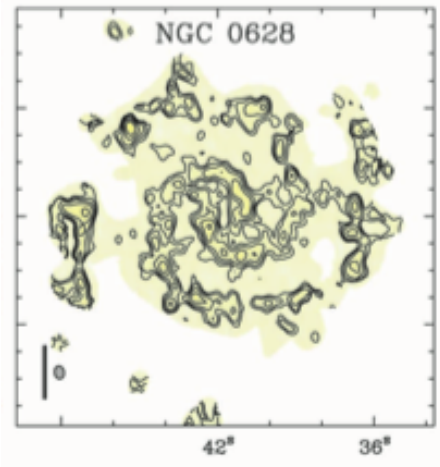

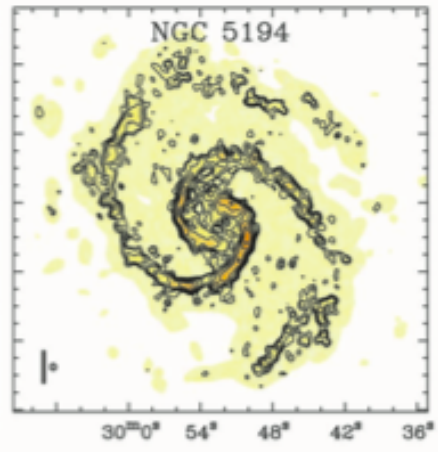

44 galaxies at ~ 6″ ang. res., a few Jy-km/s rms, vel. res. of $\Delta v = 10$ km/s.

[Helfer, et al. ApJS 145, 259 (2003)]

Molecular Gas Spiral Arms of M51

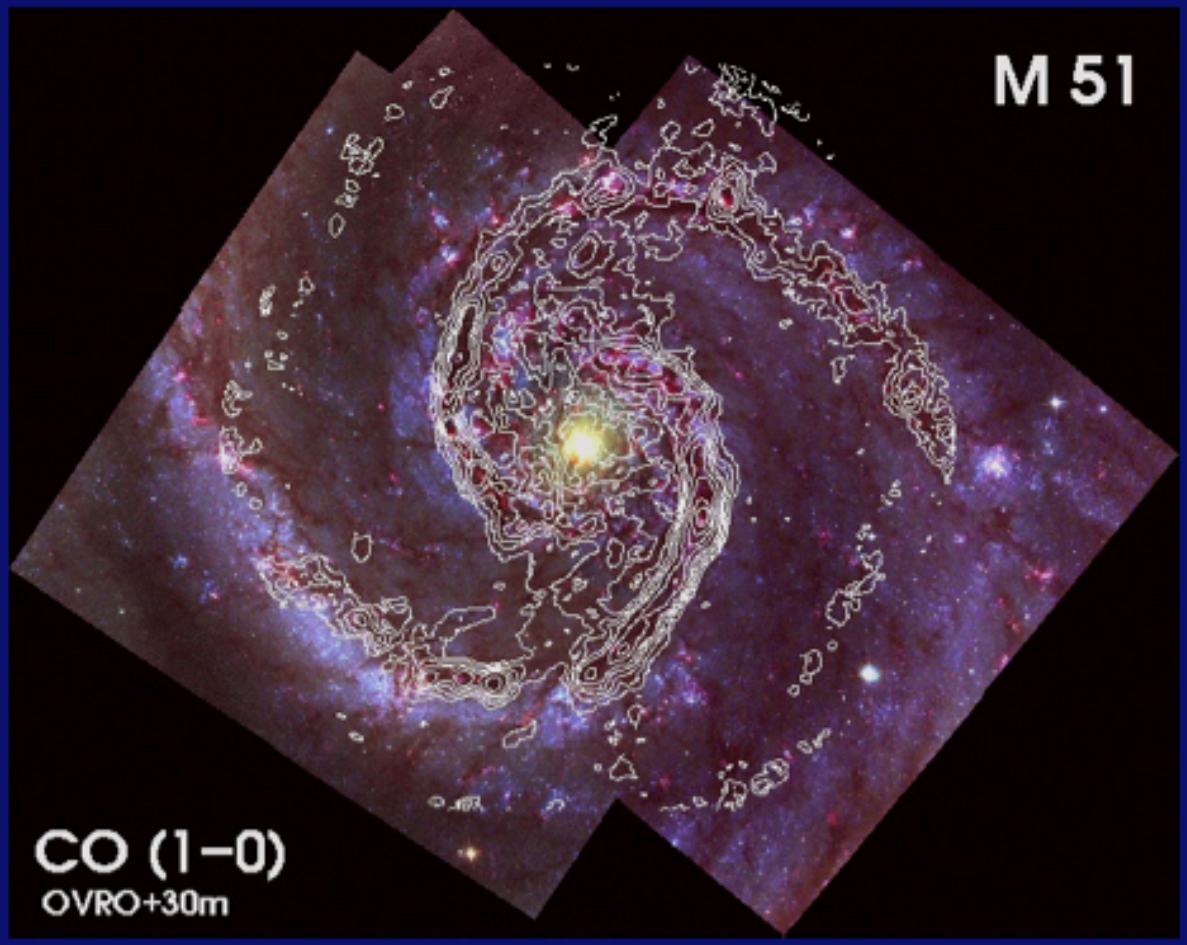

Eva Schinnerer (MPIA)
Axel Weiss (IRAM), Susanne Aalto (OSO), Nick Scoville (Caltech)

OVRO/Nobeyama Mapping of the Central Regions of 20 Nearby Spiral Galaxies Sakamoto et al. [ApJS 124, 403 (1999)]

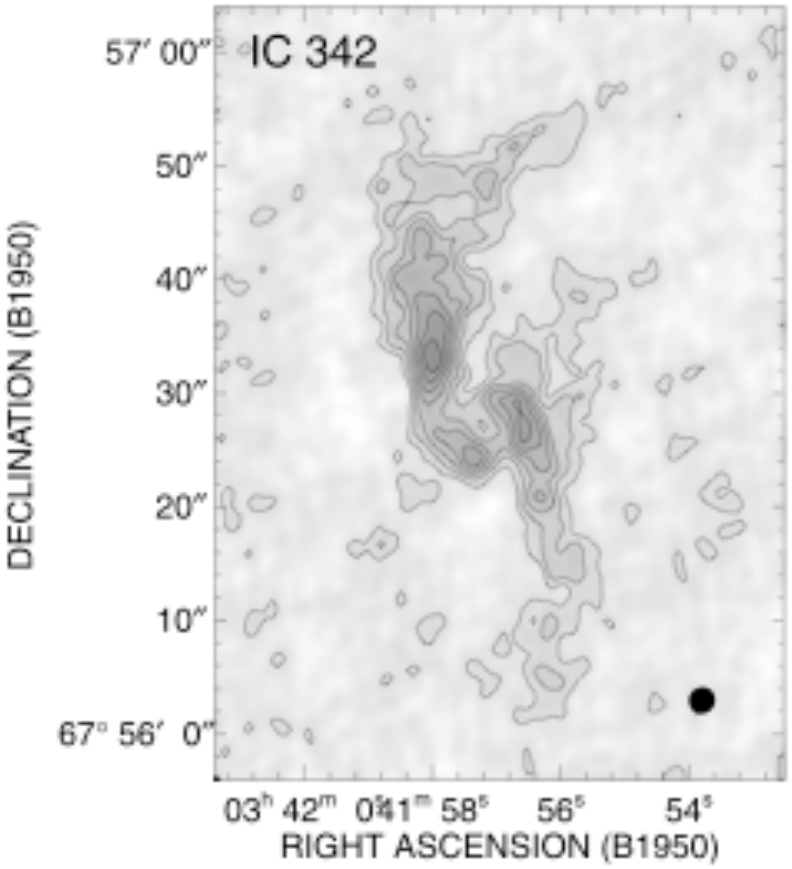

- 4′′ (300 pc) resolution;
- 1/e radii of 500 pc < that of CO in the *broad* galactic disk.

BIMA/CARMA Maps of HCN and HCO^+ - Nucleus of NGC6946 [Levine et al. arXiv:0710.0168]

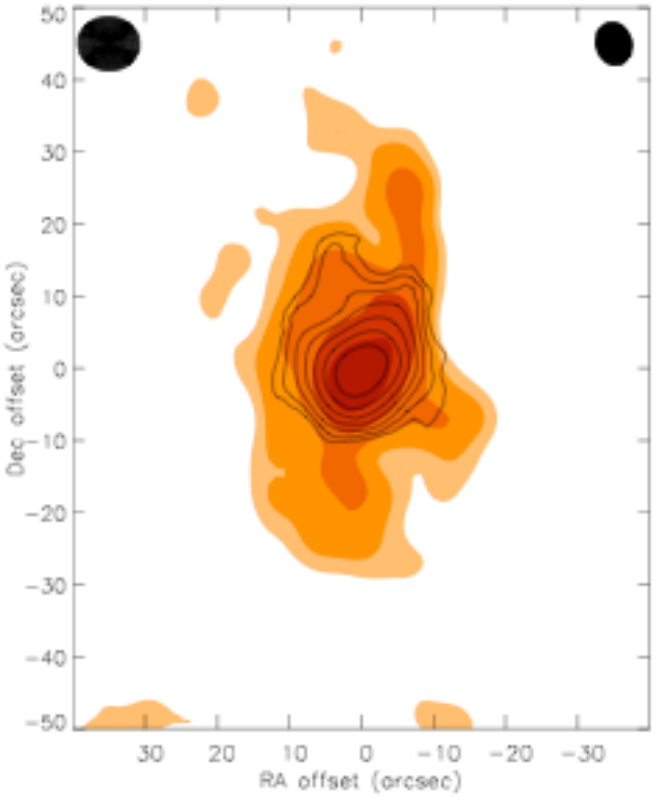

FIG. 4.— HCO^+ integrated intensity map. Red/orange colors are CO, black contour lines are HCO^+. Contours are logarithmically spaced in both CO and HCO^+, such that a contour represents $2,2\sqrt{2},4,4\sqrt{2},8...$ times 0.982 Jy/beam km s^{-1} for HCO^+ and $2,4,8,16...$ times 3.01 Jy/beam km s^{-1} for CO. The HCO^+ beam is shown in the upper left hand corner, and the CO beam is in the upper right.

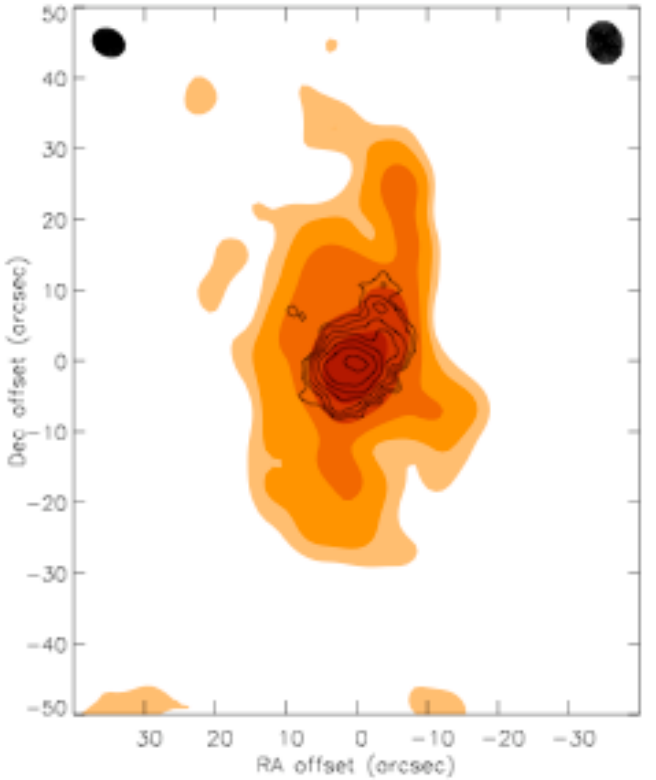

FIG. 3.— HCN integrated intensity map. Red/orange colors are CO, black contour lines are HCN. Contours are logarithmically spaced in both CO and HCN, such that a contour represents $2,2\sqrt{2},4,4\sqrt{2},8...$ times 0.636 Jy/beam km s^{-1} for HCN and $2,4,8,16...$ times 3.01 Jy/beam km s^{-1} for CO. These factors are the Q_X noise levels for each species for a point where all the channels on the line are included (see §3.2). The HCN beam is shown in the upper left hand corner, and the CO beam is in the upper right.

Molecular Line Luminosity as a Tracer of Star Formation

- L′(mol) is a measure of molecular gas, the material available to form stars;
- L(IR or FIR) is a measure of SFR or dM/dt;
- The ratio is measure of SF “efficiency”; its inverse a measure of the depletion time or SF duration;
- Noting that this ratio varies dramatically for low-mass star formation from star-forming cores to clouds as a whole, we could expect complications for high-mass SF efficiencies as measured by the above ratio.

L(FIR) vs. L′(CO) for a sample of normal spirals and interacting galaxies (LIRGs & ULIRGs) - Solomon (astro-ph/0101482)

- $L(FIR) \propto (L'_{CO})^{3/2}$.
- SFR increases more than linearly with L′(CO), or M(molecular gas), implying increased SF "efficiency".
- This correlation continues to include the high-z CO-emission galaxies.

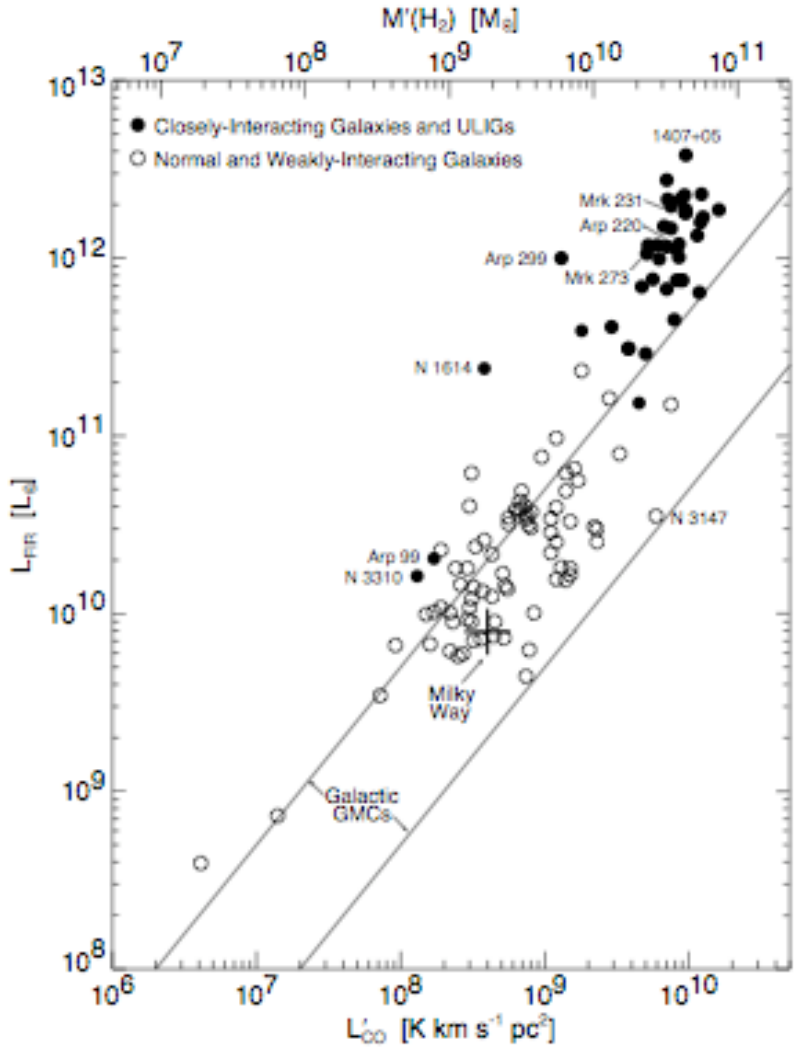

Fig. 2. FIR luminosity vs. CO (1–0) luminosity (lower scale) and molecular gas mass (top scale). (Adapted from [12] and [14]). Solid circles indicate closely-interacting galaxies, mergers and ultraluminous galaxies; open circles are isolated and weakly-interacting galaxies. The solid lines labeled GMCs bracket the $L_{\rm FIR}/L_{\rm CO}$ for Galactic giant molecular clouds with active OB star formation. The top axis is the molecular, H_2, mass assuming a Milky Way CO to H_2 conversion factor. This is an overestimate for ULIGs which have an even higher ratio of $L_{\rm FIR}/M(H_2)$. Ultraluminous galaxies have a higher $L_{\rm FIR}/M(H_2)$ than any Galactic GMC

ALMA & Nearby Galaxies

- Detect CO in normal spirals to z = 3 in 24h;
- Image CO in normal spirals to 25 Mpc at 1″ resolution, 0.1 K rms, Δv = 10 km/s; could do 700 in 1000h;
- BIMASONG required several tracks per galaxy = many days; ALMA can do same job on one of these galaxies in *seconds*.

FIR/Radio Continuum Correlation

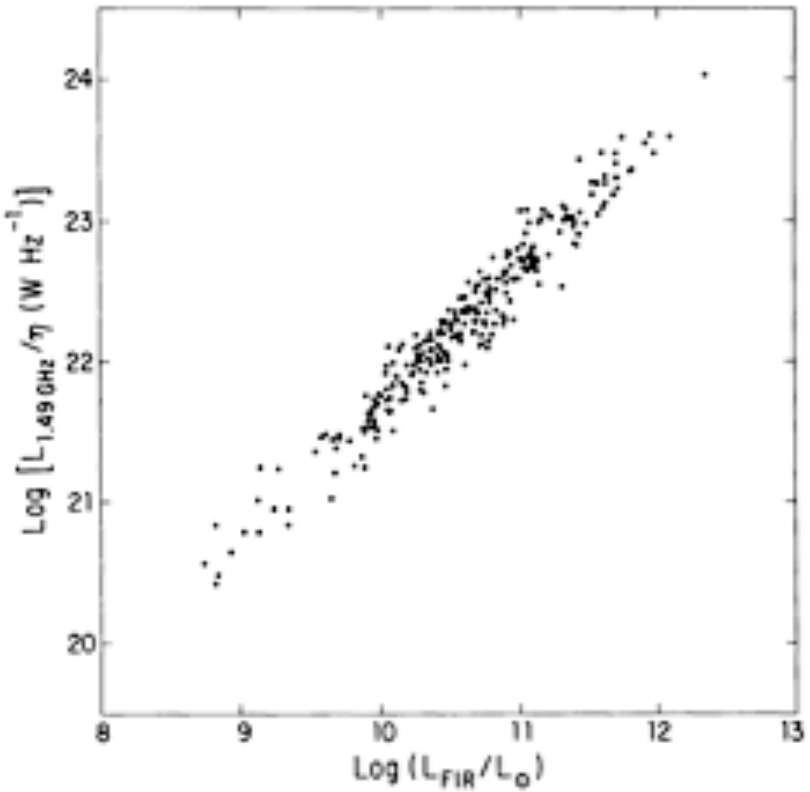

FIG. 10.—Corrected correlation of radio and FIR luminosities for the $\lambda = 60$ μm flux-limited sample of 258 galaxies without AGN. Compare with the uncorrected correlation shown in Fig. 2. *Abscissa:* log of the FIR luminosity (in units of solar luminosity $L_{\odot} = 3.83 \times 10^{26}$ W). *Ordinate:* log of the corrected radio spectral luminosity $L_{1.49\,GHz}/\eta$ (W Hz^{-1}).

Condon, Anderson, and Helou (1991) ApJ 376, 95.

FIR (W m^{-2}) = 1.26 x 10^{-14} (2.58 $S_{60\mu m}$ + $S_{100\mu m}$); S's are IRAS flux densities.

log $L_{1.49GHz}$ (W Hz^{-1}) = 1.29 log $L_{FIR}(L_{\odot})$ + 8.66, for 250 optically bright spiral galaxies without AGNs.

FIR is often (& therefore best) defined as 42.5-122.5 μm, (7.059 - 2.449 THz).

FIR/Radio Continuum Correlation

- Generally accepted explanation: the newly formed hot massive stars that heat the dust (FIR) explode as supernovae, which produce cosmic rays (radio).
- A *global* correlation - Spitzer studies show variations *within* galaxies. For example, see Murphy, et al. ApJ 651, L111 (2006).
- Holds to z = 1 [Appleton et al. ApJS 154, 147 (2004)].

CO - Radio Continuum Correlation in BIMA SONG Galaxies

- Murgia, et al. [AA 437, 389 (2005)] studied radio continuum (1.4 GHz) vs. CO in 24 BIMASONG galaxies.
- Global CO-RC is as tight as the global FIR-RC for all 24; also true *within* 9 galaxies for which higher angular resolution (6″) CO data was available.

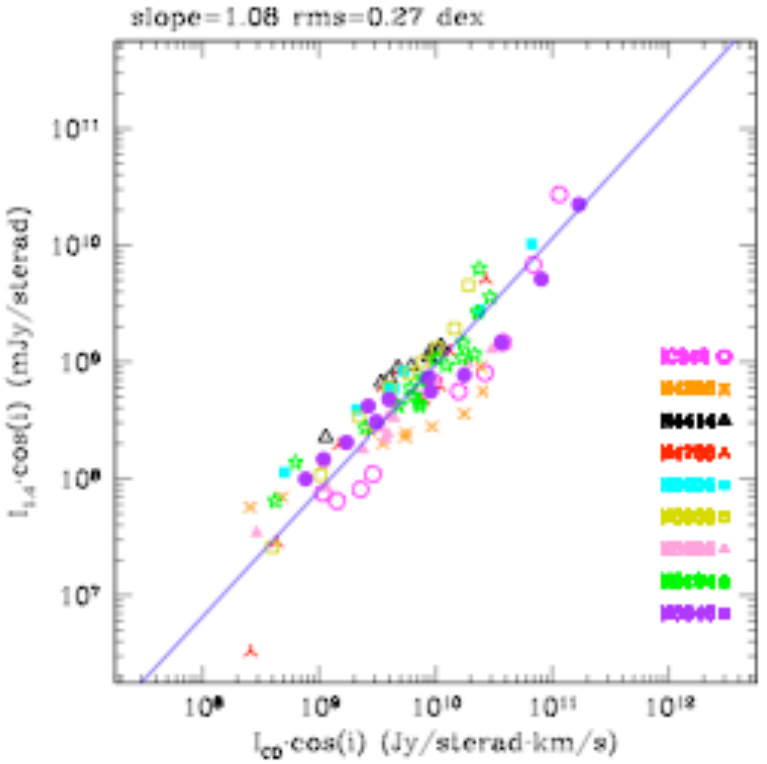

Fig. 3. CO-RC correlation in sample galaxies. Each point represents the average value in an annulus. The solid blue line is a weighted fit to the points shown which takes into account the errors in both coordinates and has a slope of 1.08.

Star Formation in Galaxies - Schmidt Laws

- originally (Schmidt, 1959) SFR $\propto$ square of the volume density;
- now, it is usually expressed in surface densities -

$$\Sigma(\mathrm{SF})\ (M_\odot\ \mathrm{yr}^{-1}\ \mathrm{kpc}^{-2}) = (2.5 \pm 0.7) \times 10^{-4}\ (\Sigma(\mathrm{gas})/M_\odot\ \mathrm{pc}^{-2})^{1.4\pm0.15}$$

see Evans [astro-ph/0706.4116] for a review;

- as SF takes place in dense molecular cloud cores, traced by HCN, Wu et al. [ApJ 635, L173 (2005)] offer the following (Galactic) "Schmidt Law" in terms of L'_{HCN}:

$$\mathrm{SFR}\ (M_\odot\ \mathrm{yr}^{-1}) = 1.4 \times 10^{-7}\ L'_{\mathrm{HCN}}\ (\mathrm{K\ km\ s}^{-1}\ \mathrm{pc}^2)$$

$$= 1.2 \times 10^{-8}\ M_{\mathrm{dense\ gas}}\ (M_\odot).$$

Star Formation Rate from FIR

SFR ($M_\odot$ per year) =

$4.5 \times 10^{-44} L_{FIR}$(ergs/s) =

$1.8 \times 10^{-10} L_{FIR}$(solar luminosities).

Kennicutt [ARAA 36, 189, (1998)]; based on studies of nearby galaxies.

(If the FIR measures the star formation rate, why worry about molecular line spectroscopy?)

- FIR is not all that easy to measure directly;
- Angular resolution in FIR is not that great;
- Other tracers of SF that are more accessible and (may) have better resolution, largely in the near-IR, are also used, but suffer from extinction;
- Molecular lines give you the physical properties *and kinematics* of the star forming gas itself.

Starburst Galaxies
[see Low et al. ARAA 45, 43 (2007) for a review of early IR astronomy]

- Mid-IR observations with the LPL 61-inch Telescope showed many spirals had IR-bright nuclei;
- M82 and NGC253 were detected at 100μm with the Lear Jet, implying heated dust;
- High IR-luminosity implied rapid star formation, such that the entire dynamical mass of the galaxy would be eaten up were it not to be limited in duration. Star formation must be occurring in a relatively short period of time, in a burst.

More Distant Star Formation: Luminous Infrared Galaxies

- Early examples were Mrk231 & Arp220;
- Large population was revealed by IRAS;
- L(FIR) ~ 10^{12} $L_{\odot}$ (~ 50 x Milky Way);
- L′(CO) ~ 10^{10} K km/s pc^2 (~ 30 x Milky Way)
- M(gas) ~ 3 x 10^{10} $M_{\odot}$, (~ 10 x Milky Way);
- SFR ~ 100 - 1000 $M_{\odot}$/year; (~ 30 - 300 x MW)
- Disk diameters (FWHM) ~ 1 - 2 kpc;
- All appear to be mergers/disturbed systems.
- See Sanders and Mirabel [AARA 34, 749 (1996)] for a review.

A few definitions from Sanders and Mirabel

- LIG - luminous IR galaxy, $L_{IR} > 10^{11} L_{\odot}$;
- ULIG - ultra luminous …, $L_{IR} > 10^{12} L_{\odot}$;
- HyLIG - hyper luminous …, $L_{IR} > 10^{13} L_{\odot}$;

- $F_{IR} = 1.8 \times 10^{-14} [13.48 f_{12} + 5.16 f_{25} + 2.58 f_{60} + f_{100}]$ (W m^{-2})

(red gives their definition of far-infrared)

Origin of ULIRGs? - Mergers of Gas-Rich Spirals - like the Antennae (NGC4038/39, Arp 244)

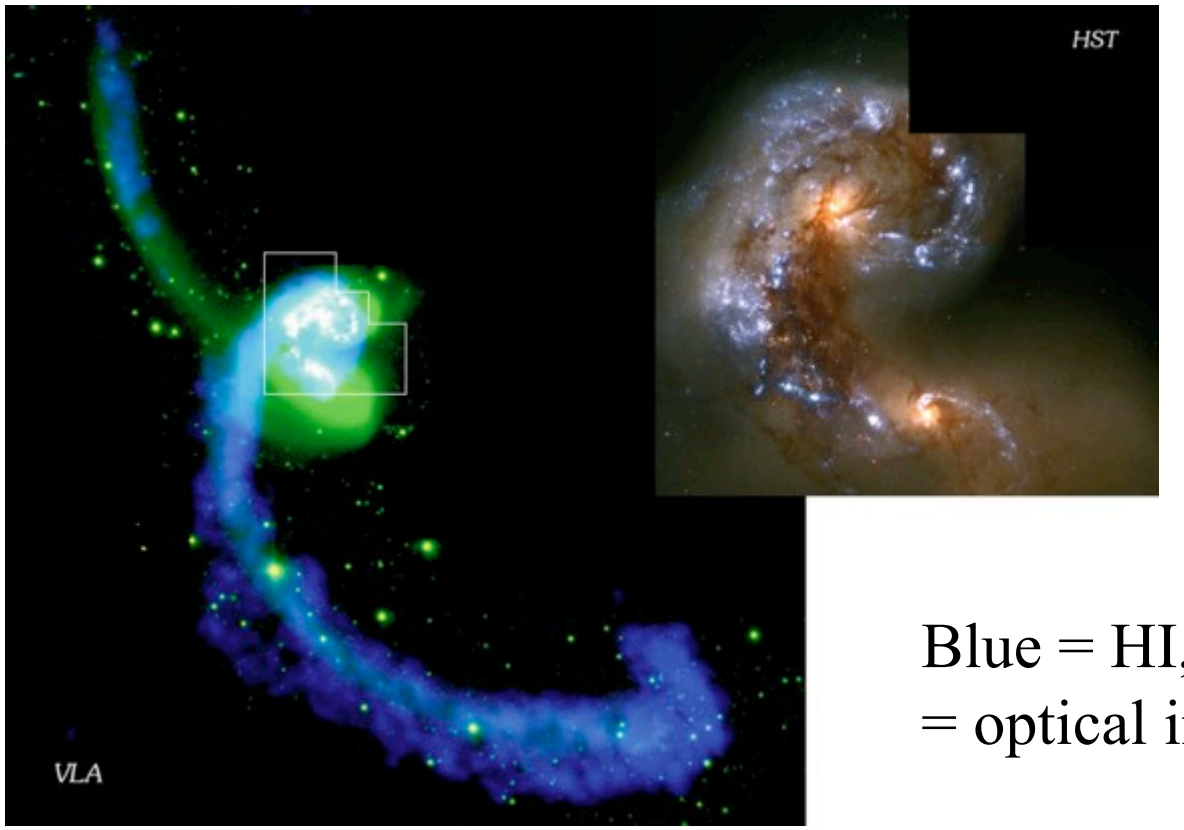

Blue = HI, Green & White
= optical image CTIO

HI/Optical Image of Arp 220

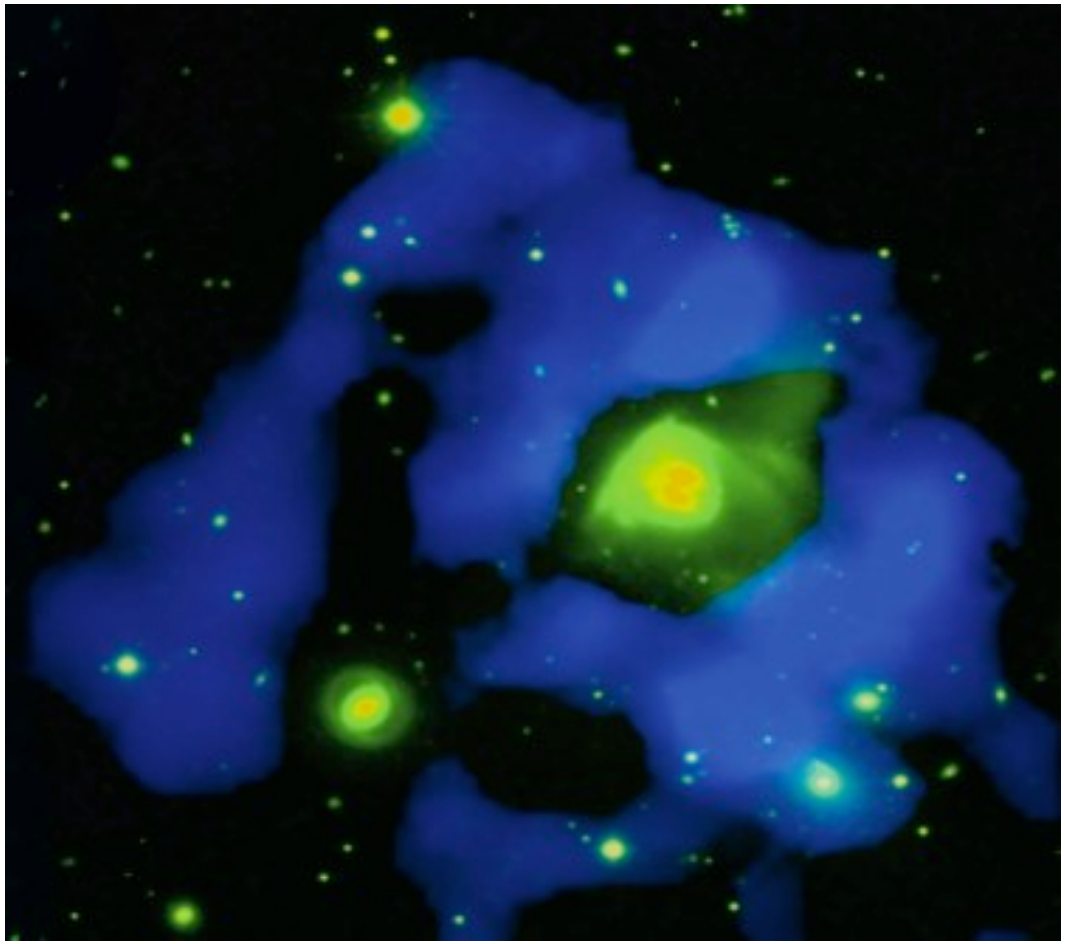

Blue = HI;

Green, Yellow, Orange = optical bands

Two Milestone Papers

Solomon et al. [ApJ 478, 144 (1997)] observed CO in 37 ULIRGs with IRAM 30m:

- 36 have $L'(CO) \sim 10^{10}$, which leads to M(gas) > M(dyn) if $\alpha = 4.6$ is used. (To calculate M(dyn), they estimate a minimum size, so they actually calculate a minimum M(dyn).)
- They argue that $L'(CO)$ measures the geometric mean of M(gas) and M(dyn), and that a new (lower) value of α is required for ULIRGs.

Downes and Solomon [ApJ 507, 615 (1998)] used the PdB to *image* 10 ULIRGs. The molecular gas is in rotating nuclear disks or rings of radius 300-800 pc.

- Some conclusions:

  - gas is turbulent with dispersion $\sigma \sim 100$ km/s, line widths FWHM ~ 100s km/s;

  - most of the CO is in "low density" gas of 300-2000 cm^{-3};

  - CO emitting gas in central disk is not from a collection of self-gravitating GMC cores like the Galaxy, but from a continuous medium.

- Their model: the merger of two spirals like the Galaxy, each with ~6000 GMCs of diameter ~50 pc and density 150 cm^{-3} within their central 5 kpc is transformed into a single ISM of radius 500 pc and density 1000 cm^{-3}, as the GMCs blend under tidal shear. The result is a huge starburst.
- Radiative transfer calculations for this model of the 10 galaxies in their survey yield values for α ranging from 0.3 to 1.3, with a mean of $\alpha = 0.8$, rather than the Galactic value of 4.6.
- *This value for α has since been widely assumed in papers published about CO emission in ULIRGs. It has also been used in virtually all papers on CO in high-redshift galaxies.*

Extreme Starbursts

- Arp 220, Arp 193, & Mrk 273 are extreme starburst galaxies;
- The starburst regions contain ~ 10^9 $M_\odot$ gas within a radius of ~ 100 pc;
- The IR luminosity of ~ 3 x 10^{11} $L_\odot$ represents the heating of 1000x the number of recently formed OB stars in 30 Doradus;
- *"We conclude that in ultra-luminous IR galaxies - even in Mrk 231, which hosts a quasar - the FIR luminosity is powered by extreme starbursts in the molecular rings or disks, not by dust-enshrouded quasars". [Downes & Solomon, 1998]*

Arp 220 - CO and Optical Images

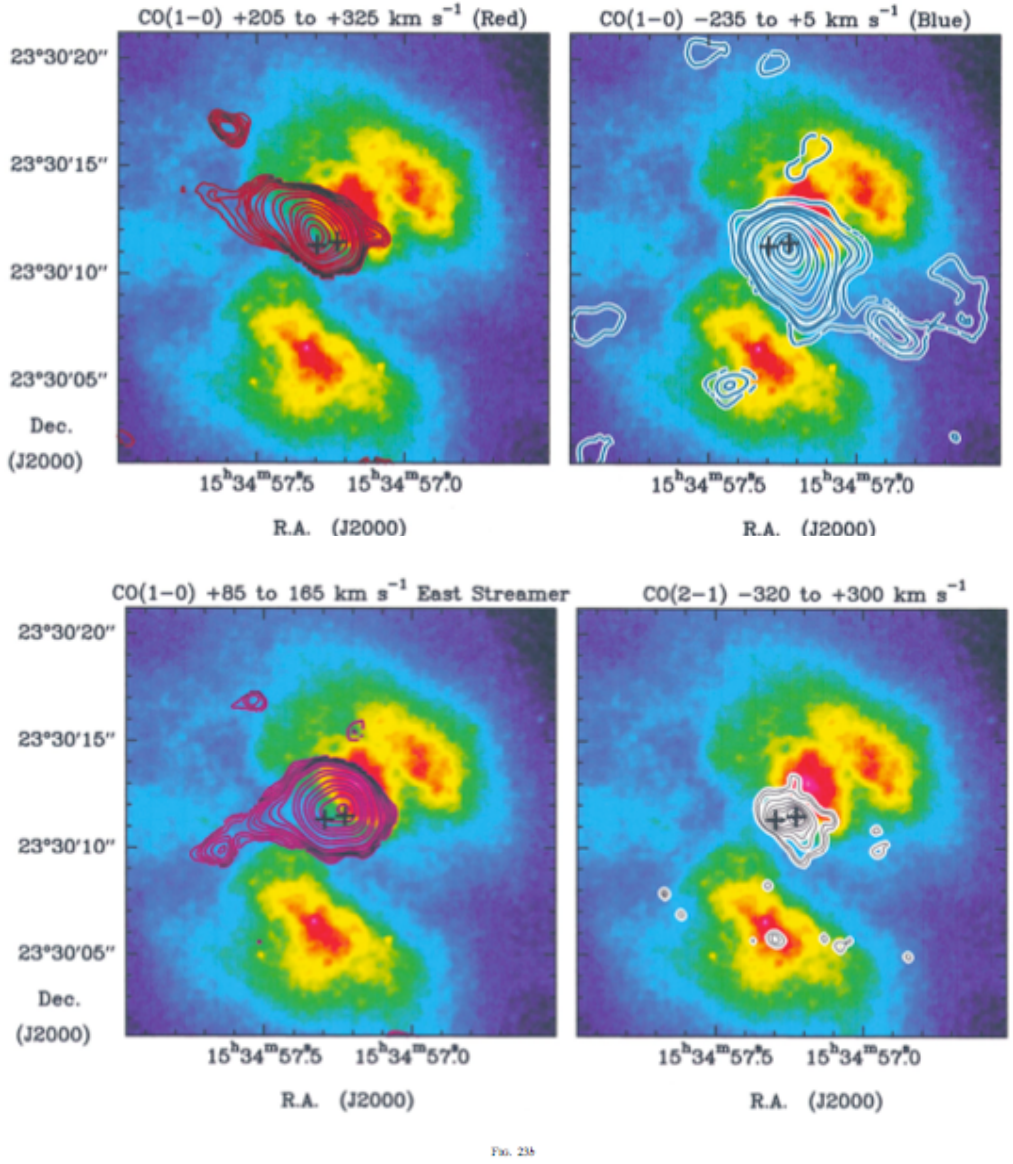

Fig. 23b

HST image in false color;

CO 1-0 contours for 3 velocity ranges & for 2-1;

With data on next slide, this is the basis of a starburst model.

Arp 220 - CO(2-1)

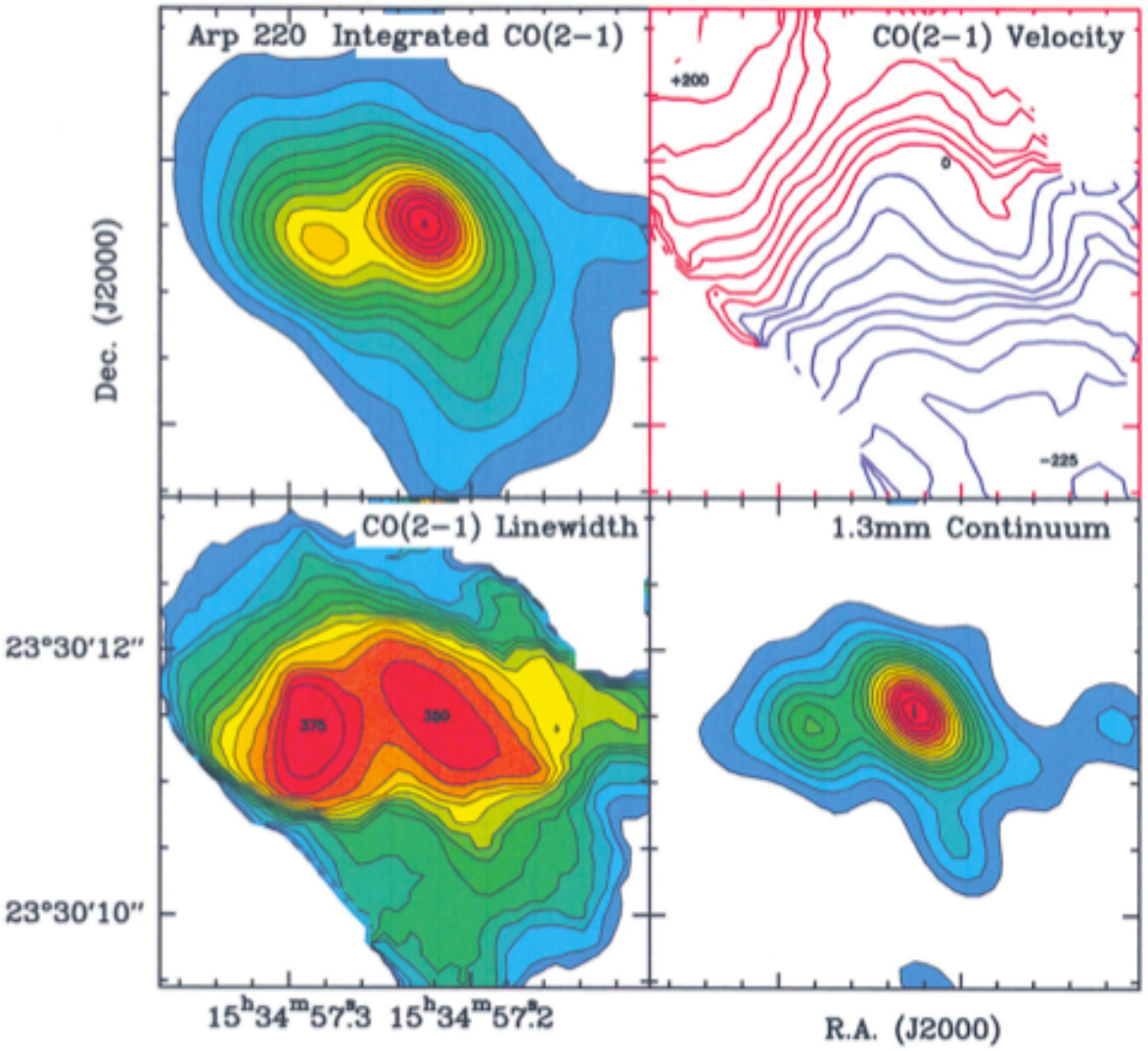
Arp 220 Integrated CO(2−1)
CO(2−1) Velocity
+200
0
−225
CO(2−1) Linewidth
375
350
1.3mm Continuum
Dec. (J2000)
23°30'12"
23°30'10"
15h34m57s.3
15h34m57s.2
R.A. (J2000)

Starburst Model for Arp 220

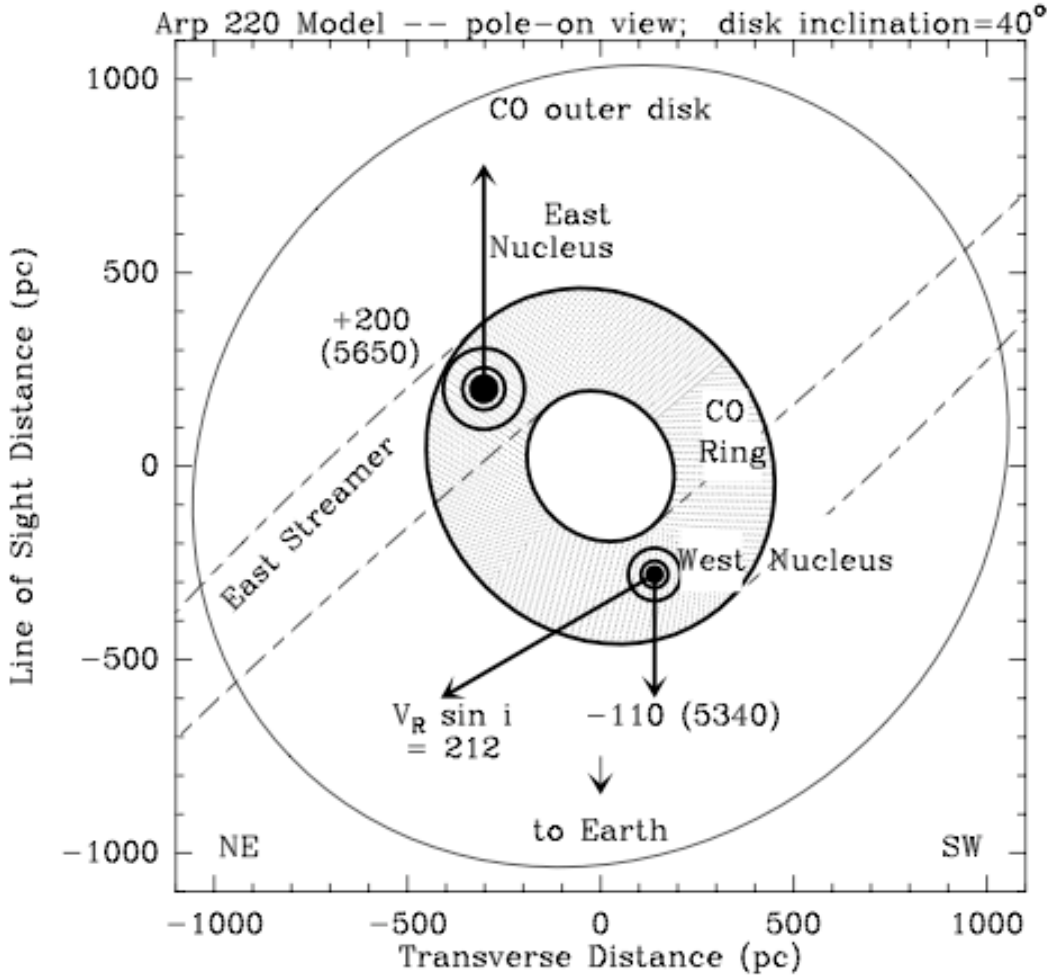

FIG. 24.—Model of the eastern and western nuclei in the molecular disk of Arp 220. The rotation velocity is 330 km s^{-1}, and the view is pole-on. The arrows indicate the observed radial components along the line of sight, at a disk inclination of 40° from face-on. Velocities are relative to a systemic velocity of cz_{hr} = 5450 km s^{-1}. Labels are in km s^{-1}, and values in parentheses are cz_{hr}.

Arp 220 in CO [Sakamoto et al. ApJ 514, 68 (1999)]

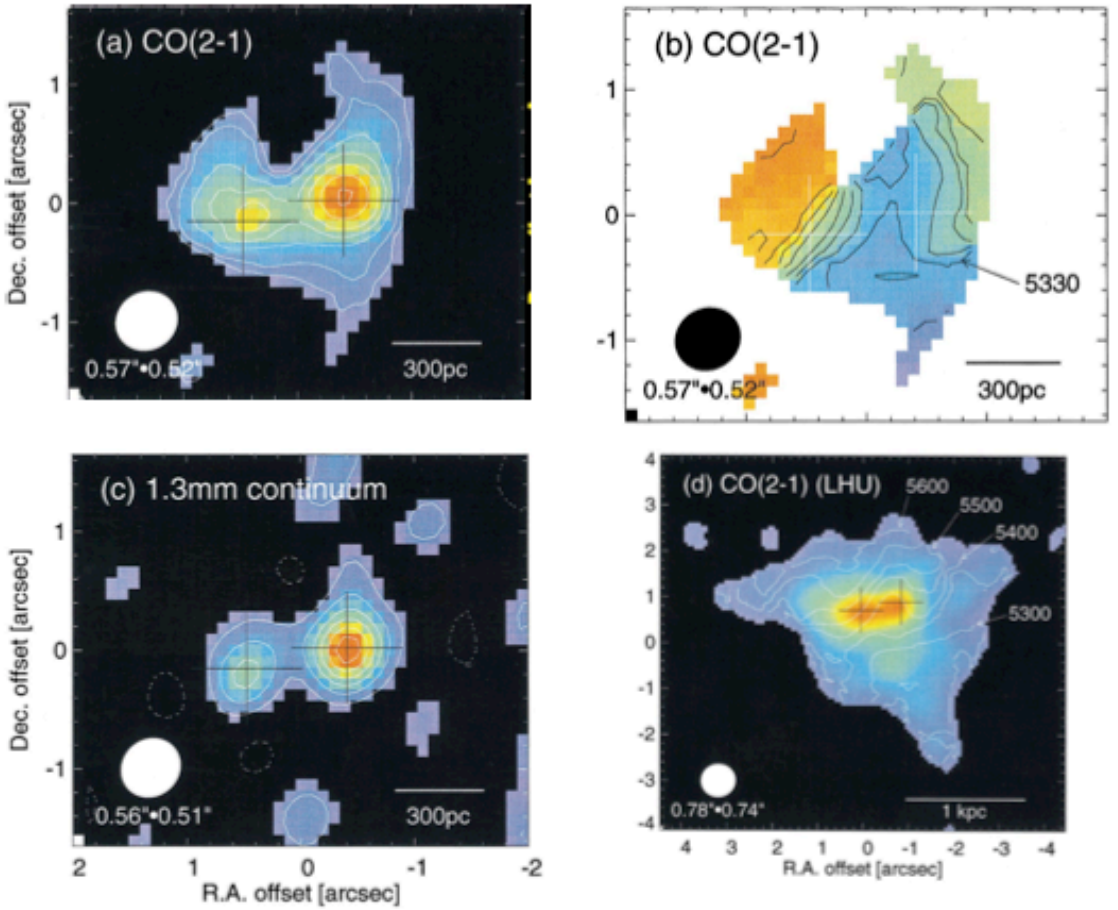

FIG. 3.—Central region of Arp 220. Crosses in each panel indicate the 1.3 mm continuum positions of the nuclei. (*a*) Continuum-subtracted CO (2–1) emission integrated over 645 km s^{-1}. Contours are at 8.5 × (1, 2, 4, 6, 8, 10, 12) Jy beam^{-1} km s^{-1}. (*b*) Mean velocity of CO (2–1) with contour intervals of 50 km s^{-1}. (*c*) 1.3 mm continuum with contour steps of 18.5 mJy beam^{-1} (2 σ) and negative contours (*dashed lines*). (*d*) CO (2–1) integrated intensity map and isovelocity contours (50 km s^{-1} increments) made from L, H, and U configuration data. The peak integrated intensity is 193 Jy beam^{-1} km s^{-1}.

A Refined Model

Arp220 has two disks, counter-rotating, that are embedded in a much larger outer disk.

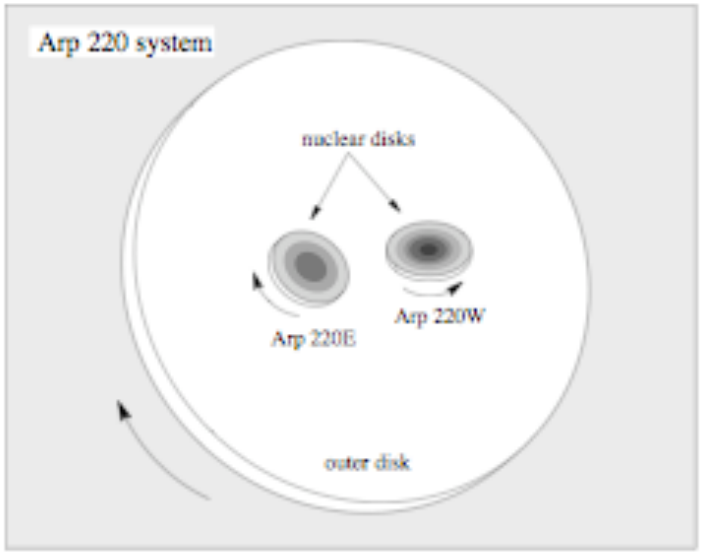

Fig. 5.— Schematic illustration of the Arp 220 disks. The two nuclear disks have radii ~ 100 pc and misaligned spin axes, probably counterrotating with respect to each other. The dynamical mass within 100 pc radius of each nuclear disk is about $2 \times 10^9 \sin^{-2} i\ M_\odot$ where i is the inclination of the disk. Gas masses in the nuclear disks are estimated to be $\sim 10^9\ M_\odot$ for each. Each of the nuclei contains a gas disk, young stars formed in the disk, and presumably an old stellar population from the nucleus of the merger progenitor. The stellar component likely has a larger scale height than molecular gas, and thus the gas disk is embedded in the stellar nucleus. Most of the far-IR luminosity of Arp 220 is from the central 100 pc diameter of the nuclear disks. The outer disk has a radius of ~ 1 kpc, formed from the gas from the progenitor galaxies and now rotating around the dynamical center of the merger. It is likely the host of a previous starburst of $\sim 10^8$ yrs ago that created the Hα bubbles ~ 10 kpc in size.

Do AGN Contribute to L(FIR) in ULIRGs?

- If the AGN is visible, as in Mrk 231, the effect is probably small - most of the AGN radiation escapes.
- But absence of evidence is not evidence for absence, and heavily obscured AGN are exactly what could contribute to L(FIR).

What is the argument for (pure) starbursts?

Case for Starburst Origin of L(FIR)

- In the Galaxy, the dust in GMC cores has clearly been heated by star formation.
- In external, undisturbed spiral galaxies, there is a (global) correlation between L(FIR) and L′(HCN), which traces dense ($n \sim 3 \times 10^3$ cm^{-3}) molecular gas similar to that in GMC cores.
- *This correlation is identical for both.*

L(FIR) vs. L′(HCN) in normal spirals, LIRGs, & ULIRGs

- Gao & Solomon [ApJ 606, 271 (2004)] give the results of a survey of HCN(1-0) in 65 galaxies: normal spirals, LIRGs, and (9) ULIRGs;
- Global SFR $\propto$ M(dense gas) over three orders of magnitude in L(IR);
- On average, L(IR)/L′(HCN) =

$$900\ [L_{\odot}/\mathrm{K\ km\ s^{-1}\ pc^{2}}]$$

The L(FIR) vs. L′(CO) correlation for normal spirals does not fit LIRGs & ULIRGs, whereas L(FIR) vs. L′(HCN) does:

L(FIR) vs. L′(CO)

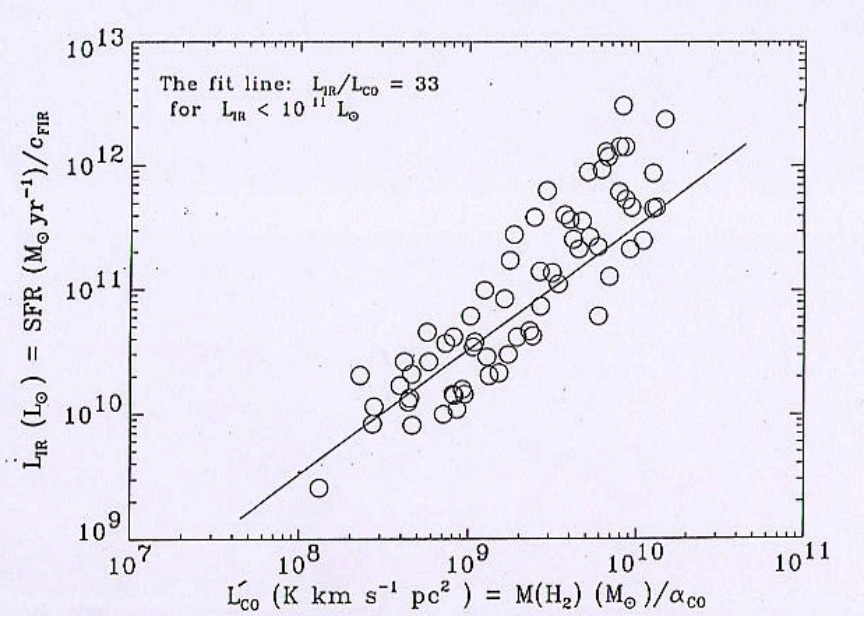

L(FIR) vs. L′(HCN)

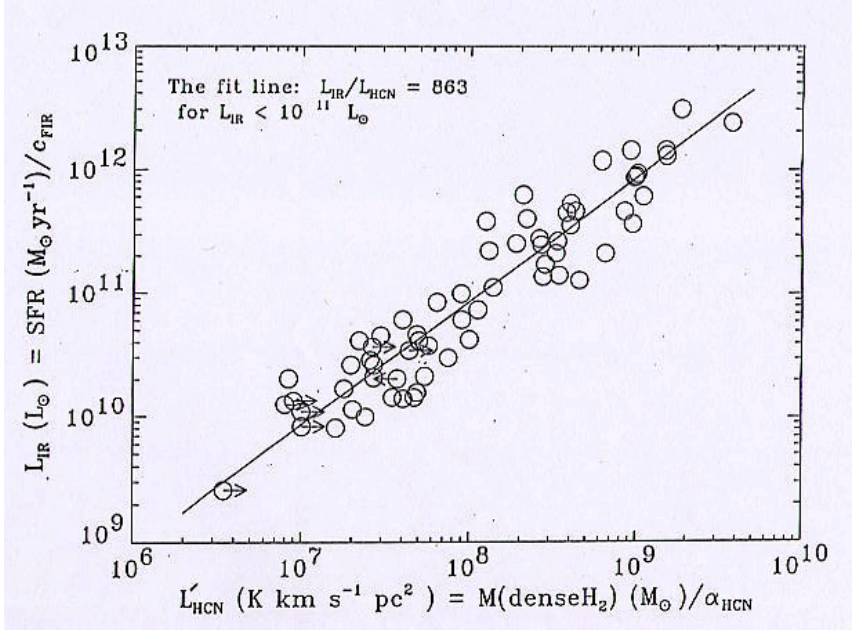

Line is best fit to normal spirals only (L(IR) < 10^{11}); it is only extrapolated to ULIRG IR luminosities.

The Gao correlation, extrapolated back, passes through the data for Galactic GMC cores:

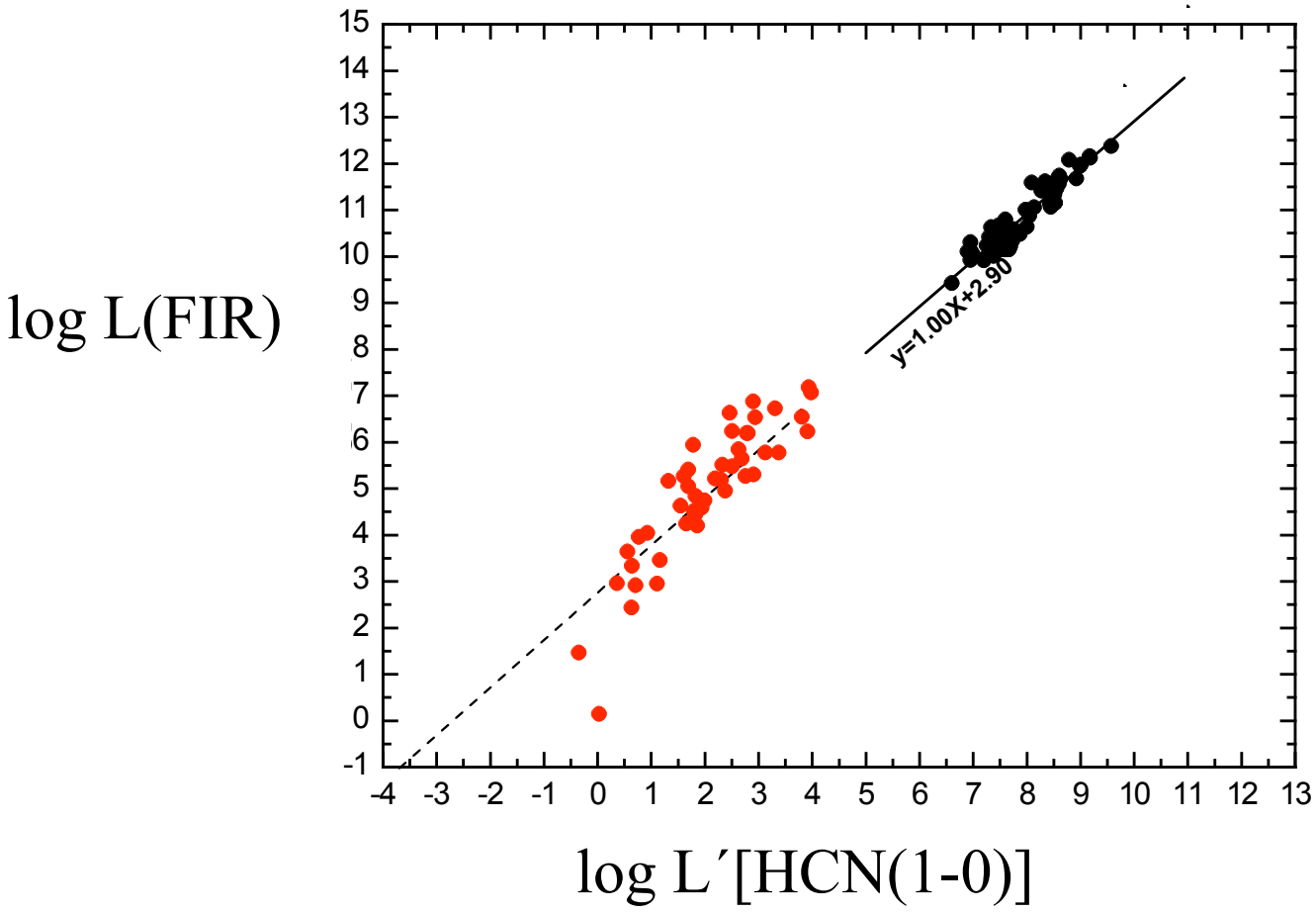

Wu et al. ApJ 635,L173 (2005)

Independent correlations are identical for both the Gao Sample and Galactic GMC cores:

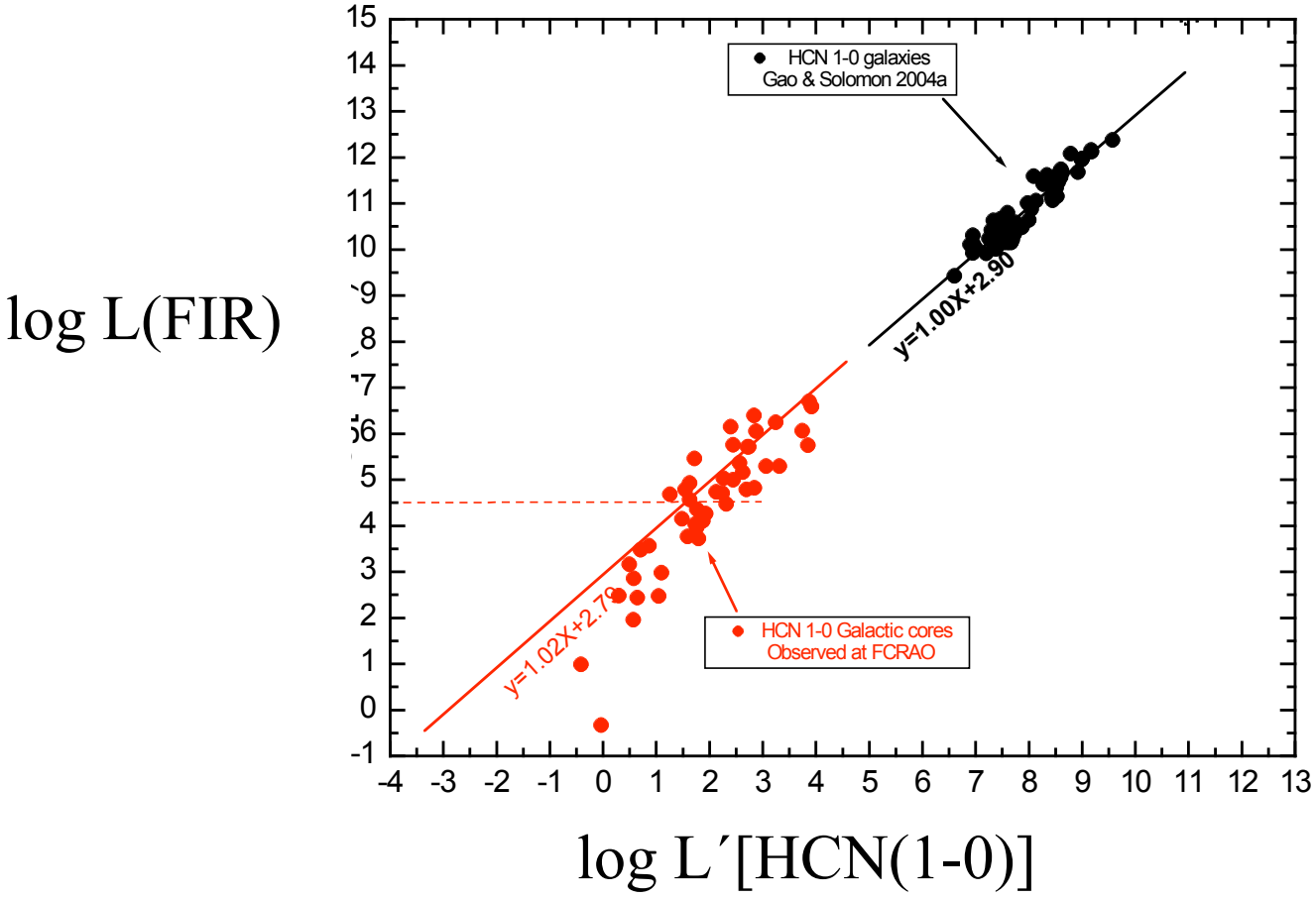

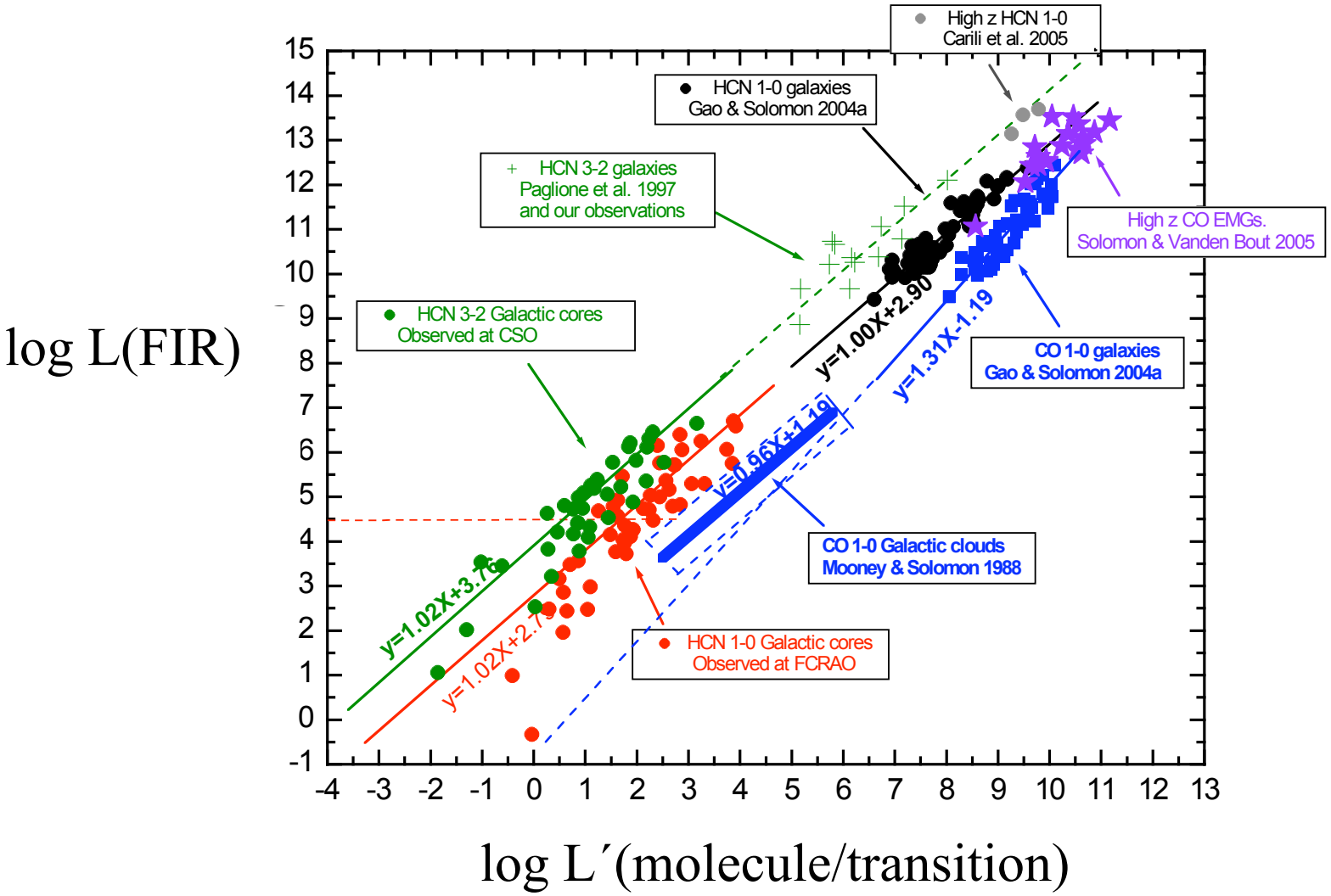
High z HCN 1-0
Carili et al. 2005
HCN 1-0 galaxies
Gao & Solomon 2004a
HCN 3-2 galaxies
Paglione et al. 1997
and our observations
High z CO EMGs.
Solomon & Vanden Bout 2005
HCN 3-2 Galactic cores
Observed at CSO
y=1.00X+2.90
y=1.31X-1.19
CO 1-0 galaxies
Gao & Solomon 2004a
y=0.96X+1.19
CO 1-0 Galactic clouds
Mooney & Solomon 1988
y=1.02X+3.76
y=1.02X+2.7
HCN 1-0 Galactic cores
Observed at FCRAO
log L(FIR)
log L´(molecule/transition)

More on AGN Contributions to L(FIR):

- Gao saw no difference in the correlations between L(IR) and L´(HCN) for galaxies with AGN and those with no known AGN.

- Farrah et al. [MNRAS 343,585 (2003)] analyzed the SEDs of 41 ULIRGs: the entire sample requires a starburst component, whereas only half require an AGN component; for 90%, the starburst component accounts for more than half the IR, and on average, the starburst component accounts for 82% of the IR.

- But there are exceptional objects, one, apparently, is the until recently prototypical ULIRG *without* an AGN, namely Arp 220!

Nothing Like Good Angular Resolution:

- IRAM PdB recently completed a long (760m) baseline, increasing the angular resolution at 230 GHz to 0.3″;
- Downes & Eckart [A&A 468, L57 (2007)] imaged Arp 220 West in CO(2-1) and in 1.3mm continuum;
- The images show that the continuum source is compact (0.19″x 0.13″), smaller than the CO disk, with T_B=90K. There is CO absorption at this location, which means the Wien side of the dust SED must be deeply attenuated: T_d=170K, τ =1.7 @ 25μm, with the opacity varying as $\lambda^{-\beta}$ and ß = -1 shortward, ß = -2 longward is best model.

1.3mm Image and Inferred SED of Arp220

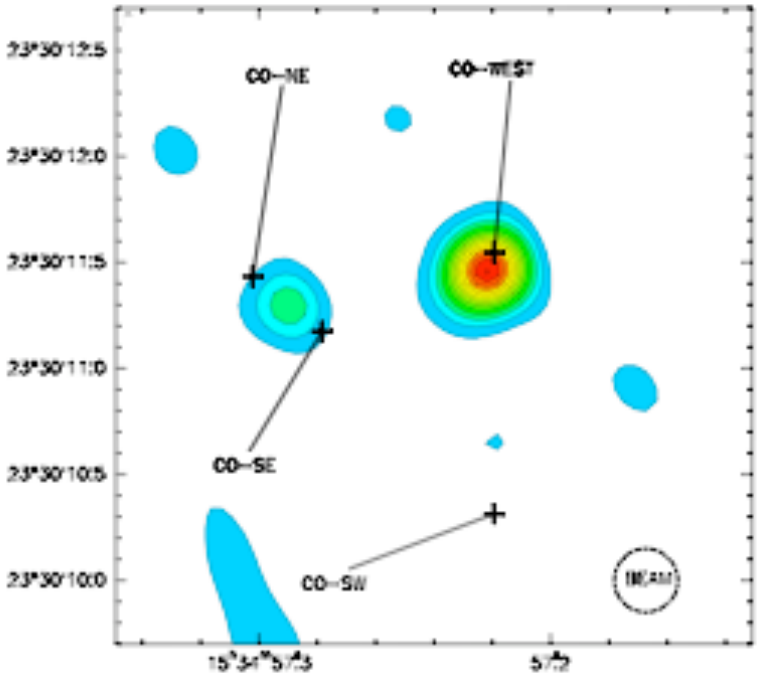

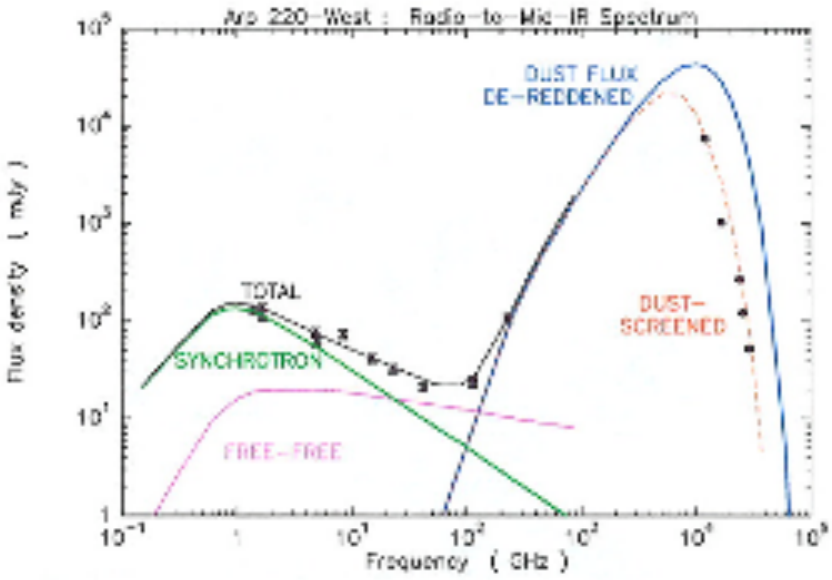

Fig. 2. Continuum map at 1.3mm (229.4 GHz). Contour steps are 6 mJy beam^{-1}. The Arp 220-West peak is 79 mJy beam^{-1}, and the East peak is 23 mJy beam^{-1}. Note that the continuum peaks do not coincide with the CO(2–1) peaks, which are marked with crosses. The beam is 0.30″ (lower right).

New Images Reveal Strong CO Absorption in Center of Arp 220 West, Coincident with the Position of the 1.3mm Source

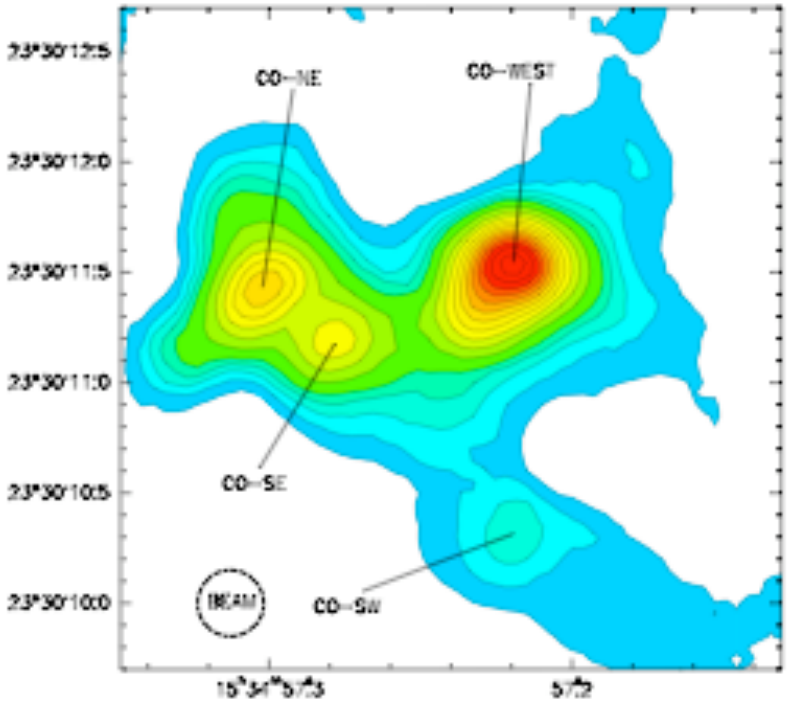

Fig. 1. The central 3″ of Arp 220 in CO(2–1) integrated over 770 km s^{-1}, with the 1.3 mm continuum subtracted. The beam (*lower left*) is 0.30″ with T_b/S = 266 K/Jy. Contours are 2 to 10 by 2, then 14 to 54 by 4 (in Jy km s^{-1}). The CO-West peak is 56.5 Jy km s^{-1}; CO-NE is 33.4 Jy km s^{-1}.

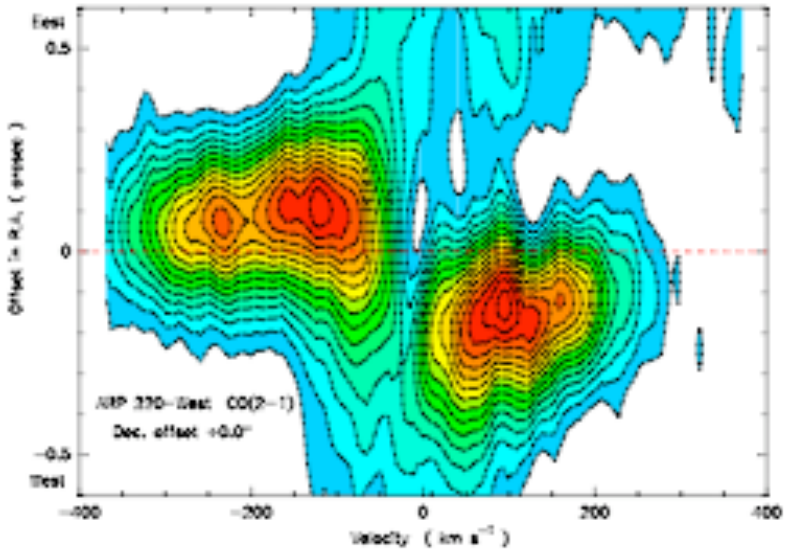

Fig. 3. East-west CO(2–1) position-velocity cut, through the West nucleus. CO(2–1) contours are in steps of 10 mJy beam^{-1}, with the 1.3 mm continuum subtracted. The CO ring around the West nucleus covers velocities from −370 to +300 km s^{-1}, and is cut by absorption at −60 to +40 km s^{-1}. Velocity offsets are relative to 226.422 GHz (cz_{hel} = 5450 km s^{-1}). RA offsets are relative to the West continuum peak, indicated by the horizontal line (position in Table 1).

- The CO absorption confirms the presence of the foreground dust that attenuates the short side of the SED;
- L(IR) ~ 9 x 10^{11}, implying M(gas) ~ 10^{9}; inferred radius of 30 pc implies a rotational velocity of 370 km/s, as is seen in FWHM of the CO line;
- Gas density is > 5000 $M_{\odot}$ pc^{-3}, ~10x stellar density in cores of giant ellipticals;
- CO is in a cooler (50K) ring surrounding a hot (170K) dust source;

A Black Hole?

- Luminosity and size of the dust source imply a surface brightness of ~ 5 x 10^{14} $L_{\odot}$;
- Equivalent to 10,000 O-stars, or 30x the luminosity of M82 from 1/1000th the volume;
- *"This means the true source of the Arp 220-West luminosity cannot be a starburst. It can only be black hole accretion disk."*

A Recent E-Mail from Downes on This Subject

"When we were observing Arp 220 ten to fifteen years ago, we were usually thinking of a scale size of one arcsec (or slightly more) for the CO and the FIR, and then it was plausible that on this scale (360 to 400 pc) that ALL of the IR luminosity could be coming from a big starburst. Most people gradually adopted this view, especially after the VLBI maps of the supernova remnants. Nowadays, if we are thinking about a radius of 0.1 arcsec (36 pc), and if the Keck mid-IR maps indicate that around 70% of the total IR luminosity could be coming from that little region, then we have to re-think the amount that might be due to an AGN. You're right, though, the FIR luminosities of the Arp 220 main disk, and also the East nucleus, are probably all due to super star clusters."

Summary

- Sanders & Mirabel suggested an evolutionary connection between ULIRGs and QSO might exist;
- Starburst lifetimes are short compared with the QSO phase; “Arp 220” objects are should be rare;
- PDS456 may be another example [Yun et al. astro-ph/0310340];
- Final caution - MERLIN and global VLBI observations reveal SNRs in Arp220-West, do not confirm the presence of an AGN, but cannot rule out a small ($M < 2 \times 10^7$) black hole.

A Spectroscopic Study of Arp 220 & NGC6240 by Greve et al. [astro-ph/0610378] is Instructive on Modeling Spectra

- observed CO, ^{13}CO, C^{18}O, HCN, HNC, HNCO, CS, and HCO^{+};
- made LVG models to infer masses of dense gas;
- HCO^{+}/HCN/CS probe progressively denser gas, by factors of 10, than CO;
- make predictions for HERSCHEL.

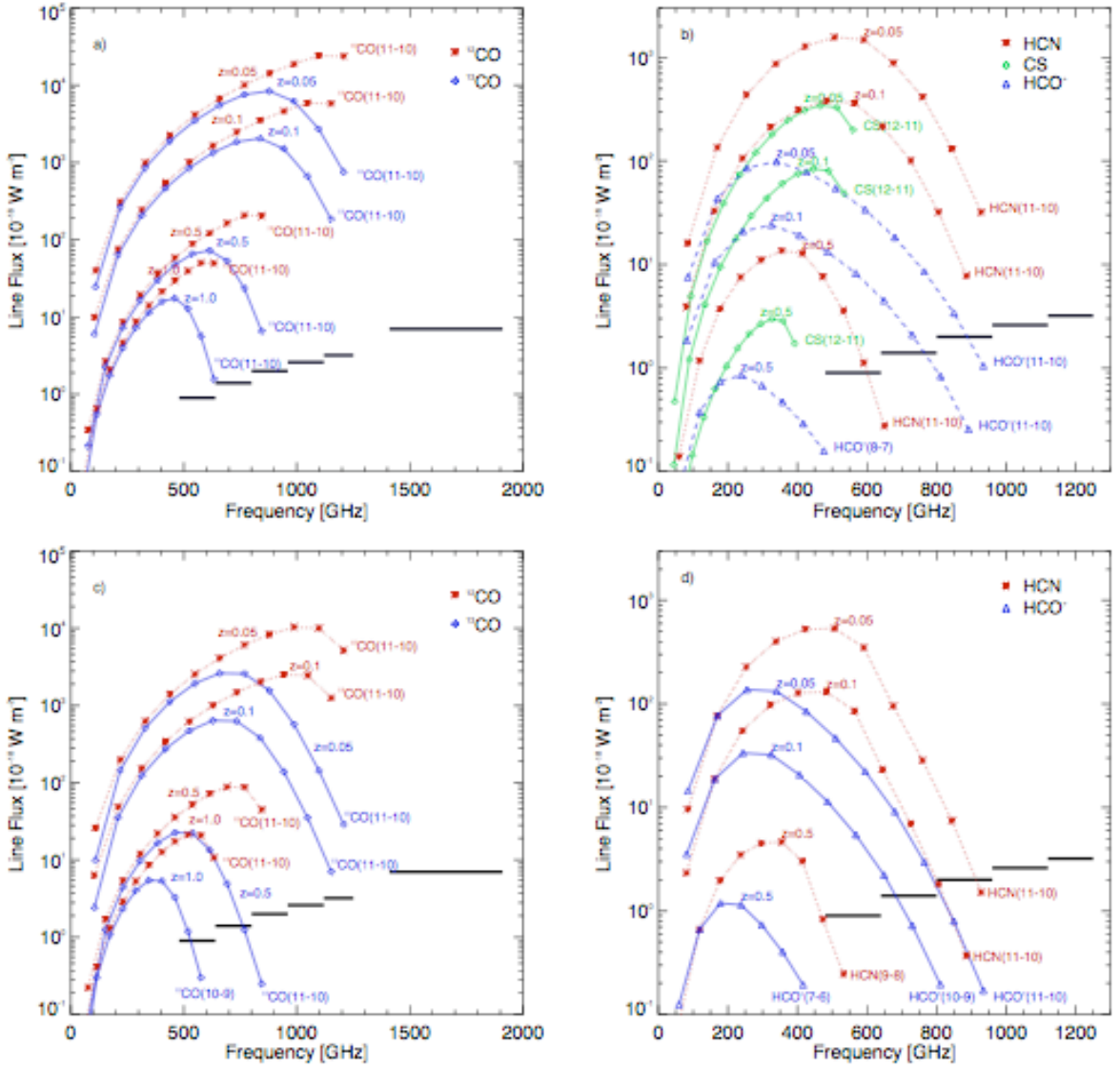

FIG. 4.— **Top panels:** integrated line flux strengths of the full $^{12}CO/^{13}CO$ (left) and HCN/CS/HCO^+ (right) rotational ladders as predicted by the dense gas template of Arp 220. The line fluxes are shown for Arp 220-like systems at redshifts $z = 0.05, 0.1, 0.5$, and 1.0. **Bottom panels:** Same as above, except the constraints on the dense gas in NGC 6240 have been used as a template. Horizontal bars are the expected 5-σ sensitivity limits of the five HI-FI bands after 1 hr of integration.

Line fluxes of CO, HCO^+, HCN, & CS expected from Arp 220 and NGC 6240.

HERSCHEL sensitivity (5σ after 1 hour) shown as horizontal black bars.

Other Density Tracers in ULIRGs?

- Baan et al. [arXiv:0710.0141] have analyzed lines of HCN, HNC, HCO^+, CN, CO, and CS in 37 IR-luminous and mega-OH maser galaxies, plus literature data on another 80;
- Usual dependence of L′(mol) on L(FIR);
- Relation for CS is steeper, implying different excitation?
- Claim to see differences among the galaxies related to the radiative excitation environment.

High Redshift Star Formation - The Early (Universe) Molecular (Emission Line) Galaxies (EMGs)

- EMG definition = galaxy seen in molecular lines (and/or forbidden atomic carbon lines) at a redshift $z > 1$;
- There are ~ 40 known EMGs, galaxies seen in CO;
- Of these, 5 are seen in HCN, 2 in HCO+, 1 in HNC, (1 in CN), 4 in [CI], and 1 in [CII];
- Maximum CO redshift, so far, is $z = 6.4$.

First detection of an EMG – IRAS F10214

- R. L. Brown had detected HI absorption in 3C196 at z = 0.436 and was interested in making a high-z CO detection;
- Our early efforts to detect high-z CO using the NRAO 140-Foot were comic failures;
- Rowan-Robinson et al. [Nature 351, 719 (1991)] reported obtaining a spectrum of IRAS F10214 that implied z = 2.3 and L(IR) ~ 10^{14} $L_{\odot}$, an *apparently* very luminous IR galaxy (now known to be lensed, mag = 17);
- Receipt of the (hardcopy!) preprint in the NRAO library prompted an immediate search for CO on the NRAO 12m.
- (R-R's spectrum of F10214 was obtained by luck - they were observing another candidate galaxy, but with a long slit that also fell across F10214!)

The discovery line was not beautiful, but convincing enough to claim a detection:

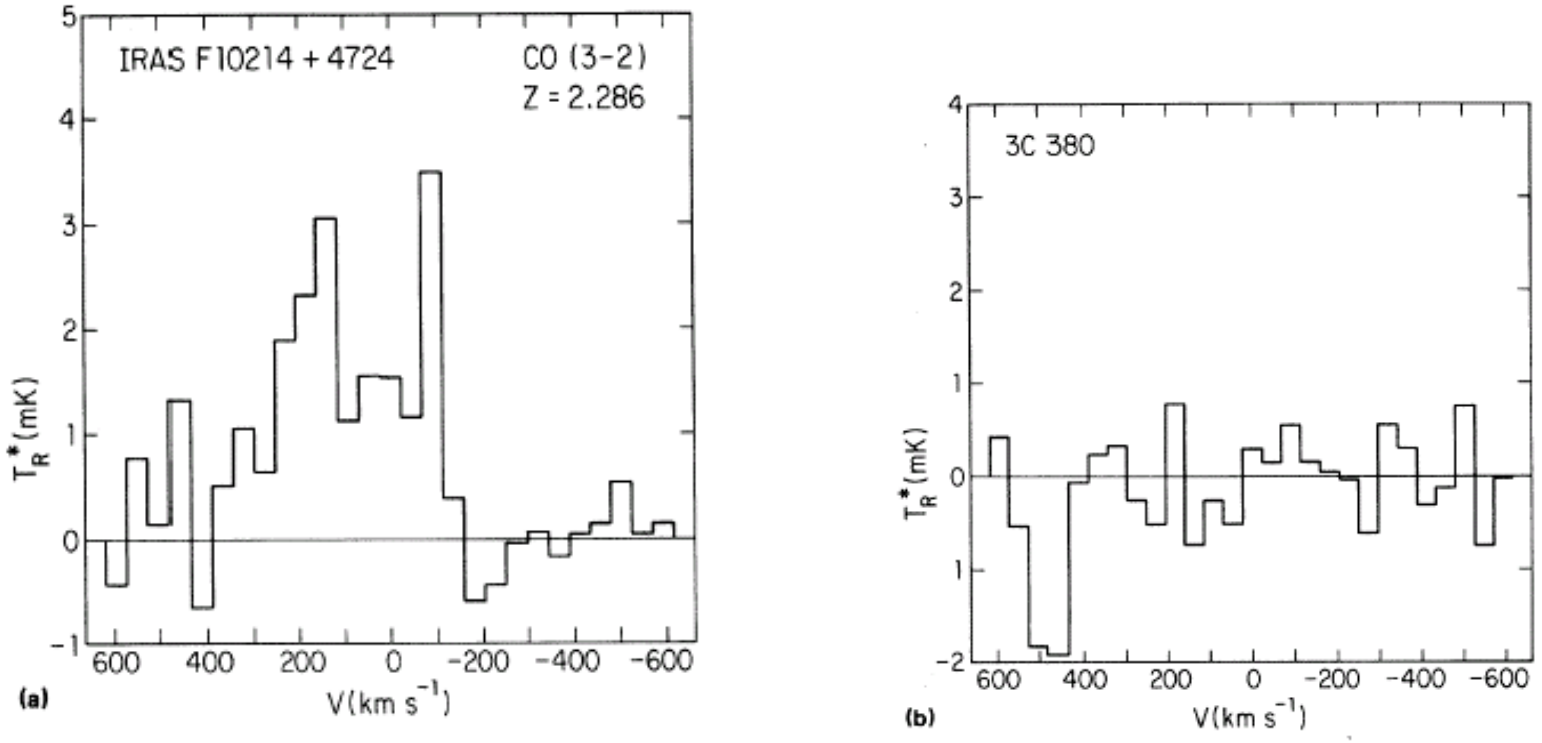

The last line in the paper reporting this detection [AJ 102, 1956 (1991)] reads “IRAS F10214+4724, a galaxy at redshift greater than 2, will be an ideal target for the Millimeter Array (an early concept for ALMA).”

Two Lessons from Personal Experience

- Do not procrastinate when it comes to observing proposals - submit as soon as possible after you have an idea. We were very lucky to have the 12-Meter idle and available at just the right time.

- Do be deliberate when it comes to publishing your result, however exciting, making sure you have the done the analysis correctly and have not ignored a more conservative interpretation. We made several mistakes in the analysis and did not allow for the possibility of gravitational lensing.

Calculating L′

The source luminosity L′(K km-s^{-1} pc^2) is given by

$L' = 3.25 \times 10^7 \nu_{obs}^{-2} D_L^{\,2} (1+z)^{-3} S \Delta v$, where

ν_{obs} is the observed frequency in GHz, D_L is the luminosity distance in Mpc, and $S \Delta v$ is the line strength in Jy km-s^{-1}.

[For $z \ll 1$, you recover the usual distance dependence:
$L' = 3.25 \times 10^7 \nu_{obs}^{-2} D^2 S \Delta v$.]

Derivation:

By definition of D_L, the monochromatic spectral luminosity is given by $L(\upsilon_{rest}) = 4\pi D_L^2 S_{CO}(\upsilon_{rest})$,

where $S_{CO}(\upsilon_{rest})$ is the flux density of CO in the rest frame.

$$L_{CO} = \int L(\upsilon_{rest})d\upsilon_{rest} = 4\pi D_L^2 \int S_{CO}(\upsilon_{rest})d\upsilon_{rest},$$
$$= 4\pi D_L^2 \int S_{CO}(\upsilon_{obs})d\upsilon_{obs}$$

by conservation of energy.

$$L_{CO} = 4\pi D_L^2 (\upsilon_{obs}/c) \int S_{CO}(\upsilon_{obs})dv$$
$$= 4\pi D_L^2 [\upsilon_{rest}/(1+z)c] S_{CO}(\upsilon_{obs})\Delta v, \text{ and}$$

changing units, $L_{CO} = 1.04 \times 10^{-3} D_L^2 \upsilon_{rest}(1+z)^{-1} S_{CO}(v)\Delta v$,

where, $L_{CO}(L_\odot)$, D_L(Mpc), υ_{rest}(GHz), & $S_{CO}\Delta v$(K km/s pc^2).

Cosmological Distances

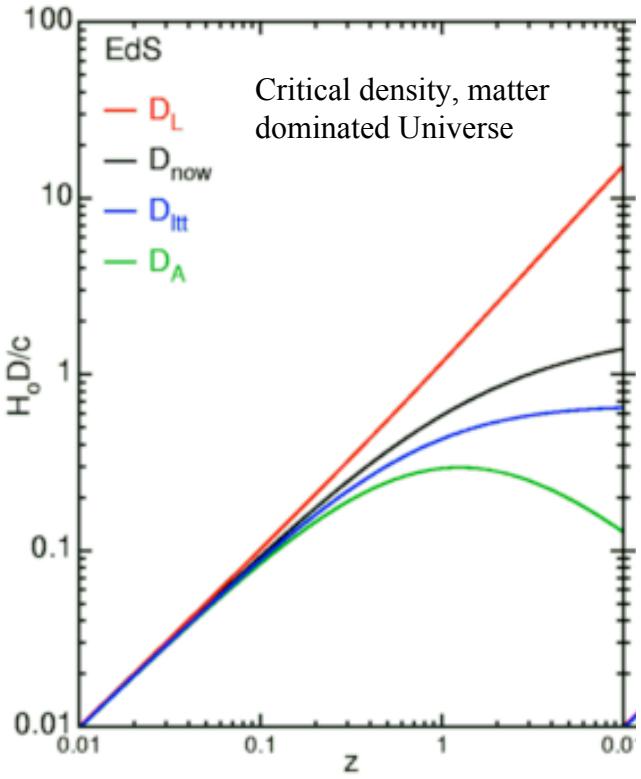

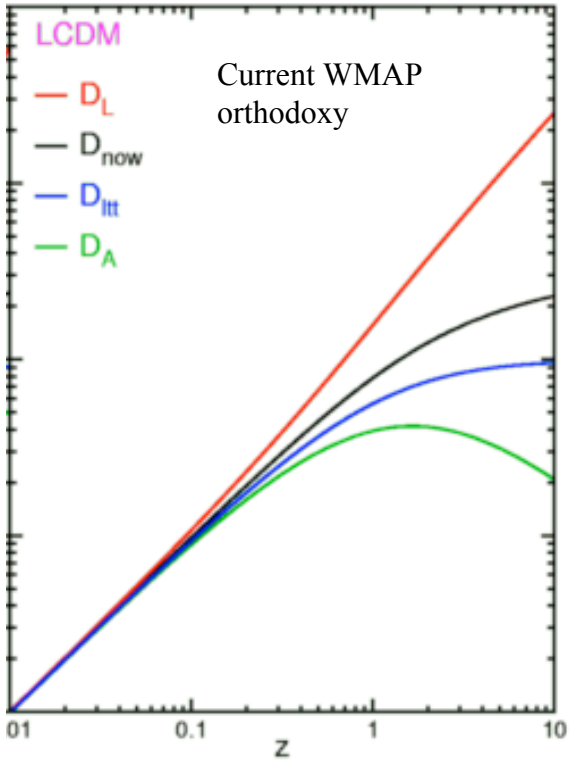

That the early Big-Bang Universe was a black body, requires

$D_L = D_A(1+z)^2$

http://www.astro.ucla.edu/~wright/CosmoCalc.html

EMG List (~ 2004) & Detection Telescopes

Quasars	Submm Galaxies	Radio Galaxies	Lyman Break Galaxy	Extremely Red Object
Q0957	J02396	53W002	MS1512 cB58	HR10
F10214	J16371	B3 J2330		
H1417	J16368	TN J0121		
J1409	J16366	6C1908		
Q0018	J04431	4C60.07		
MG0414	J16359	4C41.17		
Q1230	J14011	TN J0924		
J0911.4	J02399			
J04135	J22174			
MG0751	J09431			
APM08279				
J13120				
PSS J2322				
BRI 1335				
BRI 0952				
BR 1202				
SDSS J1148				

NRAO 12m **NRAO VLA**

IRAM PdB Interferometer

OVRO **Nobeyama** **ATNF**

Most EMGs were discovered by the IRAM PdB Interferometer, the most powerful facility in the world today for their study

“Redshift Magic” Helps (the negative K-correction): mm fluxes are roughly independent of redshift

M82 scaled to ULIRG luminosity, ISO data; Beelen and Cox

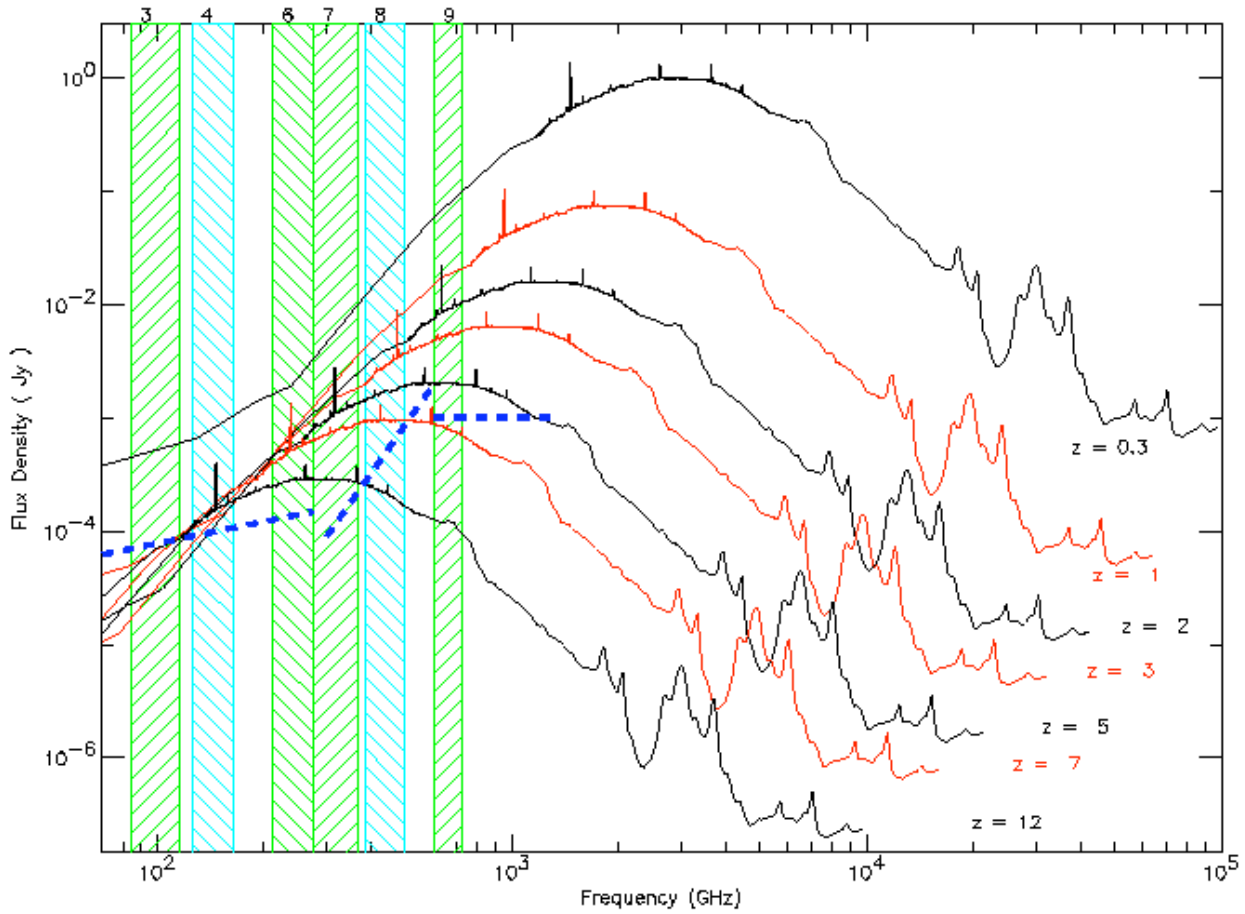

As do gravitational lenses - here, an Einstein Ring.
Roughly 2/3 of EMGs are lensed.

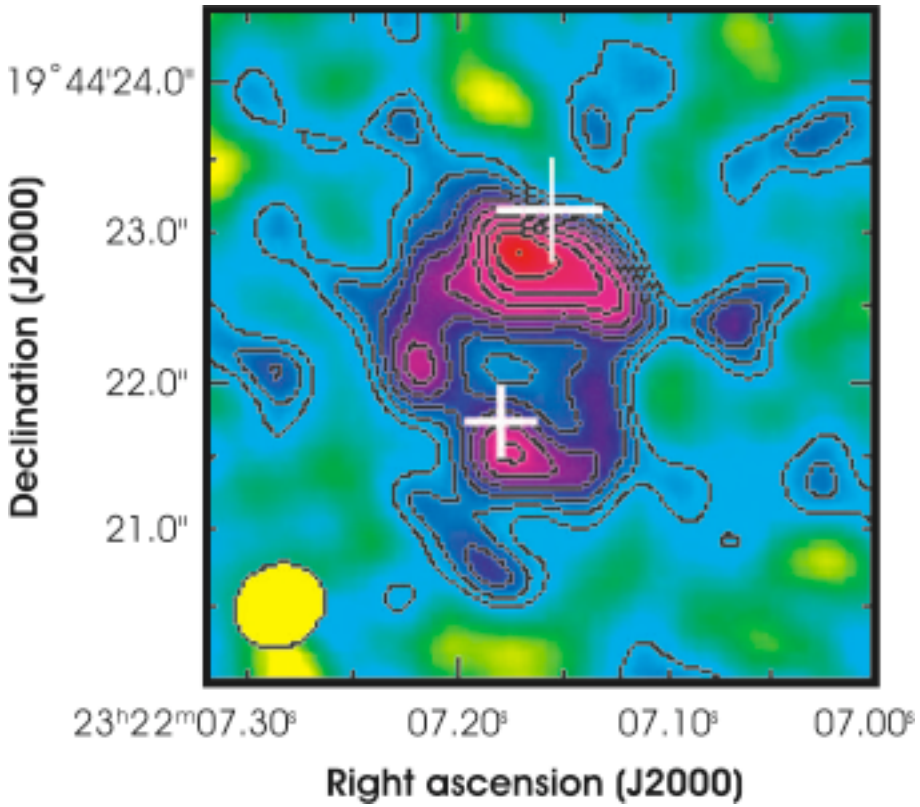

PSS2322 imaged in CO(2-1) emission using the VLA, at a resolution of 0.6′′.

Magnification = 7

[Carilli et al. Science 300, 773 (2003)]

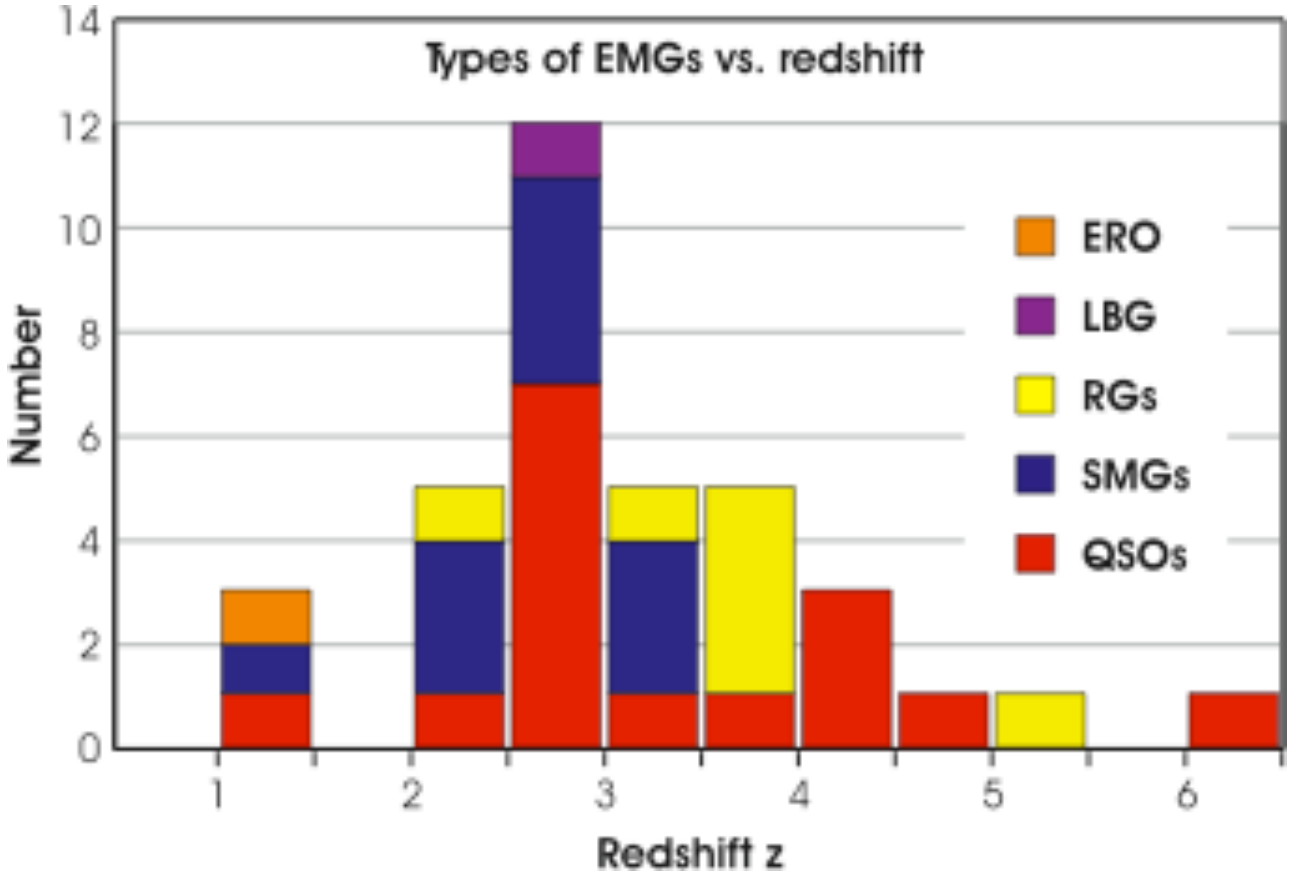

Types of EMGs: 16 quasars;, 11 submm galaxies, 7 radio galaxies, 1 extremely red object, and 1 Lyman break galaxy; total of 36. There are six new CO detections not in plot - four SMGs (z~2) - and two quasars (z~5).

Selection Effects

- Instrumentation: best sensitivity in 3mm band at 75-120 GHz $\Rightarrow z > 2$ for CO(2-1), or $2.8 < z < 4$ for CO(3-2); for $z < 2$ there are very few detections, and for $z > 4$, higher J lines must be observed or a lower frequency facility must be used;

- Knowledge of the redshift drives the choice of objects for a search; this is fading as "z-machines" come on line with large bandwidth spectrometers (Z-Spec, ZEUS, Zpectrometer, RSR), see the ASP Conf. Series, volume 375, ed. Baker et al. (2006);

- No blind survey has been done, but will be possible over small patches of sky with z-machines;

- Best strategy for ALMA searches: start with galaxies detected in submm (LABOCA, SCUBA2, . . .).

The Types of EMGs Detected in CO Reflect the Search Techniques Used

- QSO: Search optically identified quasars for strong (S > 3 mJy) mm continuum emission (from heated dust) followed by a search for CO emission at the quasar (optical) redshift;

- Submm Galaxies: Make a blind survey for galaxies with strong FIR emission, get optical redshifts, search for CO;

- Radio Galaxies: Search for CO in high-z radio galaxies with strong mm/submm/FIR continuum emission and known redshift;

- EROs: Search for CO in unusually red, FIR luminous galaxies with known redshifts.

A QSO Example - the Cloverleaf

Image of the Cloverleaf in CO(7-6) emission, lens magnification = 11:

- resolution = 0.5″;
- lens model implies a molecular disk of radius r = 800 pc, a surface density $\sigma = 10^4\ M_\odot\ pc^{-2}$, $M_{gas} = 3.2 \times 10^{10}\ M_\odot$, and $M_{dyn}\sin^2 i = 3.2 \times 10^{10}\ M_\odot$.

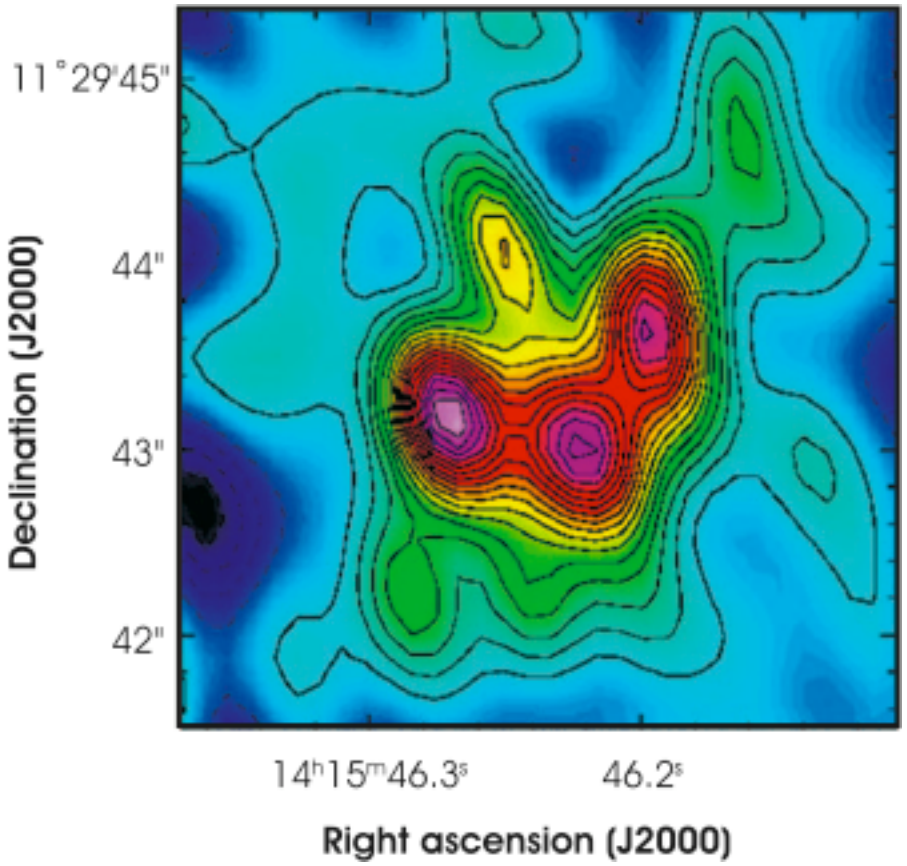

Venturini & Solomon ApJ 590, 740 (2003). Image made from data of Alloin et al. A&A 321, 24 (1997).

Gray-Body Dust Emission

The dust emission is assumed to be thermal emission from an optically thin medium:

$$S_\nu \propto [1-\exp(\tau_\nu)]\, B_\nu(T) \propto \tau_\nu\, B_\nu(T)$$
$$\propto \kappa_\nu\, B_\nu(T) \propto \kappa_0\, (\nu/\nu_0)^\beta\, B_\nu(T),$$

where, S_ν is the specific flux density, κ_ν the mass absorption coefficient, $B_\nu(T)$ the Planck function, and $\beta = 1 - 2$, typically.

Dust Luminosity

By definition of the luminosity distance,

$L_d = 4\pi D_L^2 \int S_\nu d\nu$.

In astronomical units,

$L_d = (2.5 \times 10^{-11}) 4\pi D_L^2 \int S_\nu d\nu$,

where, L_d is in solar luminosities, D_L is in Mpc, S_ν is in mJy, and $d\nu$ is in Hz. (The flux density integral can be taken either in the rest frame or the observer's frame, as $S_\nu d\nu$ is fixed by conservation of energy.)

Typical Data Analysis

- Flux density measurements are converted to the rest frame: $S(rest)/S(obs) = \nu(obs)/\nu(rest) = (1+z)^{-1}$.
- Curves of the form $S = S_0 \nu^{3+ß} [\exp(h\nu/kT) - 1]^{-1}$ are fitted to the data points, varying S_0 and T.
- T and ß are highly correlated, and it is difficult to vary both even if there are many data points; typically one fixes ß at some mid-range value, say 1.5, and varies only T.
- Note that S_0 contains everything necessary to fix the units, which are typically in mJy.

T(dust) - ß Degeneracy

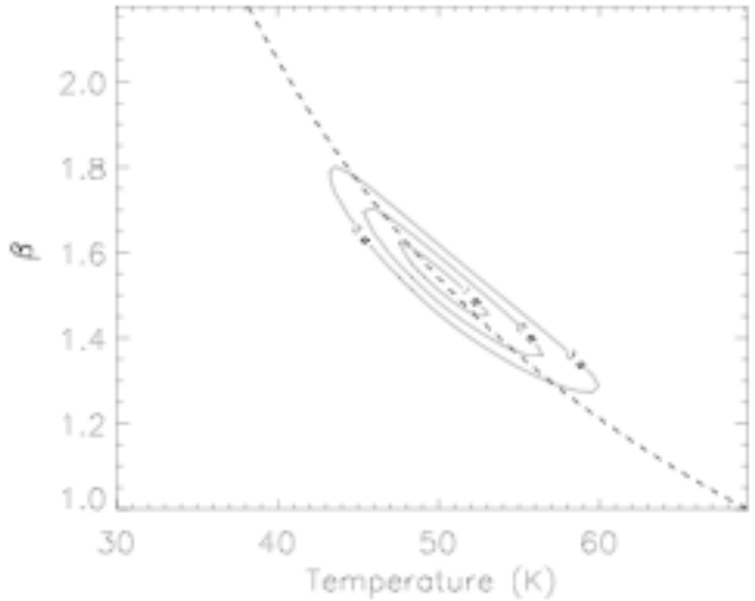

FIG. 5.—Contours of χ^2 in the β-T_{dust} plane for the combined SEDs of the high-z quasars shown in Fig. 4. Contours represent the 1, 2, and 3 σ uncertainties. The dashed line represents the β-T_{dust} degeneracy (see text for details). [*See the electronic edition of the Journal for a color version of this figure.*]

Luminosity Conventions

It is useful to define the *dust luminosity*, L_d, as the integral from zero to infinity.

Some authors refer to this as the *far-infrared luminosity*, L_{FIR}, but that is better defined as the integral from 2.45 to 7.06 THz, corresponding to the wavelength range 42.5 - 122.5 μm, to be consistent with the conventions established in the IRAS era.

Note: the integral $\int x^{3+\beta} [\exp(x)-1]^{-1}$ from zero to infinity is given by $\Gamma(4+\beta)\, \varsigma(4+\beta)$, where Γ is Euler's Gamma Function and ς is Riemann's Zeta Function, which can be useful in calculating dust luminosities.

Dust Masses

Because the dust luminosity is also given by:

$L_d = 4\pi M_d \int \kappa_\nu B_\nu(T)\, d\nu$,

one can show that in astronomical units,

$M_d = (8.27 \times 10^{14})\, S_0\, \kappa_0^{-1}\, D_L^{\,2}$,

where, M_d is in solar masses, S_0 is in mJy, κ_0 is in cm^2/g, and D_L is in Mpc.

SED of the Cloverleaf (z = 2.6): Three-Component Model

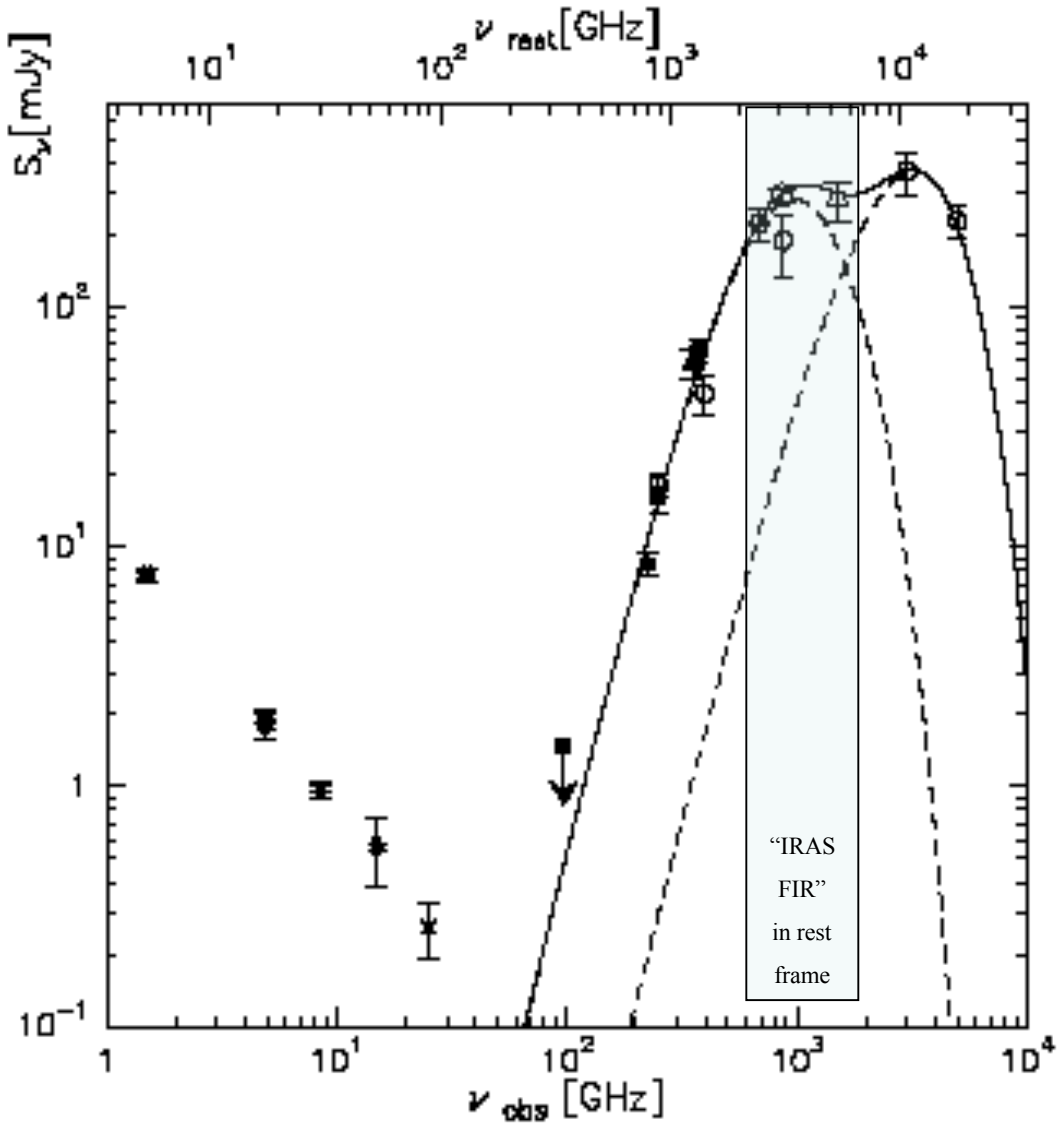

Weiss, et al. A&A 409, L41 (2003).

Three components:

1% of dust in a warm (T_d=115K) mid-IR component, heated by AGN;

99% of dust in a much more massive cool (T_d=50K) far-IR starburst component;

L(FIR) = 5.5 x 10^{12} $L_\odot$
M(dust) = 1.5 x 10^8 $M_\odot$
using m = 11;

and the radio continuum of synchrotron radiation from SN cosmic rays and the AGN.

A Solid Detection of CN

[Riechers et al. ApJ 666, 778 (2007)]

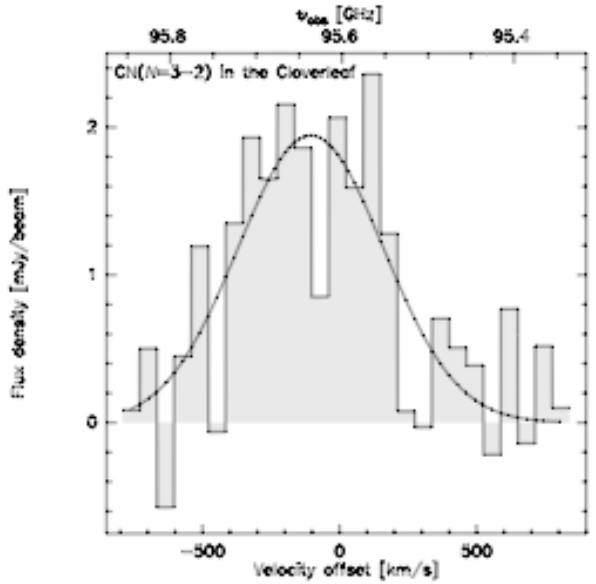

FIG. 4.—Spectrum of the CN($N = 3 \rightarrow 2$) emission at a resolution of 63 km s^{-1} (20 MHz). The velocity scale is relative to the tuning frequency of 95.603 GHz. The rms per velocity bin is 0.8 mJy. The solid line shows a Gaussian fit to the data. [*See the electronic edition of the Journal for a color version of this figure.*]

CN (N=3-2; a blend of 19 lines!) detected in the Cloverleaf (z = 2.56)

L(FIR)/L′(CN) falls within the scatter of values for ULIRGs.

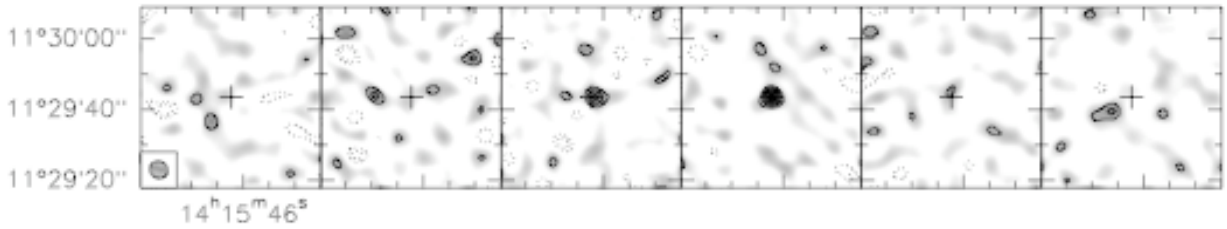

FIG. 3.—Channel maps of the CN($N = 3 \rightarrow 2$) emission (same region as shown in Fig. 2). One channel width is 80 MHz, or 252 km s^{-1} (at 95.4355, 95.5155, 95.5955, 95.6755, 95.7555, and 95.8355 GHz; frequencies increase with channel number). Contours are shown at $(-3, -2, 2, 3, 4, 5)\ \sigma$ ($1\ \sigma = 0.4$ mJy beam^{-1}). The beam size ($5.3'' \times 4.9''$) is shown in the bottom left corner; the cross indicates the same position as in Fig. 2. [*See the electronic edition of the Journal for a color version of this figure.*]

PAH Emission in the Cloverleaf

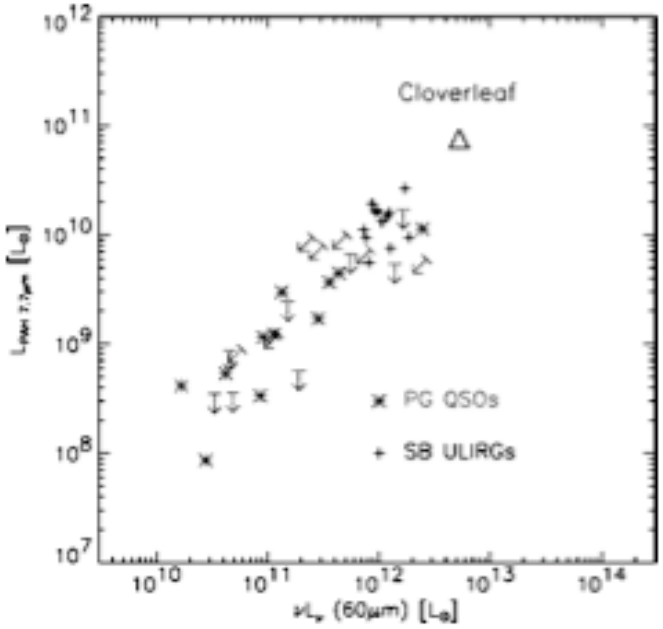

FIG. 3.—Relation of 7.7 μm PAH luminosity and rest-frame FIR luminosity for the Cloverleaf and for local PG QSOs and starbursting ULIRGs from Schweitzer et al. (2006). [*See the electronic edition of the Journal for a color version of this figure.*]

- First detection by Spitzer of PAH emission at high-z was reported by Lutz et al. [ApJ 661, L25 (2007)] for the Cloverleaf: the 6.2 & 7.7μm features;
- L(PAH) / L(60μm) is on the relation for PG QSOs and ULIRGs.

Quasar EMG SEDs

- EMG SEDs are typically sampled at longer wavelengths, on the Rayleigh-Jeans side: 1.3mm (MAMBO, Bolocam); 450 and 850 μm (SCUBA), (SCUBA2 and LOBACA in future);
- the SED peak for typical EMG T_d ~ 30K is 100 μm (rest frame) or ~ 350 μm (obs) for z~2.5;
- The SHARC2 detector on the CSO can detect as little as 10 mJy at 350 μm (in good weather!).

Observations by Wu, et al. (unpublished) at the CSO using (SHARC2)

RX J0911.4

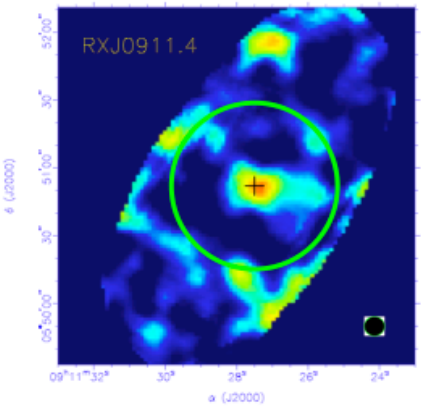

SMM J14011

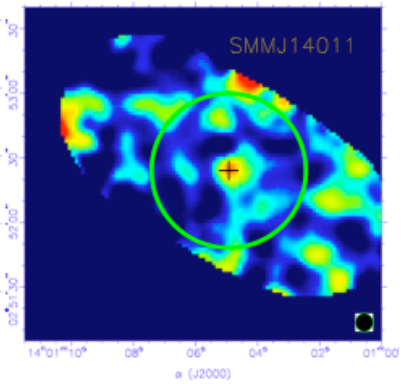

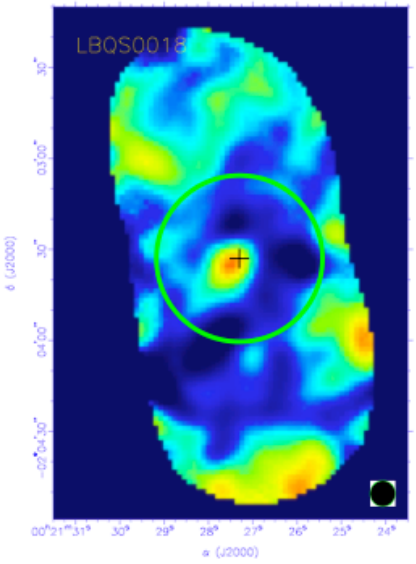

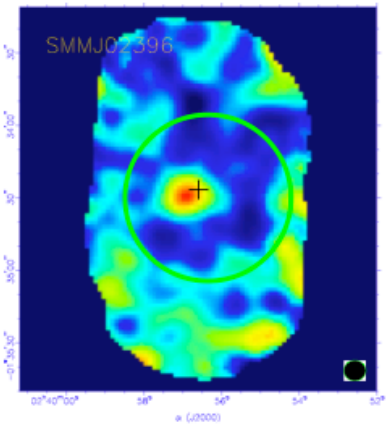

LBQS0018

SMM J02396

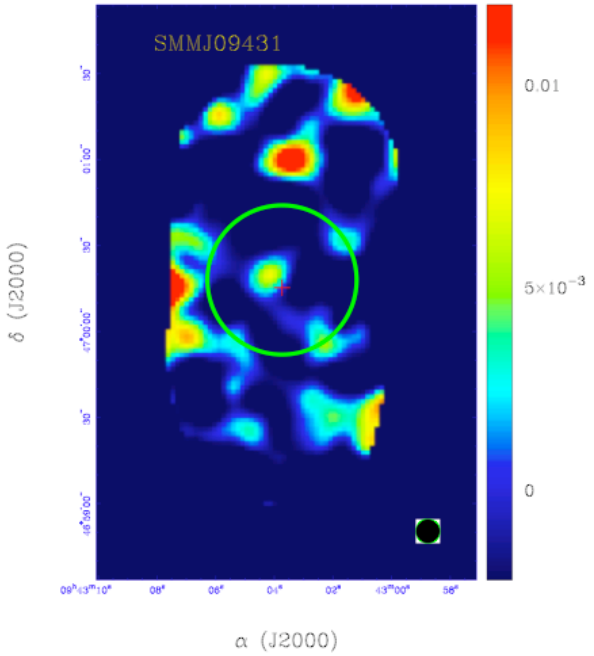

SMM J09431

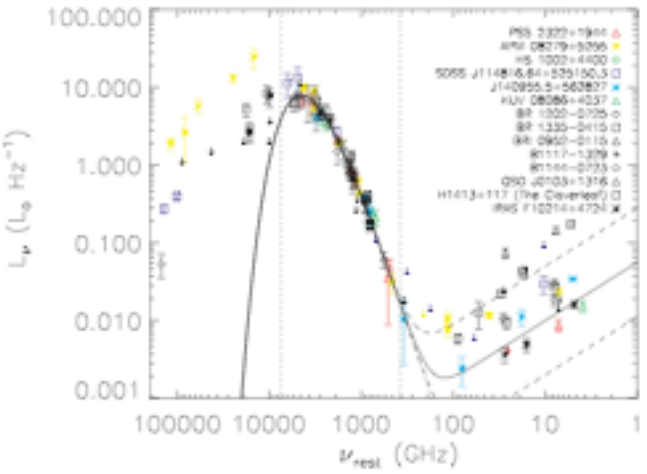

FIG. 4.—Combined SED, in the rest frame, for all the high-z quasars from this paper and sources discussed in Benford et al. (1999) and Priddey & McMahon (2001; see references therein and in our Fig. 2). The SEDs have been normalized to the far-IR luminosity of PSS 2322+1944. Each quasar is represented with a different symbol, identified in the panel. The best fit to the rest-frame far-IR data together with the derived radio continuum are shown using the same definitions as in Fig. 2. The corresponding dust temperature and spectral index are displayed in Fig. 5. The two vertical dot-dashed lines delineate the wavelength domain defined as the far-IR in this paper.

Beelen et al. [ApJ 642, 694 (2006)] present SHARC2 data for six EMGs and a summary for the SEDs of other EMGs (quasars).

Plot normalizes L(FIR) to that of PSS2322.

Mean T_d = 50K and ß = 1.6

APM08279 - A Remarkable QSO Example of an EMG

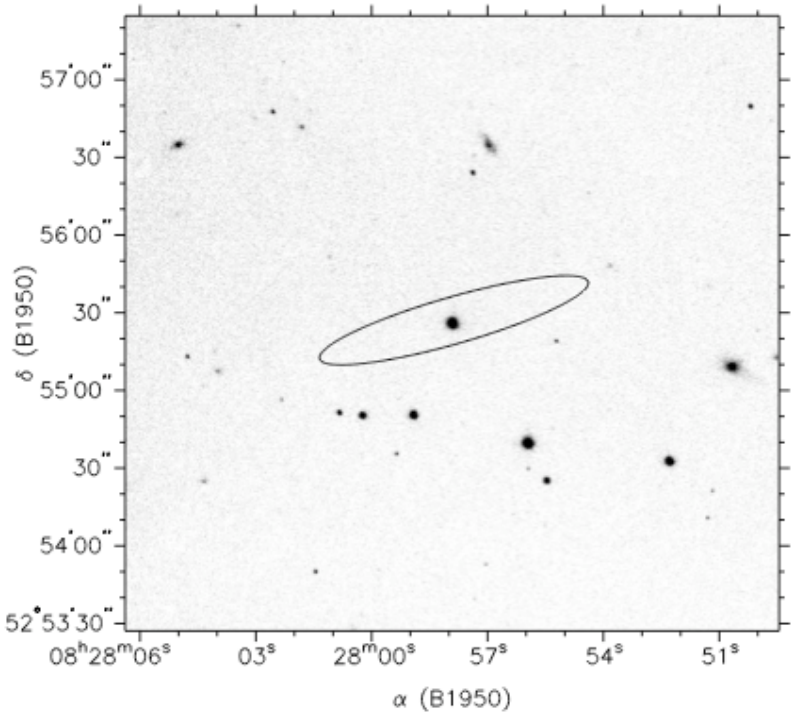

IRAS error ellipse on PSS

Irwin et al. [ApJ 505, 529 (1998)] identify IRAS F08279 with a BAL quasar, z = 3.87.

R = 15.2 & S(60μm) = 0.5 Jy ⇒ an *apparent* L(bol) ~ 5×10^{15}.

Lens mag ~ 100 makes this more reasonable, but still large; the host galaxy contains a very hot, massive starburst that makes it an above-average EMG.

CO is seen up to J=11-10
[Weiß, et al. A&A 467, 955 (2007)]

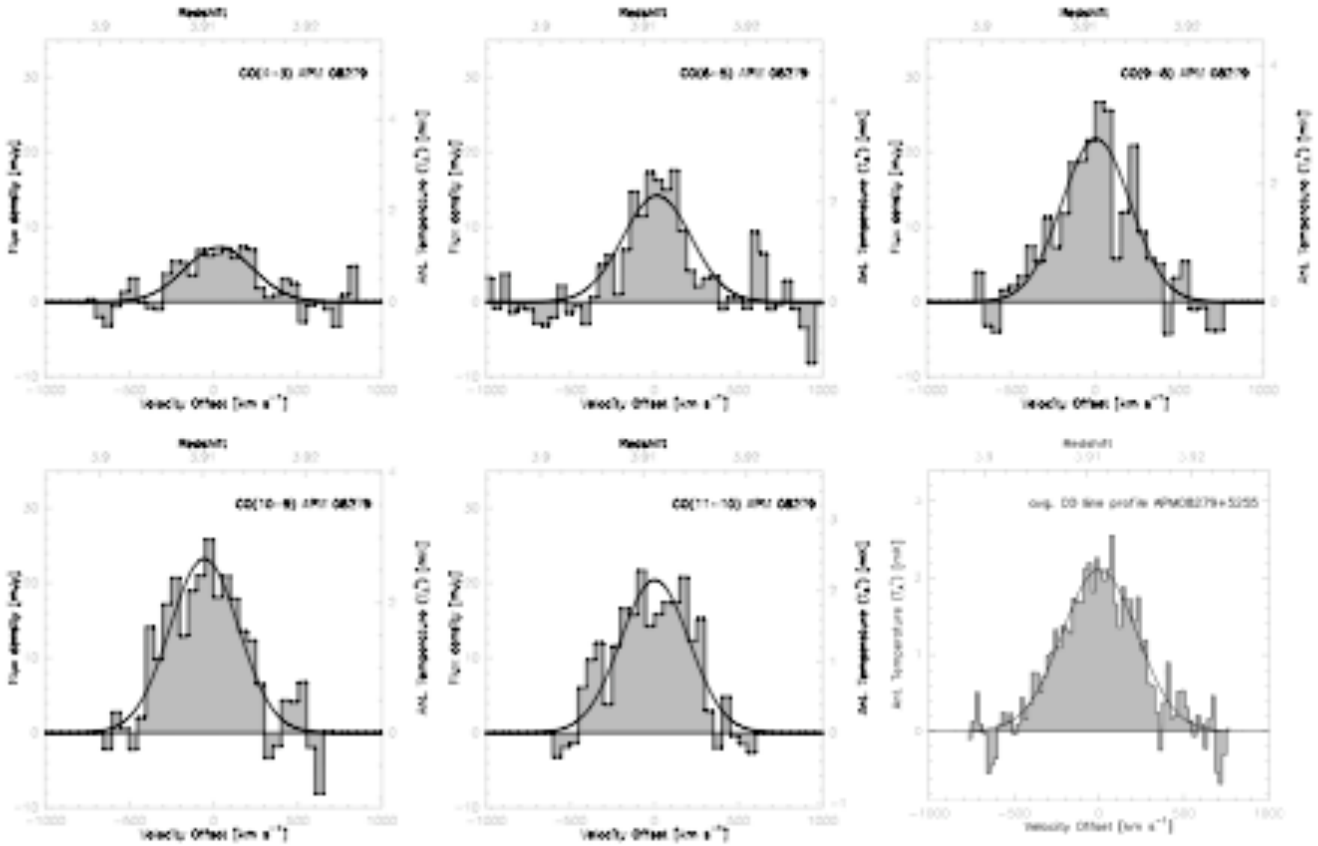

Fig. 1. IRAM 30 m telescope spectra of CO 4–3, 6–5, 9–8, 10–9, 11–10 and the average CO spectrum from APM 08279+5255, with Gaussian fit profiles superimposed. Velocity scales are relative to a redshift of $z = 3.911$. The velocity resolution for individual spectra is 50 km s^{-1}. For the average spectrum, the velocity resolution is 22 km s^{-1}. The individual spectra are plotted on the same scale in flux density (*left axis*).

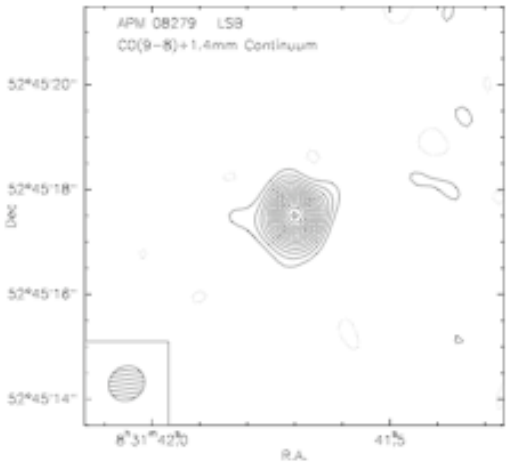

Fig. 3. Map of an 8″ field around APM 08279 made with the IRAM Interferometer at 1.4 mm. The signal is the CO(9–8) line integrated over 760 km s^{-1}, plus the 1.4 mm dust emission at the highest spatial resolution (uniform weighting, beam: 0.″71×0.″64 (*lower left inset*)). Contours start at 3σ = 1.35 mJy beam^{-1} and increase in steps of 3σ. The peak is 19.4 mJy beam^{-1} (43σ) and the spatially-integrated flux is 33.9 mJy.

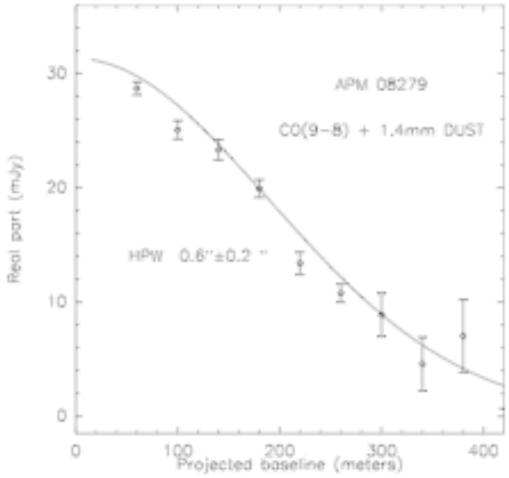

Fig. 4. Size measurement with the IRAM Interferometer: visibility amplitudes of the signal in the receivers' lower sideband at 1.4 mm. The signal is the CO(9–8) line integrated over 760 km s^{-1}, plus the 1.4 mm dust emission. The plot shows the real part of the visibility amplitude vs. the projected antenna spacing, for u,v-plane data averaged in circular bins 40 m wide, with error bars of $\pm 1\sigma$. The solid curve is a circular Gaussian fit with half-power width 0.″6 ± 0.″2.

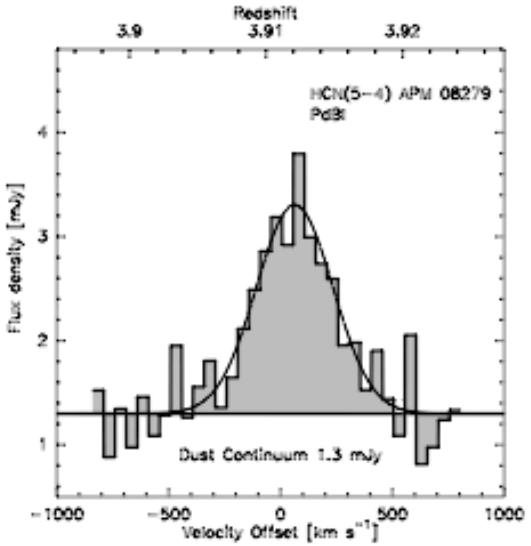

Fig. 5. HCN(5–4) spectrum from APM 08279+5255 obtained with the IRAM Interferometer. The line profile appears above the dust continuum of 1.3 mJy. The velocity scale is relative to a redshift of $z = 3.911$, the beam is 7.″2 × 5.″4 at PA 81°, and the channel width is 15 MHz (49.84 km s^{-1}). The rms noise in the spectrum is 0.47 mJy.

HCN (5-4) is remarkably strong, too strong for best fits to LVG models of the CO lines [Wagg et al. ApJ 634, L13 (2005)].

PdB observations of cont. and CO(9-8) resolve source with a size 0.6±0.2″.

Detection of HCO+

[Riechers et al. ApJ 645, L13 (2006)]

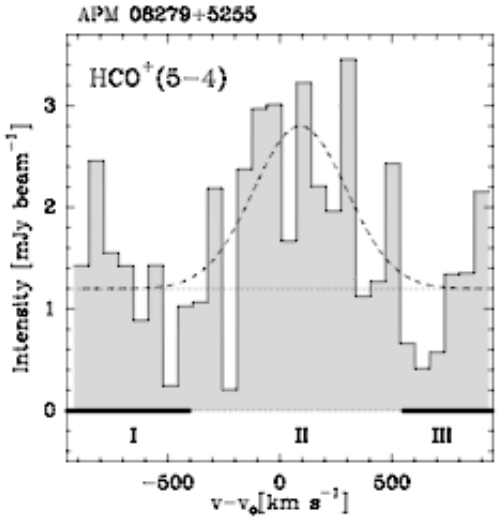

FIG. 1.— Spectrum of the HCO^+ (5–4) line detected towards the peak of integrated line intensity in APM 08279+5255 at (α, δ)=($08^h31^m41.73^s$, $52°45'17.4''$). For the sake of comparison, velocities (v-v_0) have been re-scaled with respect to the CO redshift of z=3.911 determined by Downes et al. (1999). The dashed line shows the Gaussian fit to the HCO^+ (5–4) emission and the highlighted channels in intervals I and III identify the range for line-free continuum emission.

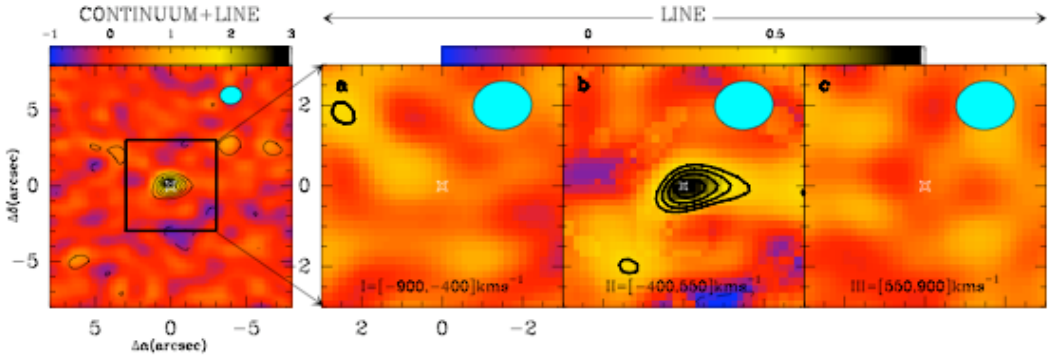

FIG. 2.— The left panel shows the total (continuum+line) velocity-integrated emission map in APM 08279+5255. The *total* emission has been integrated from v-v_0=-900 to 900 km s^{-1}. Levels are -3σ, 3σ to 15σ in steps of 3σ (1σ=0.17 Jy km s^{-1}). Panels a–to–c show the HCO^+ (5–4) line emission maps obtained after subtraction of the continuum source for the three velocity intervals (I, II, III) defined in Figure 1: I=[-900,-400] km s^{-1} (a), II=[-400,550] km s^{-1} (b), III=[550,900] km s^{-1} (c). Levels in panels a–to–c are -0.39, 0.39, 0.52, 0.65, 0.78Jy km s^{-1} (equivalent to -3σ, 3σ, 4σ, 5σ, and 6σ for channel II). To derive the continuum map we used channels I and III (see Figure 1). The filled ellipse in each panel represents the $1.46''\times1.20''$ (PA=94°) synthesized beam. ($\Delta\alpha$, $\Delta\delta$)–offsets in arcsec are relative to the peak of Continuum+Line emission at ($08^h31^m41.73^s$, $52°45'17.4''$), identified by the diamond marker.

Detection of HNC (and CN?)

[M. Guélin et al. A&A 462, L45(2006)]

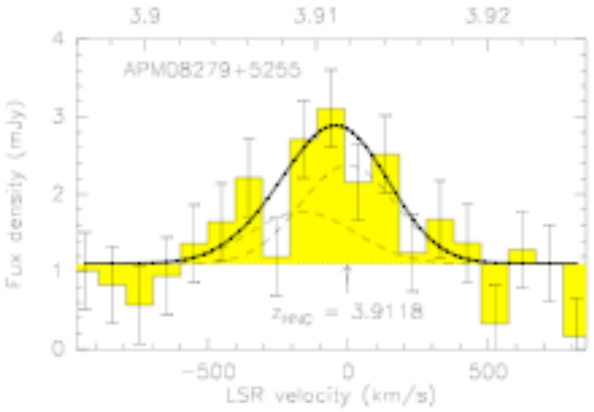

Fig. 1. Spectrum of the HNC(5–4) and CN (4–3) emissions from APM 08279+5255. The velocity scale is relative to the HNC frequency redshifted by $z = 3.9118$. The velocity resolution is 97 km s^{-1}, the r.m.s. noise 0.5 mJy. The smooth line represents the best fit synthetic spectrum and the dashed lines the contributions from CN (right) and HNC (left) to this spectrum.

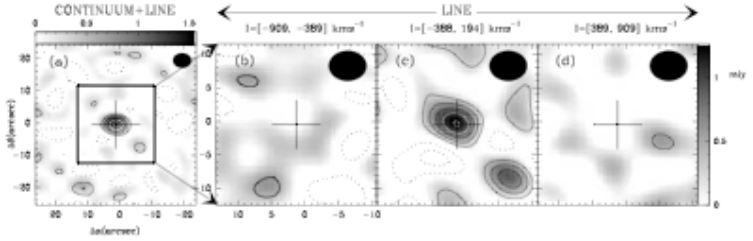

Fig. 2. a: Total (continuum+line) emission map of APM 08279+5255 integrated from −909 to 909 kms^{-1} and centered on 92.29 GHz. Levels are -2σ (dashed) and 2σ to 10 σ in steps of 2 σ (σ = 0.15 mJy/beam). **b-d**: Velocity-channel maps obtained after subtraction of a point-like 1.1 mJy continuum source, located at the position of maximum emission. The data have been averaged over the three velocity intervals delineated in Fig. 1. **b:** I = [−909, −389], **c:** I = [−388, +194] and **d:** I = [389, 909] kms^{-1}. The emission from the HCN(5–4) and CN (4–3) lines appears in the central channel (**c**). Contours are -2σ, -1σ (dashed) and 1σ to 5σ in steps of σ for (c) and -2σ and 2σ for (b) and (d) (with 1σ = 0.25 mJy/beam). The synthetized beam is shown as a grey ellipse on the top right corner. The offsets (in arcseconds) are relative to the peak of the continuum+line emission at (08^{h}31^{m}41^{s}69, 52°45′17″12) (J2000), shown by the crosses.

- HNC (J=5-4) is detected and CN (N=4-3) is tentatively detected.
- HNC/HCN and CN/HCN line intensity ratios are 0.6 and 0.4, respectively.
- excitation of lines may not be purely collisional.
- clear indication of need for caution with ALMA - there will be many lines!

Like HCN, HNC and HCO^+ are surprisingly strong in APM08279

- The molecules can be collisionally excited, but for HCN this requires ~100x the Galactic abundance to account for the line strength. This might be possible if the chemistry were driven by x-ray ionization;
- Radiative excitation of the HCN in the IR stretch/bend modes at 3, 5, and 14 μm is a more obvious possibility;
- This can work for the other molecules as well;
- Both possibilities are discussed by Aalto et al. [astro-ph/0612122] for the apparent overabundance of HNC in Arp 220, NGC 4418, and Mrk 231.

SMA Continuum Imaging [Krips et al. arXiv:0710:4956]

- At 0.4″ resolution, source is resolved into two components;
- Lens model implies an intrinsic source diameter of ~ 80 pc & mag = 90;
- 1mm dust continuum source size < near IR from HST: favors models where AGN is dominant source of heating for dust.

Two - Component Fit to SED

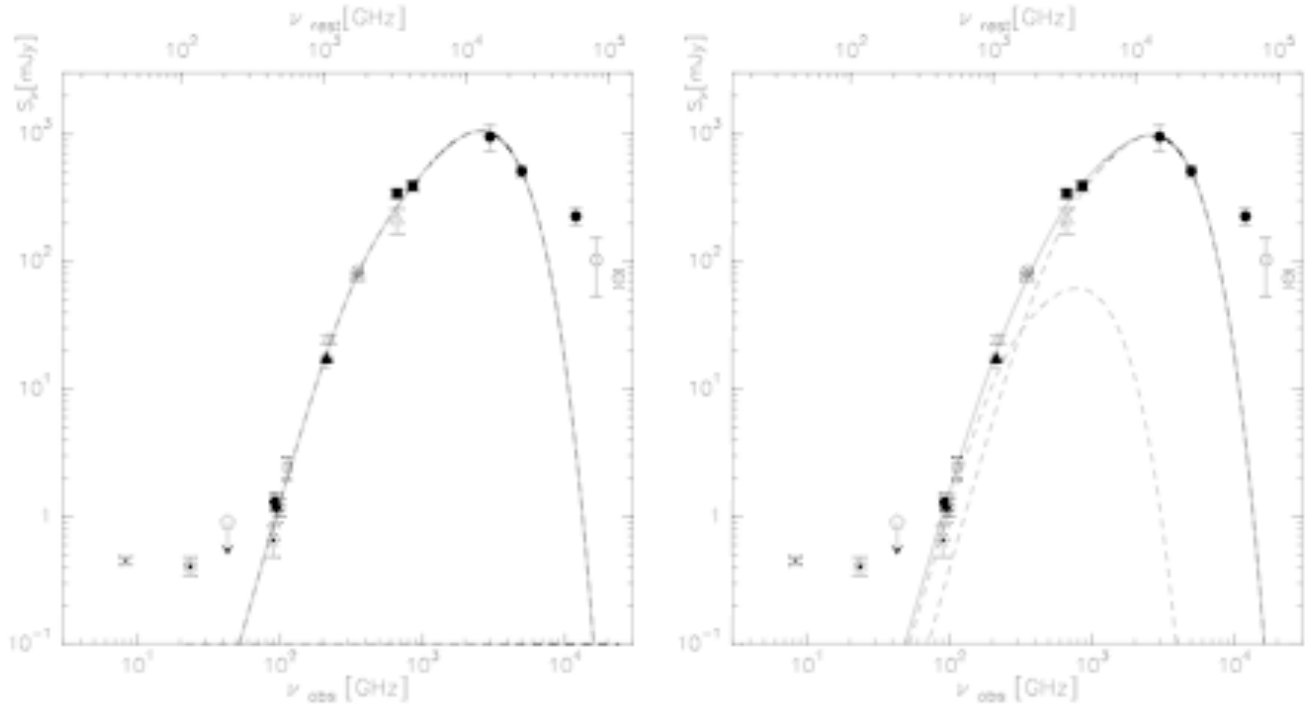

Fig. 6. Single component (*left*) and two component (*right*) dust models for APM 08279+5255. The continuum fluxes are from Irwin et al. (1998), Lewis et al. (1998, 2002a), Downes et al. (1999), Egami et al. (2000), Papadopoulos et al. (2001), Barvainis & Ivison (2002), Wagg et al. (2005), Beelen et al. (2006) and this work.

A one - component model fits the data equally well as two components. Use caution in fitting Planck curves to SEDs.

Parameter	1-Comp.	2-Comp. "Warm"	2-Comp. "Cool"
T(dust)	215±10	220±30	65±18
M(dust)	7.5×10^8	2.1×10^8	2.6×10^9
L(FIR)	2.0×10^{14}	2.0×10^{13}	1.7×10^{14}
Filling Factor		70%±10%	30%±10%
Size(radius)	680±30 pc		

The most distant QSO (near end of the Epoch of Re-ionization) is SDSS J1148+5251 at z=6.4

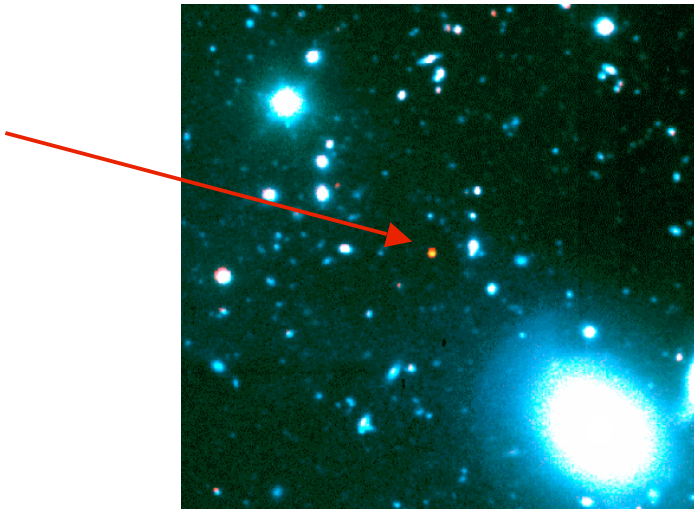

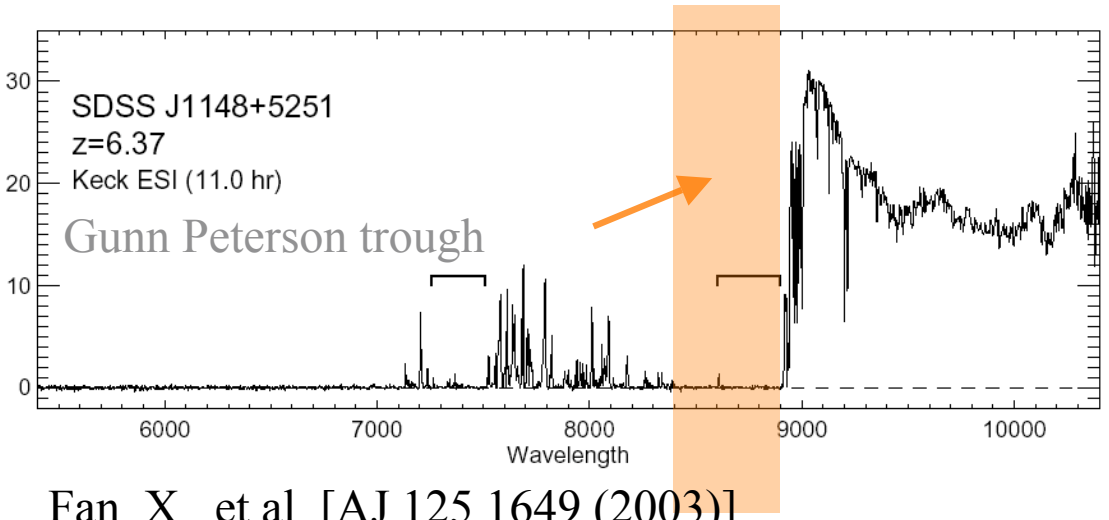

Fan, X., et al. [AJ 125,1649 (2003)]

Age ~ 870 Myr

One of the first luminous sources

M_{BH} ~ 1-5 x 10^9 $M_\odot$

M_{dust} ~ 10^8 $M_\odot$

SFR ~ 3000 $M_\odot$ per year

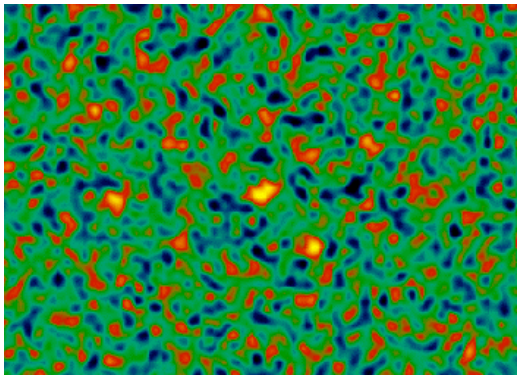

Bertoldi et al. [A&A 406, L55 (2003)]

Origin of the Dust in J1148?

- Standard mechanism - formation in cool winds from evolved stars - takes too long (J1148 is only 870 Myr from B-B);
- Maiolino et al. [Nature 431, 533 (2004)] and Strada et al. [astro-ph/0703349] show that reddening is suggestive of silicates and amorphous carbon grains, the dust that is formed in type-II supernovae;
- see Venkatesan et al. [ApJ 640, 31 (2006)] for details and caveats.

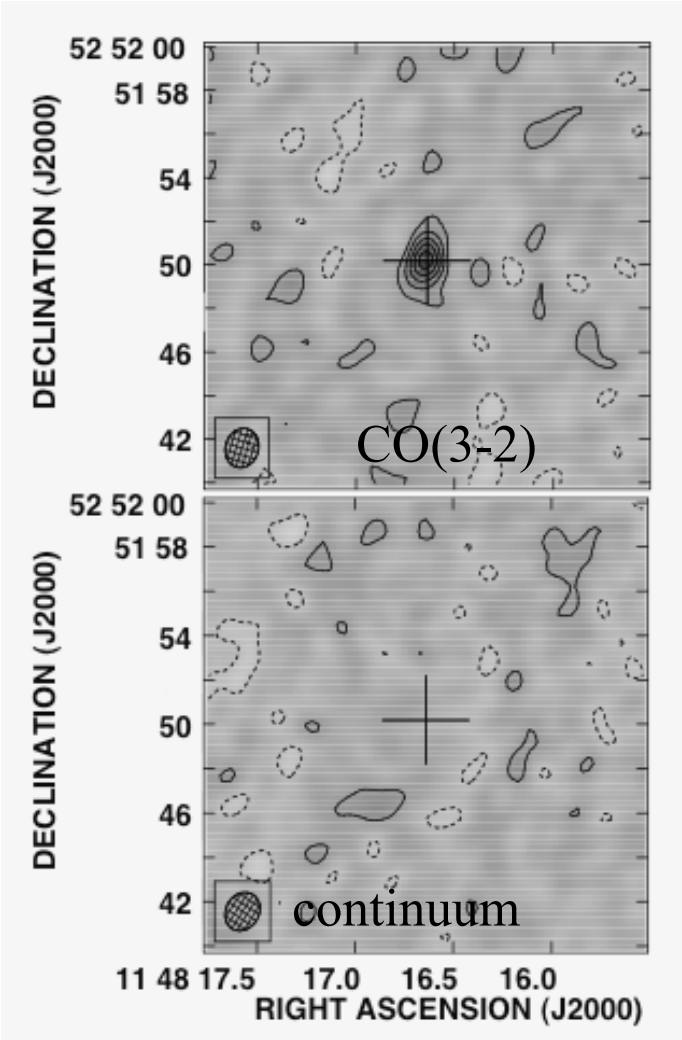

Molecular gas at end of EoR
CO Emission in J1148

Molecular gas mass:

$M_{H2} = 2 \times 10^{10}\ M_\odot$

Mass in C and O: ~ $3 \times 10^7\ M_\odot$

-> Pop III stars?

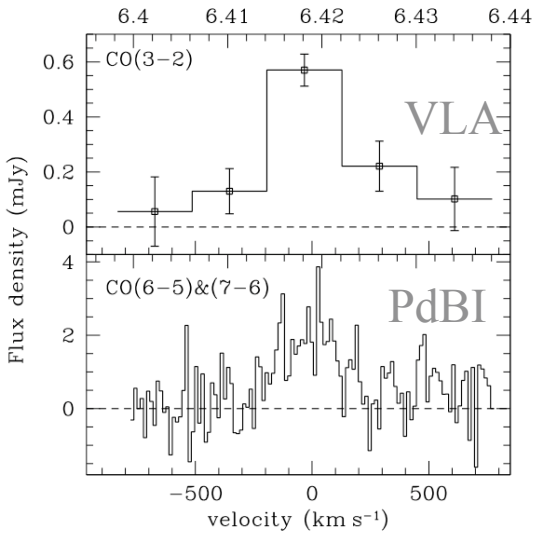

$z = 6.419$

$T_k = 60$ K,

$n = 10^{4.5}$ cm^{-3}

Walter et al. Nature 424, 406 (2003)
Bertoldi et al. A&A 409, L47 (2003)

A merger ?

CO(3-2) image from VLA (B-configuration), with a resolution of 0.17 x 0.13´´.

Two components resemble ULIRGs:

M_{gas} = 0.5 x 10^{10} for each component,

$M_{dyn}\sin^2 i$ = (0.7-2.0) x 10^{10} for "binary".

Not a lot of mass left for stars after the BH.

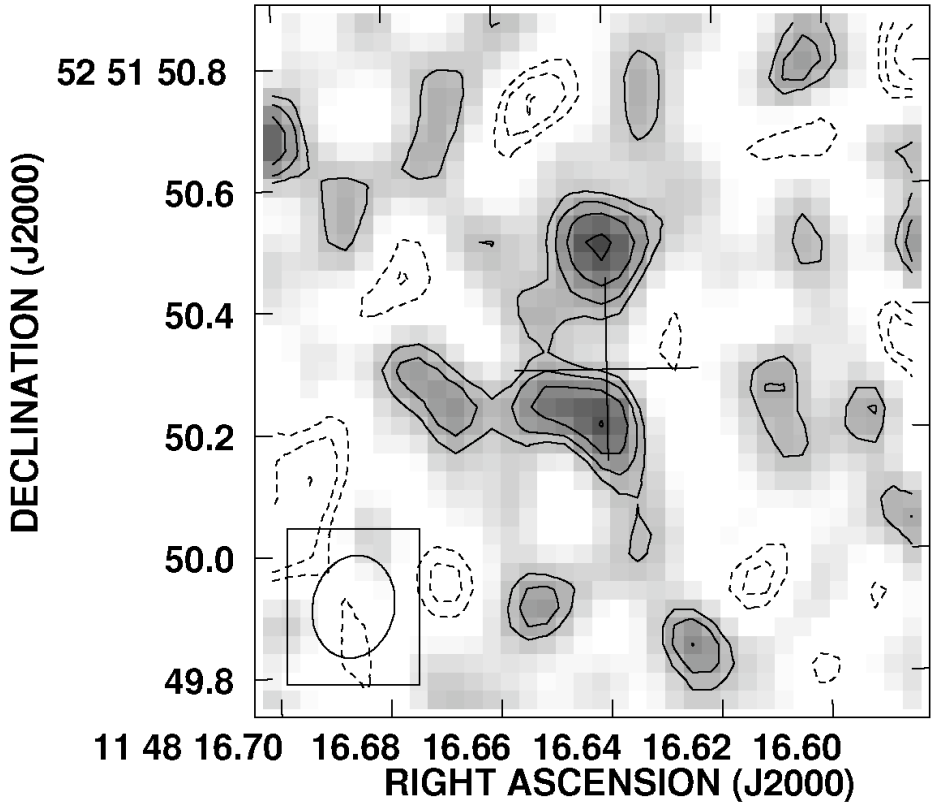

Walter et al. ApJ 615, L17 (2004).

Models of J1148-like Systems

- See Li et al. [astro-ph/0608190v2] and Robertson et al. [astro-ph/0703456v2];
- Bottom line - it is plausible to form a J1148 (z~6) through a series of mergers of gas-rich galaxies that begin in a rare peak in the cosmic density field (z~14).

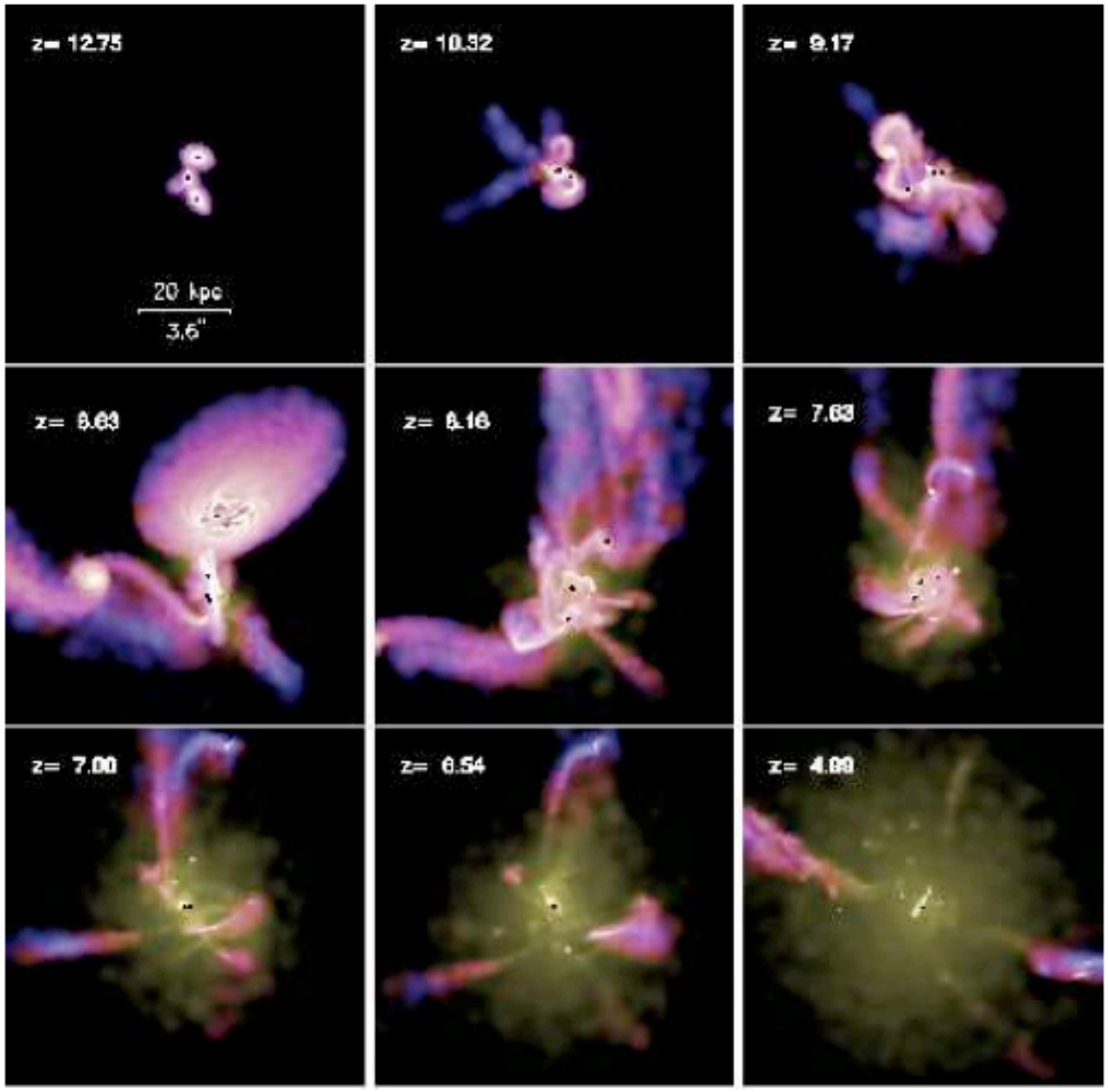

FIG. 5.— History of the quasar host shown in selected snapshots. The images give the projected gas density, color-coded by temperature (blue indicates cold gas, yellow indicates hot, tenuous gas). The black dots represent black holes. There are eight galaxies in total, engaging in seven major mergers along the timeline of the merger events as listed in Table 1. *Top panels* show interactions in the early stage from $z \sim 13$ to 9. *Middle panels* show the last major mergers between $z \sim 9$–7, and *bottom panels* show the final phase. All the galaxies coalesce at $z \approx 6.5$, creating an extremely luminous, optically visible quasar (see Figure 6). At this time, there are three black holes, but the luminosity is dominated by the most massive one, which is more than two orders of magnitude larger than the others. These black holes merge into a single one at later time. The scale bar indicates a size of 20 kpc (comoving), corresponding to an angular size of 3.6″ at redshift $z = 6.5$.

Figure 5 in Li et al.

Blue = cold gas

Yellow = hot, tenuous gas

Black dots = BHs

8 galaxies in 7 mergers

1 galaxy left at z ~ 6.5 but still 3 BHs, one dominant by factor of 100; BHs merge into one later

20 kpc (3.6″ @ z = 6.5) bar is co-moving

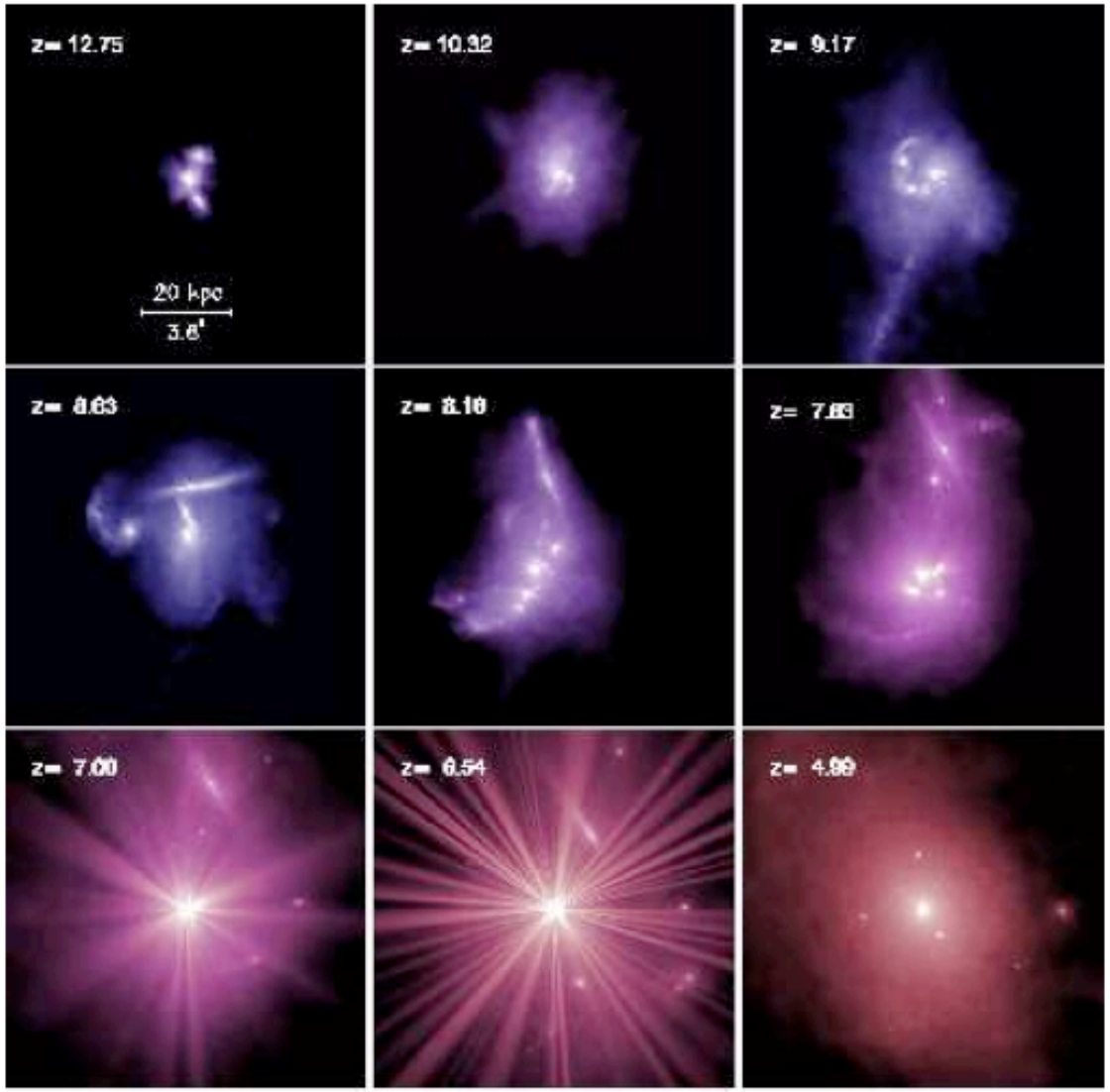

FIG. 6.— Same as Figure 5, but here the images show the projected stellar density, color-coded by the specific star formation rate (star formation rate per unit stellar mass). Blue indicates massive star formation in the galaxies, while red indicates little star formation. To illustrate the quasar activity, we have generated "rays" around the quasar. The number and strength of the rays are proportional to the bolometric luminosity of the black holes. These rays are artificial and serve only as a visual guide. The systems in *top panels* are blue, small and perturbed. The quasars appear very faint and buried. In the *middle panels*, strong interactions between galaxies boost star formation and black hole accretion, creating highly irregular morphologies and extremely blue galaxies. The quasars are heavily obscured by dense gas. At a later stage (*bottom panels*), feedback from the black holes quenches star formation, allowing the galaxy color to redden. The quasar becomes optically visible as strong outflows blow out the gas. It has a maximum luminosity around $z \approx 6.5$ when all the galaxies coalesce. After that, both the quasar activity and star formation gradually die down, leaving behind an aging stellar spheroid.

Figure 6 in Li et al. (2007), same as Figure 5 but:

Blue = intense *formation

Red = little * formation

Rays indicate AGN activity: # & length ∝ L(bol) of BH

Max luminosity at z~6.5 when all components merge into one galaxy

Recent Continuum Detections of z>5 SDSS QSOs

Wang, et al. observed 13 SDSS quasars (z>5) [arXiv:0704.2053] :

8 at the VLA (1.4 GHz) were detected,

and 4 of 11 with MAMBO/30m (1.3mm) were detected.

SFR ~ 1000 $M_{\odot}$ per year.

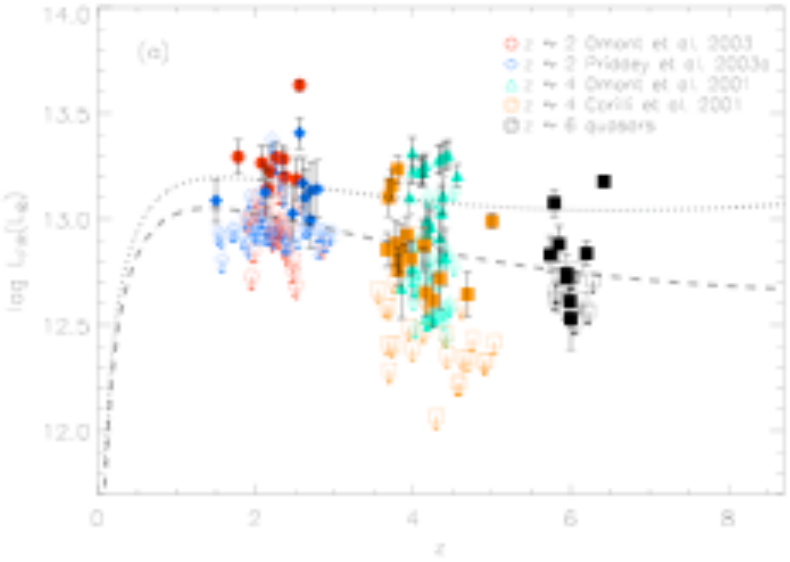

Fig. 1 The logarithm of the FIR luminosity versus redshift for different QSO samples observed at (sub)mm wavelengths (Wang et al. 2007). The open symbols with arrows denote upper limits. The dashed and dotted lines represent the typical 3σ detection limits of MAMBO at 250 GHz and SCUBA at 350GHz, namely $S_{250} = 2.4$mJy, and $S_{350} = 8.5$ mJy, respectively.

Three 350μm Detections of z > 5 QSOs [Wang et al. preprint]

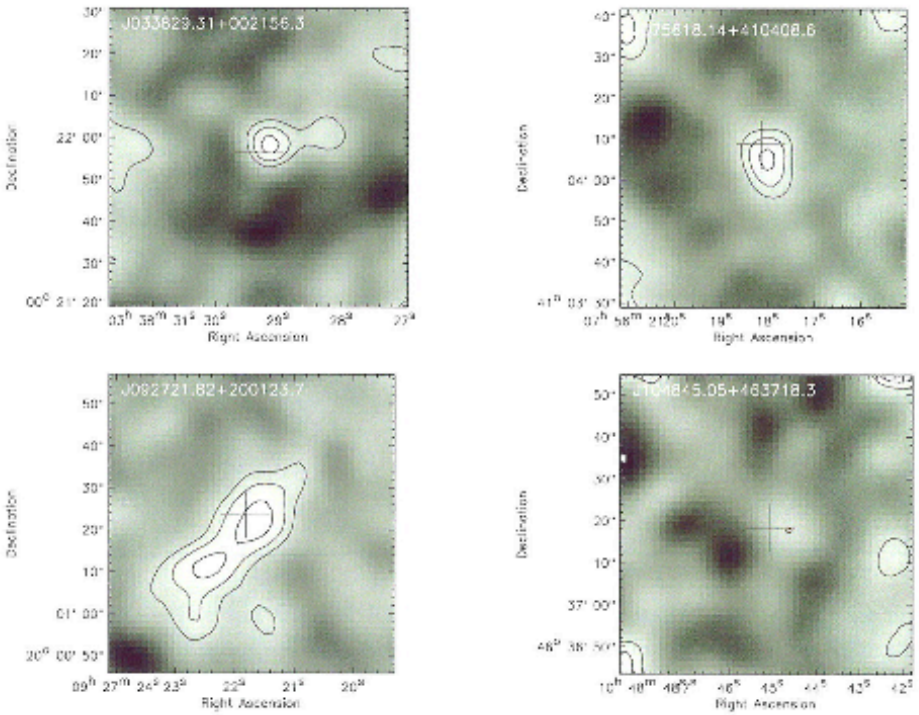

Fig. 1.— The SHARC-II maps of the four z≥5 quasars at 350 μm, smoothing to a beam size of FWHM = 12.4″. The contour levels are (2, 3, 4) × 4.0 mJy beam^{-1} for each of the four maps. The crosses mark the positions of the optical quasars.

L(FIR) ~ 10^{13} $L_\odot$

M(dust) ~ 10^8 $M_\odot$

T(dust) ~ 45 K

SFR ~ 2000-3000 $M_\odot$ per year.

~ 1/3 optically selected QSOs are HLIRGs.

J033829 has been detected in CO.

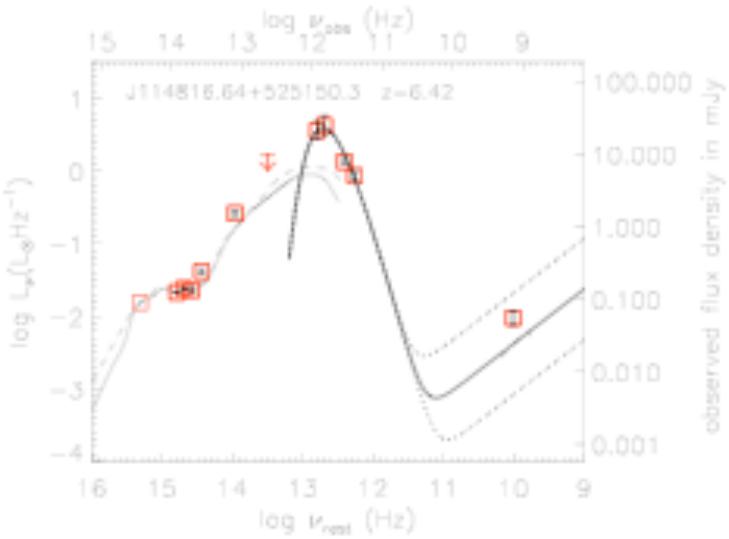

Fig. 3 The SED of J1148+5251 from the rest frame near-IR to the radio (Jiang et al. 2007; Wang et al. 2007; Beelen et al. 2006). The models at rest frame frequencies, $\nu > 10^{13}$ Hz are two standard QSO SEDs including emission from hot ($\sim$ 1000K) dust. The rest-frame far-IR through radio model entails a 55K modified black body, plus synchrotron radio emission that follows the radio-FIR correlation for star forming galaxies (Beelen et al. 2006; Wang et al. 2007). The dashed lines indicate the range defined by star forming galaxies (Yun et al. 2000).

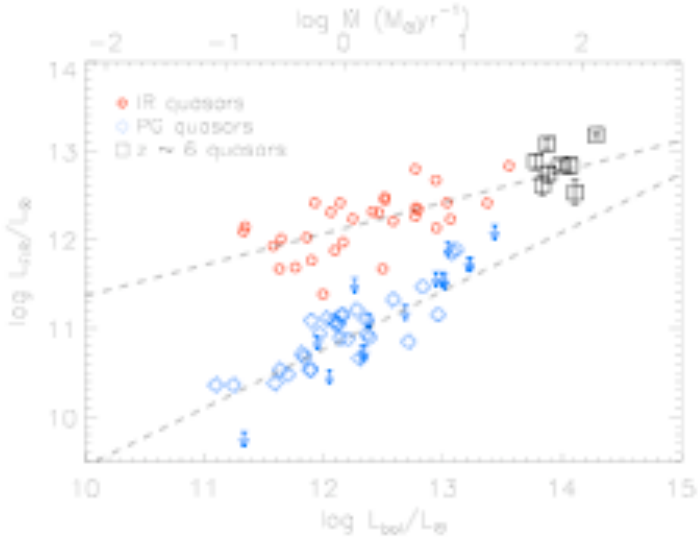

Fig. 4 Correlation of L_{FIR}–L_{bol} for QSO host galaxies. The (sub)mm detected z$\sim$6 quasars are plotted as black squares with error bars denoting 1σ r.m.s.. The local IR and PG quasars from Hao et al. (2005) are plotted as red circles and blue diamonds with arrows denoting upper limits in L_{FIR}. The dashed lines represent the linear regression results for the two local quasar samples.

SED of J1148 and other z>5 submm-detected QSO host galaxies is consistent with L(FIR)/L(bol) for IR luminous quasars, which reside in mergers with co-eval starbursts [Carilli, et al. astro-ph/0703799; and Hao et al. ApJ 625, 78 (2005)].

Recent CO Detections of $z > 5$ SDSS QSOs

- Maiolino et al. [arXiv:0707.3335] reports detecting CO(5-4) at $z = 5.0267$ in SDSS J033829.31+ 002156.3;
- Carilli et al. [arXiv:0707.2339] report detections of CO(5-4) and (6-5) at $z = 5.7722$ in SDSS J0927+2001;
- Detections like these are limited to HLIRGs with present facilities.

SDSS J0338, z = 5.03

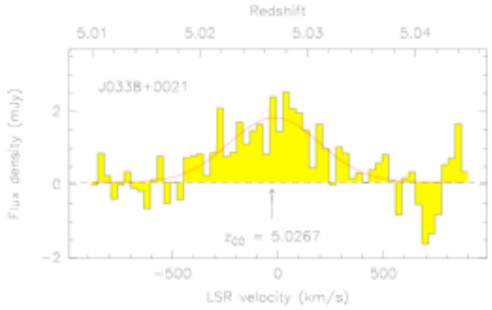

Fig. 1. CO(5–4) spectrum of SDSSJ0338+0021 (sum of A and D conf.) rebinned to 10 MHz (31.4 km s^{-1}). The red line shows a single gaussian fit to the line. Velocities are relative to the MgII redshift.

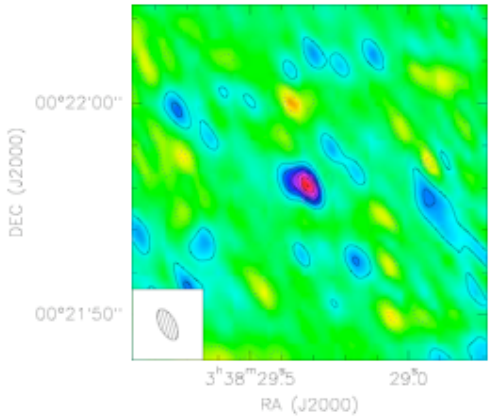

Fig. 2. CO(5–4) cleaned map of SDSSJ0338+0021 (from both configurations A and D) obtained by integrating in velocity from −300 to +230 km s^{-1} with contours in steps of and starting at 1σ = 0.14 Jy $beam^{-1}$ km s^{-1} .

SDSS J0927, z = 5.77

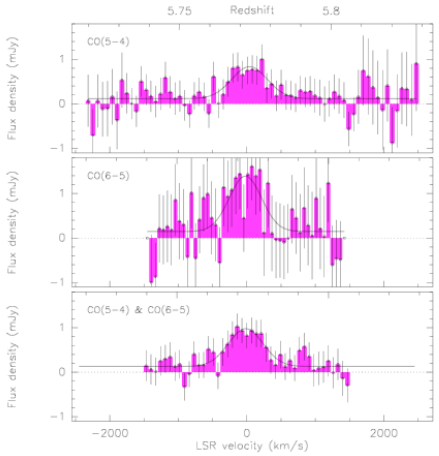

Fig. 1.— The spectra of the CO 5-4 (upper), 6-5 (middle) and the sum of the 5-4 and 6-5 (lower) emission from SDSS J0927+2001 at $z = 5.77$. Also shown are Gaussian fits to the lines with parameters as given in Table 1. All spectra are smoothed to 70 km s^{-1} $channel^{-1}$, and each independent channel is displayed. The rms per channel varies across the band, although typical values in the combined 5-4 and 6-5 spectrum are 0.3 mJy $beam^{-1}$.

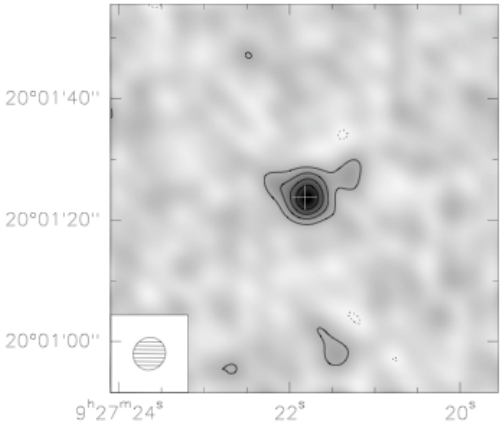

Fig. 2.— An image of the sum of the velocity integrated CO 5-4 and CO 6-5 line emission from J0927+2001 at $z = 5.77$. Contour levels are: 0.14 Jy km s^{-1} $beam^{-1}$. The rms on the image is 0.07 Jy km s^{-1} $beam^{-1}$. The cross indicates the position of the optical QSO.

Growth of SMBHs in EMG Quasars

- For SDSS J1148, z = 6.42, the CO data yield a gas mass comparable to the dynamical mass estimate of $\sim 5 \times 10^{10}\ M_{\odot}$, which is $<< M_{Bulge} \sim 10^{12}\ M_{\odot}$ implied by the SMBH - σ(bulge) relation [Gebhardt et al. ApJ 539, L13 (2000)], were it to apply at high redshifts [Walter et al. ApJ 615, L17 (2004)];

- SMBH appears to have formed prior to the spheroidal galaxy;

- 8 EMG quasars, in addition to J1148, all with massive starbursts, show the same behavior (open circles in plot at right) [Shields et al. ApJ 641, 683 (2006)].

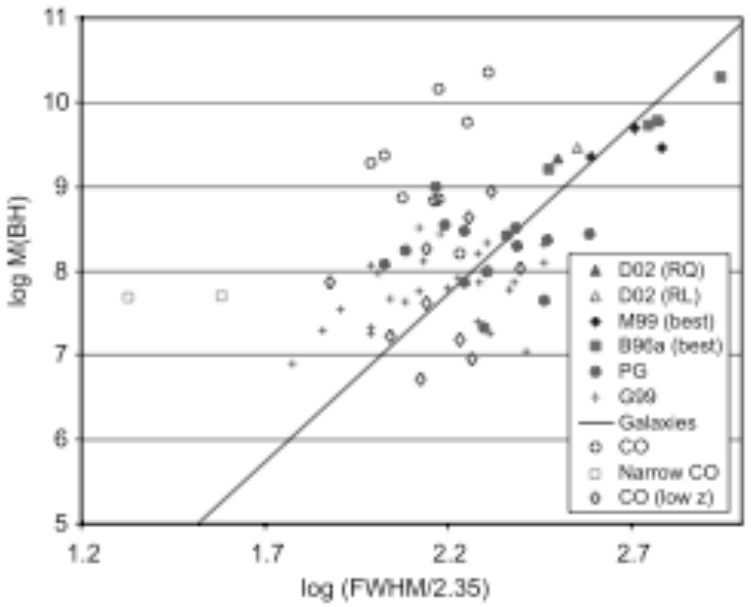

FIG. 3.—Plot of the M_{BH}-σ_* relationship using $\sigma_{[O\,III]}$ and σ_{CO} as surrogates for σ_*. Open circles are the nine CO QSOs from this paper; open squares and diamonds are the low-redshift CO QSOs. Other points are from Fig. 2 of S03, based on $M_{BH}(H\beta)$ and $\sigma_{[O\,III]}$ (see S03 for legend and references). The solid line is eq. (1). [*See the electronic edition of the Journal for a color version of this figure.*]

See also, Kurk et al. [arXiv:0707.1662] for an analysis of five SDSS z ~ 6 quasars, and Ho et al. [arXiv:0707.3436] for a discussion of the CO Tully-Fisher Relation.

Detecting Molecular Gas at Redshifts z > 6

- *Gunn-Peterson sets in at z>6 ⇒ observing the first luminous objects in the Universe is limited to radio through near-IR;*

- ALMA only observes CO with J > 8, which may not be excited, but the EVLA *can* observe the lower J lines.

- CII at 1900 GHz is observable and strong: 1% of entire galaxy luminosity in low-metallicity galaxies, 0.5% in high-z starburst galaxies (but only 0.05% in ULIRGs): in J1148 at z=6.4, CII is 12 mJy vs. CO(3-2) of 2 mJy.

- With only 10 antennas (early science), ALMA can detect CII in an QSO EMG at z = 6.6.

COSMOS and EMGs

- COSMOS is a deep multi-wavelength survey,

principally HST imaging, of 2 sq deg on the equator;

- None of the 108 Ly-a emitters found were detected at 1.4 GHz to a limit of 30 μJy (3σ) individually, or 2.5 μJy (2σ) in a stacked average;
- None of the 10 Ly-a emitters for which MAMBO data exist were detected to a limit of 2 mJy (2σ).

See ApJS, volume 172 (2007) for articles on early results.

Submillimeter Galaxies

- For a review, see Blain et al. [Physics Reports 369, 111 (2002)];
- Installing the Submm Common-User Bolometer Array (SCUBA) on the JCMT in 1997 provided 450 & 850 μm detectors, 91 and 37 respectively, in a 2.5′ FOV;
- SMMs were rapidly detected, and > 200 are now known, all at high-z;
- However, relatively few have been studied in detail, the lack of angular resolution (14.7′′ @ 850) impeding identification and gathering of spectroscopic redshifts.

- MAMBO (1.25mm) is a complementary facility on the IRAM 30-Meter (10.7′′ resolution x 37 bolometers in a 7′ FOV with limiting sensitivity ~ 1mJy;
- SHARC2 (350 μm) and BOLOCAM (144 elements @ 1.1, 1.4, & 2.1 mm) on the CSO give ~ 30′′ resolution in a ~ 7.5′ FOV @ 1mm, ~ 10′′ @ 350 μm with a ~ 2.5′ FOV;
- Future instruments include: SCUBA2, LABOCA on APEX, and ALMA.

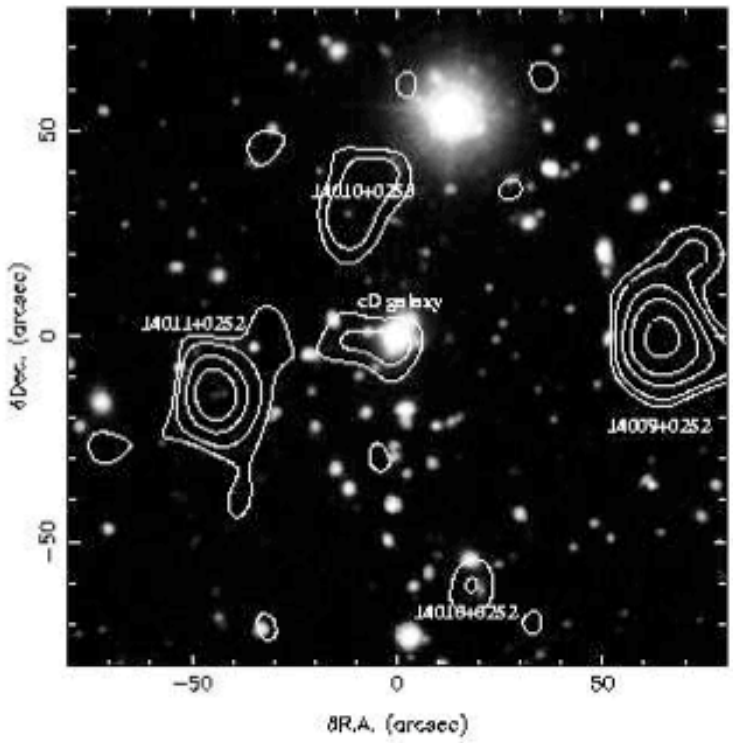

Fig. 1. A comparison of deep optical and submm views of the sky. The background image is a 3-color optical image of the rich cluster of galaxies Abell 1835 at the low/moderate redshift $z = 0.25$ (Smail et al., 1998b) taken using the 5-m Hale telescope, overlaid with the 14-arcsec resolution contours of a SCUBA 850-μm submm-wave image of the same field (Ivison et al., 2000a). North is up and East to the left. The brightest SCUBA galaxies at $(-45,-15)$, (65,0) and (20,−60), and the central cD galaxy (Edge et al., 1999), all have clear radio detections at a frequency of 1.4 GHz in images with higher spatial resolution than the SCUBA contours, obtained at the Very Large Array (VLA), supporting their reality. The bright SCUBA galaxy at $(-45, -15)$ is associated with SMM J14011+0253, an interacting pair of galaxies at redshift $z = 2.56$ in the background of the cluster (Frayer et al., 1999). Spectacular fragmented structure appears in the Easterly red component of this galaxy in *Hubble Space Telescope (HST)* images (Fig. 18).

Optical vs. Submm Sky

Submm resolution makes source identification an issue.

Observed Rest Frame SEDs

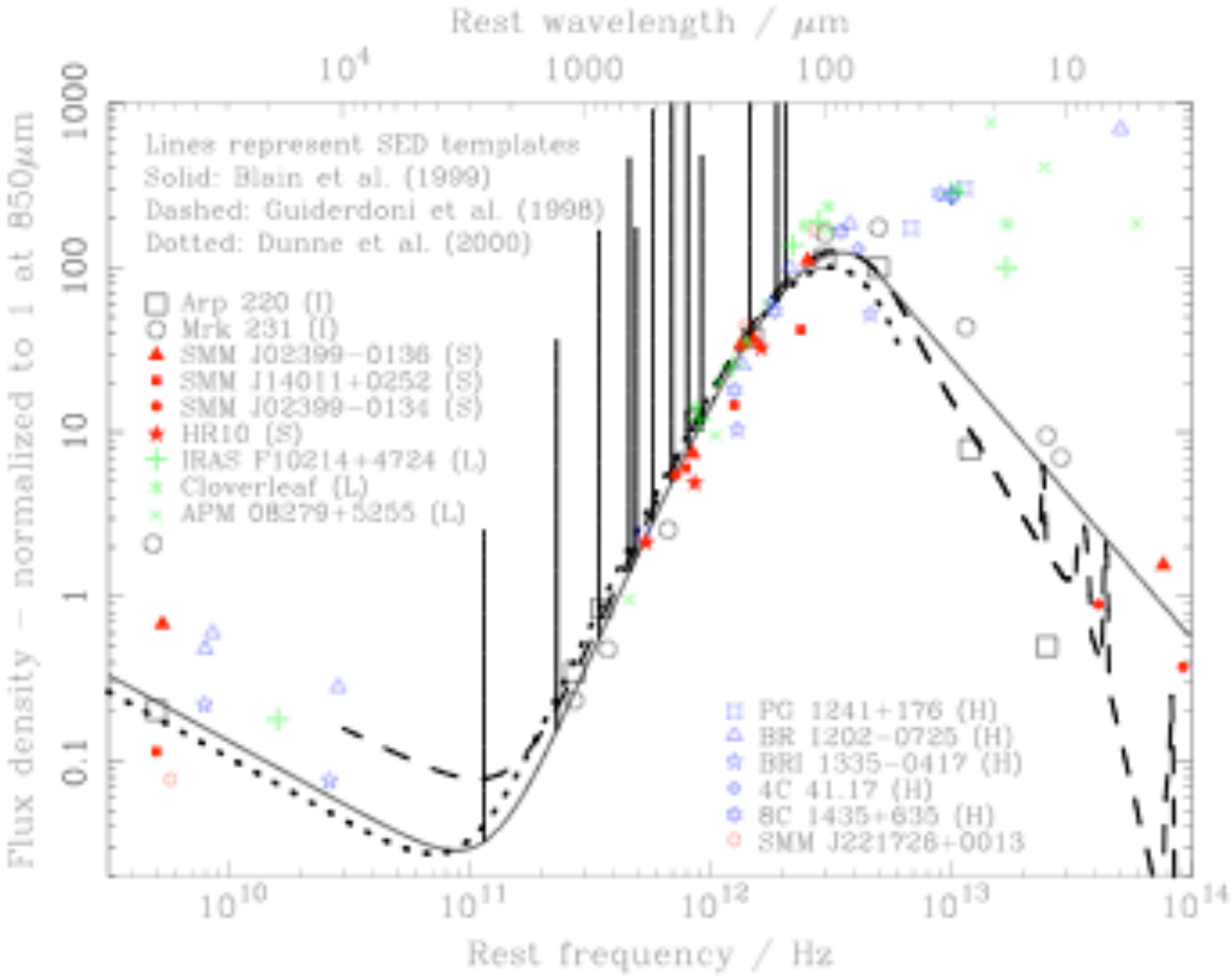

Effect of K-Correction and T-z Dependence on Flux Density

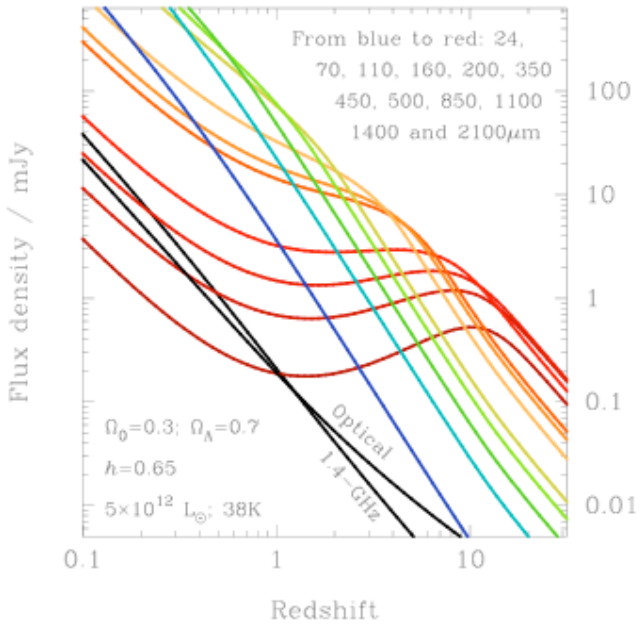

Fig. 4. The predicted flux density of a dusty galaxy as a function of redshift in various submm atmospheric windows, and at shorter wavelengths that will be probed by forthcoming space missions. Note the powerful K correction in the mm and submm wavebands at wavelengths longer than about 250 μm, which yields a flux density that is almost independent of redshift. The template spectrum is chosen to reproduce the typical properties of distant submm-selected galaxies (Fig. 2). Subtle effects due to the additional heating of dust by the CMB, and fine details of the radio SED of galaxies are not included; these effects are illustrated in Fig. 8.

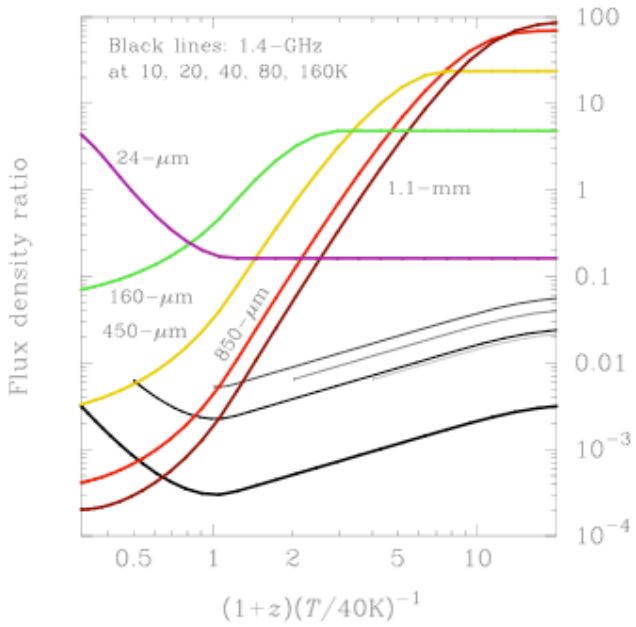

Fig. 6. The ratio of flux densities expected in different observing bands as a function of the degenerate redshift/dust temperature parameter, compared with the flux density expected in the 70-μm band at which the *SIRTF* satellite will be very sensitive. Where the lines have steep gradients, measured colors from multi-band data locate the peak of the dust SED accurately in the observer's frame, providing a measurement of temperature–redshift. The degeneracy between T_d and z can be lifted slightly by including radio data (Blain, 1999a; Yun and Carilli, 2002), if the dust temperature is greater than about 60 K (see also Fig. 7). If deep near-IR and optical images can be included, and the optical counterpart to the galaxy can be readily identified, then conventional photometric redshifts can be determined from stellar synthesis models. However, care must be taken as it is unclear whether the SEDs of very dusty galaxies have familiar restframe-optical spectral breaks.

Carilli - Yun Redshift Indicator
[Carilli & Yun ApJ 513, L13 (1999)]

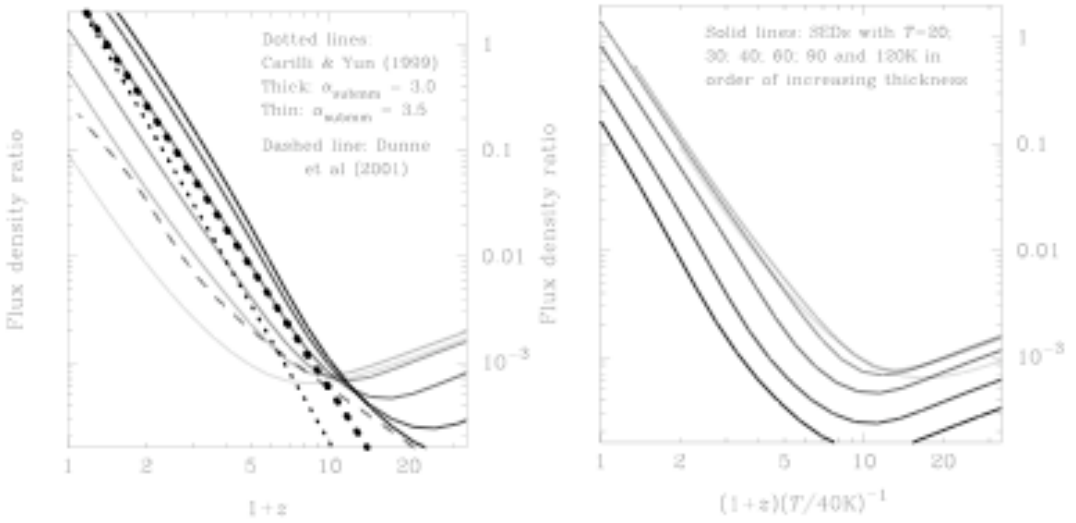

Fig. 7. The behavior of the Carilli–Yun 1.4-GHz to 850-μm radio–submm redshift indicator. The left panel shows the ratios of 1.4-GHz:850-μm flux density predicted from empirical SEDs by Carilli and Yun (1999; dotted lines) and Dunne et al. (2000; dashed line; see also Carilli and Yun, 2000). Predictions for the ratio based on the results of Blain (1999a) are also shown assuming radio–far-IR SEDs with various dust temperatures, but which all lie on the far-IR–radio correlation (Yun et al., 2001; solid lines). The flux ratio is a good indicator of redshift, clearly separating high- and low-redshift galaxies. Both synchrotron and free–free radio emission are included, and the dust temperature and radio properties evolve with redshift self-consistently, as modified by the CMB. In the right panel, the solid curves are replotted as a combined function of temperature and redshift, emphasizing that for $T_{\rm d} < 60\,{\rm K}$, the inferred temperature and redshift are degenerate, just as for a thermal spectrum (Fig. 6). For $T_{\rm d} > 60\,{\rm K}$ the flux ratio becomes a non-degenerate redshift indicator.

Ratio of 1.4 GHz to 850 μm flux can separate low and high-z sources.

Expected Signals from Typical SMM

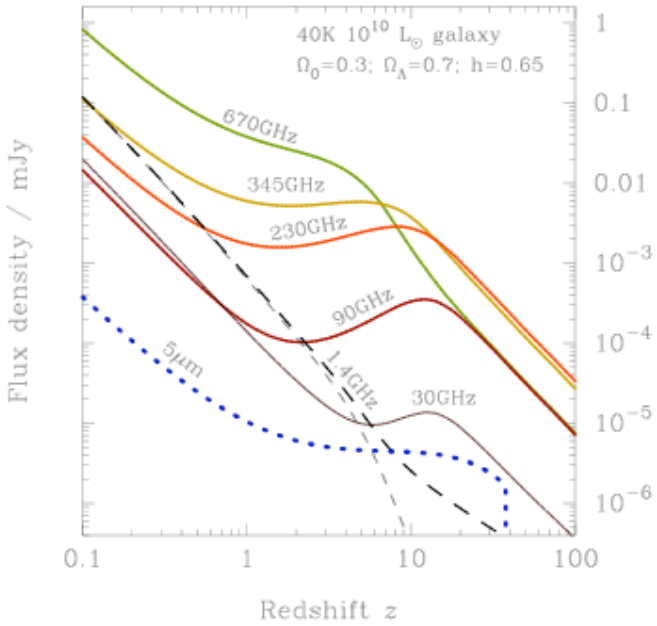

Fig. 8. Some key features of flux density–redshift relations expected at a range of wavelengths, extending to very high redshifts. CMB heating of dust at $z > 10$ prevents the mm-wave K correction from assisting the detection of very high redshift galaxies: the flux density–redshift relation has the same redshift dependence beyond $z \simeq 15$ at 230, 90 and 30 GHz. CMB cooling of relativistic electrons suppresses synchrotron radio emission beyond $z \sim 5$, as shown by the thin dashed line. Realistic free–free emission is also included in the model represented by the thick dashed line (Condon, 1992; Yun et al., 2001), significantly increasing the radio emission expected from very high redshifts. An estimate of the flux density from a 3×10^4-K stellar photosphere at 5 μm is also shown, cutoff at the redshift beyond which Lyman-α absorption is redshifted through the band. Note that there is probably a maximum redshift above which dust does not exist, and so beyond which thermal emission from dust can never be detected; this effect is not included here.

At 230 GHz, the expected flux density is virtually constant at ~ 2 mJy for z = 0.2 - 20.

ALMA should detect one SMM galaxy every hour in a random field - confusion problem?

Source Counts

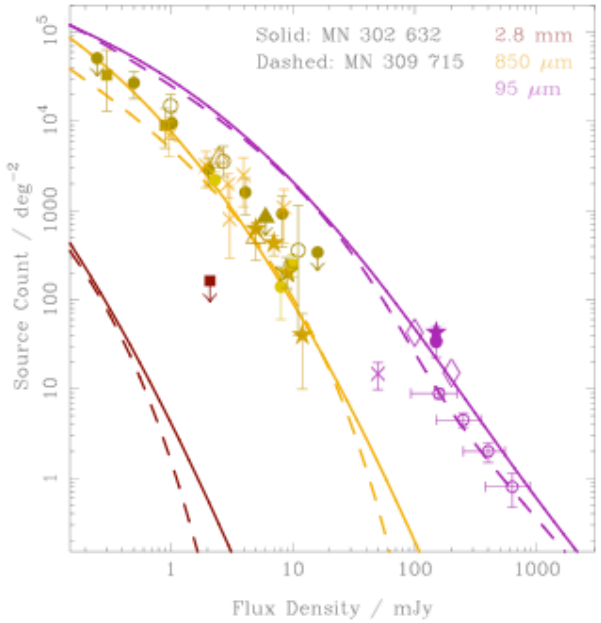

Fig. 9. A summary of count data from several mm, submm and far-IR surveys. The overplotted curves are derived in models that provide good fits to the compilation of data, and are updated from the results in the listed MNRAS papers (Blain et al., 1999b, c). Identical symbols represent post-1999 data from the same source. The errors are shown as 1σ values unless stated. The 2.8 mm data (square) is from Wilner and Wright (1997). At 850 μm, in order of increasing flux (less than 15 mJy), data is from Blain et al. (1999a), Cowie et al. (2002) with 90% confidence limits; Hughes et al. (1998), Chapman et al. (2001b), Barger et al. (1999a, 1998), Smail et al. (1997), Eales et al. (1999, 2000) consistent with the increased area reported by Webb et al. (2002a), Borys et al. (2001), Barger et al. (2000) and Scott et al. (2002). The data points between about 2 and 10 mJy are consistent with a steep integral source count $N(>S) \propto S^{\alpha}$, with a power-law index $\alpha \simeq -1.6$. The counts at brighter flux densities are likely to steepen considerably; note that the counts must turn over at fainter flux densities to have $\alpha < -1$ to avoid the background radiation intensity diverging. At 95 μm, the data is from Juvela et al. (2001), Kawara et al. (1998), Matsuhara et al. (2000), Serjeant et al. (2001) and Linden-Vornle et al. (2000).

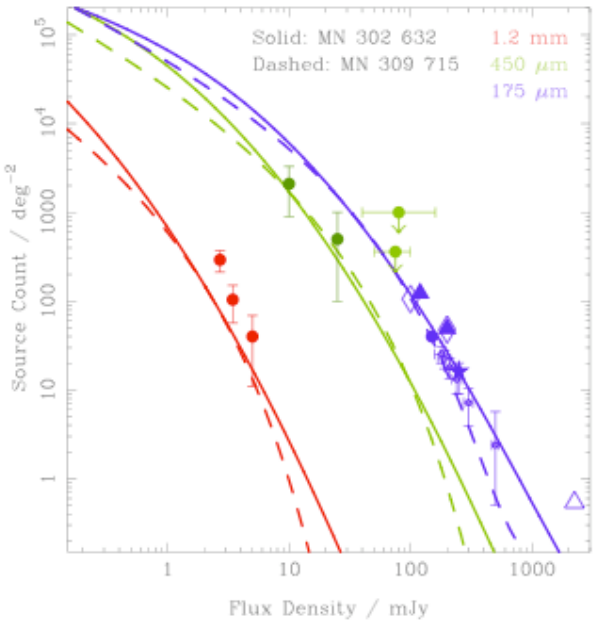

Fig. 10. Counterpart to Fig. 9 for three other observing bands. The data at 1.2 mm (circles at flux densities less than 10 mJy) are from Bertoldi et al. (2001), Carilli et al. (2000) and Carilli (2001). The data at 450 μm (circles at 10–50 mJy) are from Smail et al. (2002), with limits from Smail et al. (1997) and Barger et al. (1998). The data at 175 μm (100 mJy) are from Kawara et al. (1998), Puget et al. (1999), Matsuhara et al. (2001), Juvela et al. (2001), Dole et al. (2001) and Stickel et al. (1998).

History of SF in Universe

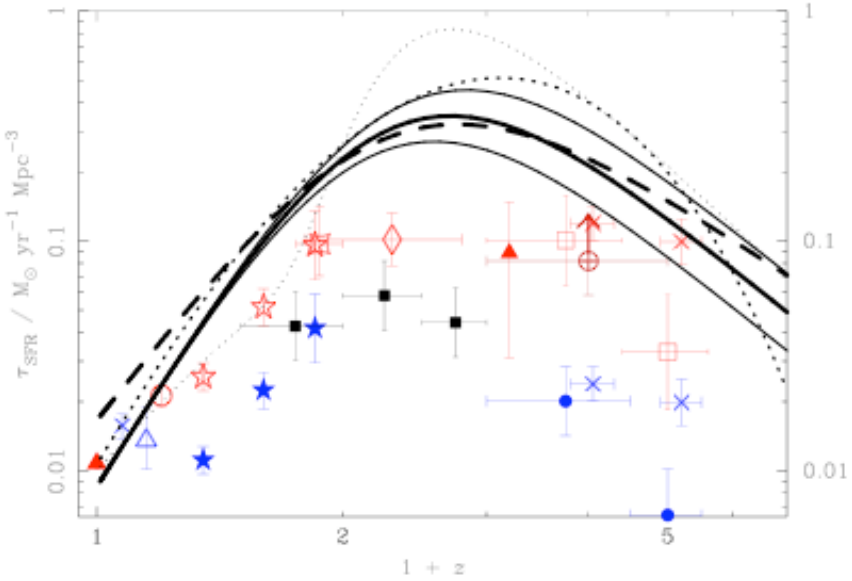

Fig. 21. The history of energy generation in the Universe, parameterized as a star-formation rate per unit comoving volume. The absolute normalization of the curves depends on the assumed stellar IMF and the fraction of the dust-enshrouded luminosity of galaxies that is generated by AGN. The points show results derived from a large number of optical and near-IR studies, for which detailed references can be found in Blain et al. (1999b) and Smail et al. (2002). The most important results are from Lilly et al. (1996; filled stars) and Steidel et al. (1999; high-redshift diagonal crosses). The up-pointing arrow comes from the submm-based estimate of Hughes et al. (1998). An important new measurement of the extinction-free low-redshift star-formation rate from radio data, that is not plotted, has been obtained by Yun et al. (2001): $0.015 \pm 0.005\,M_\odot\,yr^{-1}$. The thick solid and dashed lines represent the current best fits to far-IR and submm data in a simple luminosity evolution model and a hierarchical model of luminous merging galaxies respectively, as updated to reflect additional data and a currently favored non-zero-Λ cosmology. The thinner solid lines show the approximate envelope of 68% uncertainty in the results of the luminosity evolution model. The thin and thick dotted lines represent the best-fitting results obtained in the original derivations (Blain et al., 1999b, c).

- Submm points (red) generally lie above the optical points (blue);
- Black lines are best-fit models to submm data.

Detection of SMM J14011 in CO

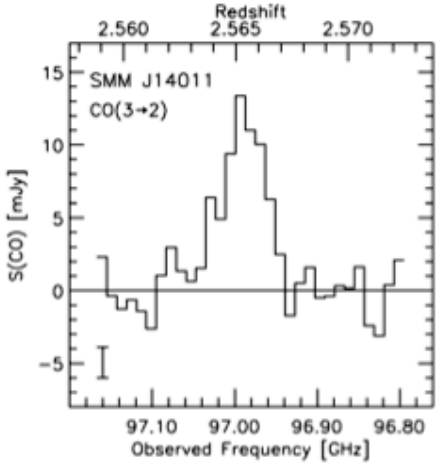

FIG. 1.—CO (3 → 2) spectrum for SMM J14011 observed with the Owens Valley Millimeter Array. The data have been smoothed to 24 MHz (74 km s^{-1}), and the channel separation is 12 MHz. The 1 σ rms error of each channel is shown in the lower left-hand corner.

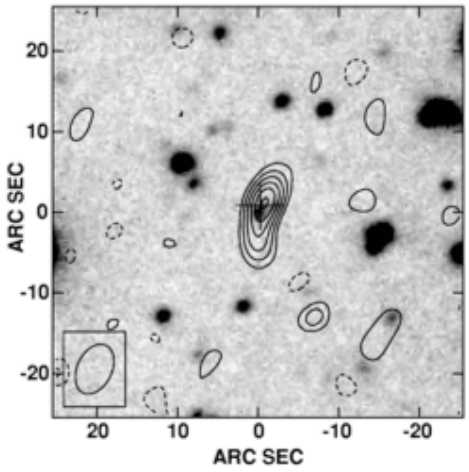

FIG. 2.—Integrated CO (3 → 2) map averaged over 104 MHz (322 km s^{-1}) overlaid on an optical *I*-band image taken at the Palomar 5 m (Smail et al. 1998a). The positional offsets are relative to the optical position, and the cross marks the position of the SCUBA source (Ivison et al. 1999). The 1 σ rms error is 0.32 Jy km s^{-1} beam^{-1}, and the contour levels are 1 σ × (−3, −2, 2, 3, 4, 5, 6, 7). The synthesized beam size for the observations is shown in the lower left-hand corner (6.″5 × 4.″3, PA = −26°).

CO(3-2) was first detected by Frayer et al. [ApJ 514, L13 (1999)] using OVRO. Note the N/S elongation of the CO emission.

J14011 - A Massive Disk?
Ivison et al. ApJ 561, L45 (2001)

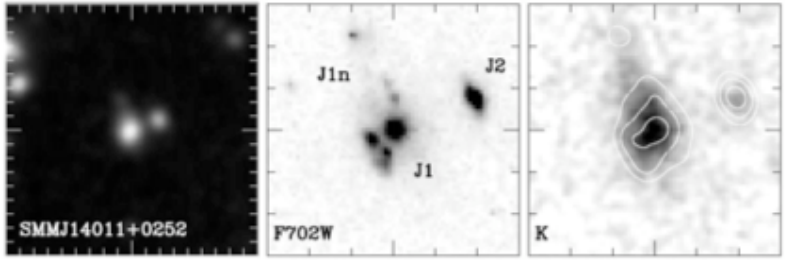

FIG. 1.—Three views of SMM J14011+0252: a true-color $UR_{702}K$ image (using U-band data from I00), the *HST* F702W frame, and the UKIRT K-band image. The true-color frame is 18″ × 18″, while the F702W/K-band views are zoomed to give a 6″ × 6″ field to better illustrate the internal structure of this galaxy. We identify the two UV-bright components of SMM J14011+0252 on the F702W panel: the morphologically complex J1 and the compact, blue component J2, as well as the diffuse, very red component, J1n. We overlay a contour plot of the seeing-matched F702W image on the K-band panel to contrast the optical/IR morphologies (the contours are in 1 mag increments starting at $\mu_K = 24.0$ mag arcsec^{-2}). North is up, and east is to the left; minor tick marks denote 1″ increments. [*See the electronic edition of the Journal for a color version of this figure.*]

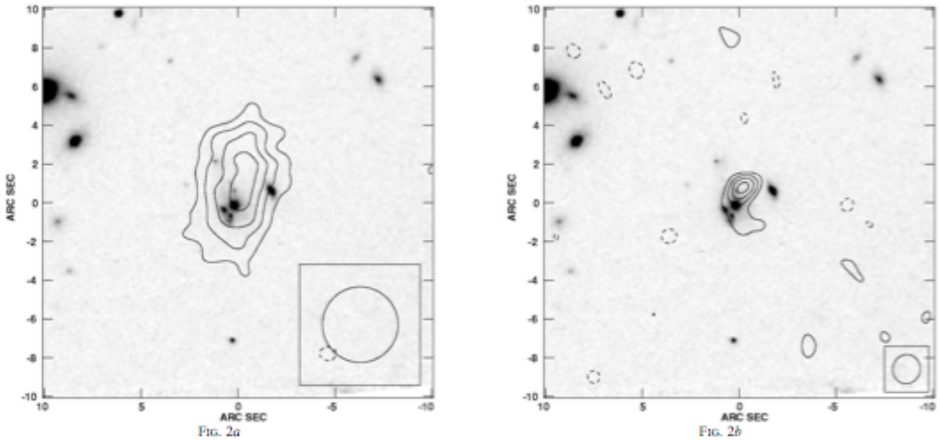

FIG. 2a FIG. 2b

FIG. 2.—(*a*) Combined OVRO/BIMA CO image of SMM J14011+0252, with a noise level of 0.8 mJy beam^{-1}. (*b*) VLA 1.4 GHz map, with a noise level of 12 μJy beam^{-1}. The CO and radio emission are cospatial, peaking ~1″ north of J1. The CO subtends 6″.6 ± 1″.4 in the north-south direction, the radio somewhat less. All contours are plotted at −3.5, −2.5, 2.5, 3.5, 4.5, and 5.5 × σ; positions are relative to the position of J1, shown as a gray scale; synthesized beams are shown.

CO(3-2) 1.4 GHz

- Combining HST, VLA, and CO data from OVRO and BIMA, the CO emission was identified with J1n;
- It was argued that the CO emission was extended on scales > 10 kpc, much larger than is seen in ULIRGs, assuming a lens magnification of 3-5;
- The host galaxy for the starburst was classified as an ERO.

J14011 is a strongly lensed ULIRG-like galaxy [Downes & Solomon, ApJ 582, 37 (2003)]

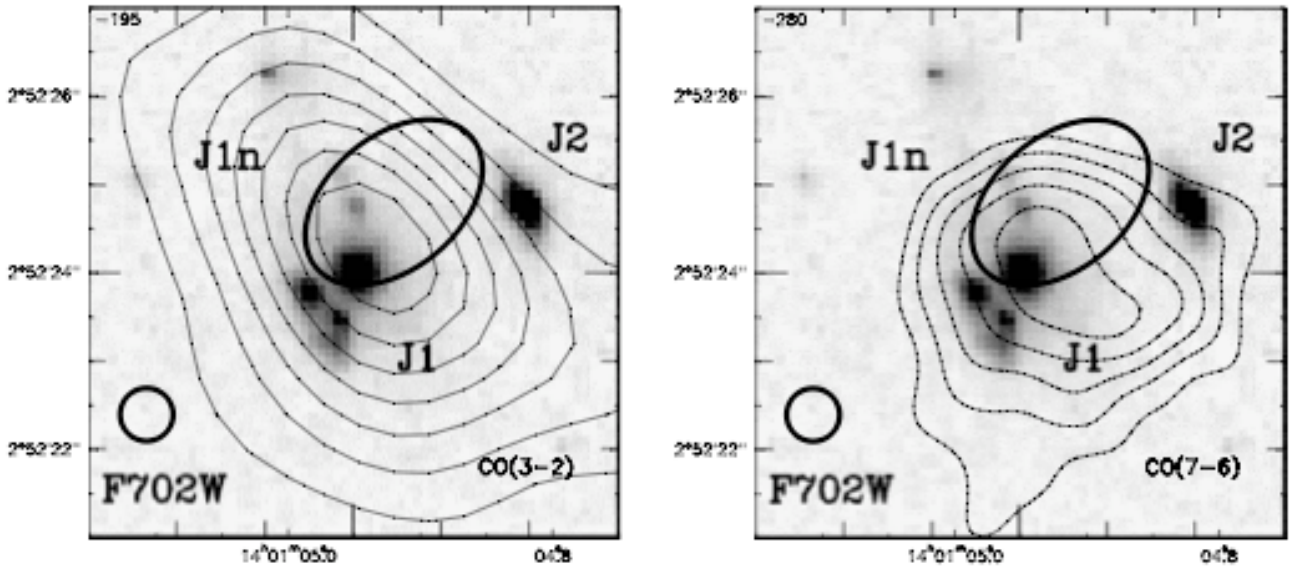

FIG. 4.—CO contours superposed on the *HST* F702W image from Ivison et al. (2001) and compared with VLA half-width at 1.4 GHz. *Left:* CO (3–2) map, with same contours as in Fig. 2, beam 3.″3 × 2.″3 at P.A. 50°. *Right:* CO (7–6) map, with same contours as in Fig. 3a, beam 2.″2 × 2.″0 at P.A. 48°. In each diagram, the dark ellipse shows the 2.″3 × 1.″5 half-power widths of the 1.4 GHz nonthermal VLA source, as derived by Ivison et al. (2001). The 1 σ error quoted by those authors for the optical position is ±0.″3 (small circle above the F702W label).

Their model has a lens magnification of 25 ± 5 and CO emission extended over only 2″ instead of 6.6″, which implies a source diameter of only 700 pc.

Adding SPIFFI Data to the Mix

Nesvadba, et al. [ApJ 657, 725 (2007)]

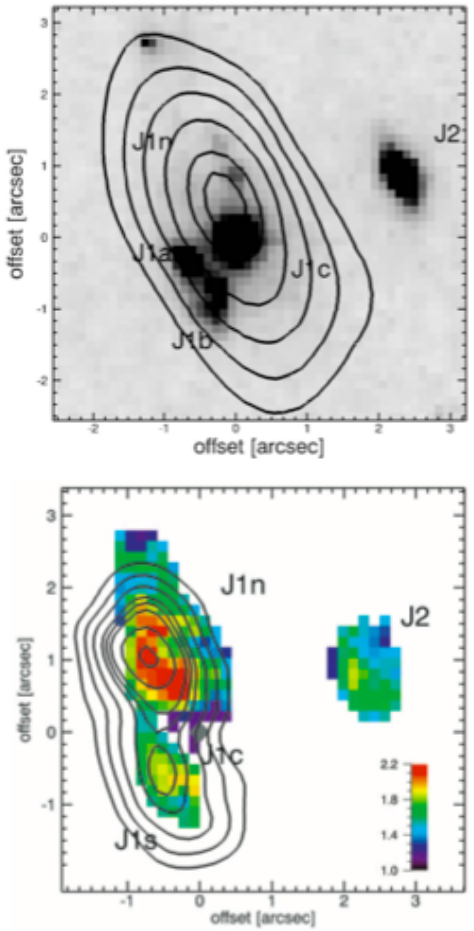

FIG. 3.—$J - K$ color distribution of SMM J14011+0252 as in Fig. 2, but with the model of J1c removed. Contours indicate Hα line emission in steps of 2 σ with the lowest contour representing 3 σ. The contribution of strong Hα emission has been removed when calculating the $J - K$ colors. North is up and east to the left.

- J1c is a foreground object;
- CO emission is identified with J1n and J1s = J1a+J1b;
- Model of SPIFFI data with J1c removed shows coincidence of Hα contours with J-K color image and with J1n and J1s, which appear to be co-rotating disks;
- J2 is part of system - orbital velocity implies M(dyn) ~ 10^{11} $M_{\odot}$ for J1ns;
- they detect a superwind.

SMM J16359 - a triply imaged SMG with mags = 15, 22, & 8; total = 45 [First detected by Sheth et al. ApJ 614, L5 (2004)]

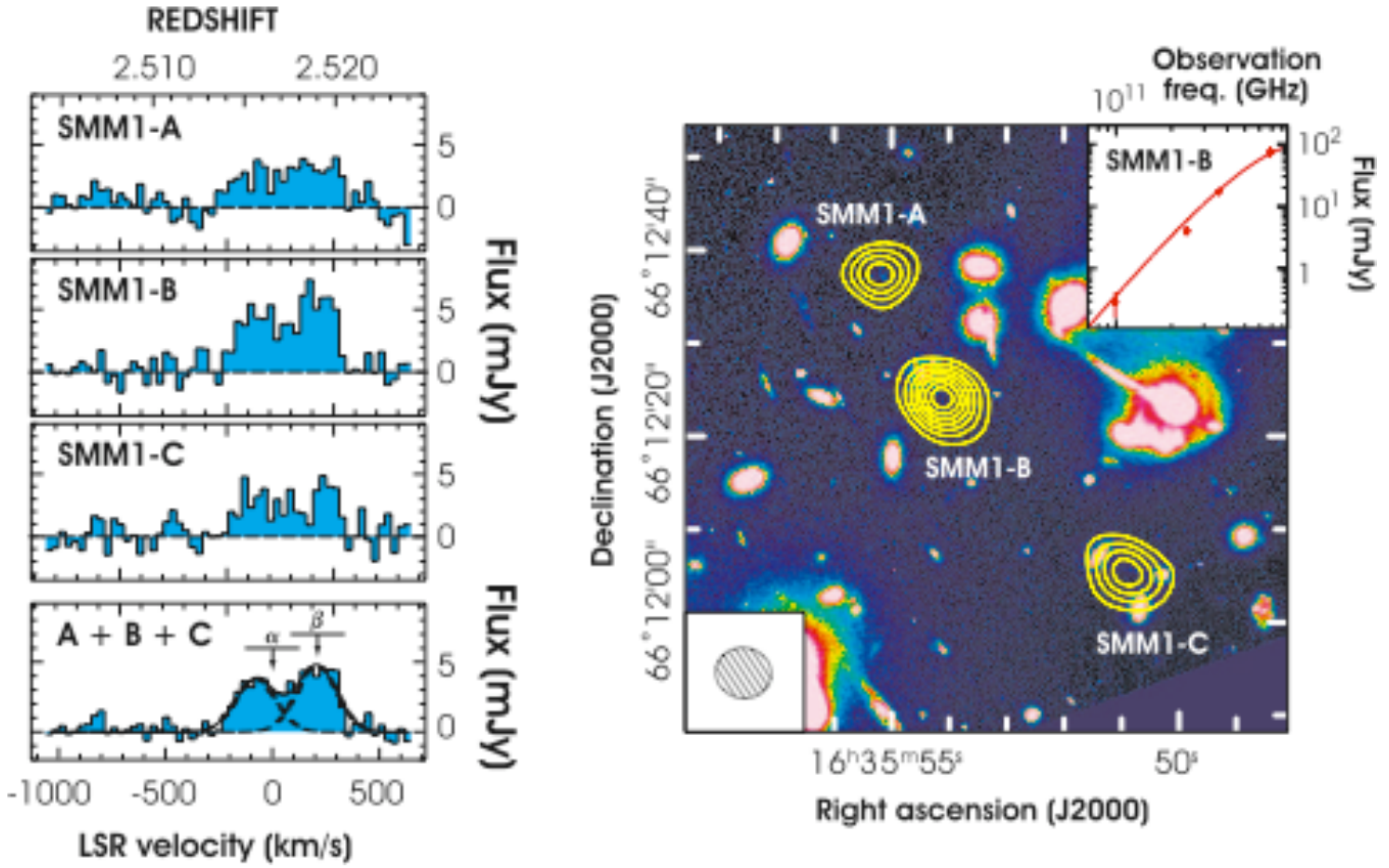

Kneib et al. MNRAS 349, 1211(2004) ; and A&A 434, 819 (2004).

- High magnification enables a CO detection in a somewhat low-luminosity SMM, as L(FIR) ~ 10^{12} $L_{\odot}$;
- There are two velocity components, at -70 and +210 km/s wrt the overall mean velocity of +70 km/s;
- Conclude that the two components are separated by 1.5 - 3.0 kpc and within a radius of 1.5 kpc M(dyn) ~ 10^{10} $M_{\odot}$;
- M(gas) ~ 5 x 10^{9} $M_{\odot}$, comfortably < M(dyn);

Weiß et al. [A&A 440, L45 (2005)] have detected CO(3-2), (4-3), (5-4), and (6-5) in J16359.

- All lines are double-peaked;
- Physical conditions in two components are similar;
- (5-4) is sub-thermal, suggesting cooler conditions than in QSO EMGs.

SMM J16359 is the only SMM galaxy to be detected in HCN

- Gao et al. have detected HCN(1-0) using the VLA [ApJ 660, L93 (2007)];
- HCN image hints at double source but needs more S/N to be convincing.

Imaging the "FIR" in SMGs [Chapman et al. ApJ 611, 732 (2004)]

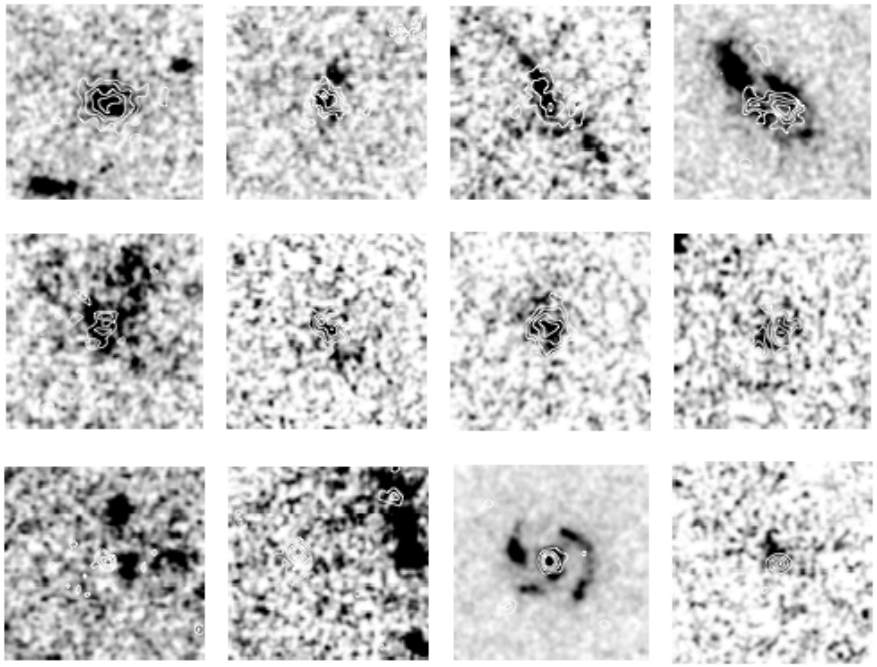

FIG. 3.—Comparison of MERLIN/VLA radio data (0".2–0".3 synthesized beam size, shown as contours) for 12 of our SMGs with the *HST* STIS clear imaging filter 50CCD and ACS $b_{435} + i_{775}$ imaging (as noted in Table 1). The *HST* images have been smoothed with a Gaussian of FWHM 0".2 to match the effective resolution of the radio map. The first two rows show sources where the radio is clearly extended along a portion of the rest-frame–UV imaging, whereas the final four panels on the bottom row reveal point sources in the radio, likely associated with a single UV component. Radio contour levels begin at 3 σ and increase in linear steps scaled to the peak of the radio emission. Each panel is 3" on a side, and they are ordered from top left as in the same sense as Table 1.

- Invoking the FIR-radio correlation, they used MERLIN/VLA to produce "FIR" images at a resolution of 0.3″ of 12 galaxies;
- 8 are resolved by this technique on scales of 1″ (~ 10 kpc);
- SFR rates are typically ~ 1700 $M_{\odot}$ per year.

SMG Spectroscopic Redshift Survey [Chapman et al. ApJ 622, 772 (2005)]

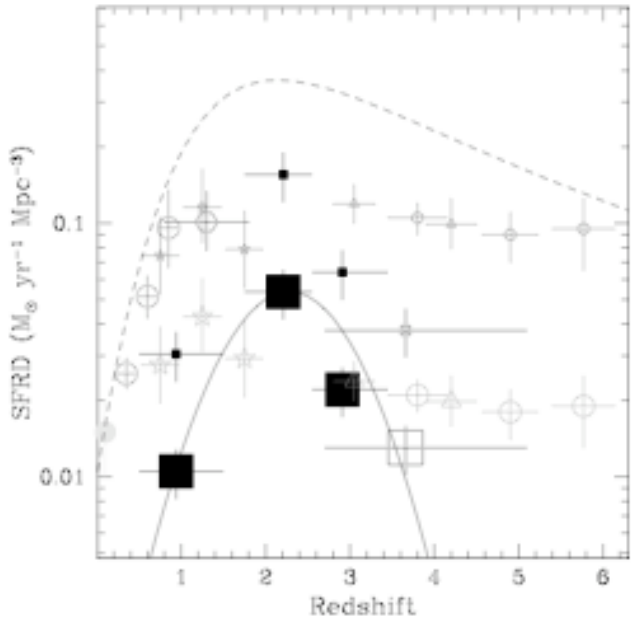

FIG. 12.—Evolution of the energy density (parametrized by SFRD) in the universe with epoch. Our new submillimeter measurements (*large squares*, shown at the median value for each redshift bin) are compared with the published estimates from optical/UV surveys and radio/IR tracers of the star formation density. The open square indicates the SMGs without radio identification, at the median redshift derived from our modeling of Fig. 4. The smaller symbols for the optical estimates indicate dust-corrected estimates. A Gaussian fit is shown for the four submillimeter galaxy points, tracing an evolution comparable to luminous radio-selected quasars (Shaver et al. 1998). For the submillimeter sources, the smaller points show a simple redshift-independent correction to the luminosity density to match the submillimeter extragalactic background down to 1 mJy. The dashed line is the best fit for a simple parametric model constrained by the counts of sources in the FIR/submillimeter and the spectrum of the extragalactic background (Blain et al. 2002). Other UV-, mid-IR–, and radio-derived points are from Giavalisco et al. (2004; highest z, *circles*), Steidel et al. (1999; $z = 3$–4, *triangles*), Connolly et al. (1997; $z = 1$–2, *stars*), Yan et al. (1999; $z = 1.3$, *hexagon*), Flores et al. (1999; $z = 0.3$–1, *circles*), Yun et al. (2001; low z, *solid circle*).

- Used Keck to get z's for 73 SMGs;
- Mean z = 2.2;
- Show that *dust corrected* UV luminosities "rarely hint" at huge L_{bol} implied by submm;
- Means inferred SFR from both must be *summed* in plot at left.

Interferometric Surveys of SMGs

- Greve et al. [MNRAS 359, 1165 (2005)] used the IRAM PdB to make 5 new CO detections and summarize the properties of all 12 known CO SMGs;
- Tacconi et al. [ApJ 640, 228 (2006)] imaged 8 SMGs in CO at the IRAM PdB;
- Using the SMA, Iona et al. [arXiv:0602226] have imaged 2 SMGs in 890μm continuum, and Younger et al [arXiv:0708:1020] another 7;
- Kovacs et al. [arXiv:0604591] have imaged 15 SMGs with SHARC2.

Greve et al. Survey Results

- $\langle L'(CO) \rangle = (3.8 \pm 2.0) \times 10^{10}$ K km s^{-1} pc^2
- $\langle M(gas) \rangle = (3.0 \pm 1.6) \times 10^{10}$ $M_\odot$ within 2 kpc radius, about 4x that of ULIRGs, but comparable to EMGs;
- $\langle FWHM \rangle = 780 \pm 320$ km s^{-1} with double-peaked lines common, suggesting mergers;
- $\langle M(dyn) \rangle = (1.2 \pm 1.5) \times 10^{11}$ $M_\odot$ within a typical source diameter of 0.5″ (~ 4 kpc);
- Median M(gas) and SFR ~ 700 $M_\odot$ per year imply τ(burst) ~ 40 Myr;

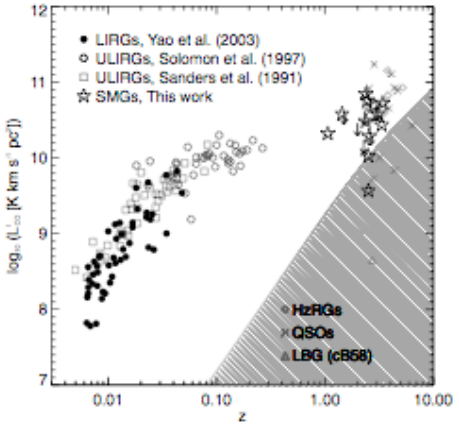

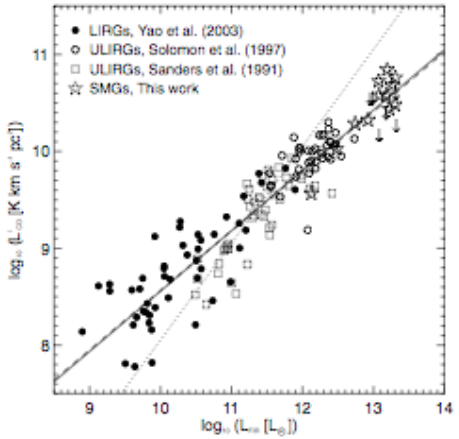

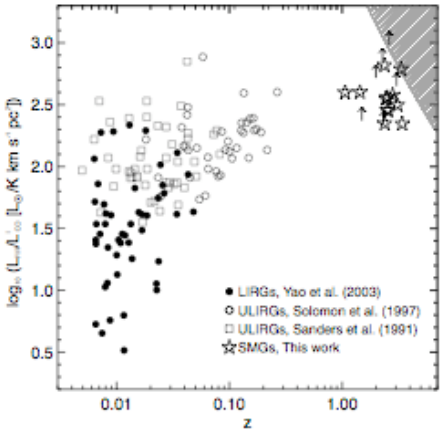

Tacconi et al. Survey

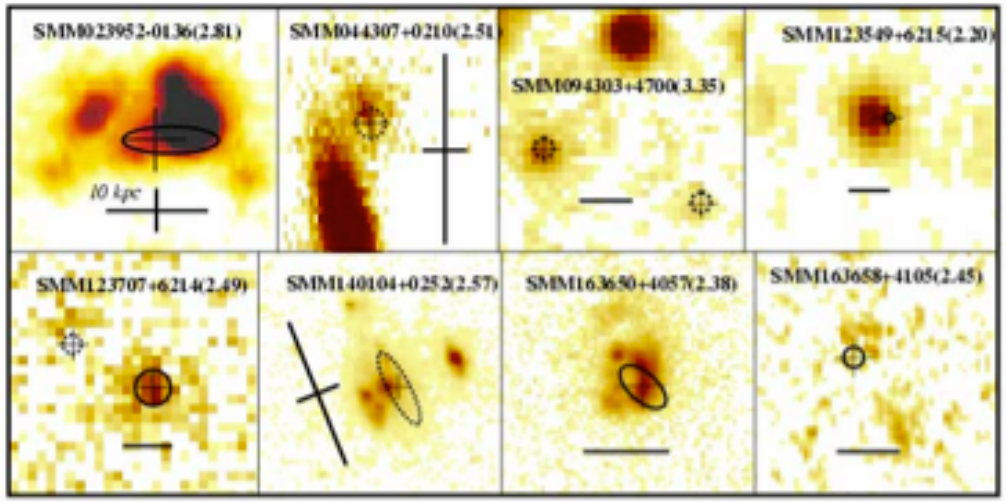

Optical/IR images with CO ellipses imposed; thin cross is SMG position; thick line is 10 kpc (cross for lensed sources).

- Median FWHM diameter is ≤ 0.5″ (4 kpc), and there is no evidence of cold, very extended dust/molecular gas;
- Double-peaked line profiles suggest mergers;
- Maximal starbursts - 10^{10} - 10^{11} $M_{\odot}$ converted to stars in few 10s Myr;
- SMGs are scaled-up versions of local ULIRGs.

Spitzer and EMGs

- Huynh et al. [astro-ph/0612520v2] searched the central GOODS-N region at 70 μm, trying to detect the 30 known ($S_{850} > 2$ mJy) SMGs. They detected 2, both relatively nearby ($z = 0.5$ & 1.2);
- Lutz et al. [astro-ph/0504431] detected PAH emission in 2 SMGs at $z \sim 2.8$, confirming star formation in these sources;
- Next to nothing has been done to observe EMGs;
- Lack of sensitivity, especially at 70 and 160 μm, makes Spitzer marginal for high-z SED studies.

Molecular Gas in Radio Galaxies

CO has been detected in (7) high-z radio galaxies (HzRGs):

53W002	z = 2.4	
B3 J2330	3.1	de Breuck, et al. [A&A 401, 911 (2003)]
TN J0121	3.5	
6C1908	3.5	
4C60.07	3.8	
4C 41.17	3.8	Greve, et al. [arXiv:0707.4482]
TN J0924	5.2	Klamer, et al. [ApJ 621, L1 (2005)]

B3 J2330+3927
[De Breuck et al. A&A 401, 911 (2003)]

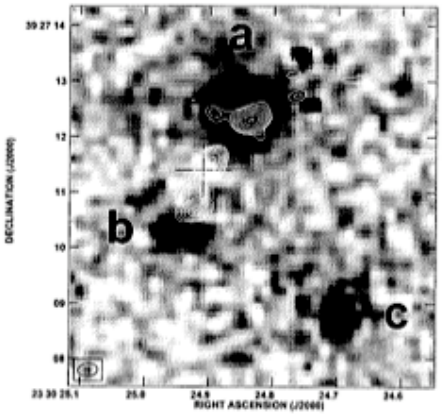

Fig. 2. 8.46 GHz VLA map of B3 J2330+3927 overlaid on our Keck K_S-band image (subject to a 0.″5 uncertainty in the registration). We identify 3 components *a*, *b*, and *c*, which may be part of the same physical system (the 2 small peaks west and north-west of object *a* are bad pixels). The cross marks the position in the NVSS catalogue, which is within 0.″2 from the position found in the 1.4 GHz A-array data of Vigotti et al. (1999). The FWHM of the synthesized 8.46 GHz VLA beam is shown in the bottom left corner.

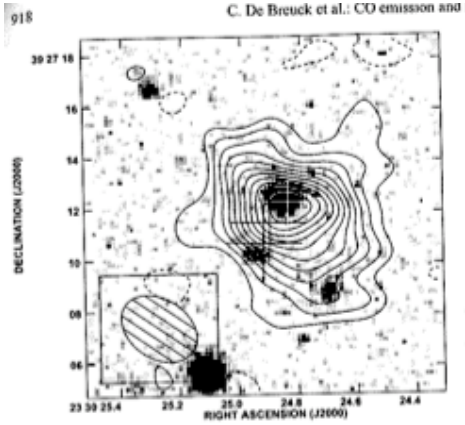

Fig. 7. Integrated CO $J = 4-3$ emission towards B3 J2330+3927 overlaid on the Keck/NIRC K-band image. Contour levels start at 2 σ, and increase by 1 σ, with $\sigma = 0.2$ mJy Beam^{-1} (negative contours are dotted). The 3 crosses mark the positions of the radio components in Fig. 2. The FWHM of the synthesized beam is shown in the bottom left corner.

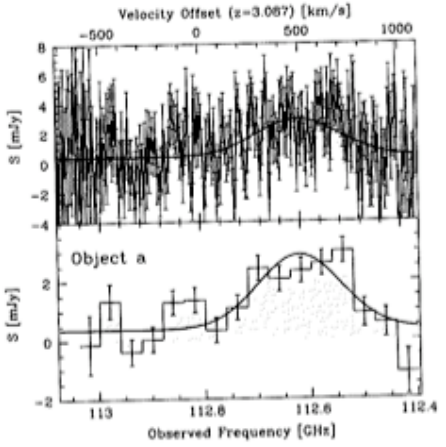

Fig. 8. CO $J = 4-3$ spectrum of B3 J2330+3927 extracted at object *a*. The top panel shows the unbinned spectrum, while the bottom panel has been re-binned with $\Delta\nu_{\rm bin} = 40$ MHz (106.5 km s^{-1}). The velocity scale is with respect to the central frequency of CO $J = 4-3$ at $z = 3.087$. The solid line is a Gaussian fit with an underlying continuum emission.

Keck K-band image shows three components surrounding the (VLA) 8.6 GHz radio emission; CO(4-3) emission, also surrounds these components, implies major starburst; M(gas) ~ $7 \times 10^{10}\, M_\odot$ from CO.

4C41.17 (z = 3.8)
[De Breuck et al. A&A 430, 11 (2005)]

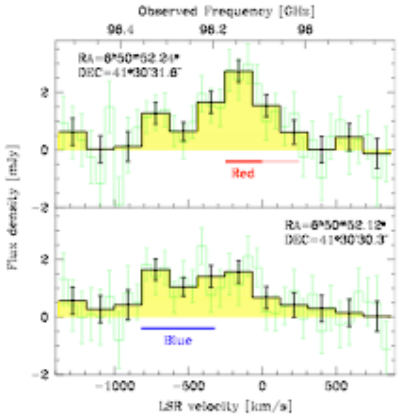

Fig. 1. CO (4–3) spectra at the positions of the red (*top panel*) and blue components (*bottom*). The thin green line shows the data in 62 km s^{-1} channels, and the thick black line in 184 km s^{-1} channels. Error bars are 1σ, and velocities are relative to 96.093 GHz (z_{LSR} = 3.79786). The red and blue bars indicate the linewidths; the thick part of the red bar marks channels used in Fig. 3, left. Note that these two positions are less than a beam size away, and are therefore not fully independent.

Table 1. Observed and derived parameters for CO(4–3) in 4C 41.17.

Parameter	Red component	Blue component	Total
RA(J2000)[a] (peak)	6^{h}50^{m}52^s.24	6^{h}50^{m}52^s.12	6^{h}50^{m}52^s.17
DEC(J2000)[a] (peak)	41°30′31″.6	41°30′30″.3	41°30′30″.9
$\int S_{CO}\,dV$ [Jy km s^{-1}]	1.2 ± 0.15	0.6 ± 0.15	1.8 ± 0.2
Central velocity[b] [km s^{-1}]	−130 ± 50	−550 ± 100	−285 ± 100
Velocity width [km s^{-1}]	500 ± 100	500 ± 150	1000 ± 150
L'_{CO}(4–3) [K km s^{-1} pc^2]	4.4×10^{10}	2.2×10^{10}	6.7×10^{10}
M(H$_2$) [$M_\odot$]	3.6×10^{10}	1.8×10^{10}	5.4×10^{10}

[a] Positional uncertainty 0.03 in RA and 0.″3 in Dec.
[b] Relative to 96.093 GHz (z = 3.79786).

- Two components separated by 1.8′′ (13 kpc) and 400 km/s, similar to 4C60.07;
- (A) M(gas) ~ 3.6x10^{10} $M_\odot$ and (B) M(gas) ~ 1.8x10^{10} $M_\odot$;
- M(dyn) ~ 6x10^{10} $M_\odot$, < typical for HzRGs [Rocca-Volmerange et al. A&A 415,931 (2004)];
- Coincident in position with radio core.

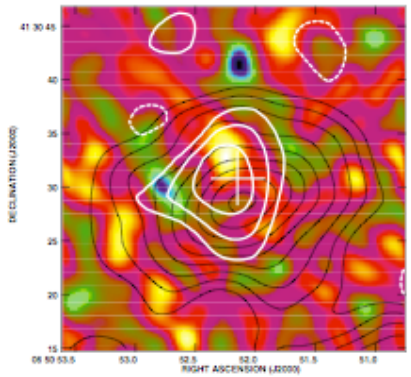

Fig. 4. Thermal dust emission in 4C 41.17. The colourscale shows the 1.2 mm PdBI map convolved with a 3.″0 Gaussian (not corrected for the 20″ primary beam). Superposed are the 850 μm SCUBA map (thin black contours; beam 14″) and our 1.2 mm MAMBO map (thick white contours; beam 11″). Contours are −2, 2, 3, 4, 5, 6, 7, 8, 9 and 10σ, with σ = 1.2 and 0.8 mJy beam^{-1} for the SCUBA and MAMBO maps, respectively. The white cross indicates the cm-radio core.

L(dust) ~ 1.5 x 10^{13} $L_\odot$ implying a SFR ~ 3000 $M_\odot$ per year

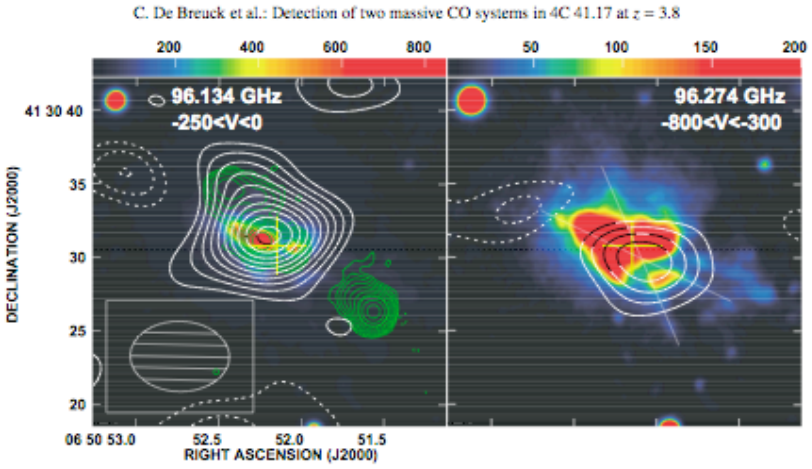

Fig. 3. Velocity-averaged CO maps (thick/white+black contours) of the red (*left*) and blue (*right*) components. CO contours are −3, −2, 2, 3, ..., 10σ, with σ = 0.2 mJy beam^{-1}. The lower left inset shows the CO beam. The two CO maps are superposed on the Lyα image, each with its own colour scheme to show the two dark lanes in the Lyα. The thin green contours (*left panel*) show the 1.4 GHz radio map (Carilli et al. 1994), and the yellow cross indicates the radio core. The thin straight lines (*right panel*) indicate a possible AGN or starburst emission-line cone.

CO contours for the two components on Lyα image;

Green contours are 1.4 GHz radio cont.

Obscured BH in each component?

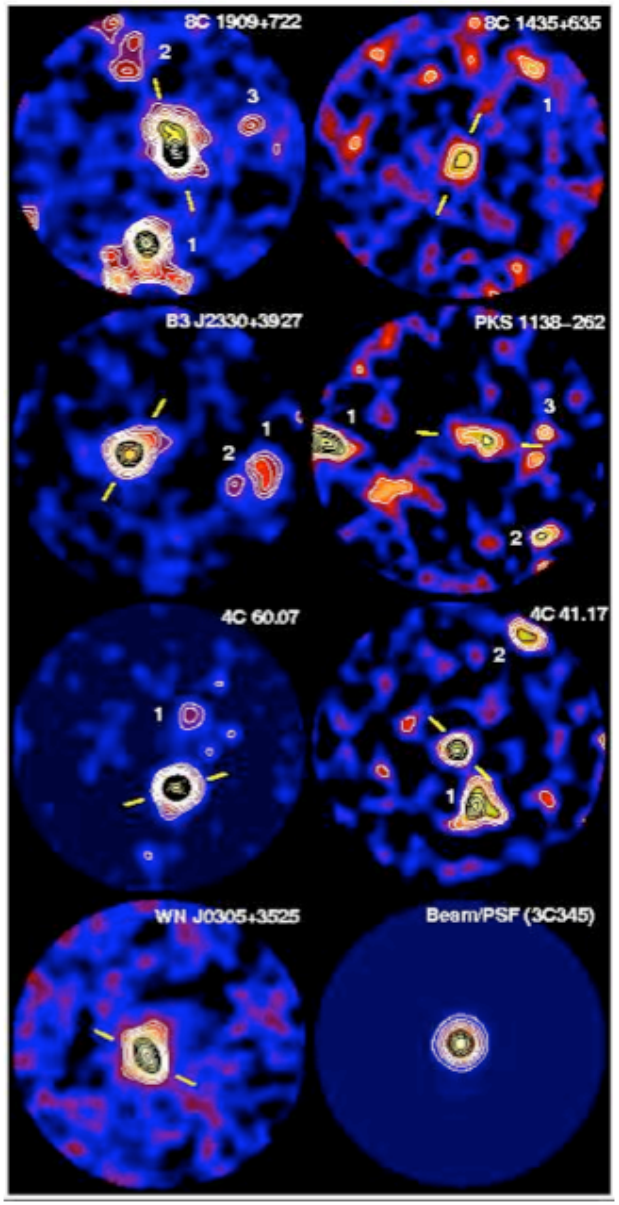

Clusters of galaxies have massive ellipticals at their cores. High-z radio galaxies may mark such systems in the early Universe. Are they located at the centers of clusters?

The 850μm images [Stevens et al. Nature, 425, 264 (2003)] of 5 HzRGs (3 are CO-detected) suggest that this is so. If this FIR emission is from dust heated by starbursts, these cluster galaxies and the central radio galaxies all contain regions of prodigious star formation.

However, detailed study of one (4C41.17) does not confirm this.

4C41.17 - SHARC2 & MAMBO
[Greve et al. arXiv:070.4482]

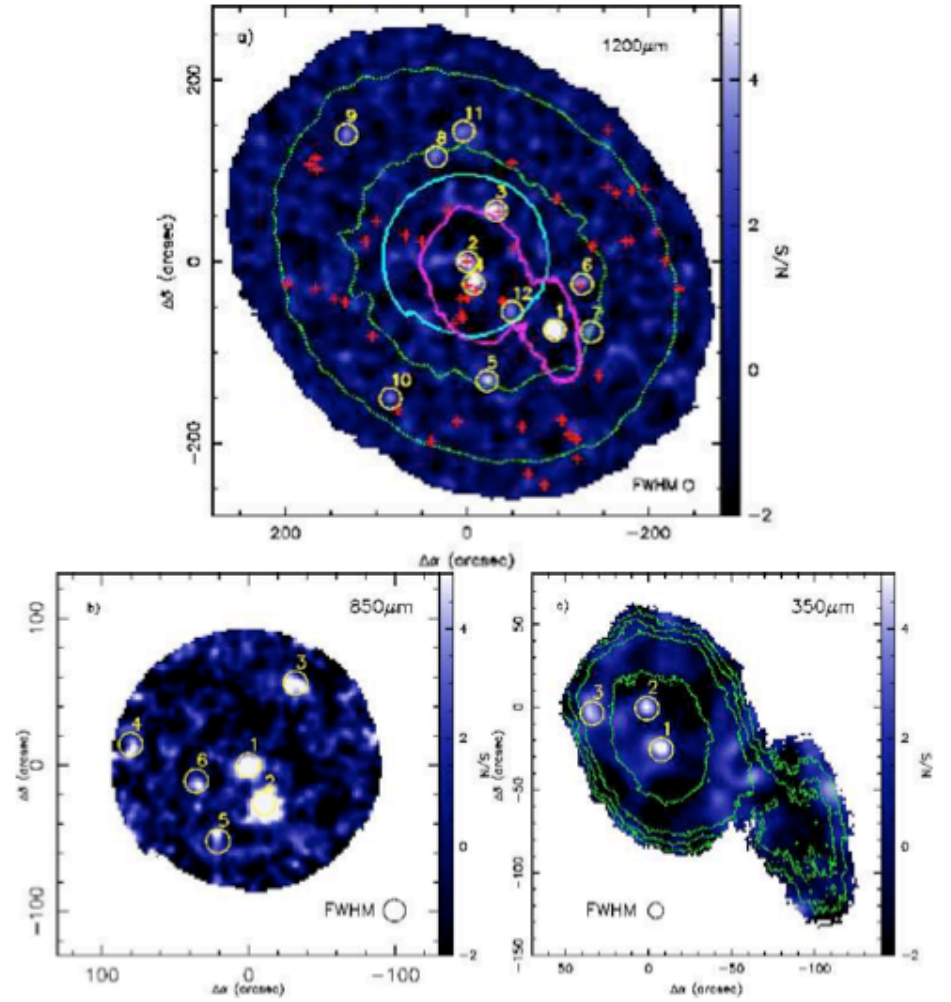

Figure 1. a) 1200-μm MAMBO signal-to-noise map centred on 4C 41.17. Green dashed contours mark the 0.5 and 1.0 mJy beam^{-1} r.m.s. noise levels across the map. Light blue and magenta curves indicate the extend of the 850-μm SCUBA and 350-μm SHARC-II maps, respectively (Ivison et al. 2000; this work). Red crosses indicates the X-ray sources detected by Chandra (Smail et al. 2003b). **b)** 850-μm SCUBA signal-to-noise map of 4C 41.17 (Ivison et al. 2000). **c)** 350-μm SHARC-II signal-to-noise map of 4C 41.17. The 40 and 60, 70 and 80 mJy beam^{-1} r.m.s. noise levels are shown as green dashed contours. In all three panels we circle sources detected at a significance $\geq$ 3.5-σ in yellow; numbering ranks them according to signal-to-noise ratio (with 1 corresponding the highest ratio). Also, the axes denote the offset (in arcseconds) from the map centre R.A. 06:50:52.2, DEC. +41:30:30.9 (J2000). The angular resolution of the MAMBO, SCUBA and SHARC-II maps are 10.7″, 14.7″ and 9.2″ (FWHM), respectively.

- 14 MAMBO detections are coincident with 3 SCUBA and 2 SHARC2 detections;
- 8 of 14 are detected by VLA (1.4 GHz) and/or Spitzer (IRAC & MIPS);
- But redshifts of 4 (Keck) are << 4C41.17, as are the inferred photometric z's of another 3;
- 4C41.17 is robustly detected by all systems.

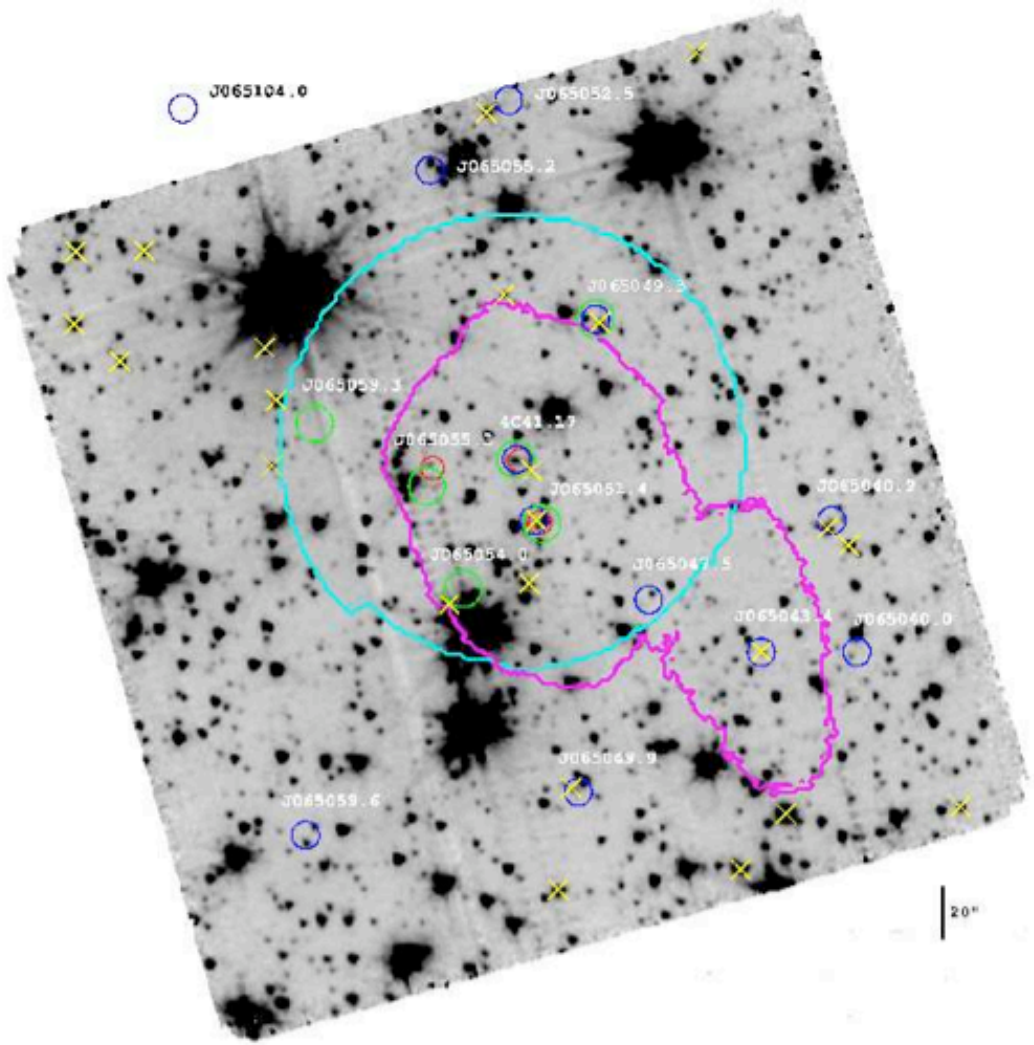

Figure 2. 5′.21 × 5′.21 IRAC 3.6-μm image (grey-scale) of the 4C 41.17 field. 350-, 850- and 1200-μm source catalogues are overlaid as red, green, and blue circles, respectively, and the diameter of the circles correspond to the FWHM of the CSO (9.2″), JCMT (14.7″), and IRAM 30m (10.7″) at those three wavelengths. Sources targeted spectroscopically with Keck/LRIS are shown as yellow crosses. For clarity, the extent of the SCUBA and SHARC-II maps have been outlined (light blue and magenta, respectively). North is up and east is left.

Conclusion: any overdensity of galaxies within 50′′ of 4C41.17 is no more than a factor of 5 compared with the typical MAMBO and SCUBA blank fields.

TN J0924-2201
[Klamer et al. ApJ 621, L1 (2005)]

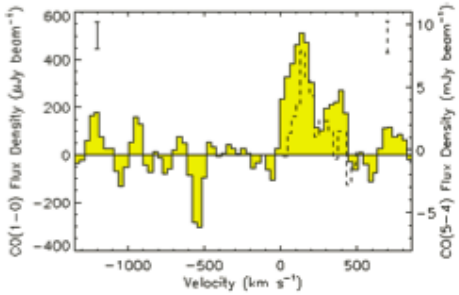

FIG. 1.—Spectra of the continuum-subtracted CO (1–0) (*shaded region*) and CO (5–4) (*dashed line*) transitions, through the peak of their respective velocity-integrated emission shown in Fig. 2. The CO (1–0) spectrum is unbinned (32 km s^{-1} bins; spectral resolution 72 km s^{-1}), while the CO (5–4) spectral channels have been rebinned into 30 km s^{-1} bins (original spectral resolution 15 km s^{-1}). The velocity axis is defined with respect to the Lyα-derived redshift of $z = 5.1989$, and the bars in the top left and right corners show the rms noise level in the CO (1–0) and CO (5–4) cubes, respectively.

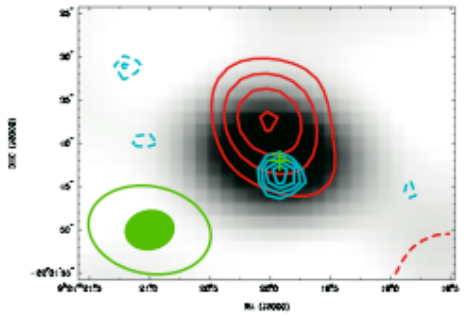

FIG. 2.—Gray-scale 18.6 GHz continuum image with CO (1–0) and CO (5–4) velocity-integrated emission overlaid in red and cyan, respectively. The continuum flux density is 0.71 ± 0.03 mJy, the CO (1–0) contour levels are ±2, 3, 4, 5 × σ, where $\sigma = 0.017$ Jy beam^{-1} km s^{-1}, and the CO (5–4) contour levels are ±2.5, 3, 3.5, 4 × σ, where $\sigma = 0.27$ Jy beam^{-1} km s^{-1}. The sizes of the 18 GHz (*open ellipse*) and 93 GHz (*filled ellipse*) restoring beams are shown in the bottom left corner; the plus sign shows the optical position of the radio galaxy. The radio lobes, illustrated with filled circles, extend 1.3 along a position angle of 29°.

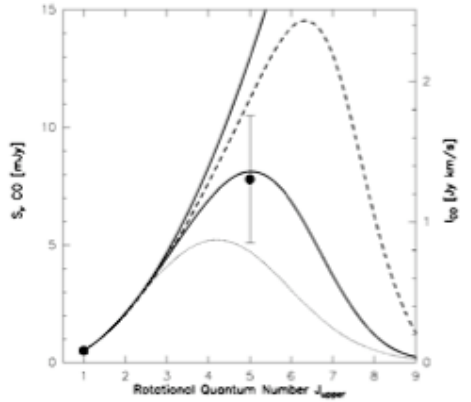

FIG. 4.—CO ladder with LVG models overlaid. The best match to the observations is log [n(H$_2$)] = 3.3, T_{kin} = 50 K, and $r > 2.0$ kpc (*solid line*). Also in agreement with the observations are log [n(H$_2$)] = 4.0, T_{kin} = 30 K, and $r > 2.9$ kpc (*dashed line*) and log [n(H$_2$)] = 2.7, T_{kin} = 150 K, and $r > 2.2$ kpc (*dotted line*). The condition for optically thick, thermally excited gas is the solid, parabolic fit. The error bars are 1 σ noise estimates and do not include the uncertainty in the absolute flux scale (§ 3).

- TN J0924 is the most distant known radio galaxy, z = 5.2;
- Detected by the ATCA in CO(5-4) and (1-0);
- Curious separation of components by 18 ± 8 kpc (?);
- No detection at 850 μm implies 5x less dust than the typical CO-detected HxRG (similar to 53W002 at z = 2.4).

Molecular Gas in a Lyman Break Galaxy

- LBGs are large population of high redshift galaxies - can they be observed in CO?
- Baker [ApJ 604, 125 (2004)] detected CO in MS1512 cB58 (z=2.7), but only because it is gravitationally lensed with mag = 32. The CO luminosity is only 4.3×10^8, ~ 100x smaller than typical EMG.
- Greve & Sommer-Larsen [astro-ph/0608683] simulated CO emission from a LBG, getting results similar to Baker's, that suggest LBGs will be a major targets for ALMA.

Is cB58 a Cautionary Tale?

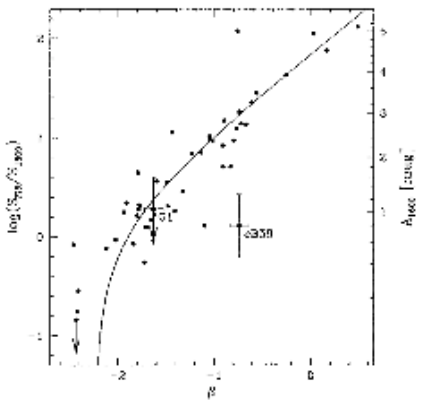

Figure 1. The relation between $S_{FIR}/S_{0.0}$ and β for local UV-selected galaxies (filled circles) with the best fitting parametrization, [illegible] and the positions of cB58 and G1 with respect to this relation.

Yes, if you are stuck with present facilities:

cB58 does not fit the relation established for local starbursts between S(FIR)/S(UV) and β, the UV spectral index [vdWerf et al. (2000)].

S(1.3mm) ~ 1 mJy.

UV implies more FIR than exists.

However, the inferred SFRs are similar:

Hα implies 24 $M_{\odot}$/year, & L(FIR) implies 18 $M_{\odot}$/year.

Note: although larger than the SFR in the Galaxy, this rate is much smaller than typical for other classes of EMGs. It will be easily detectable by ALMA.

CO Luminosity vs. Redshift

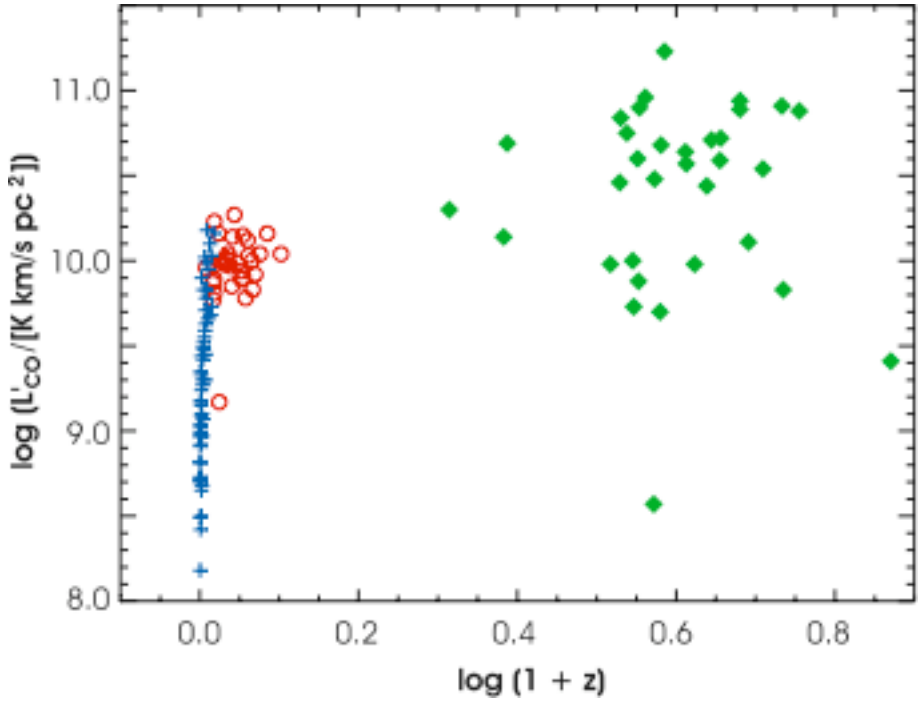

Blue crosses are normal spirals, red circles are ULIRGs, and green diamonds are EMGs.

FIR Luminosity (Star Formation Rate) vs. CO Luminosity

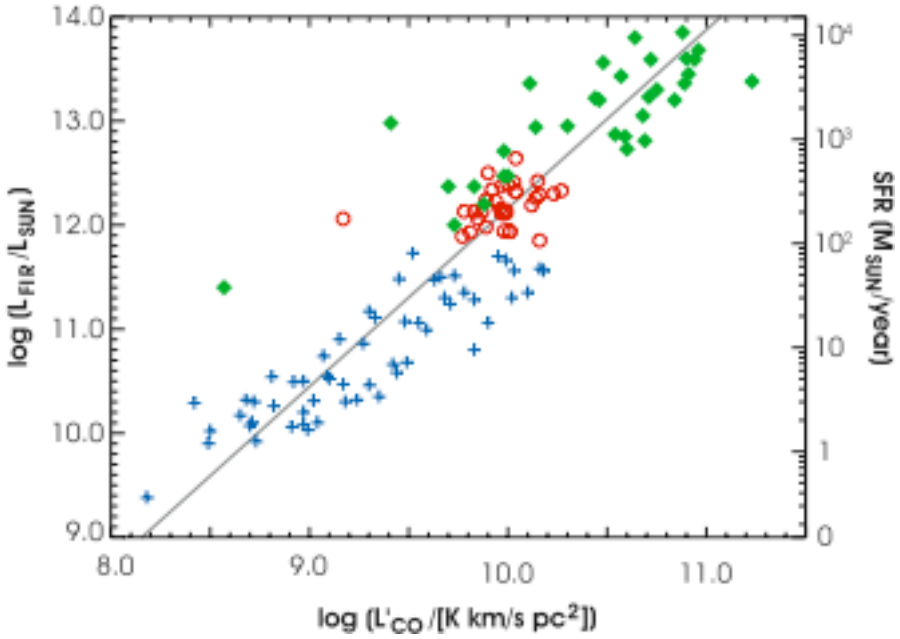

Blue crosses are normal spirals, red circles are ULIRGs, and green diamonds are EMGs.

Star Formation Efficiency & Duration vs. FIR Luminosity

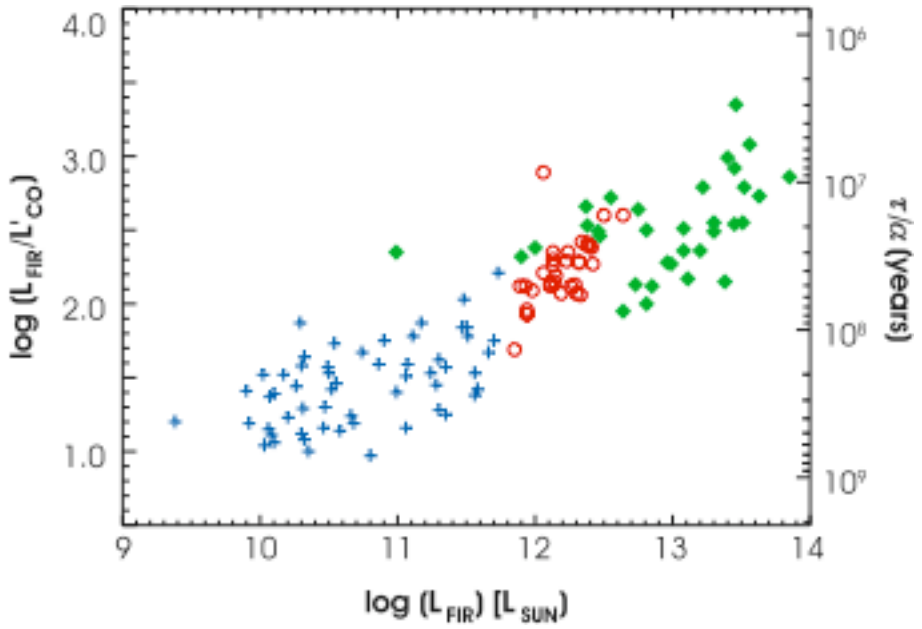

Blue crosses are normal spirals, red circles are ULIRGs, and green diamonds are EMGs.

Star Formation Efficiency vs. Redshift

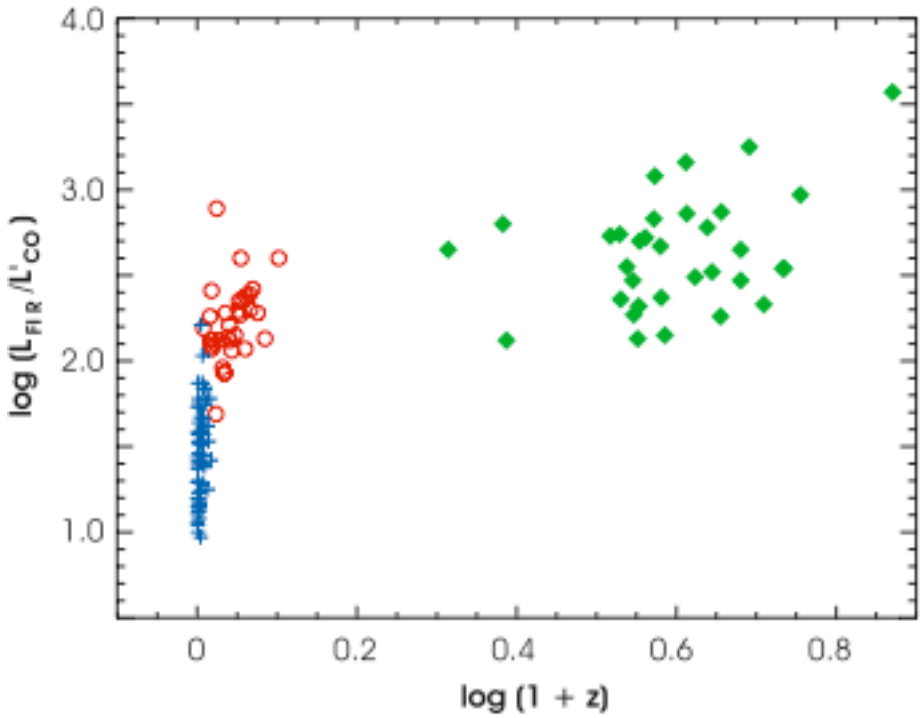

Blue crosses are normal spirals, red circles are ULIRGs, and green diamonds are EMGs.

Molecular Mass vs. Redshift

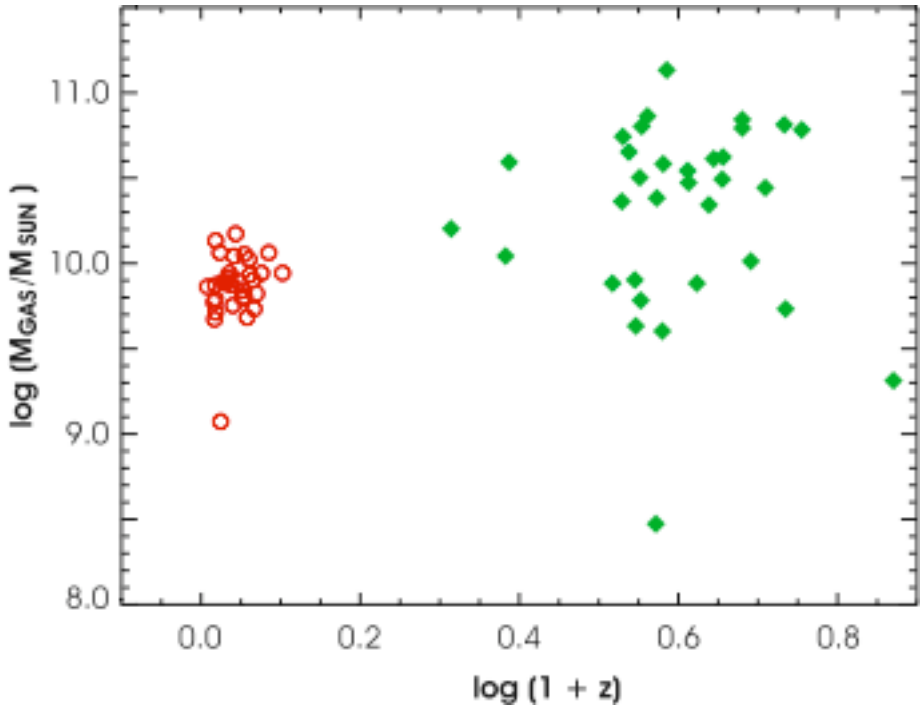

Red circles are ULIRGs, and green diamonds are EMGs.

Do EMGs Lead to Giant Ellipticals?

- The EMG starburst durations are short, as short at 1 Myr;
- There is only enough molecular gas (~ 3×10^{10} $M_{\odot}$) to make 10% of a giant elliptical galaxy;
- Further gas accretion/mergers must occur if EMGs form giant ellipticals [see Erb, arXiv: 0710.4146, for a more detailed discussion of S-K Laws and the need for gas accretion over a long time during galaxy formation.].

Is There a Cold, Extended Molecular Gas Component?

- EMGs tend to be seen in high-excitation CO lines, with the J=3-2 transition being most typical;
- these high-excitation CO lines trace hotter, denser gas compared with CO(1-0), from what we see in the Galaxy;
- CO(1-0) has been detected in only 5 EMGs (published), but a search is underway in 5 more, with 4 detections to date [Vanden Bout, Maddalena, & Solomon];
- there is no sign of a strong, cold, extended component.

CO Line "SEDs" can yield gas excitation

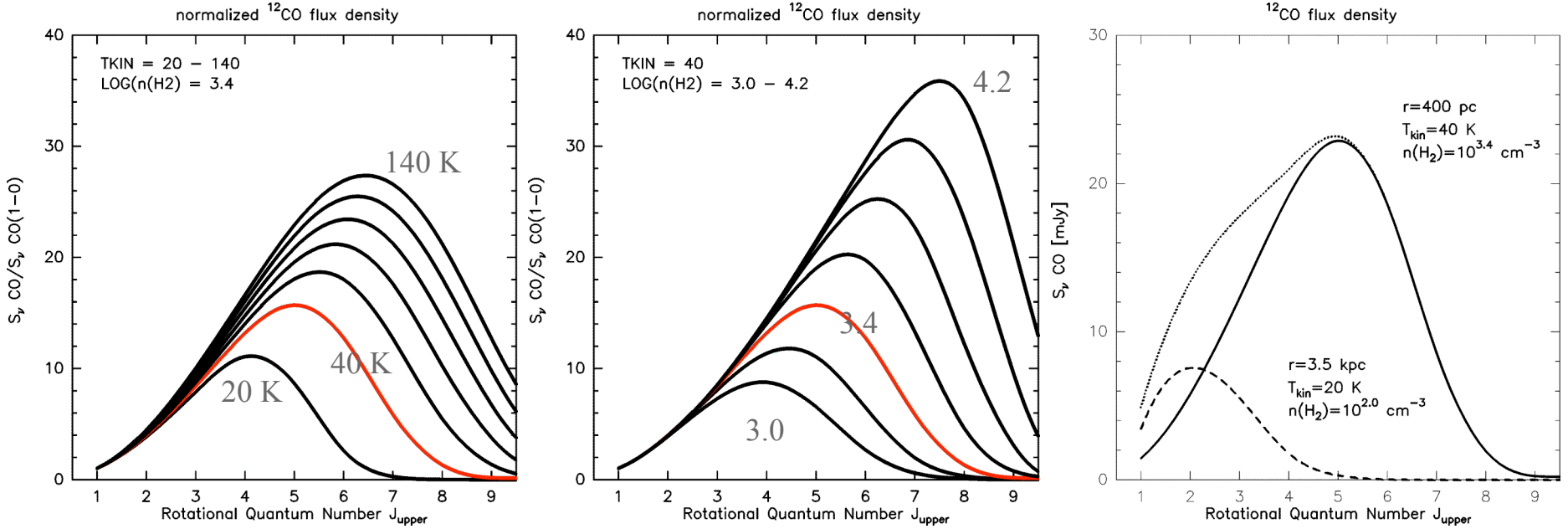

- Turnover is a measure of the CO excitation;
- Shape is temperature and density dependent;
- Shape is also sensitive to other (cold, extended) CO components.

See Riechers, et al. astro-ph/0606422.

Best fits to data reveal hot and really hot sources

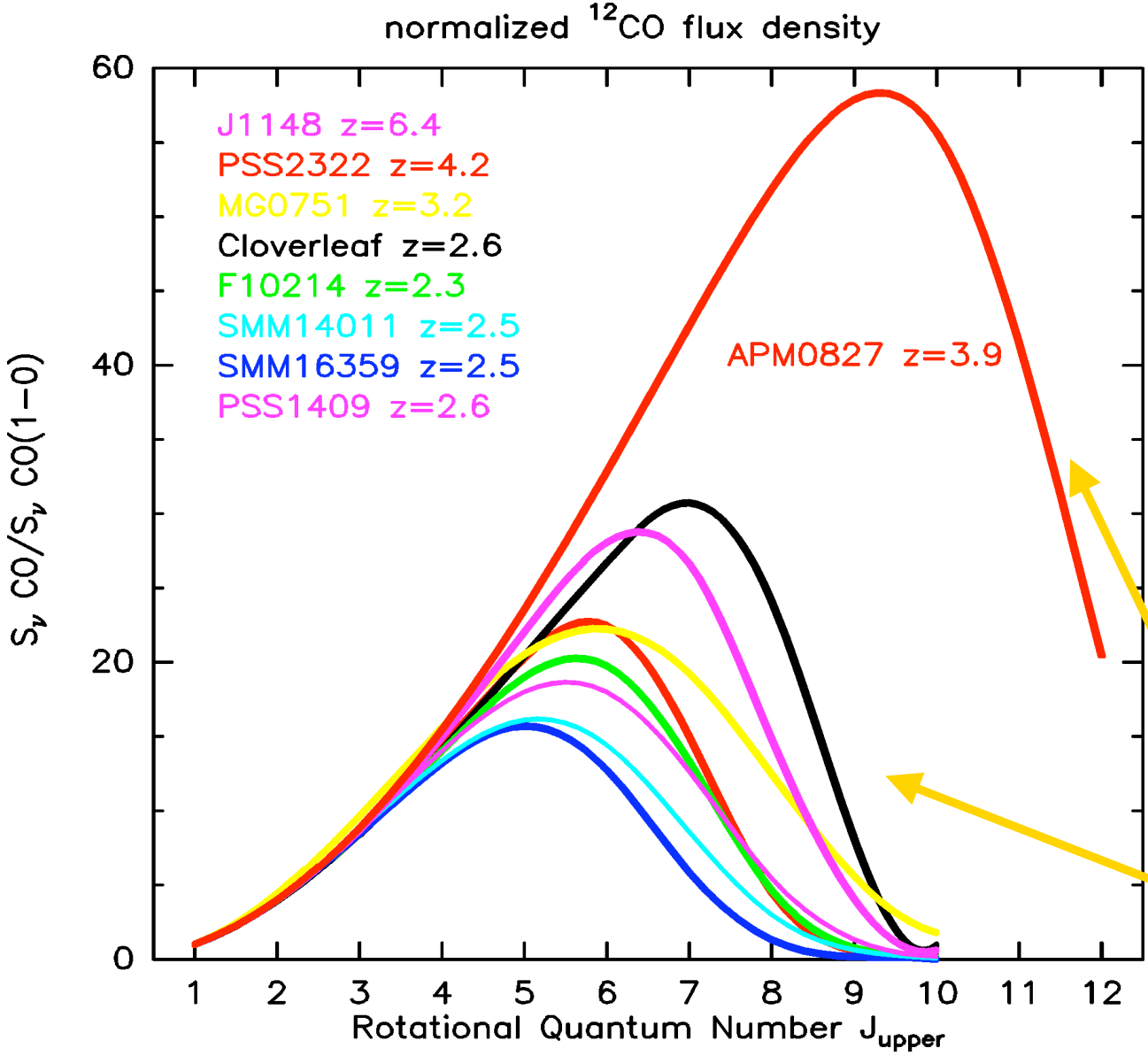

- QSO turnover: >6-5
- SMM turnover: 5-4
- compact (<1.5kpc)
- no indication of extended gas comp.

T_{kin}~80 K,
$n(H_2)$~$10^{4.6}$ cm^{-3}

T_{kin}~30–70 K,
$n(H_2)$ ~ $10^{3.3\text{-}4.2}$ cm^{-3}

Is HCN a better tracer than CO of star formation in EMGs, as it is in ULIRGs?

- HCN is difficult to detect in EMGs because it is much weaker than CO, typically, by a factor of 7;
- Even so, it has been possible to detect HCN in 5 EMGs (VLA, GBT, and IRAM PdB were used);
- Significant upper limits to HCN emission have been placed on another 7 EMGS;
- This is just enough to justify an examination of the FIR - HCN correlation in EMGs.

VLA Detection of HCN in the Cloverleaf

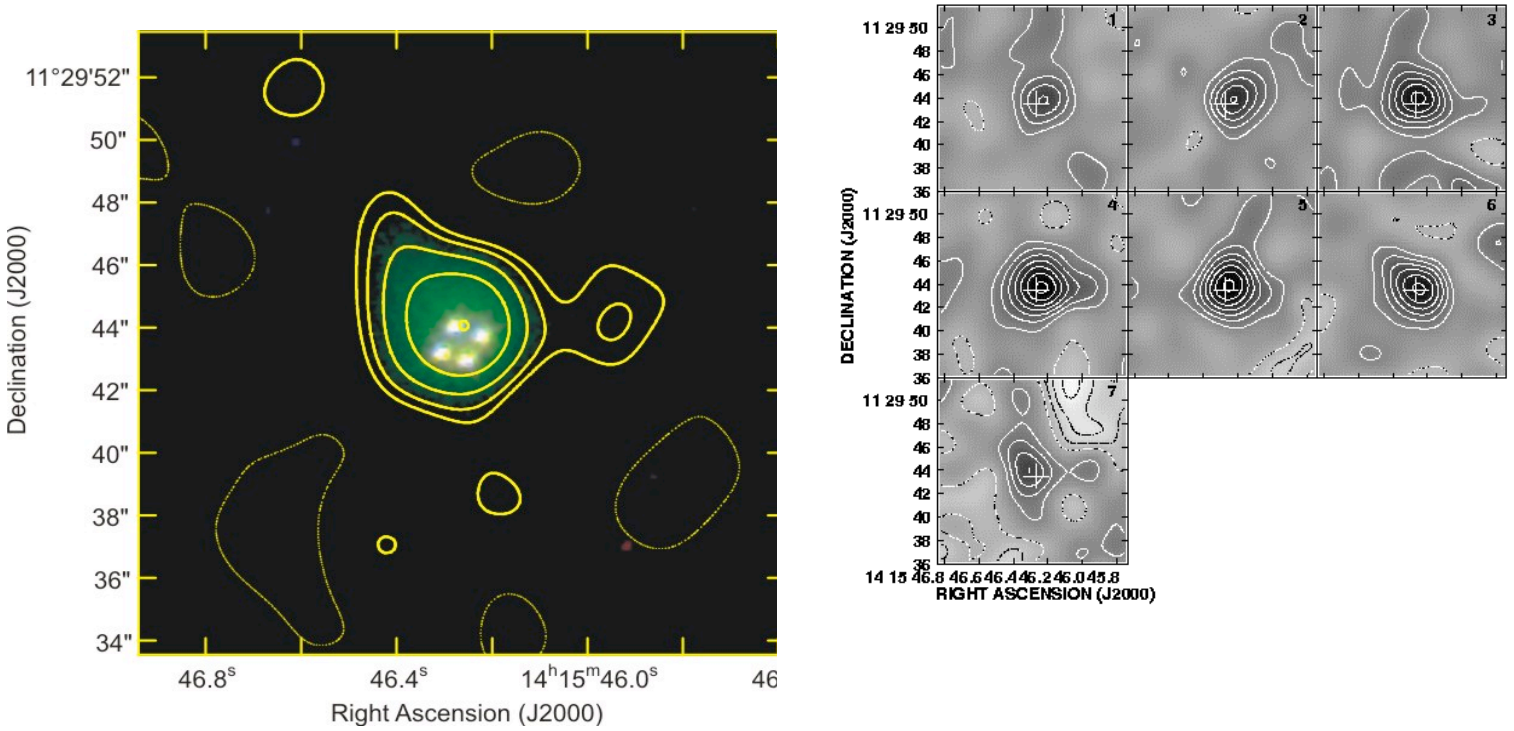

Solomon, Vanden Bout, Carilli, & Guélin, Nature 426, 636 (2004).

GBT Detection of HCN in IRAS F10214

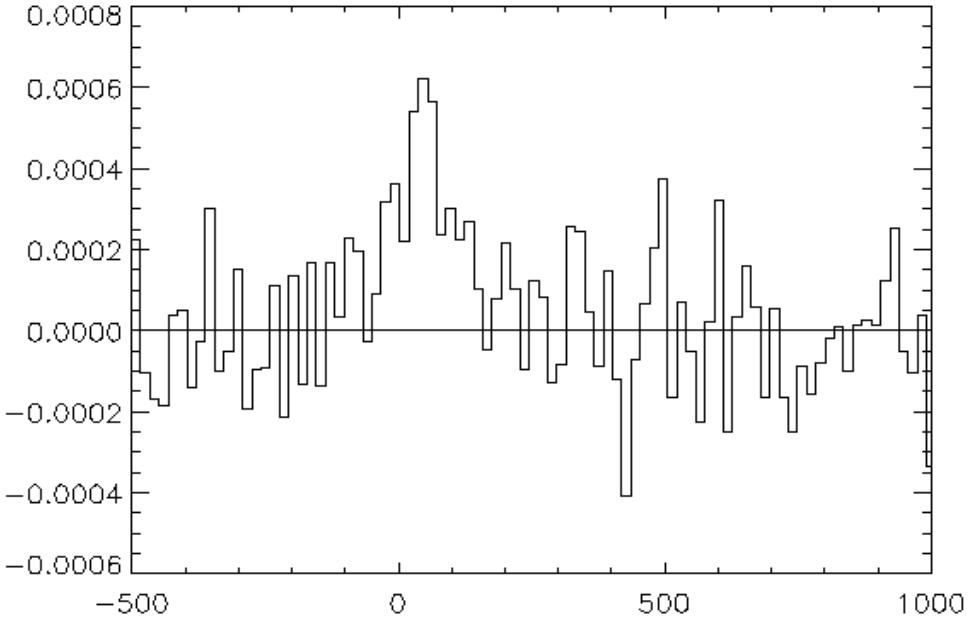

Vanden Bout, Solomon, & Maddalena ApJ 614, 97 (2004).

HCN(1-0) in J1409 - VLA

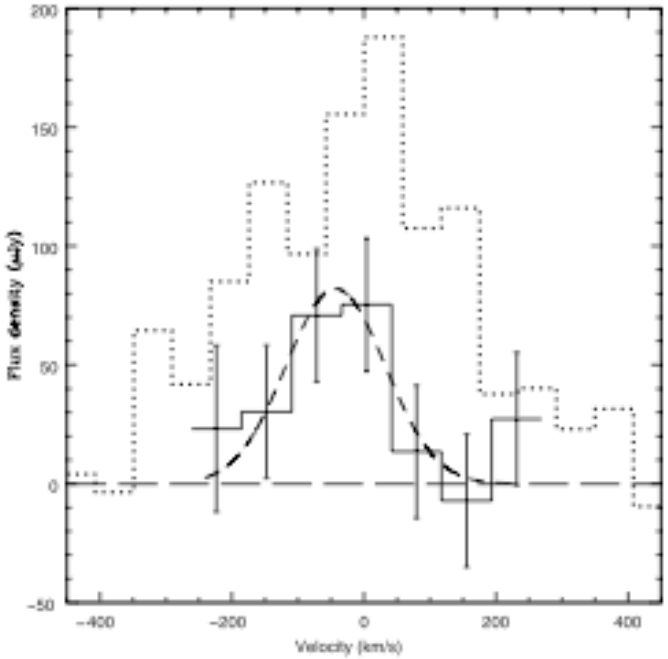

FIG. 1.—VLA spectrum of HCN (1–0) emission from J1409+5628 (*solid line plus points with error bars*) with continuum subtracted as described in § 4. Zero velocity corresponds to the CO (3–2) redshift of $z = 2.5832$. This spectrum has been Hanning smoothed, such that each channel is not independent. The rms per Hanning smoothed channel is 28 μJy. The short-dashed line shows a Gaussian fit to the data with parameters given in § 4. The dotted line shows the CO (3–2) spectrum from Beelen et al. (2004) scaled by a factor 1/40.

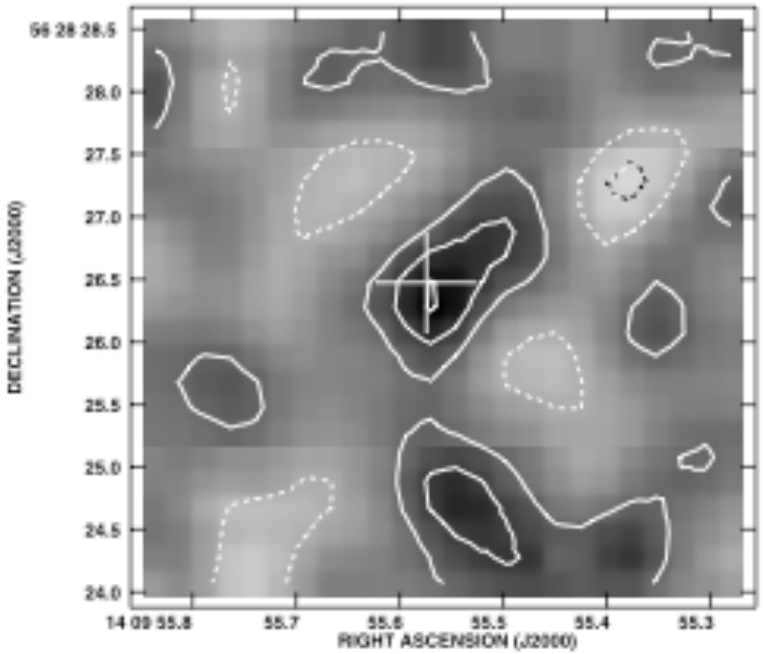

FIG. 2.—VLA image (*contours and gray scale*) of the average of the two peak channels containing possible HCN emission from J1409+5628 (see Fig. 1). The contour levels are −64, −32, 32, 64, and 96 μJy beam^{-1}, and the resolution FWHM = 1.″1. Negative contours are dashed. The radio QSO position is indicated by a cross. The rms noise on this image is 28 μJy beam^{-1}.

Carilli, et al. ApJ 618, 586 (2005).

HCN(5-4) in APM08279

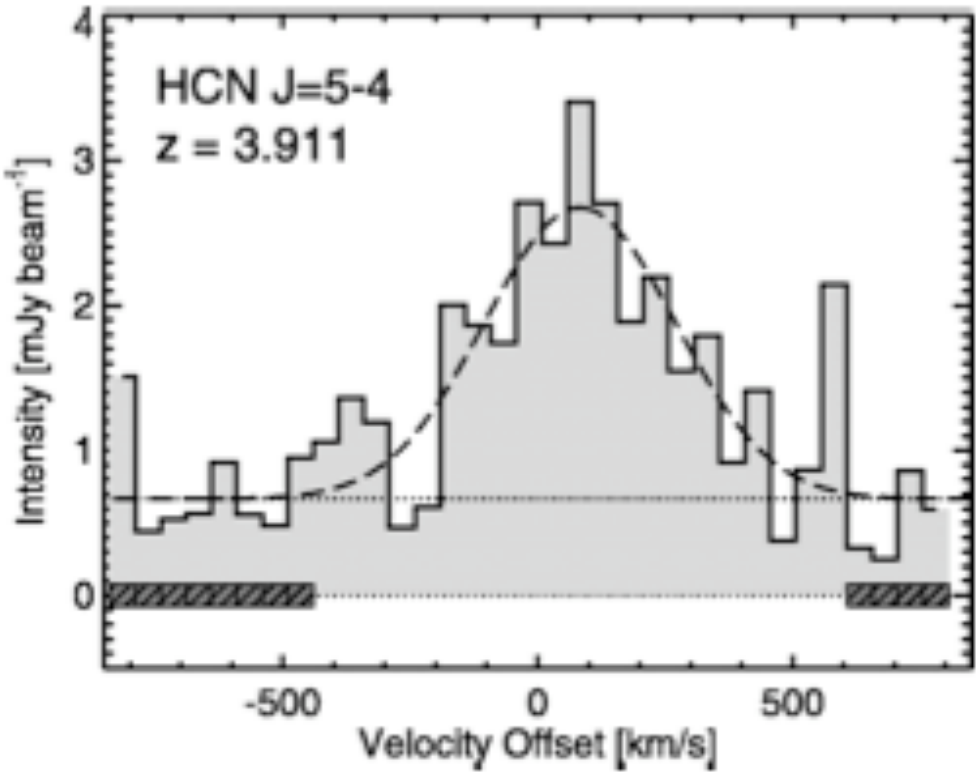

FIG. 2.—Spectrum of HCN $J = 5$–4 emission from APM 08279+5255 at 90.229 GHz, where the velocity scale is relative to the CO redshift of 3.911. The hatched regions mark the channels assumed to represent the line-free continuum level. The dashed line shows a Gaussian fit.

Wagg, et al. ApJ 634, L13 (2005).

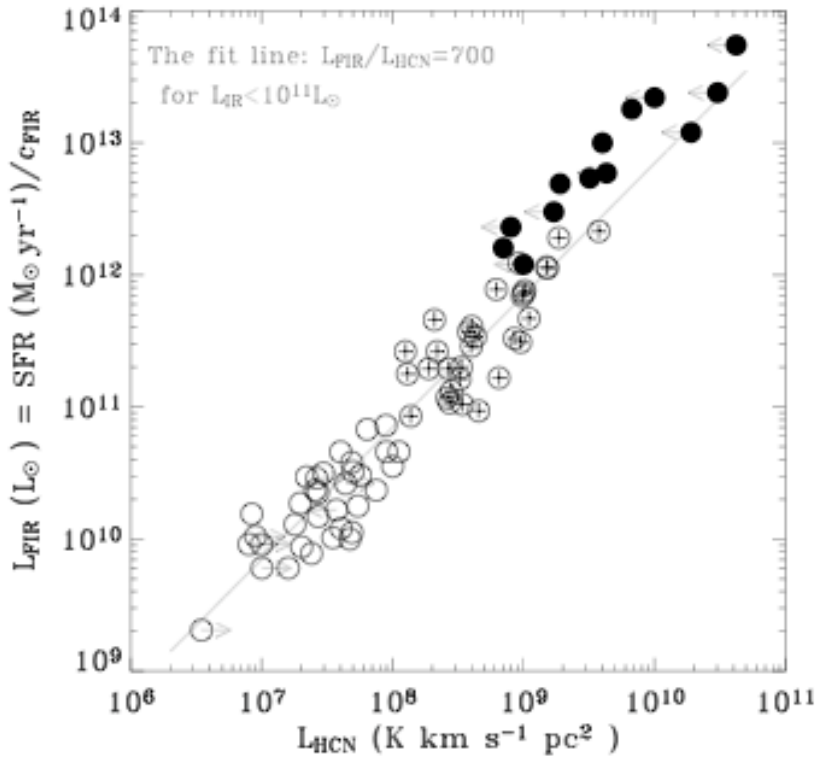

Fig. 2.— The correlation between HCN and FIR luminosities in 78 galaxies and QSOs. Limits in HCN luminosities are indicated with arrows. The high-z H/ULIGs are in solid circles and local U/LIGs with crosses. The line is the fit to the local "normal" galaxies ($L_{IR}< 10^{11}L_\odot$) with a slope fixed at unity. For entire local sample of 65 galaxies, the fit is $\log L_{FIR}=0.98\log L_{HCN}+3.0$.

Summary High-z HCN Results:

5 detections

7 upper limits

Apparent deviation from best fit of L(IR) vs. L(HCN) for low-z sources.

But, nearly all the points represent quasars. What is the correction for IR from AGN?

[Gao, et al. ApJ 660, L93 (2007)]

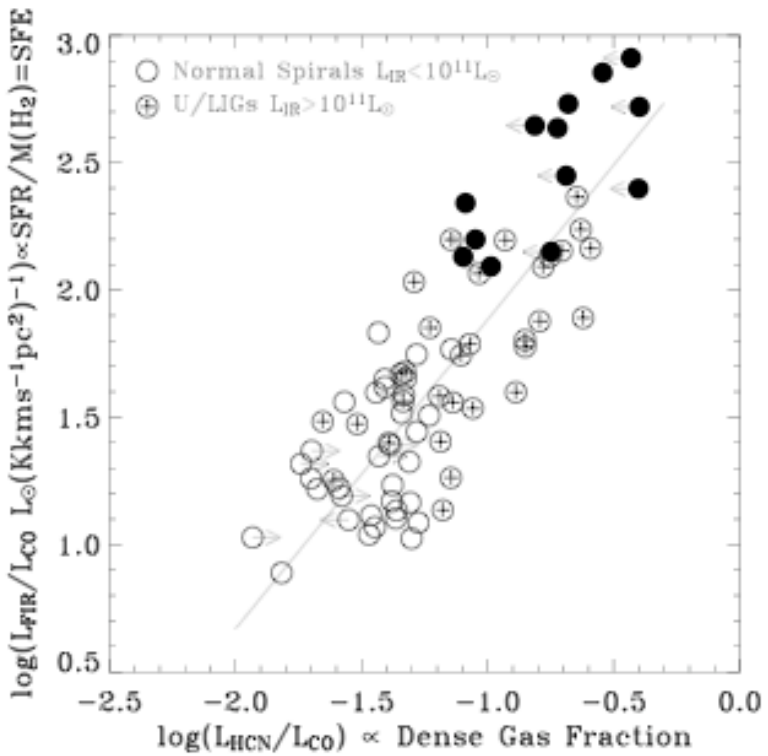

Fig. 3.— Correlation between $L_{\rm HCN}/L_{\rm CO}$ and $L_{\rm FIR}/L_{\rm CO}$ revealing the physical relationship between the HCN and FIR since both luminosities are normalized by $L'_{\rm CO}$, removing the dependence on distance and galaxy size. The line is the best fit for the local sample of GS04a. The high-z EMGs (solid circles) show some FIR/CO excess.

Normalize to L′(CO) to remove dependence on distance and galaxy size - deviation remains.

Theoretical Modeling of L(FIR) vs. L′(CO) and L′(HCN)

- Krumholz & Thompson [arXiv:0704.0792v2] have modeled Kennicutt-Schmidt Laws and reproduce the observed L(FIR) - L′(CO) and L(FIR) - L′(HCN) correlations;
- K & T predict that L(FIR) - L′(HCN) will deviate from linear for the high-z objects, as we are beginning to see.
- They also modeled HCO^+, which is intermediate to CO and HCN in its behavior as a tracer of SF.
- They conclude that the data are consistent with a *constant* SF efficiency.

K & T Model

Fractional contribution to luminosity (solid) and mass (dotted) vs. density

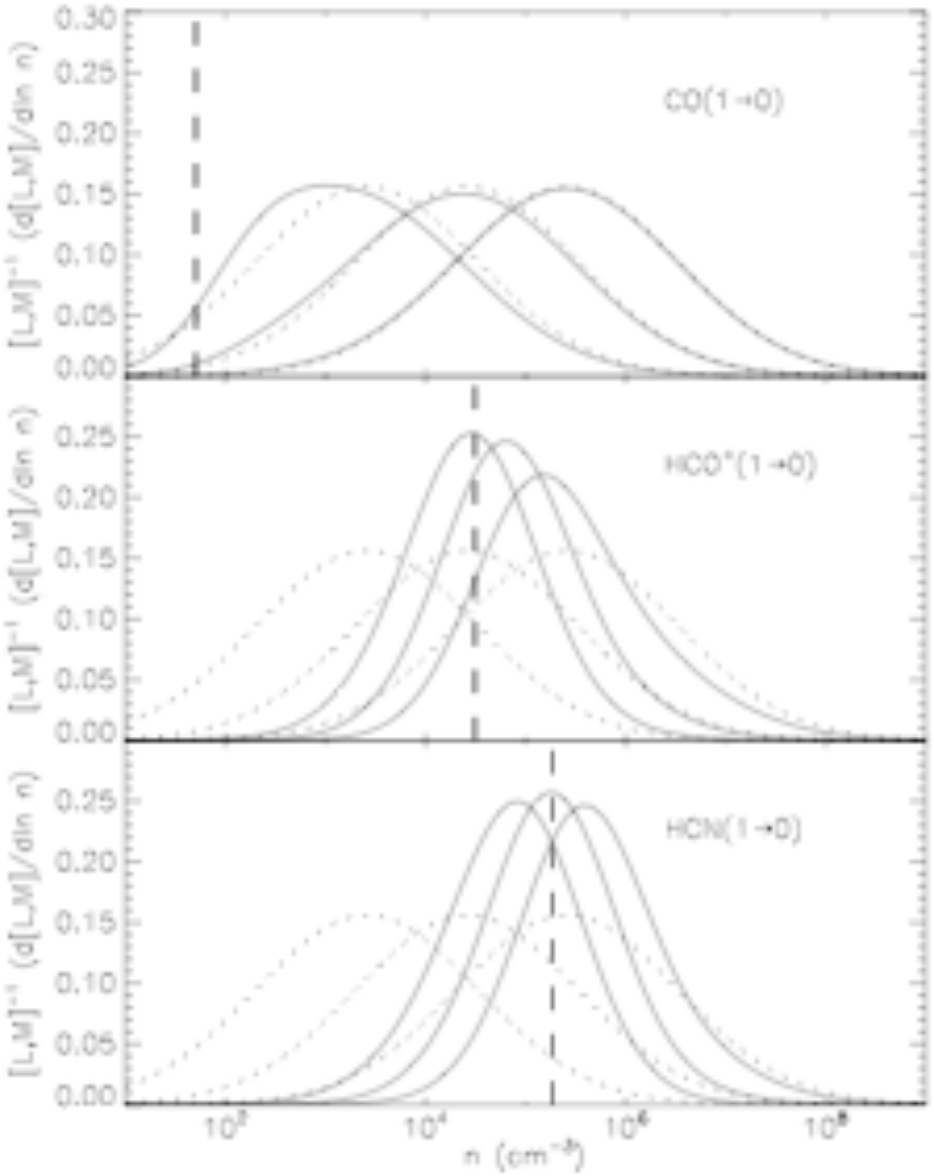

SF efficiecncy vs. mean density

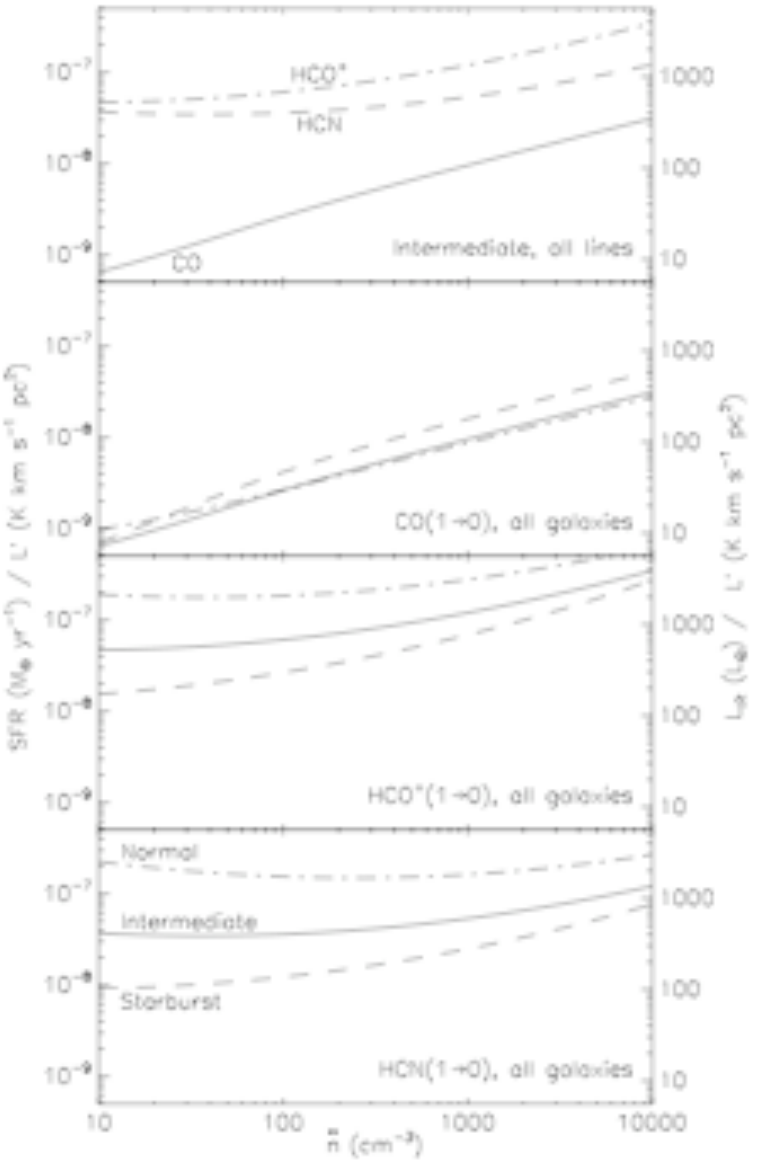

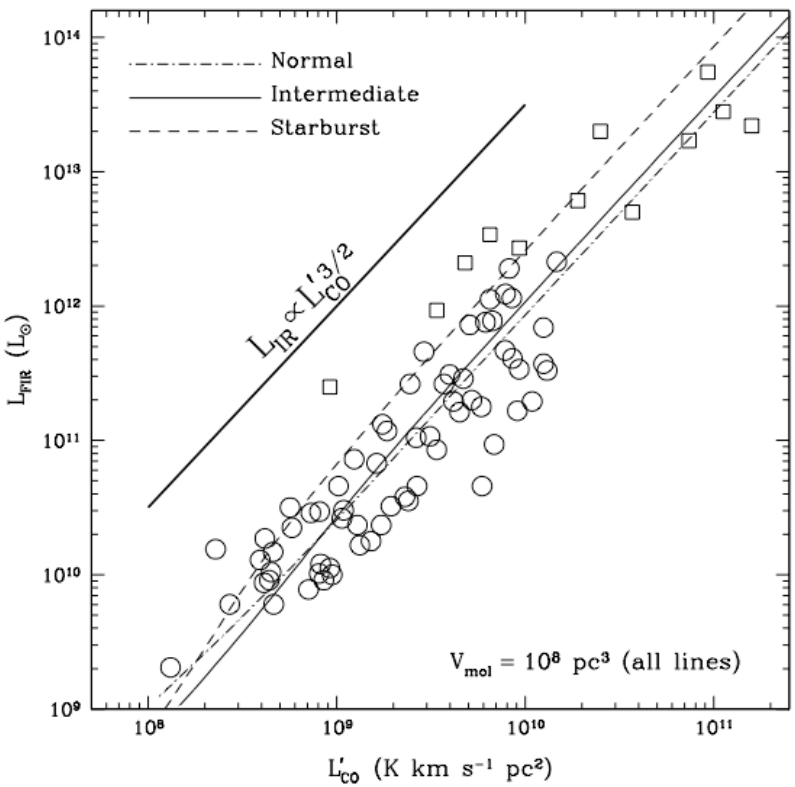

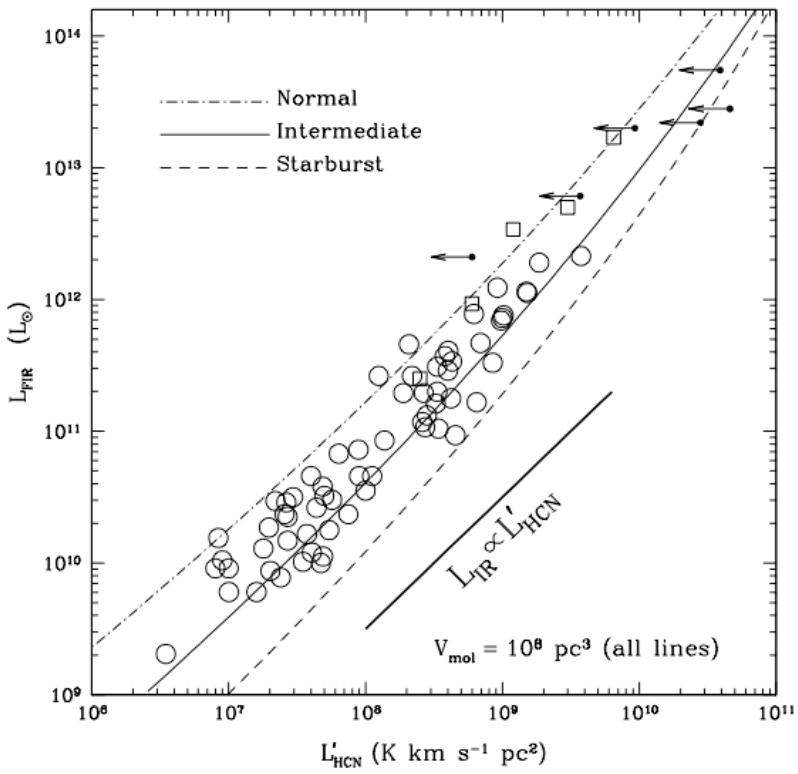

Results for L(FIR) vs. L′(CO) for source volume of 10^8 pc^3 and three types of galaxies.

The observed behavior of L(FIR) wrt L′(CO) is predicted by the model.

The linear relation of L(FIR) vs. L′(HCN) for normal spirals is confirmed but predicted to deviate from linearity for extreme starbursts.

HCO+ is also modeled, as an intermediate case between CO and HCO+.

Forbidden Carbon Lines: [CI] & [CII]

Cloverleaf

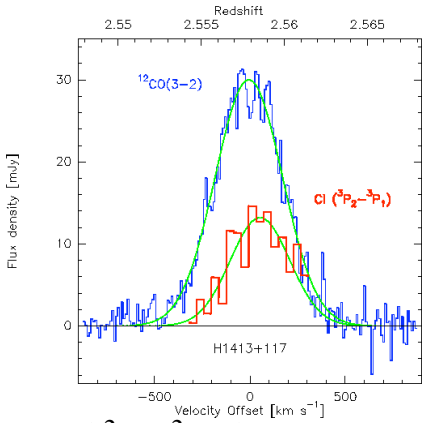

CI ($^3P_2$-$^3P_1$)
PdBI

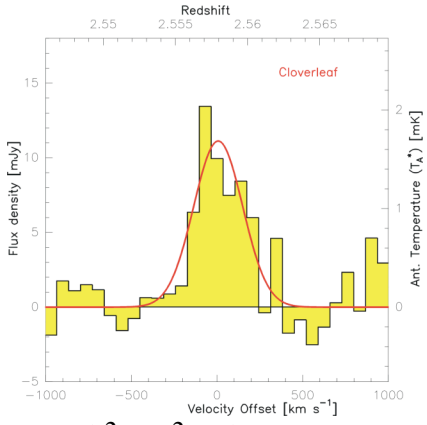

CI ($^3P_1$-$^3P_0$)
30m

F10214

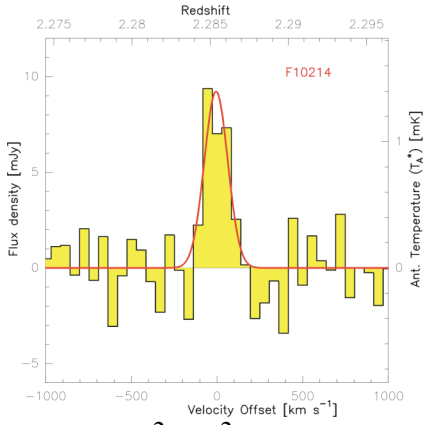

CI ($^3P_1$-$^3P_0$)
30m

SMM J14011

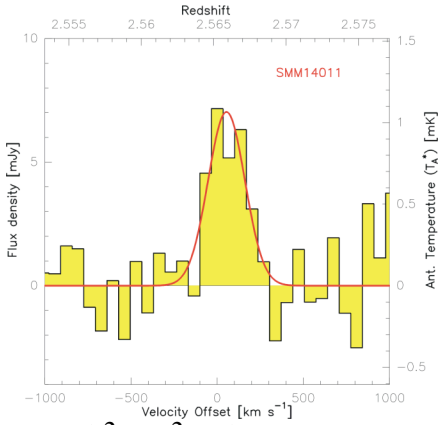

CI ($^3P_1$-$^3P_0$)
30m

$L'_{CI(21)} / L'_{CI(10)} = 0.5$, $T_{ex} = 30$ K

Weiss, et al. [A&A 429, L25 (2005)]

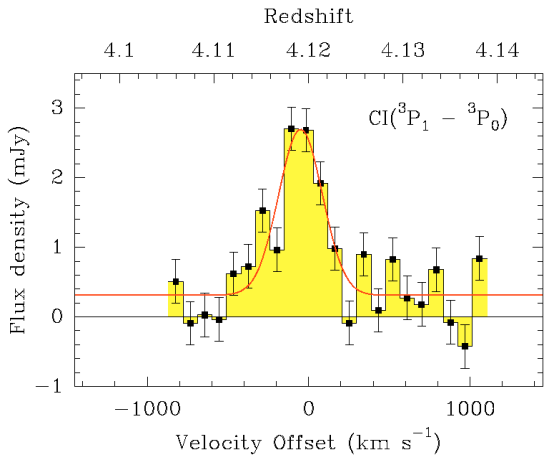

PSS2322:
CI (1-0)
IRAM PdBI

Pety et al. [A&A 428, L21 (2004)]

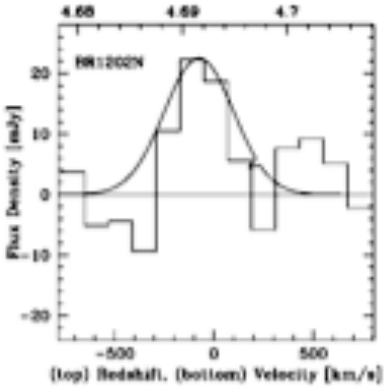

BR1202: CII line

Iono et al. [ApJ 645, L97 (2006)]

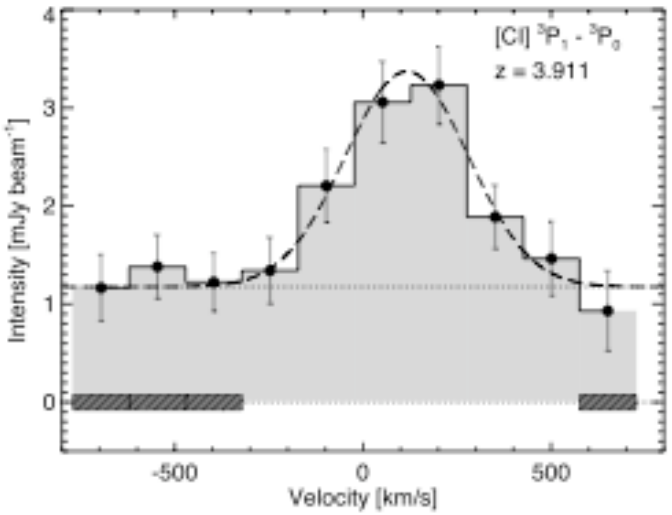

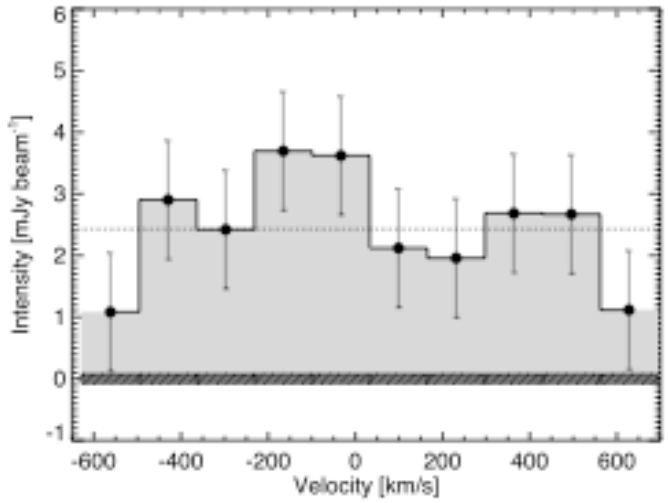

FIG. 2.—Spectra of [C I] $^3P_1$–$^3P_0$ (*top*) and H_2O 1_{10}–1_{01} (*bottom*) at the position of peak continuum intensity. Dotted lines show the fitted continuum levels, calculated from the intensity in the channels marked by the hatched regions. The dashed line shows a Gaussian fit to the [C I] $^3P_1$–$^3P_0$ emission.

[CI] in APM08279 (z = 3.91)

- $L'(CI) = 3.1 \times 10^{10}\ L_\odot$
- $M(CI) = 4.4 m^{-1} \times 10^7\ M_\odot$
- no H_2O is detected.

Wagg et al. [ApJ 651, 46 (2006)]

Carbon Lines in SDSS J1148+5251

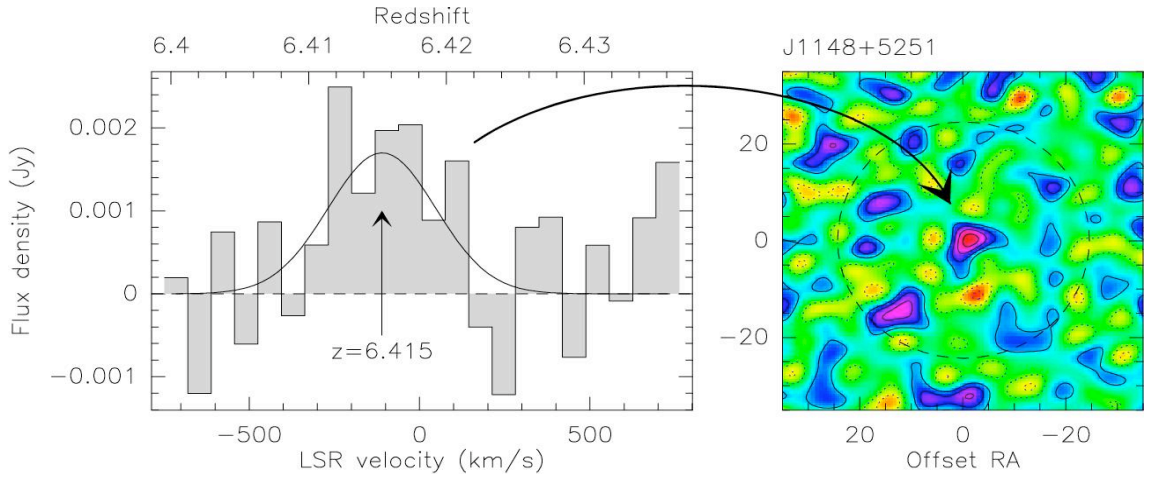

[CI] (809 GHz)
[Bertoldi et al. 2005]

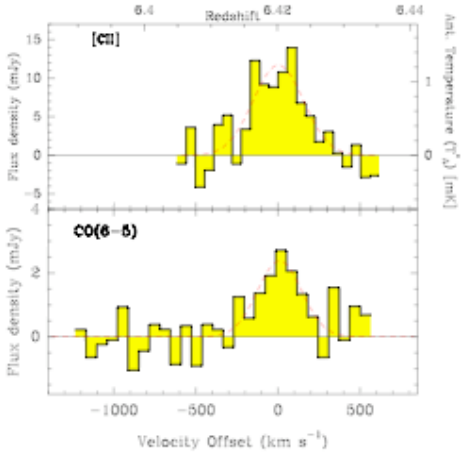

[CII] (1902 GHz)

Maiolino et al. [A&A 440, L51 (2005)]

[CI] Analysis

- [CI] $^3P_1$ - $^3P_0$ 492.160 GHz and [CI] $^3P_2$ - $^3P_1$ 809.342 GHz are readily accessible lines in high redshift galaxies;
- The critical densities for CO(1-0), [CI](1-0), and [CI](2-1) are roughly the same, suggesting a common emitting region;
- $M(CI) = 0.911 \times 10^{-4}\, Q(T_{ex}) \exp(62.5/T_{ex}) L'[CI(2\text{-}1)]$,

  $M(CI) = 1.902 \times 10^{-4}\, Q(T_{ex}) \exp(23.6/T_{ex}) L'[CI(1\text{-}0)]$,

  where, $Q(Tex) = 1 + 3\exp(-23.6/T_{ex}) + 5\exp(-62.5/T_{ex})$;
- In ULIRGs, the inferred masses of molecular gas from [CI] and CO agree if $X(CI) = 3 \times 10^{-5}$ (value in M82) and $\alpha = 0.8$, suggesting common emission region;
- [CI] in four high-z galaxies, implying $X(CI) \sim 3 \times 10^{-5}$ if CO is used to calculate M(gas) with $\alpha = 0.8$.

[CII] in EMGs

- [CII] ($^2P_{3/2}$- $^2P_{1/2}$) falls at 157.74μm = 1901.86 GHz, and can be observed with present instruments for high-z;
- The line has been used extensively to study PDRs and is the dominant coolant for IS gas;
- It has been hard to detect at high-z, suggesting a similarity between EMGs and ULIRGs, where the line is also weaker compared to CO (0.04%) than in the Galaxy;
- In J1148, a model implies SFR ~ 6.5×10^{-7} $L_{[CII]}(L_\odot)$, yielding an SFR ~ 3000 $M_\odot$ / year;
- Nagamine et al. [ApJ 647, 60 (2006)] make predictions of [CII] detectability for ALMA and SPICA.

Sizes of EMGs

- Limited information (need ALMA) but the sizes appear to be similar to ULIRGs with CO disk diameters of 1 - 4 kpc;
- SMM J02399 is claimed to be barely resolved with a diameter of 16 kpc;
- Inferred dynamical masses range from $M_{dyn}\sin^2 i$ = 0.5 - 40 x 10^{10} $M_\odot$, all greater than M(gas).
- More information on SMGs - a total of 15 have been imaged with the PdB - mean radius of ~ 2 kpc, M_{dyn} ~ 10^{11}, M_{gas} ~ 3x10^{10}, and Δv ~ 400 km/s;
- Similar to W49 or W51, but on a huge scale!

Tacconi et al. ApJ 640, 228 (2006); Greve et al. MNRAS 359, 1165 (2005); Solomon & Vanden Bout ARAA 43, 677 (2005).

Summary of EMG Properties

- $L'(CO) = 0.5\text{-}20 \times 10^{10}$ K km/s pc^2;
- $L(FIR) = 10^{12}\text{-}10^{14}\ L_\odot$

  $\Rightarrow$ SFR = 100 - 10000 $M_\odot$/year;
- Star formation efficiency,

  $L(FIR)/\ L'(CO) = 100\text{-}3000$

  $\Rightarrow$ star formation lifetime = 2-100 My;
- $M(gas) = 1 - 100 \times 10^9\ M_\odot$.

Overall Conclusion Regarding EMGs

The EMGs are similar to ULIRGs but with larger basic parameters.

There is evidence suggesting the EMGs could be mergers of ULIRGs.

Requirements for Future Studies of EMGs

- angular resolution, to measure sizes;
- sensitivity, to image unlensed population and increase sample size;
- bandwidth, to enable blind surveys;

- Atacama Large Millimeter Array (ALMA)

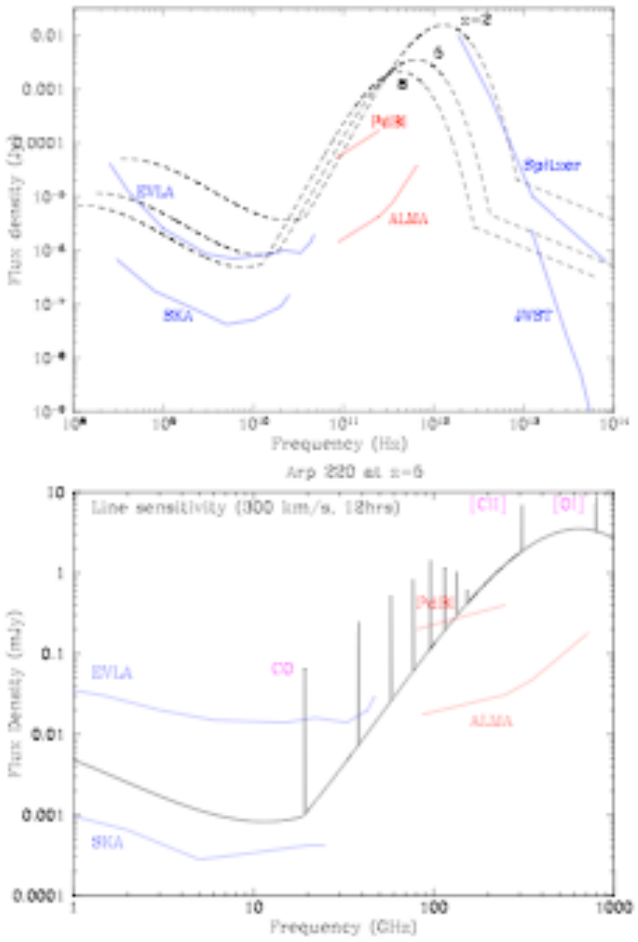

Fig. 5 Top: Continuum spectrum of an active star forming galaxy with a star formation rate ~ 100 $M_\odot$ year^{-1}, at $z = 2, 5,$ and 8. The curves show the continuum sensitivities of various telescopes in 12hours. Bottom: Line spectrum of the same galaxy, but only at $z = 5$. The line sensitivities were derived assuming a line width of 300 km s^{-1}.

Prospects at high-z for ALMA & other facilities:

A plot of sensitivity and expected continuum + lines vs. frequency from an active star-forming galaxy at z = 2, 5, 8 with a SFR of 100 $M_\odot$ / year.

Carilli, Walter, et al. [astro-ph/0703799]

Hubble Deep Field -
rich in nearby galaxies, but poor in distant galaxies

Source: K. Lanzetta, SUNY-SB

Nearby galaxies in HDF

Distant galaxies in HDF

ALMA Deep Field (ADF) -
poor in nearby galaxies, but rich in distant galaxies

Source: Wootten and Gallimore, NRAO

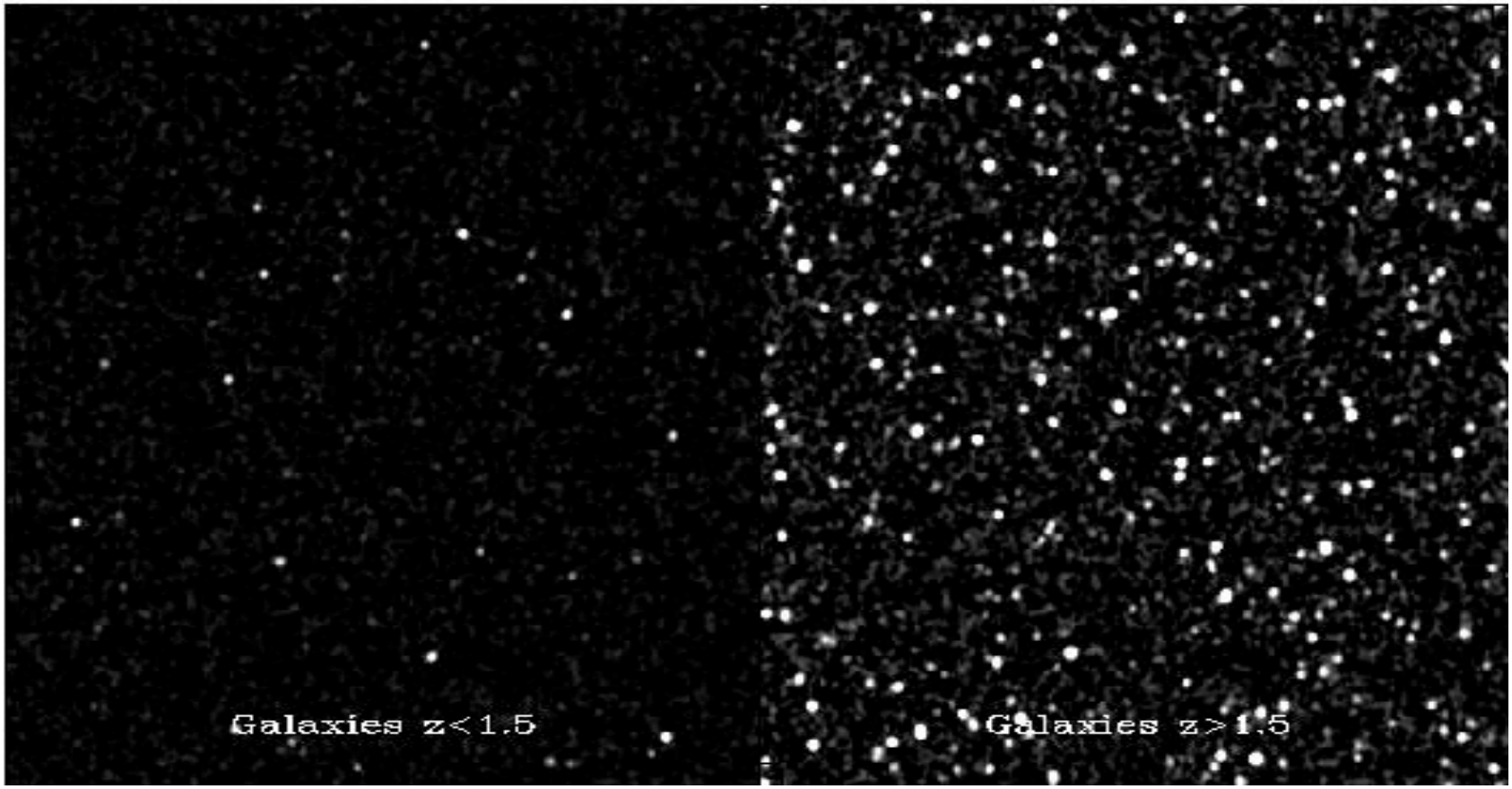

Nearby galaxies in ADF

Distant galaxies in ADF

Detecting normal galaxies at z = 3

- CO emission now detected in 40 z>2 objects, out to z=6.4. [C II] only at z=6.4 (right)
- To date only in luminous AGN and/or gravitationally lensed. Normal galaxies are 20 to 30 times fainter.
- Current millimeter interferometers have collecting areas between 500 and 1000 m^2.

[C II]

[CO]

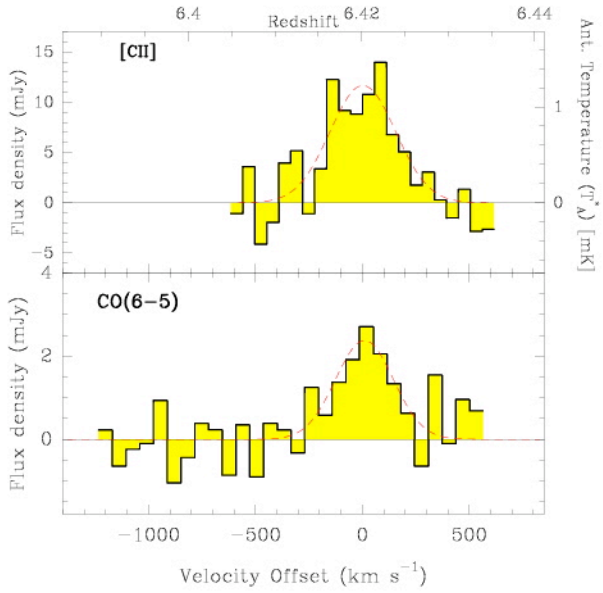

Bandwidth Compression

An entire atmospheric transmission band can be recorded in *one* observation of J1148

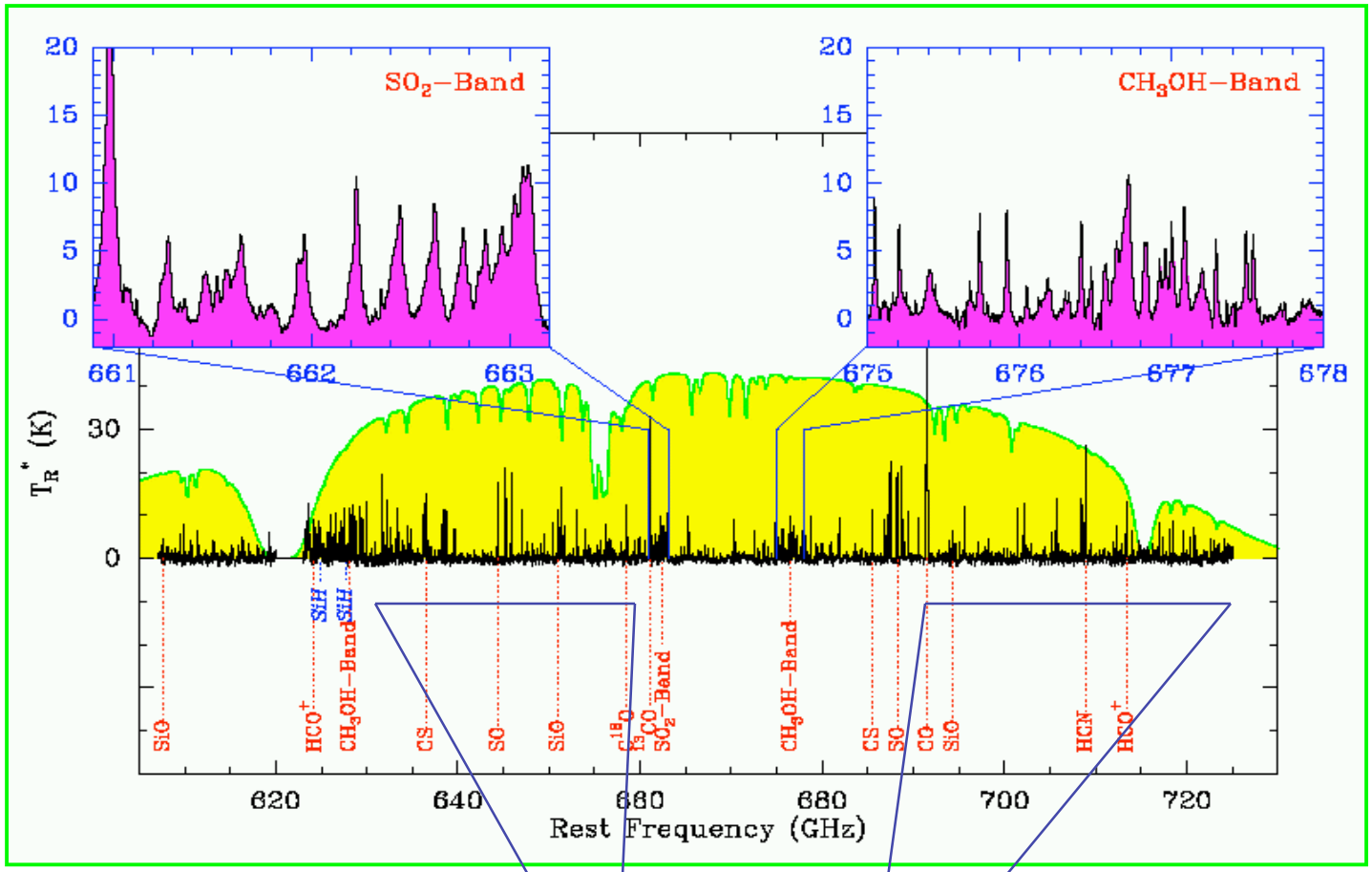

Schilke et al. (2000)

J1148+5251: an EoR ALMA Paradigm

Wrong declination! But…

High sensitivity (12hr 1σ 0.2mJy)

Wide bandwidth (2 x 4 GHz IF)

Top: USB, 94.8 GHz
- CO 6-5
- HCN 8-7
- HCO+ 8-7
- H2CO lines

Lower: LSB, 86.8 GHz
- HNC 7-6
- H2CO lines
- $C^{18}O$ 6-5
- H_2O 658GHz maser?

ALMA could observe CO-luminous galaxies (e.g. M51) at z~6.

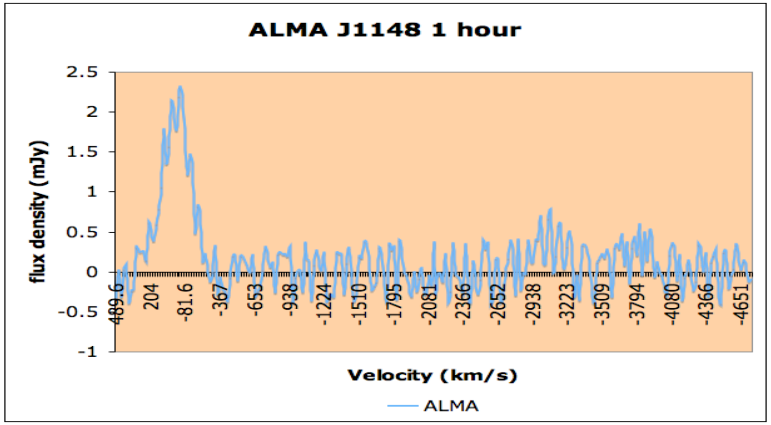

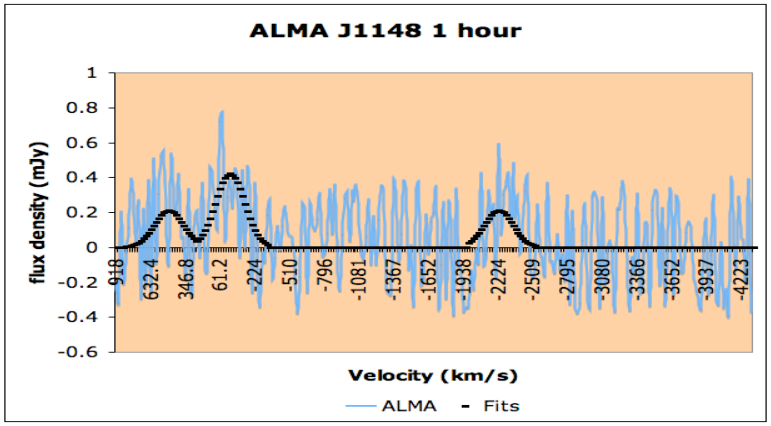

ALMA into the EoR

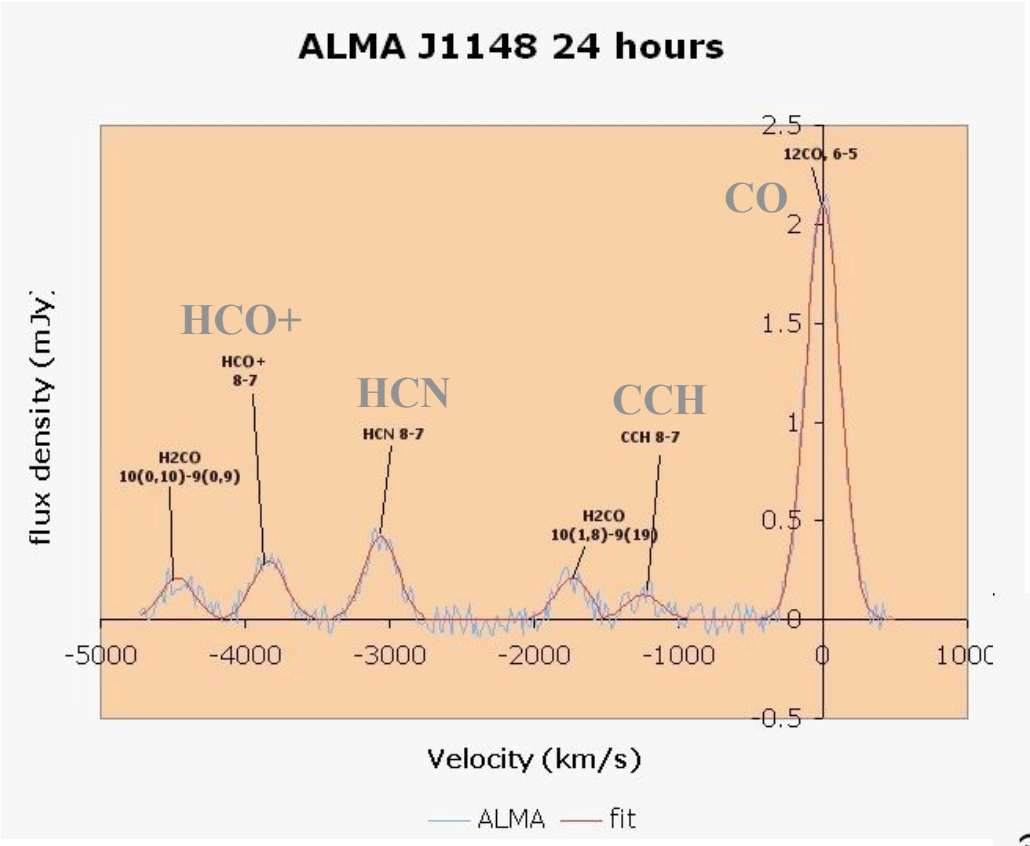

Spectral simulation of J1148+5251

Detect dust emission in **1sec** (5σ) at 250 GHz

Detect multiple lines, molecules per band => detailed astrochemistry

Image dust and gas at sub-kpc resolution – gas dynamics! CO map at 0".15 resolution in 1.5 hours

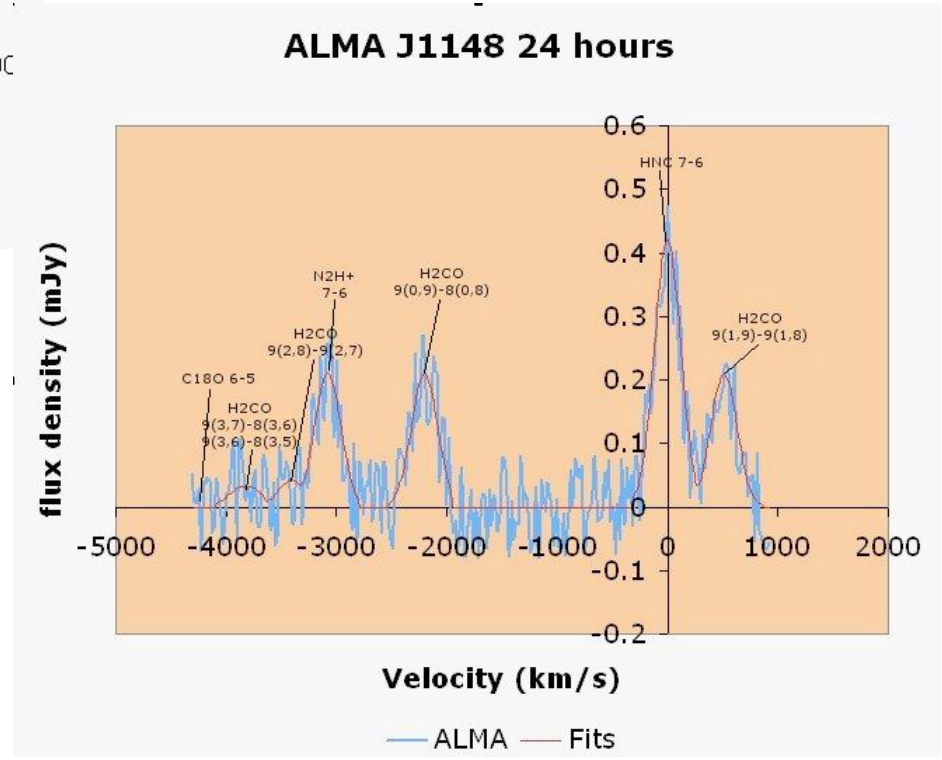

Atomic line diagnostics
[C II] emission in **60sec** (10σ) at 256 GHz
[O I] 63 μm at 641 GHz
[O I] 145 μm at 277 GHz
[O III] 88 μm at 457 GHz
[N II] 122 μm at 332 GHz
[N II] 205 μm at 197 GHz
HD 112 μm at 361 GHz

In the Meantime . . .

The most useful thing to do while waiting for ALMA is to make detailed studies of ULIRGs with the existing facilities, IRAM, CARMA, the SMA, and the ATNF, and construct models to serve as a basis for understanding higher-z galaxies. (Details are important, for example, the right value for α in high-z galaxies!)

CARMA

Recent Results: The Dense Gas in the Central Kiloparsec of NGC 6946.
Levine et al. [arXiv:0710.0168]

Sub-Millimeter Array

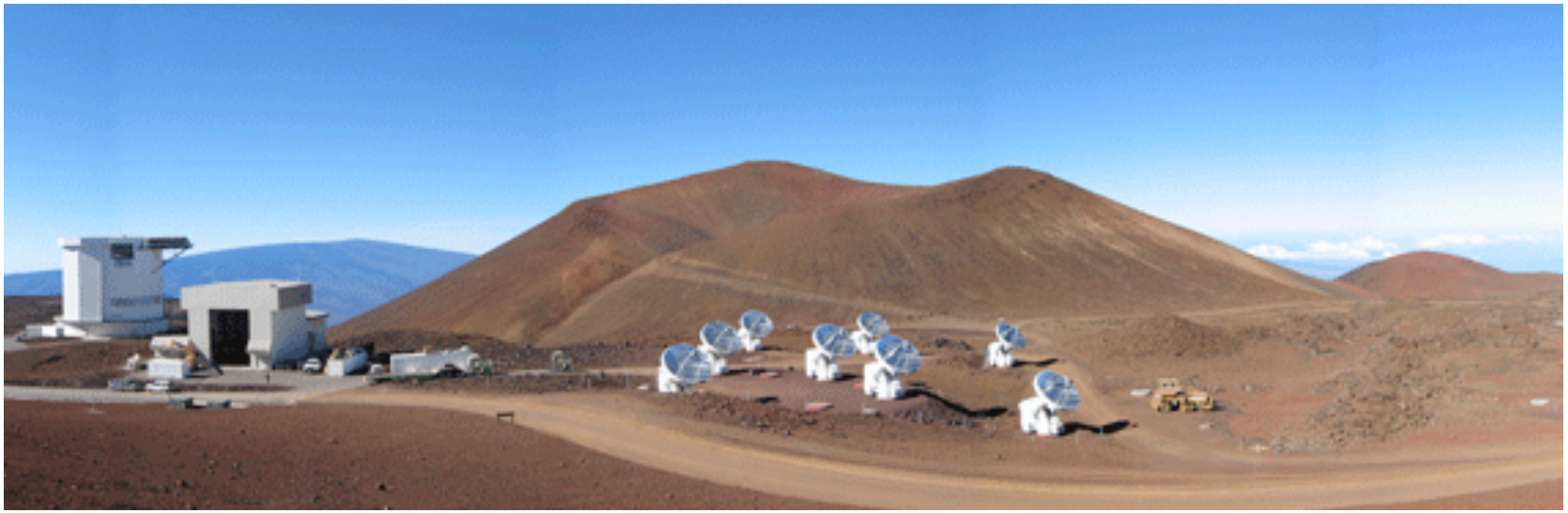

D. Iono, et al. *High Resolution Imaging of Warm and Dense Molecular Gas in the Nuclear Region of the Luminous Infrared Galaxy NGC6240* [ApJ, 659, 283 (2007), astro-ph/0701123]

J. D. Younger, et al. *Evidence for a Population of High-Redshift Submillimeter Galaxies from Interferometric Imaging* [accepted to ApJ, (arXiv:0708.1020)]

APEX - The Atacama Pathfinder Experiment

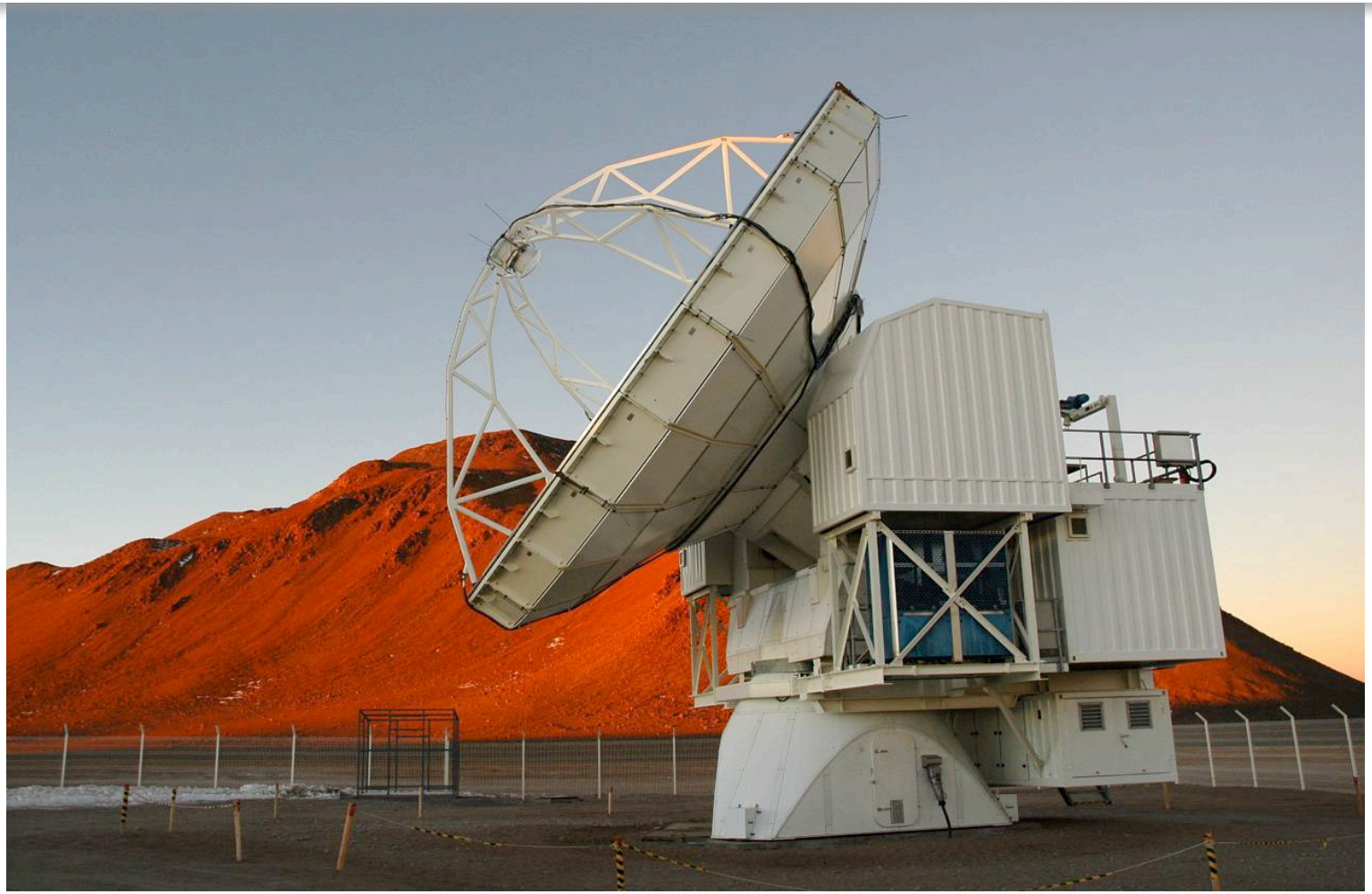

Instrument to watch for high-z studies: LABOCA is a 295-channel bolometer array operating in the 870 μm (345 GHz) atmospheric window. The angular resolution is 18.6″ (HPBW), the total field of view is 11.4, with a channel separation of about 36″ .

ATNF leap in technology: Mopra

- New 3mm, 12mm, (7mm) Rx
- Noise diode
- New spectrometer: 8GHz(!) MOPS
- New observing software
- On-the-fly mapping capability
- Better scheduling

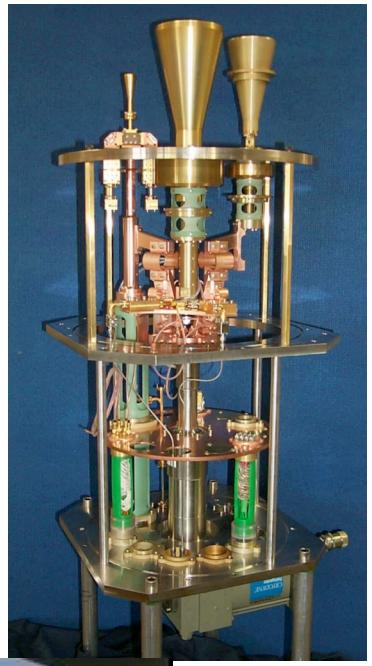

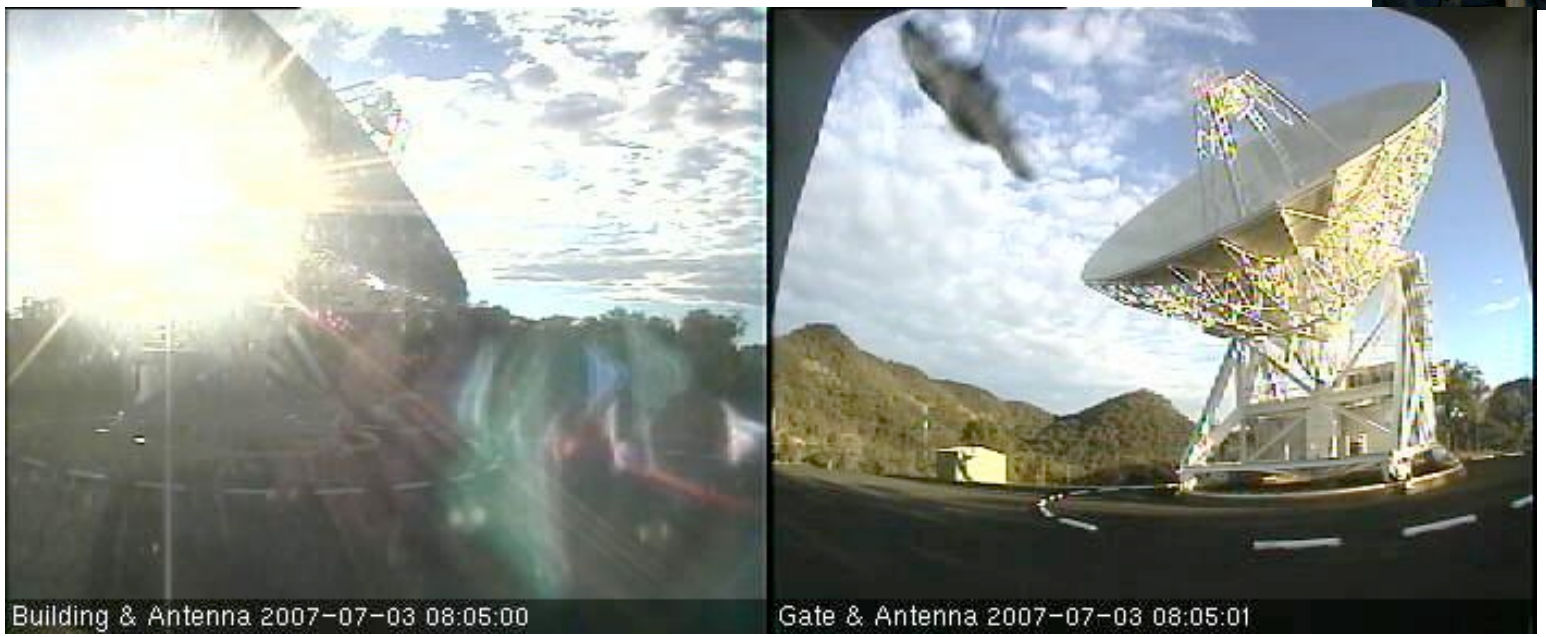

ATNF leap in technology: ATCA

- 12mm & 3mm Rx, 7mm
- Dish upgrades (outer rim)
- Track upgrades (north spur)
- additional filters
- Phase monitor
- new correlator (CABB; next season): 4GHz BW
- 115GHz upgrade?

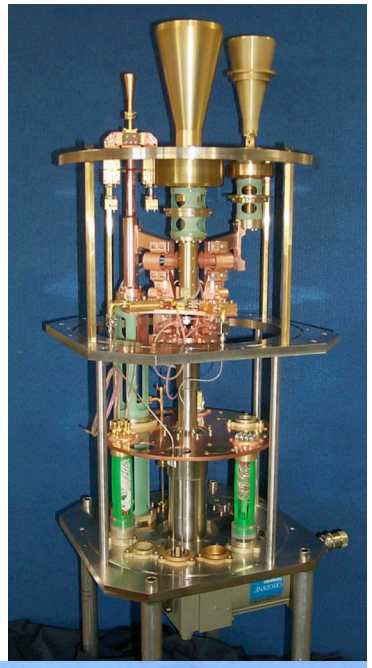

EVLA

The EVLA is the most important major facility after ALMA for radio studies of ($z > 5$) galaxies.

(The high-J CO lines are not excited and the low-J lines are shifted to cm wavelengths.)

EVLA = 10 x VLA for continuum observations; up to 8 GHz instantaneous bandwidth per polarization for spectral line observations, with new receivers covering 1 - 50 GHz.

Someday, near the ALMA site - CCAT?

ALMA Requirements

- High Fidelity Imaging
- Precise Imaging at 0.1” Resolution
- Routine Sub-mJy Continuum Sensitivity
- Routine mK Spectral Sensitivity
- Wideband Frequency Coverage
- Wide Field Imaging Mosaicking
- Submillimeter Receiver System
- Full Polarization Capability
- System Flexibility

Technical Specifications

- 50 12-m antennas, at 5000 m altitude site
- Surface accuracy ±25 μm, 0.6” reference pointing in 9m/s wind, 2” absolute pointing all-sky
- Array configurations between 150m to ~15km
- 10 bands in 31-950 GHz + 183 GHz WVR. Initially:
  - 86-119 GHz Band 3
  - 211-275 GHz Band 6
  - 275-370 GHz Band 7
  - 602-720 GHz Band 9
- 8 GHz BW, dual polarization
- Interferometry, mosaicking & total-power observing
- Correlator: 4096 channels/IF (multi-IF), full Stokes
- Data rate: 6Mb/s average; peak 60Mb/s
- All data archived (raw + images), pipeline processing

ALMA + ACA →
Atacama Large
Millimeter/submillimeter Array

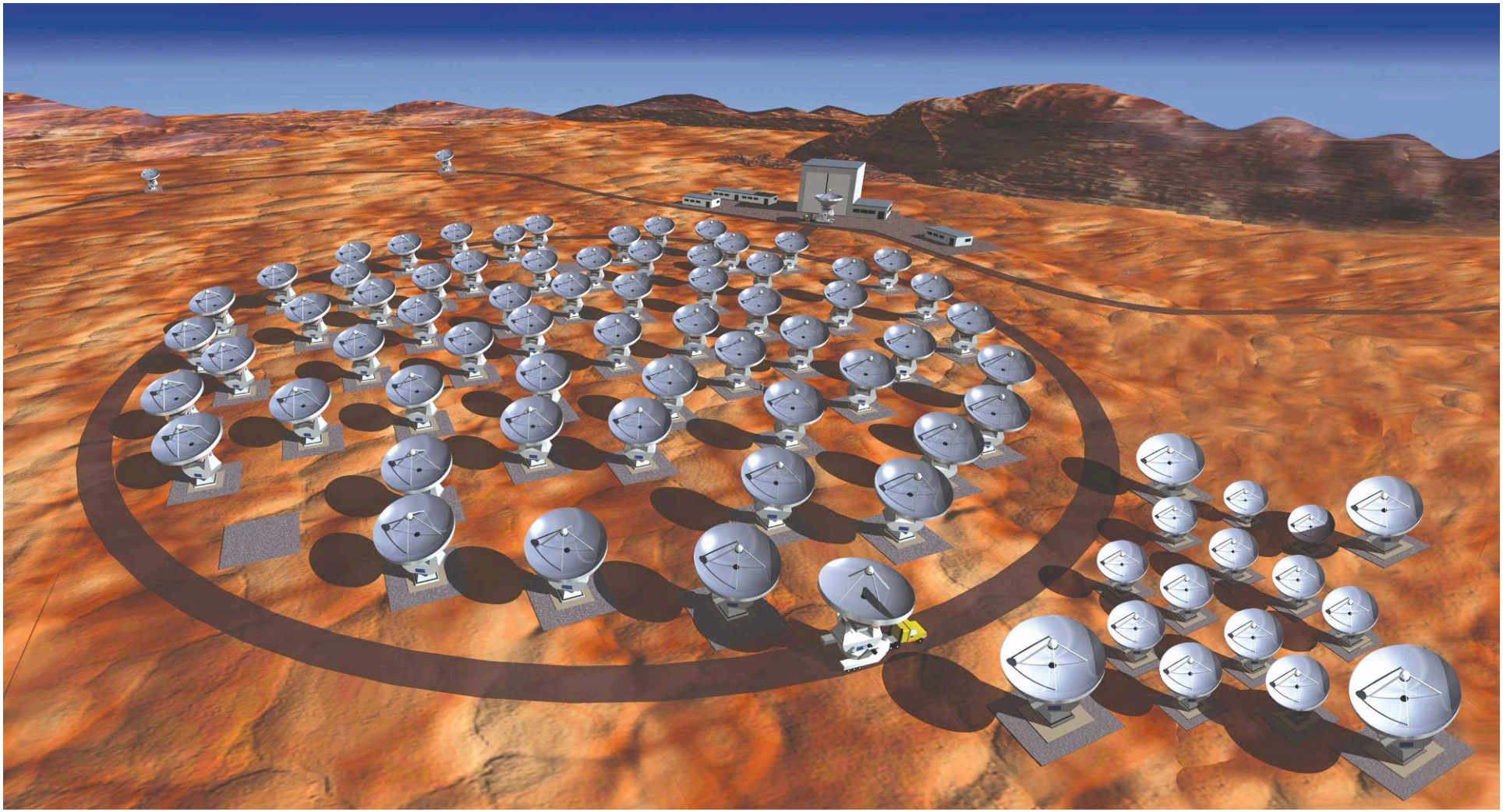

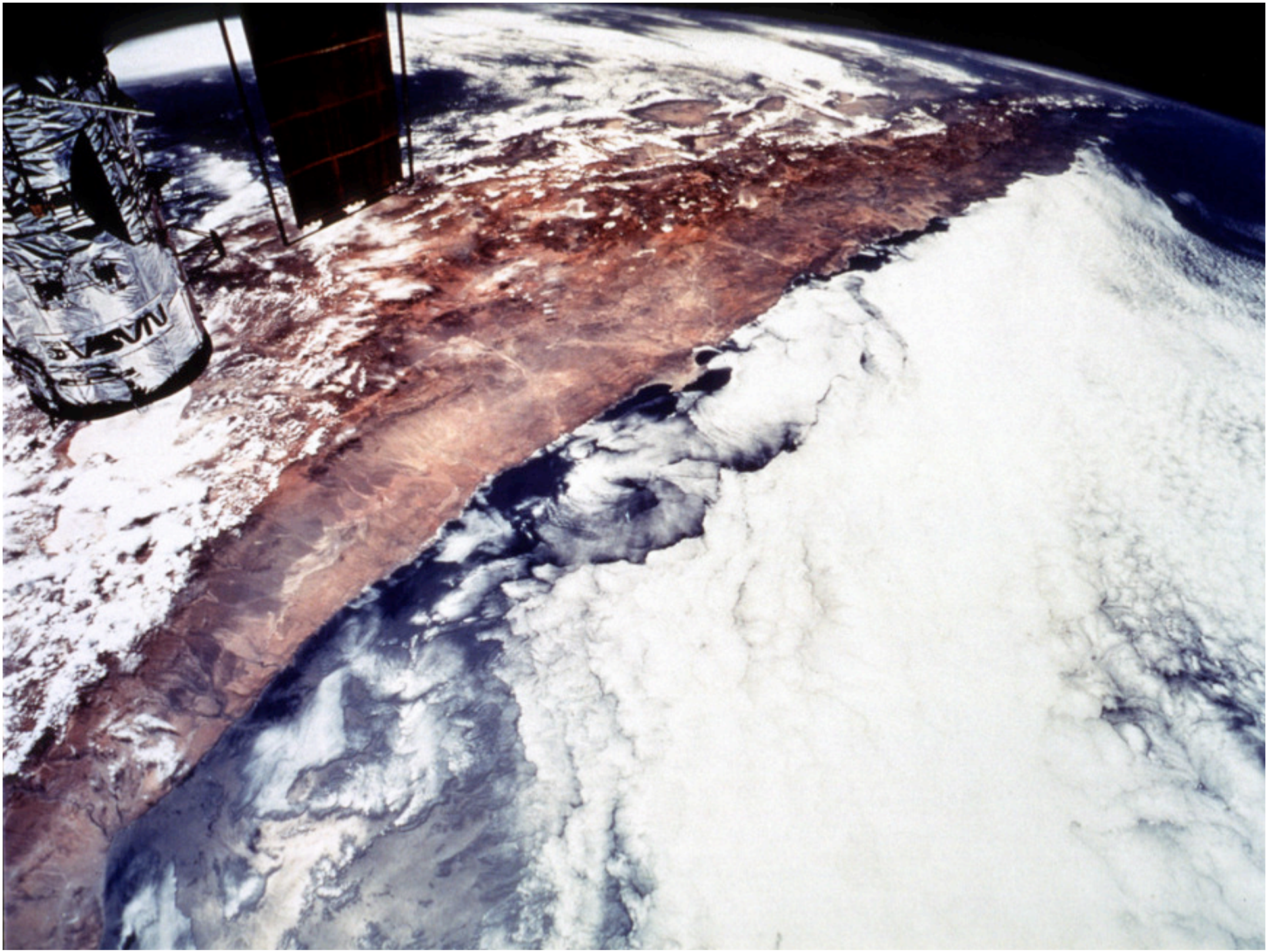

N
W
E
S
Image © 2006 NASA
Image © 2006 TerraMetrics
©2005 Google

San Pedro de Atacama,
Atacama Desert, Northern Chile

ALMA Sites
To AOS (43km)
OSF Site (15km)
PARE
60
PELIGRO

Operations Support Facility

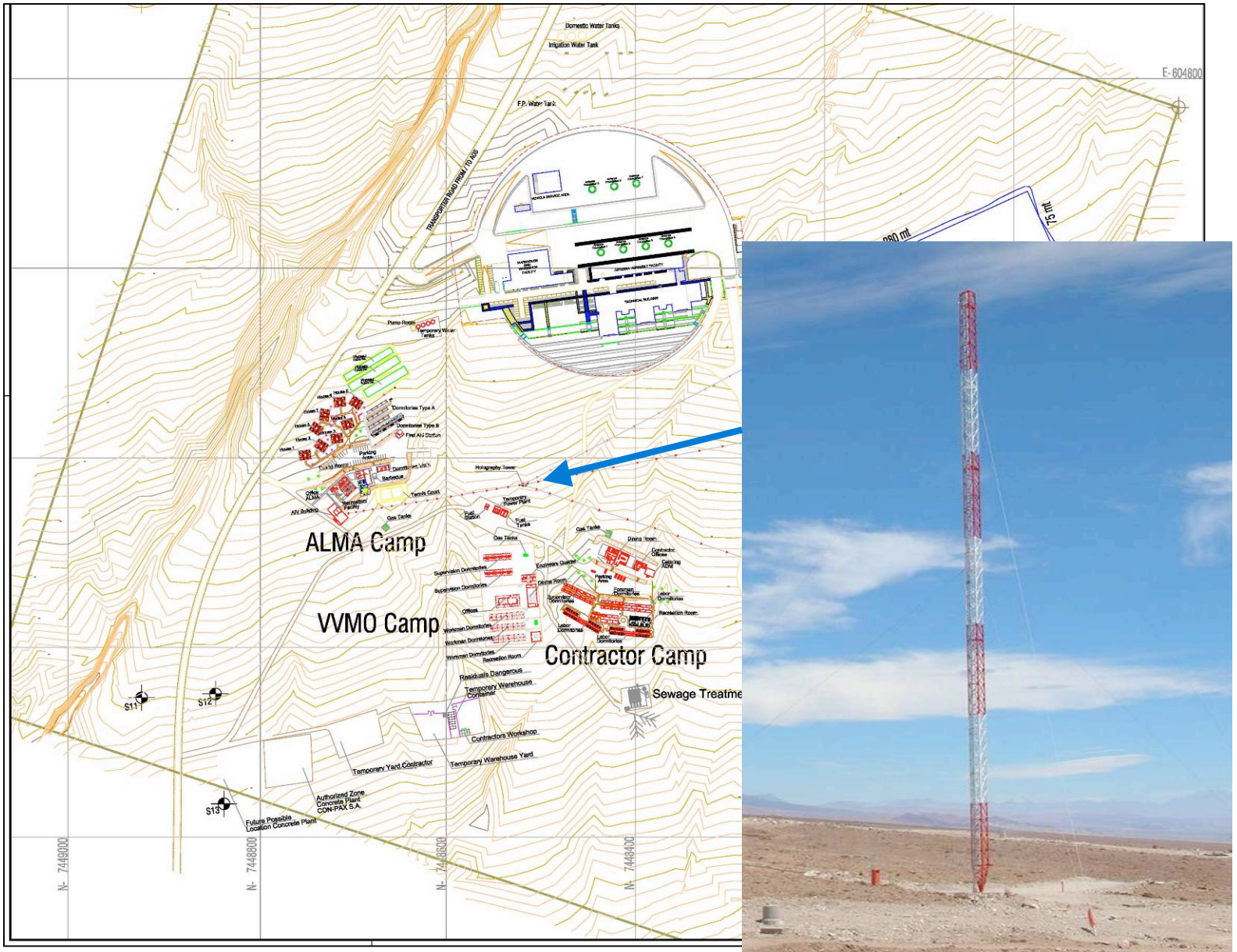

ALMA Offices

ALMA Camp

OSF Technical Facilities

AEM Contractor Area

MELCO Contractor Area

Vertex Contractor Area

Contractors Camp

Road: OSF-AOS: Transporter

Chajnantor Plateau – looking north

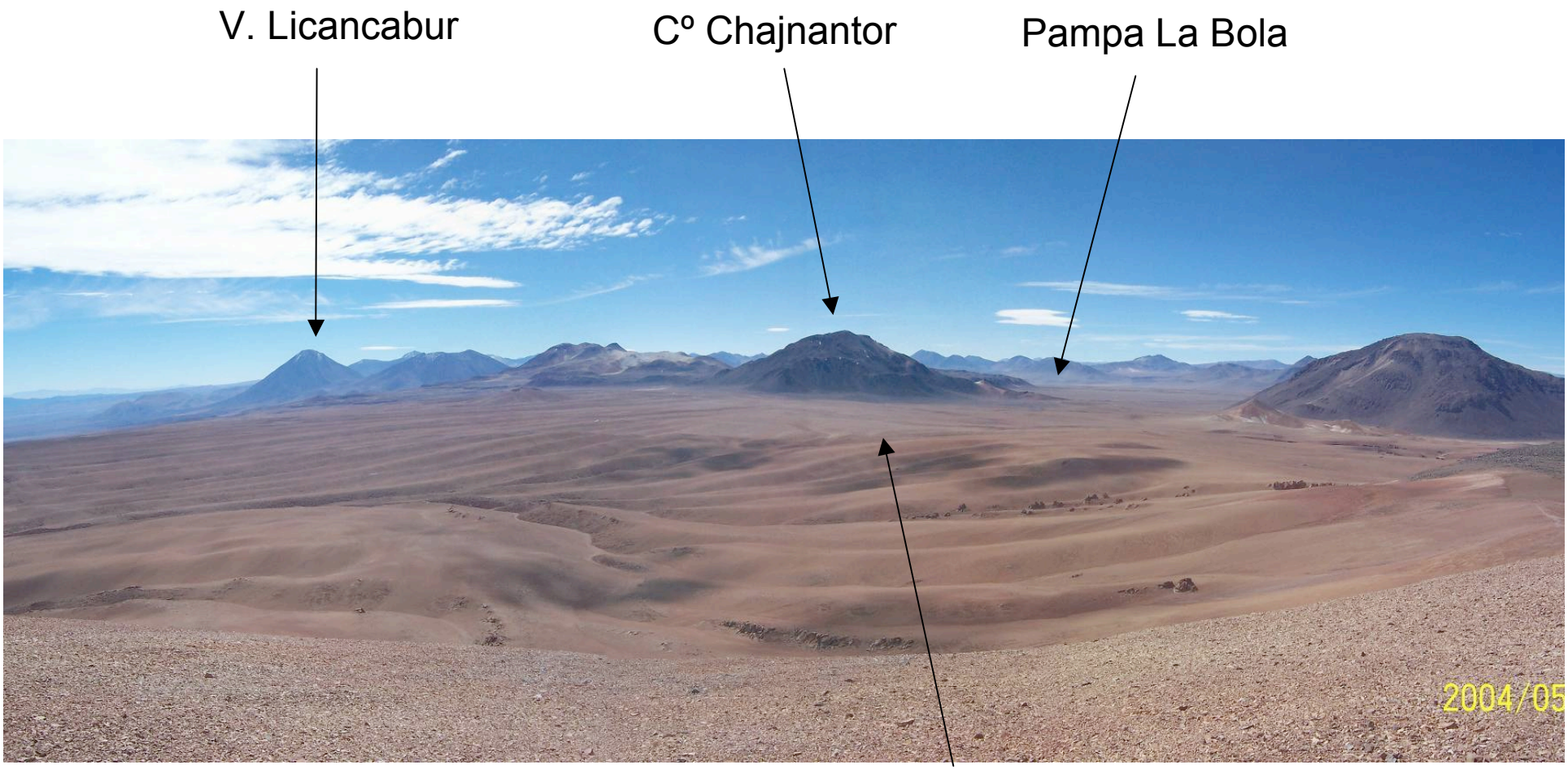

AOS Technical Building

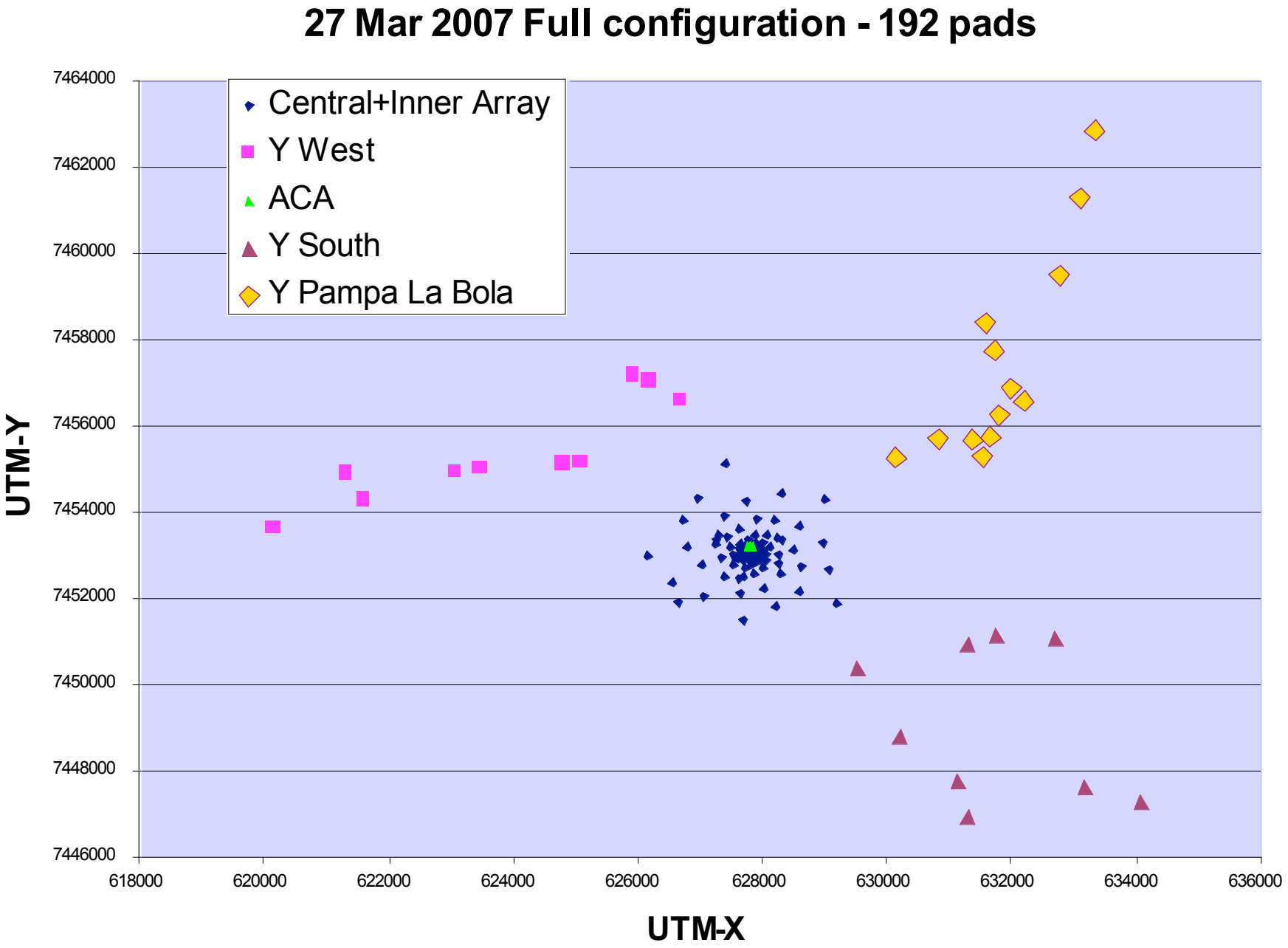
27 Mar 2007 Full configuration - 192 pads
Central+Inner Array
Y West
ACA
Y South
Y Pampa La Bola
UTM-Y
7464000
7462000
7460000
7458000
7456000
7454000
7452000
7450000
7448000
7446000
618000
620000
622000
624000
626000
628000
630000
632000
634000
636000
UTM-X

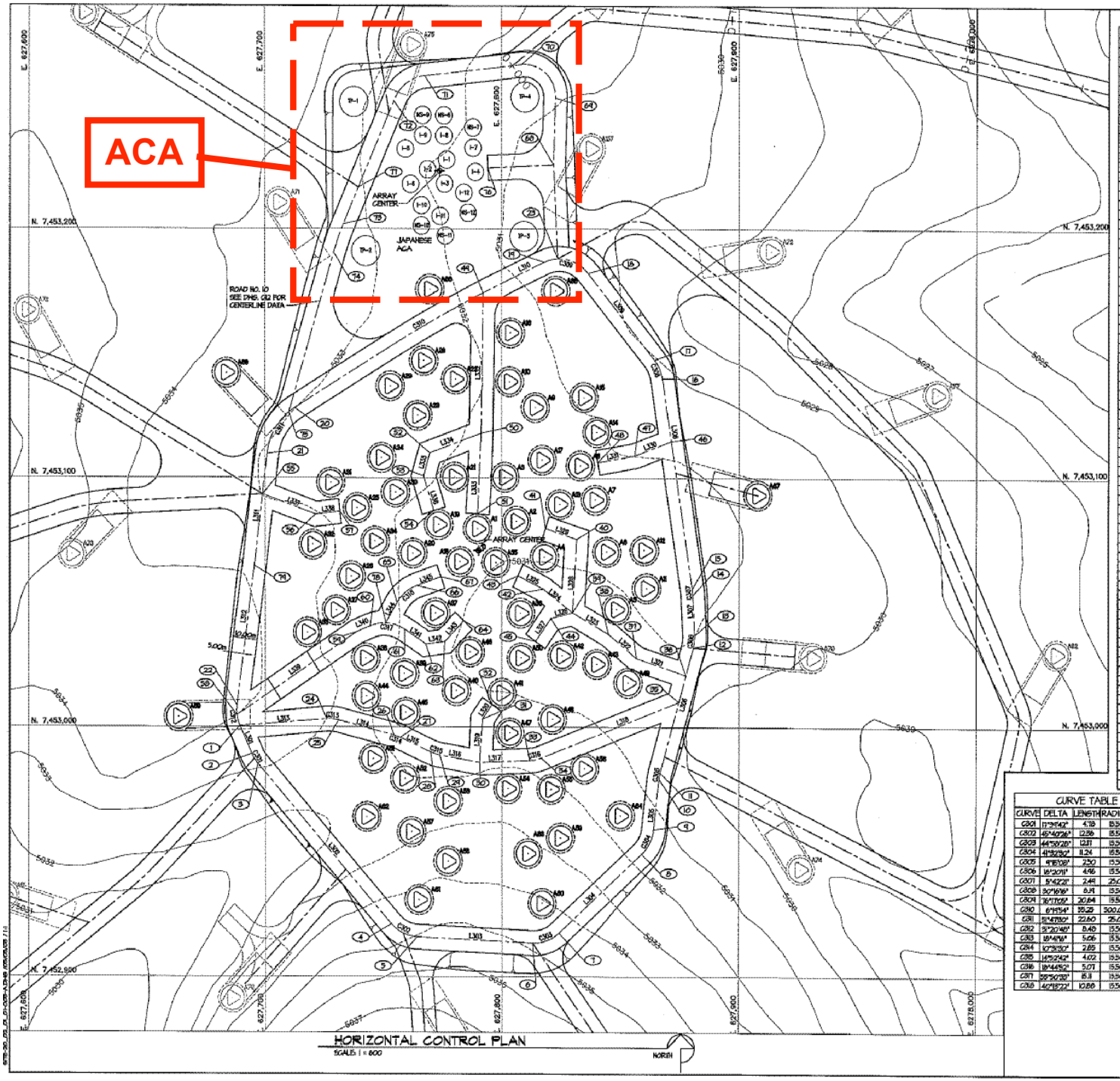

ROAD CENTERLINE DATA

NO.	NORTHING	EASTING	GRADE ELEVATION	ELEVATION	DELTA
1	7452000.48	627689.38	5088.62	5088.54	-0.08
2	7452484.13	627694.28	5088.28	5088.52	0.24
3	7452965.13	627696.85	5088.09	5088.44	0.41
4	7453263.16	627758.48	5094.36	5092.88	-1.78
5	7453485.45	627764.32	5096.04	5092.61	-2.35
6	7453813.55	627868.08	5084.86	5081.82	-3.04
7	7453871.55	627824.25	5084.40	5091.60	-2.80
8	7453944.20	627854.20	5091.96	5090.81	0.11
9	7454958.98	627864.20	5091.28	5090.78	0.50
10	7454974.31	627866.44	5090.62	5090.71	0.09
11	7454988.26	627866.92	5090.58	5090.70	0.13
12	7455028.24	627860.98	5090.66	5090.52	-0.26
13	7455071.05	627884.48	5091.00	5090.51	-0.48
14	7455053.21	627880.84	5091.00	5090.49	-0.51
15	7455095.86	627880.45	5091.00	5090.44	-0.51
16	7455140.00	627867.85	5090.14	5090.58	0.44
17	7455147.42	627864.50	5090.03	5090.66	0.65
18	7455182.25	627836.87	5090.34	5091.79	1.45
19	7455186.60	627858.02	5090.16	5091.42	1.26
20	7455211.98	627873.87	5091.01	5092.46	-0.58
21	7455309.68	627900.86	5093.00	5092.73	-0.27
22	7455308.72	627888.04	5094.00	5093.51	-0.48
23	7455368.24	627882.82	5090.82	5091.94	1.12
24	7455408.28	627826.24	5092.98	5092.86	-0.13
25	7455402.21	627834.25	5092.11	5092.11	0
26	7455396.80	627854.65	5091.40	5092.26	0.46
27	7455385.85	627857.35	5091.60	5092.34	0.44
28	7455390.00	627864.45	5091.88	5092.15	0.32
29	7455388.80	627873.36	5091.82	5092.08	0.36
30	7455385.88	627890.61	5091.88	5091.80	-0.08
31	7455402.28	627896.13	5091.86	5091.68	0.32
32	7455404.15	627898.88	5091.11	5091.51	0.40
33	7455386.54	627901.71	5091.86	5091.40	-0.46
34	7455418.88	627896.71	5091.79	5091.32	-0.43
35	7455400.21	627894.83	5090.33	5090.58	0.25
36	7455020.42	627871.81	5090.56	5090.55	-0.01
37	7455027.84	627857.02	5091.00	5090.64	-0.36
38	7455051.41	627845.26	5091.00	5090.68	-0.32
39	7455046.01	627830.08	5091.00	5090.80	-0.20
40	7455075.46	627828.11	5091.00	5090.80	-0.20
41	7455078.15	627828.61	5091.00	5090.48	-0.52
42	7455055.01	627811.68	5091.00	5090.81	-0.19
43	7455060.84	627800.27	5091.00	5091.12	0.12
44	7455043.80	627820.88	5091.00	5090.46	-0.54
45	7455084.58	627814.30	5091.00	5091.14	0.14
46	7455114.71	627811.62	5090.15	5090.44	-0.51
47	7455108.45	627826.39	5090.98	5090.54	-0.40
48	7455106.28	627840.14	5091.00	5090.80	-0.20
49	7455114.34	627792.16	5090.56	5091.27	0.31
50	7455117.45	627791.33	5091.84	5091.50	-0.34
51	7455085.54	627784.02	5091.47	5091.42	-0.05
52	7455104.45	627784.19	5092.13	5091.72	-0.41
53	7455100.73	627781.28	5092.01	5091.76	-0.31
54	7455086.81	627771.40	5091.78	5091.71	-0.08
55	7455083.82	627768.84	5093.00	5092.82	-0.18
56	7455085.32	627752.50	5093.00	5092.48	-0.52
57	7455086.41	627758.48	5092.18	5092.32	-0.46
58	7455004.71	627668.01	5094.00	5093.54	-0.46
59	7455038.25	627736.45	5092.48	5092.42	-0.06
60	7455040.86	627744.14	5092.85	5092.80	-0.05
61	7455034.28	627754.71	5091.92	5092.05	0.13
62	7455033.45	627768.06	5091.44	5091.92	0.48
63	7455034.45	627775.92	5091.71	5092.15	0.44
64	7455042.91	627783.84	5091.00	5091.56	0.56
65	7455050.05	627759.51	5092.09	5092.05	0.02
66	7455056.85	627764.15	5093.13	5091.84	0.14
67	7455060.45	627774.52	5091.47	5091.71	0.24
68	7455225.41	627822.18	5090.71	5091.45	1.27
69	7455252.10	627822.98	5091.01	5091.45	0.41
70	7455265.42	627806.56	5091.88	5091.98	0.38
71	7455280.88	627781.24	5092.48	5092.01	-0.48
72	7455280.19	627764.94	5092.13	5092.01	-0.12
73	7455300.16	627788.52	5091.24	5092.02	0.78
74	7455340.41	627824.28	5088.33	5092.02	1.69
75	7455328.38	627780.11	5093.02	5092.51	-0.51
76	7455324.26	627744.20	5091.28	5091.98	0.64
77	7455326.41	627734.45	5093.08	5092.02	-1.06
78	7455345.90	627751.28	5092.11	5092.15	0.01
79	7455364.78	627748.45	5093.84	5093.05	-0.79

CURVE TABLE

CURVE	DELTA	LENGTH	RADIUS	TANGENT
C301	11°39'42"	4.78	1550	2.41
C302	45°40'26"	12.36	1550	6.53
C303	44°59'28"	12.11	1550	6.42
C304	41°32'52"	11.24	1550	5.86
C305	4°58'08"	2.50	1550	1.25
C306	16°20'11"	4.46	1550	2.50
C307	5°42'21"	2.48	1550	1.25
C308	30°16'56"	8.11	1550	4.11
C309	76°17'05"	20.64	1550	11.77
C310	6°19'54"	55.25	500.00	27.66
C311	5°43'30"	22.80	2500	12.14
C312	3°20'46"	8.48	1550	4.36
C313	11°48'16"	5.06	1550	2.55
C314	10°35'32"	2.85	1550	1.48
C315	14°52'42"	4.02	1550	2.02
C316	19°44'52"	5.01	1550	2.56
C317	28°50'33"	8.11	1550	8.21
C318	40°18'27"	10.86	1550	5.68

LINE TABLE

LINE	LENGTH	BEARING
L301	12.36	S22°51'16"E
L302	88.48	S41°38'00"E
L303	48.62	S61°17'26"E
L304	41.15	N81°30'26"E
L305	20.44	N08°17'56"E
L306	52.24	N15°32'45"E
L307	8.45	N32°47'26"W
L308	88.26	N06°20'47"W
L309	44.85	N58°48'56"W
L310	15.52	S64°30'57"W
L311	45.24	S06°53'38"E
L312	56.41	S07°26'20"W
L313	97.06	N85°40'06"E
L314	24.15	S15°38'38"E
L315	13.90	S65°27'08"E
L316	17.11	S31°54'41"E
L317	21.19	N81°36'16"E
L318	62.35	N68°43'46"E
L319	11.46	N28°40'30"E
L320	7.18	N84°41'28"E
L321	21.41	N11°39'51"W
L322	15.21	N60°38'26"W
L323	11.44	N80°28'50"W
L324	15.65	N62°42'55"W
L325	12.01	N68°41'01"W

LINE TABLE

LINE	LENGTH	BEARING
L326	4.53	S18°07'20"W
L327	7.31	S85°13'48"W
L328	21.44	N08°11'07"E
L329	13.85	N12°07'36"W
L330	16.56	S64°01'49"W
L331	15.82	S80°06'29"W
L332	56.34	S00°52'42"W
L333	32.40	S02°40'18"W
L334	28.03	S64°42'37"W
L335	7.56	S25°46'51"W
L336	14.58	S71°02'41"E
L337	24.00	S32°52'03"E
L338	10.47	N89°27'50"E
L339	60.04	N86°38'40"E
L340	6.24	N81°30'06"E
L341	10.82	S66°58'21"E
L342	7.93	N82°45'31"E
L343	8.58	N48°39'48"E
L344	7.31	N30°14'26"E
L345	10.77	N10°27'46"E

ARCHITECTURE ENGINEERING TECHNOLOGY
M3 Engineering + Technology Corporation
Tucson, Arizona
Tel. (520) 293-1188
FAX No. (520) 293-8177

Revisions

Description	Date

Drawing Title
CENTRAL CLUSTER
HORIZONTAL CONTROL PLAN

Discipline Sheet Number
C1

M3PN 03082.01

NATIONAL RADIO ASTRONOMY OBSERVATORY
operated by ASSOCIATED UNIVERSITIES INC. in agreement with THE NATIONAL SCIENCE FOUNDATION
ALMA PROJECT - ASG SITE
CENTRAL SITE
ANTENNA FOUNDATION PACKAGE
949 N. CHERRY AVE.
CAMPUS BLDG. 65
TUCSON, AZ 85721-0655

SIZE: E | SCALE: 1:1 | DRAWING NO.: SITE-20.02.01.01-003-A-DWG | REV: A

APPROVALS	NAME	DATE
ALMA ASSISTANT DIRECTOR	Steven Rahlfes	2003-05-05
DES:		2003-05-05
JTU:		2003-05-05

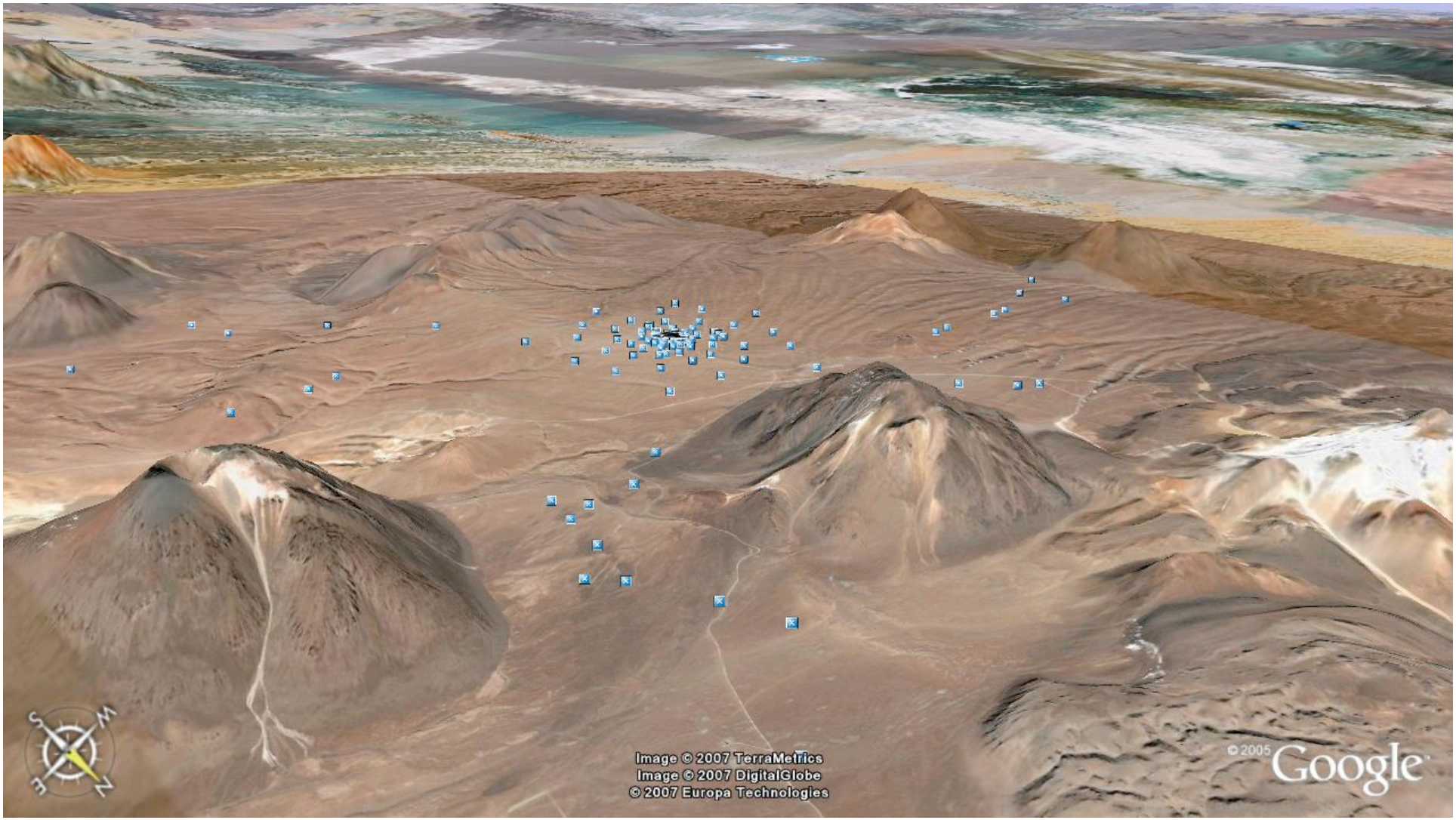
Image © 2007 TerraMetrics
Image © 2007 DigitalGlobe
© 2007 Europa Technologies
© 2005 Google

Antenna Status

- Vertex:
  - Delay: insulation. ~4-8 weeks?
  - This week: reviewing acceptance plans.

- ALMA-J:
  - 12-m antennas:
    - Three at OSF - AI
    - Remaining antenna: 2008

  - 7-m antennas:
    - Contract for #1 (prototype) signed early April.
    - Remaining 11 contract: April 2008

- AEM:
  - On schedule since PPDR.
  - Technical issue: metrology tiltmeters: new testing at ATF promising.
  - Steel fabrication started in Spain, cabin being manufactured in France.

Antenna Prototypes at ALMA
Test Facility: 2005

Vertex #1: August 2007
SKY TRAK

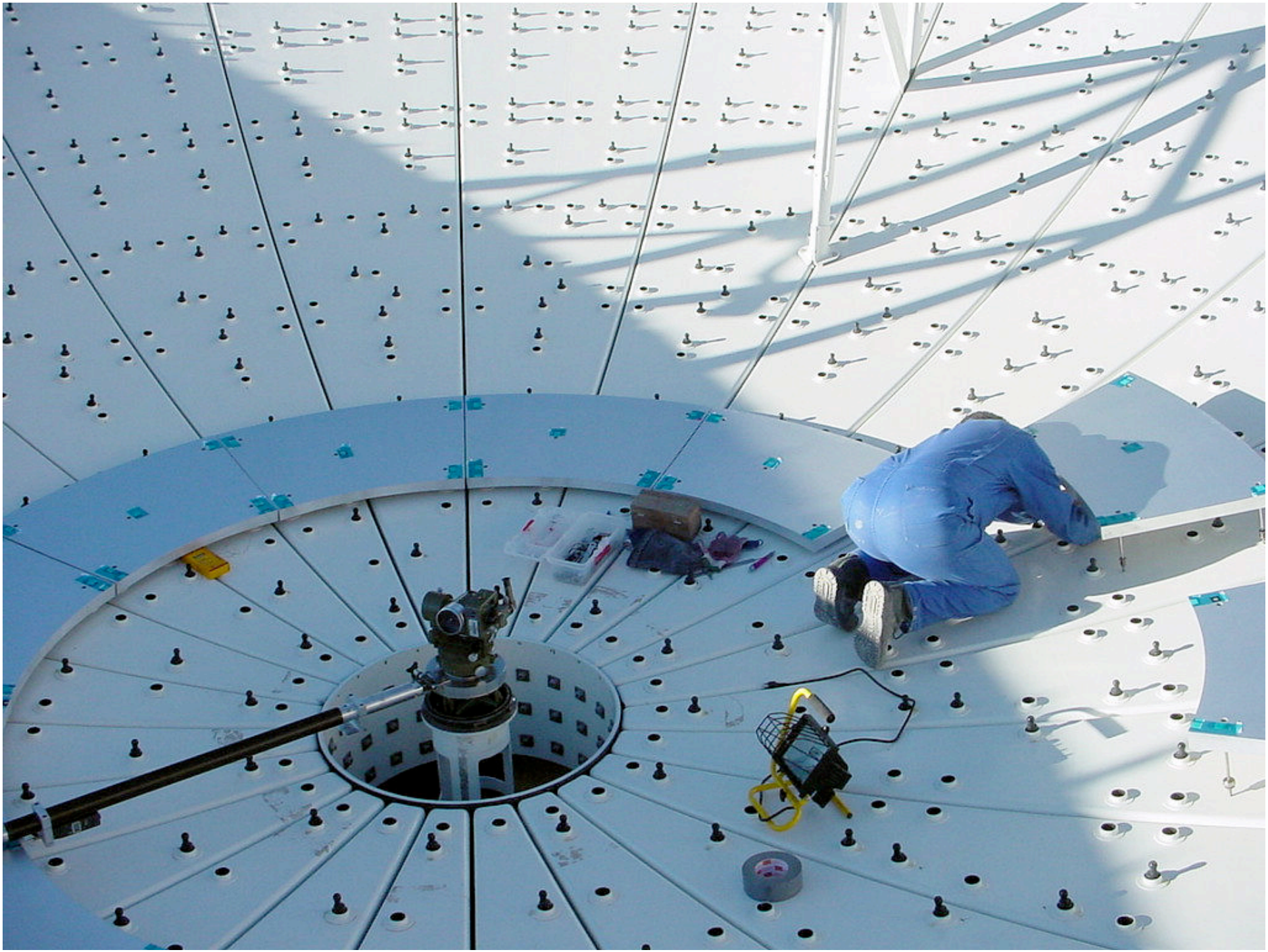

MELCO #1-3: August 2007

MELCO : August 2007

ALMA Transporter

Transporter – May 2007

Antenna Transporter

Atmospheric Opacity

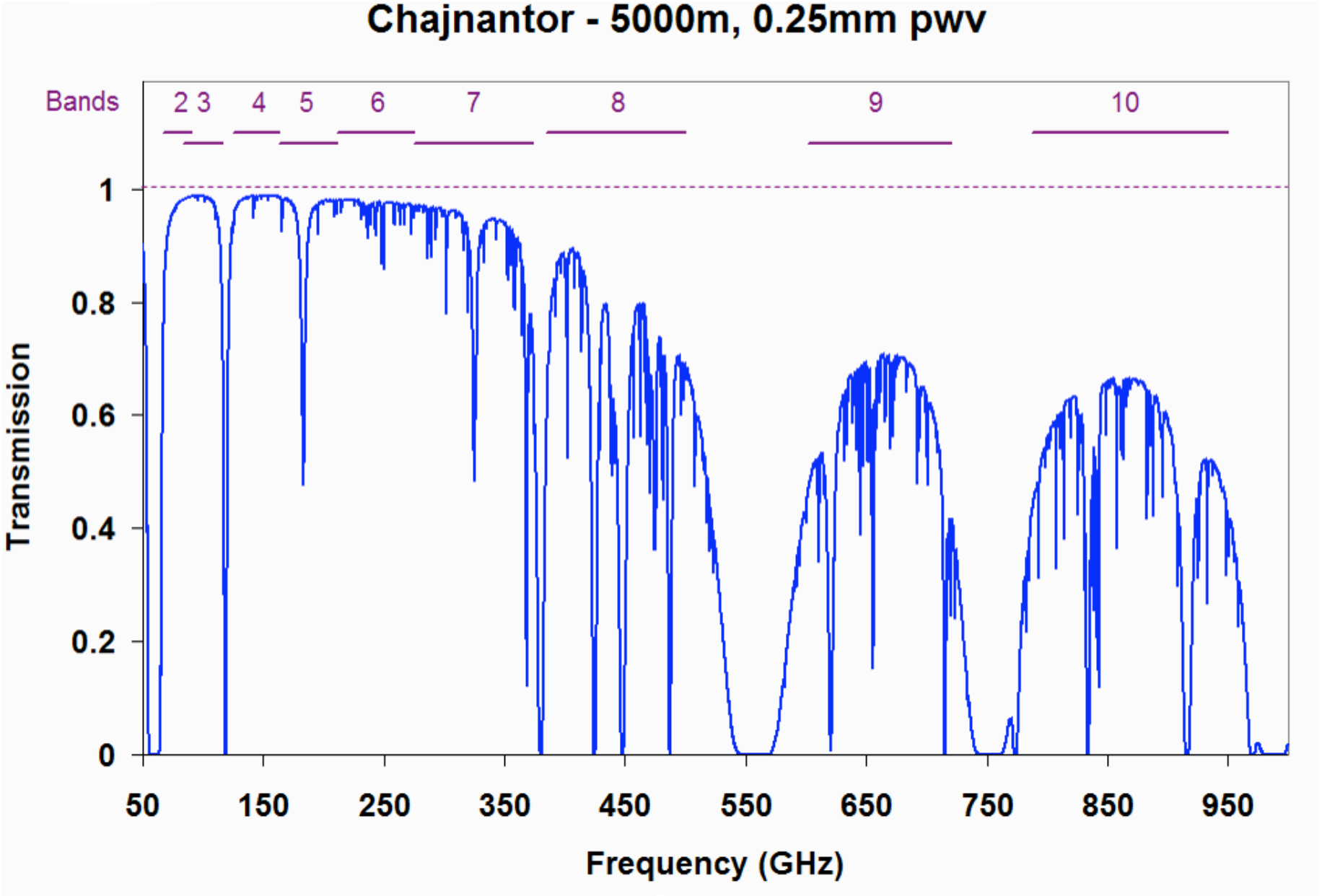

Receivers/Front Ends

ALMA Band	Frequency Range	Receiver noise temperature		Mixing scheme	Receiver Type	Supplier
		T(Rx) over 80% of RF band	T(Rx) at any RF frequency			
1	31.3 – 45	17 K	28 K	USB	HEMT	Not assigned
2	67 – 90	30 K	50 K	LSB	HEMT	Not assigned
3	84 – 116	37 K (40K)	62 K (50K)	2SB	SIS	HIA
4	125 – 169	51 K(45K)	85 K (~55K)	2SB	SIS	NAOJ
5	163 - 211	65 K	108 K	2SB	SIS	OSO
6	211 – 275	83 K (40K)	138 K (60K)	2SB	SIS	NRAO
7	275 – 373	147 K (75K)	221 K (100K)	2SB	SIS	IRAM
8	385 – 500	196 K (160K)	294 K (~270K)	2SB	SIS	NAOJ
9	602 – 720	175 K (120K)	263 K (150K)	DSB	SIS	NOVA
10	787 – 950	230 K	345 K	DSB	SIS	NAOJ ?

- Dual, linear polarization channels:
  - Increased sensitivity
  - Measurement of 4 Stokes parameters
- 183 GHz water vapour radiometer:
  - Used for atmospheric path length correction

Receivers/Front Ends

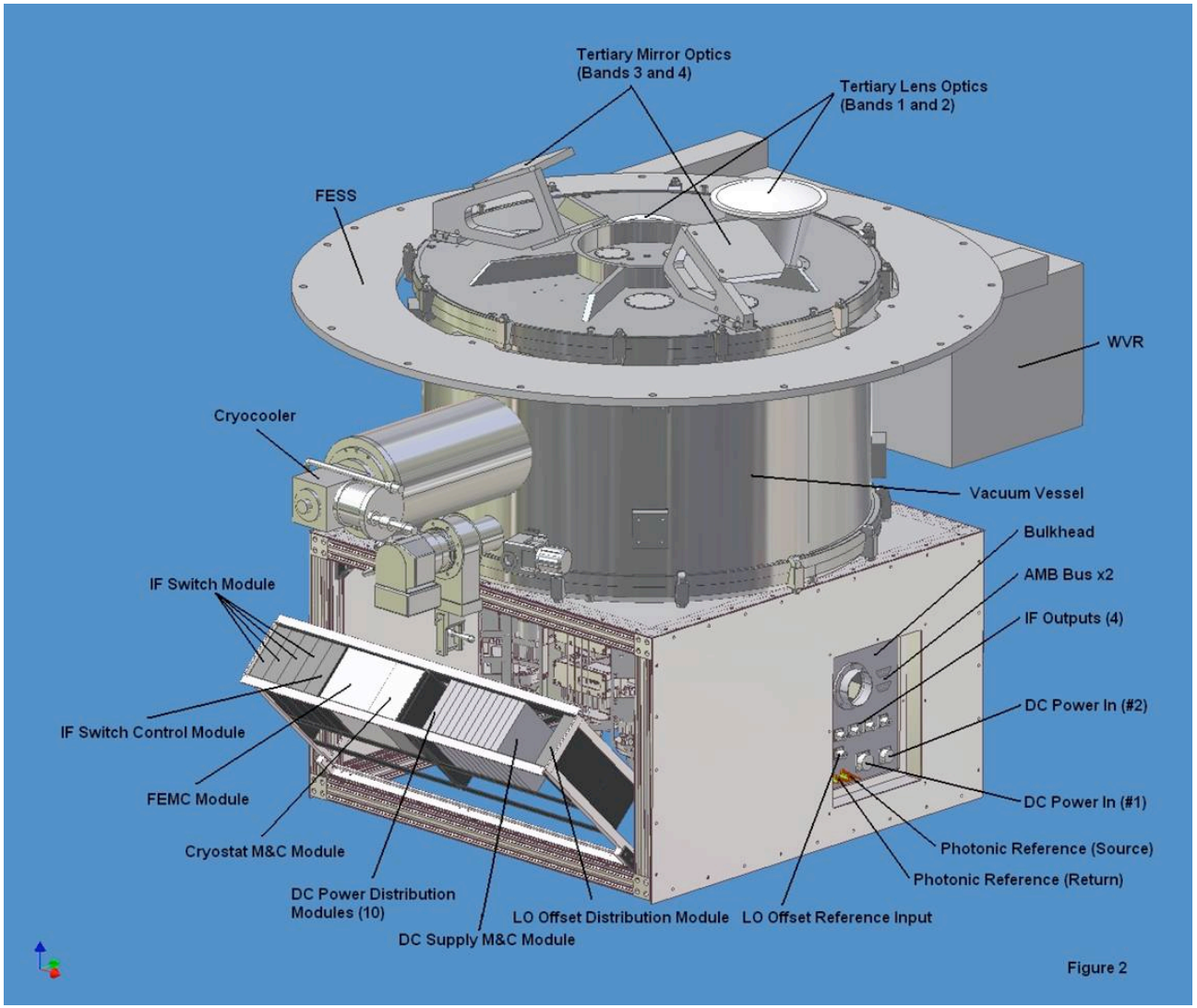

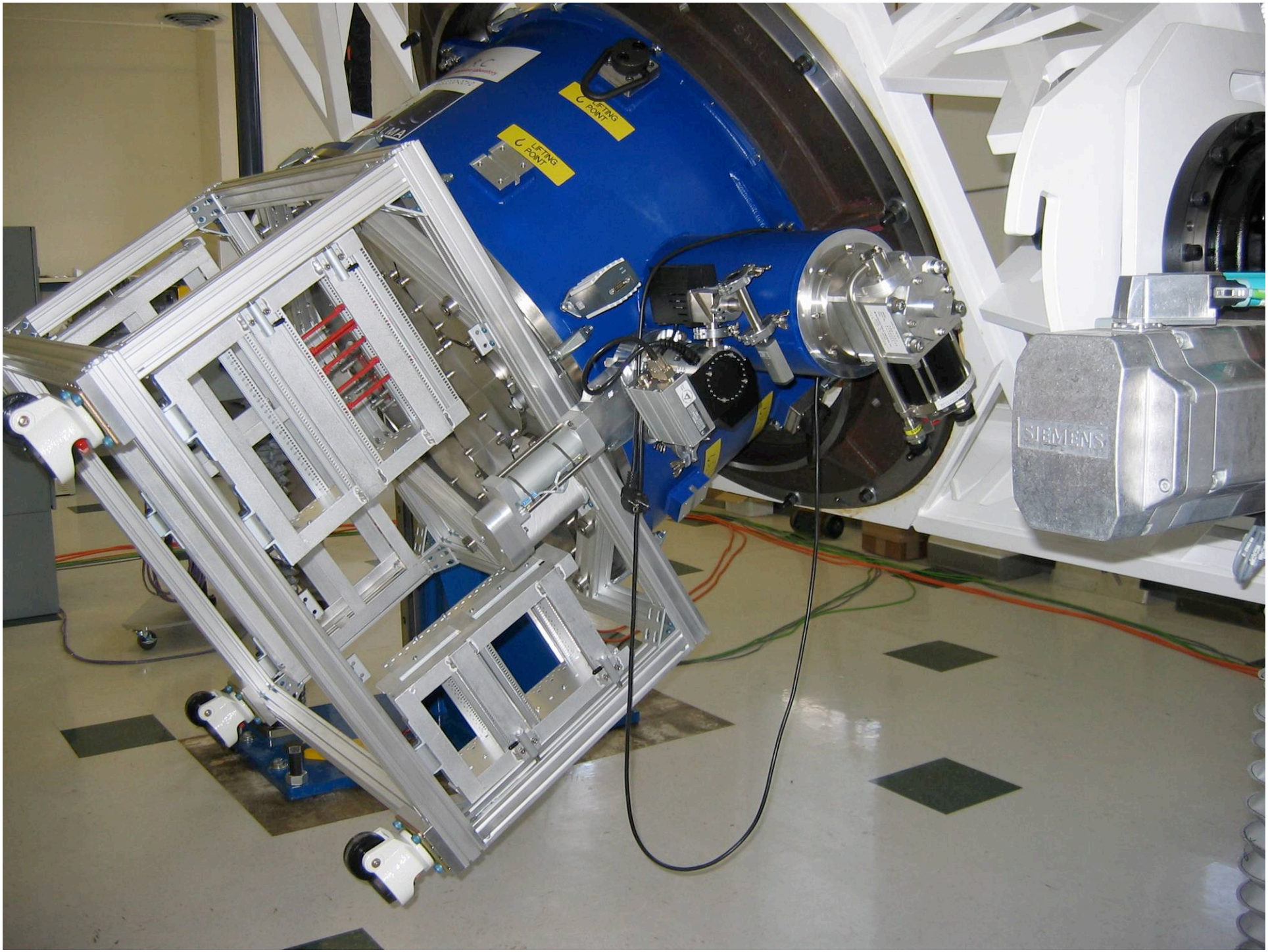
LIFTING POINT
LIFTING POINT
SIEMENS

FE #1 (4 cartridges)

Band 3

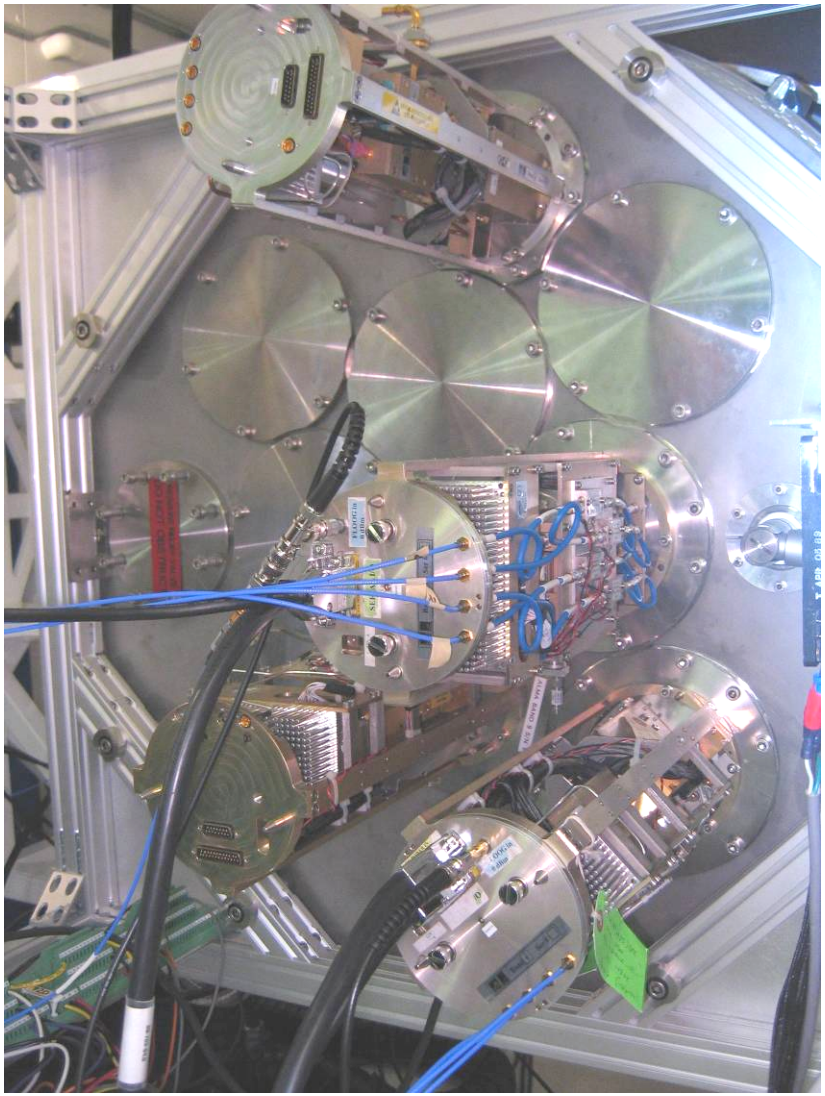

Band 7

Band 9

Band 6

Back End → Correlator (digital transmission) + central LO

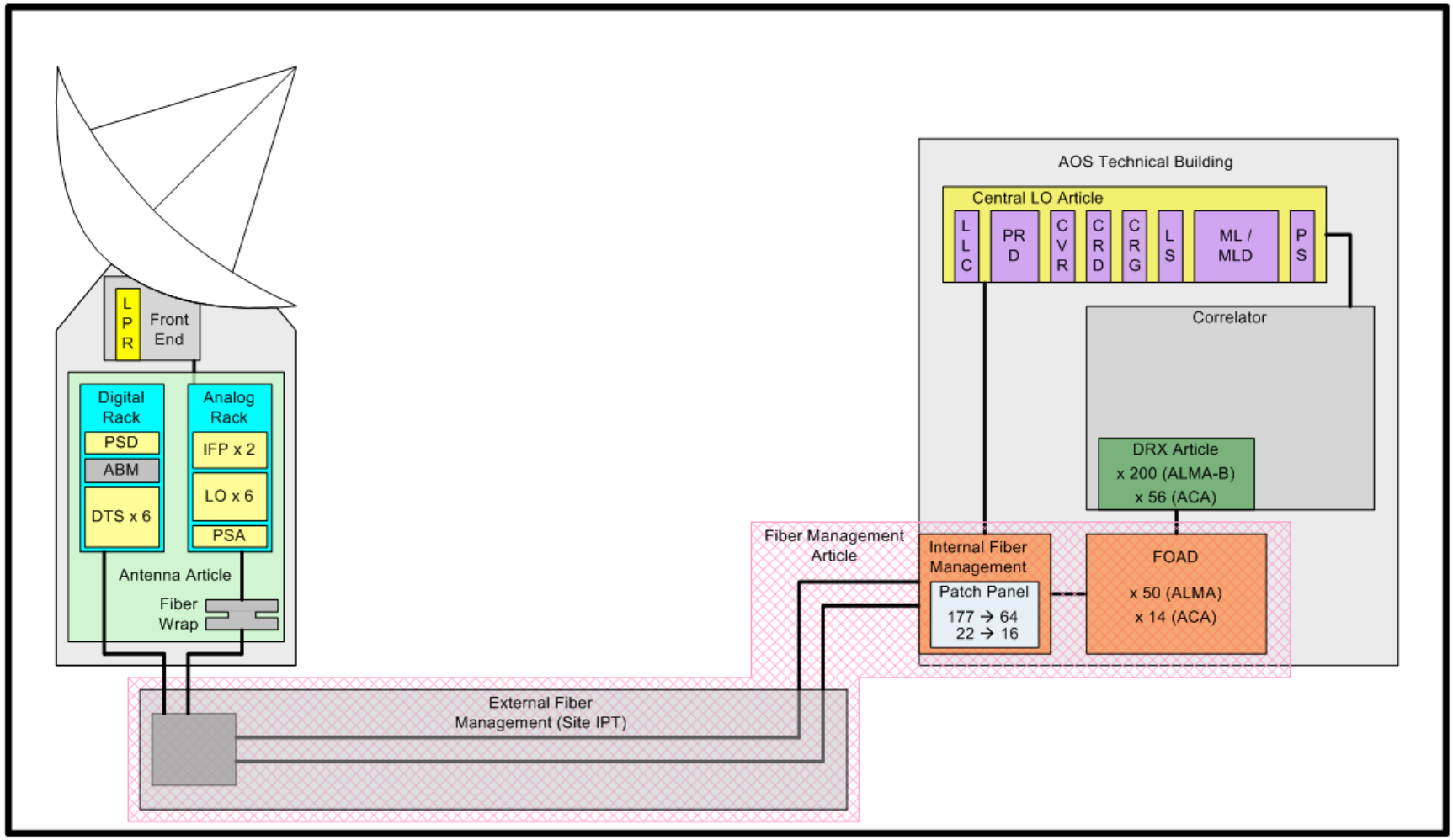

Back End – LO, DTS

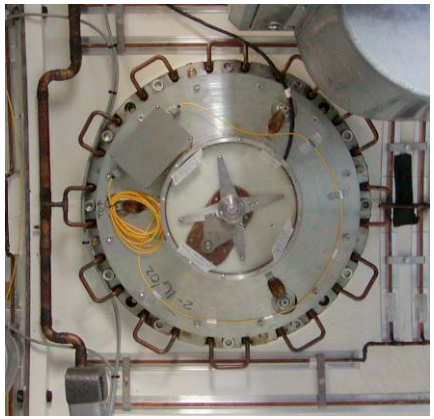

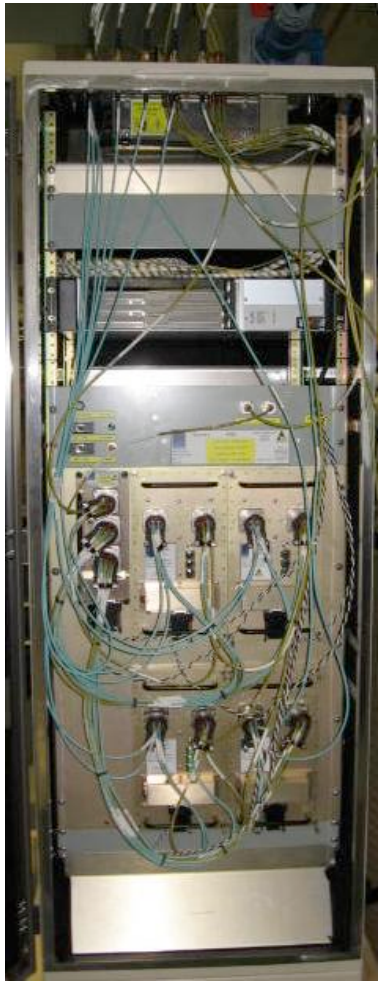

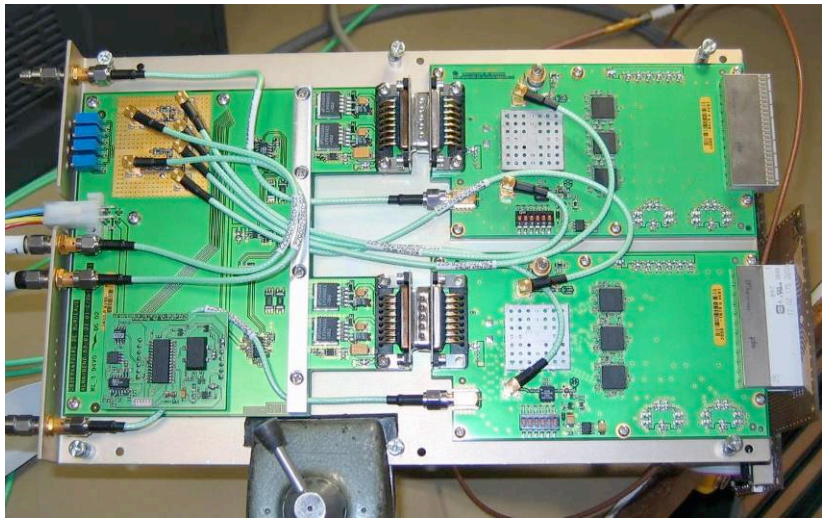

Correlator Specifications

Number of antennas	64
Number of IF pairs per antenna	4
Max. sampling rate per IF pair	2 x 4 GHz
Digitizing format	3 bit, 8 level
Correlating format	2 bit, 4 level
Max. delay range	30 km
Channels per IF pair	4096
Autocorrelation channels per baseline	1024
Polarization	Full stokes (4 products)

…plus ACA Fujitsu correlator (16-station)

Correlator Quadrant (1 of 4)

Complete correlator contains 2912 printed circuit boards and 5200 interface cables; there are more than 20 million solder joints.

Second quadrant in production + 2nd new test correlator

+ Fujitsu 16-ant correlator (same specs)…

Computing

- The fundamental output of the CIPT will be a ~2M SLOC "end to end" software system running on over 200 computers on 4 continents.
- Difficult distributed development – software engineering practices, travel
- Using CASA as the offline system (also AIVC)
- Combined: bilateral & East-ASIA development team

ALMA-J

- New partner: Agreement signed between the NSF-ESO-NINS Sept 2004/July 2006.

  - Four additional 12-m antennas (total power)
  - Twelve 7-m diameter antennas in compact configuration: Atacama Compact Array
  - Separate ACA correlator
  - Receiver: Bands 4, 8… 10

Atacama Compact Array – ACA

- Significantly improves low surface brightness sensitivity of ALMA; add precision total power data
- Full interoperability: Array-wide subarraying & cross-correlation.

Santiago Central Office

ESO Vitacura

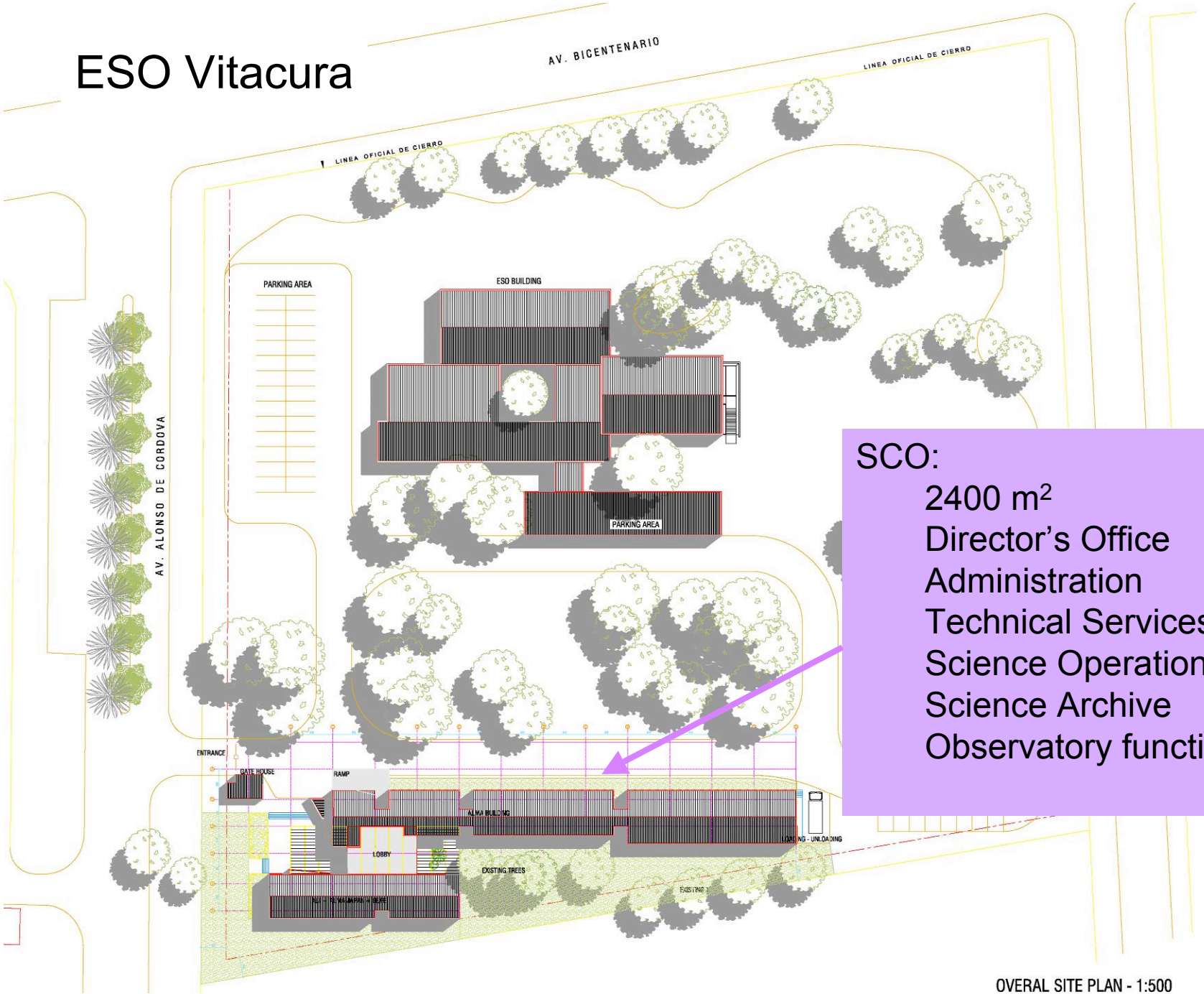

SCO:

- 2400 m^2
- Director's Office
- Administration
- Technical Services
- Science Operations
- Science Archive
- Observatory functions

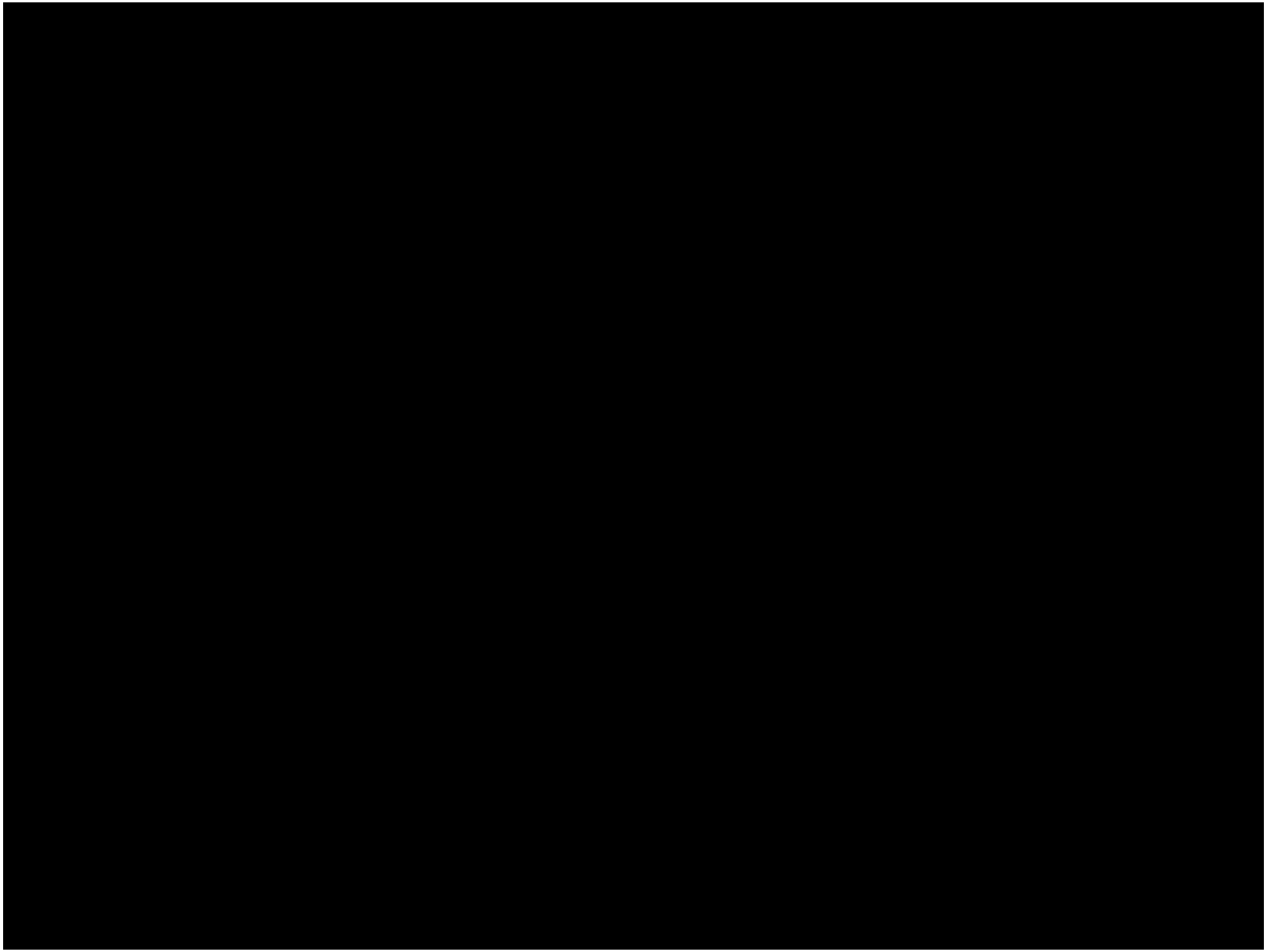

www.alma.info

The Atacama Large Millimeter Array (ALMA) is an international astronomy facility. ALMA is a partnership between Europe, North America and Japan, in cooperation with the Republic of Chile. ALMA is funded in North America by the U.S. National Science Foundation (NSF) in cooperation with the National Research Council of Canada (NRC), in Europe by the European Southern Observatory (ESO). ALMA construction and operations are led on behalf of North America by the National Radio Astronomy Observatory (NRAO), which is managed by Associated Universities, Inc. (AUI), on behalf of Europe by ESO, and on behalf of Japan by the National Astronomical Observatory of Japan.